

Properties of Fragmentation Photons in p+p Collisions at 200GeV Center-of-Mass Energies

J. A. Hanks

Professor Brian Cole

Submitted in partial fulfillment of the
requirements for the degree of
Doctor of Philosophy
in the Graduate School of Arts and Sciences

COLUMBIA UNIVERSITY

2010

©2010

J. A. Hanks

All Rights Reserved

Abstract

Properties of Fragmentation Photons in p+p Collisions at 200GeV Center-of-Mass Energies

J. A. Hanks

The strong modification to the production of final state hadrons in heavy ion collisions is a key signature of the hot dense medium produced at energies achieved at the Relativistic Heavy Ion Collider (RHIC). Understanding the mechanisms for the parton energy loss responsible for these modifications is challenging and difficult to constrain with straightforward hadronic measurements, making it necessary to turn to more discriminating probes. One example of such a probe is photons produced by partons as they fragment, fragmentation photons, because the production mechanisms for such photons are similar to those for hadrons, but once produced, fragmentation photons will not interact directly with the medium.

The challenge of distinguishing the signal for such jet-associate photons out of the large decay background motivates first making such measurements in the simple p + p environment. Combining data collected by the PHENIX detector during 2005 and 2006, the yield for fragmentation photons was measured to be on the order of several percent of all photons measured in association with a hadron with transverse momentum between 2 and 5 GeV/c. The use of two-particle correlations coupled

with a sophisticated method for identifying and removing decay photons has made it possible to further study the jet properties of these fragmentation photons, in the form of p_{out} and $\sqrt{\langle j_T^2 \rangle}$. These results will help to constrain both the underlying theoretical description of direct photon production in $p + p$, and modifications expected in heavy ion collisions.

Contents

List of Figures	vi
List of Tables	xxx
Acknowledgments	xxxiii
Dedication	xxxv
1 Introduction - Motivation from the Quark-Gluon Plasma	1
1.1 A new state of matter	2
1.2 The heavy ion environment	6
1.2.1 Elliptic flow	7
1.3 Energy loss and jets	10
1.3.1 Jet modification	13
1.4 Direct photons	17
1.4.1 Thermal photons	19
1.4.2 Direct photons from jets	20
1.4.3 Direct photon correlations	24
1.5 Statement of purpose	25

2 QCD and the photon	27
2.1 Quantum Chromodynamics	27
2.2 Perturbative QCD in practice	36
2.2.1 Deep inelastic scattering and factorization	37
2.2.2 e^+e^- annihilation and fragmentation functions	44
2.3 QCD in hadronic collisions	49
2.3.1 k_T smearing	51
2.4 Jets and parton showering	54
2.4.1 Jet rates	55
2.4.2 Jet shape	56
2.4.3 Parton showering	63
2.5 Direct photons	66
2.5.1 Photons at leading order	67
2.5.2 Photons beyond leading order	71
3 Detection	79
3.1 RHIC	80
3.1.1 Accelerating to RHIC	81
3.2 PHENIX Overview	83
3.3 PHENIX Central Tracking	85
3.3.1 The Drift Chamber	86
3.3.2 The Pad Chambers	88
3.4 The Electromagnetic Calorimeter	89

3.4.1	Electromagnetic showering	90
3.4.2	Pb-scintillator vs. Pb-glass	92
3.5	Electron identification	94
3.6	Event and Vertex detectors	95
3.6.1	Triggering on rare physics	97
3.7	Data acquisition and event reconstruction	99
3.7.1	Track reconstruction	101
3.7.2	Cluster reconstruction and calibration	104
4	Hadron-Photon correlations and jets	108
4.1	Data and event selection	109
4.1.1	Run quality	110
4.1.2	Hadron cuts	116
4.1.3	Photon cuts	121
4.2	Two particle correlations	132
4.2.1	Detector acceptance and event mixing	133
4.2.2	The underlying event	138
4.3	Efficiency corrections	149
4.3.1	Triggered data sets	151
4.4	Extracting physics beyond per-trigger yields	156
4.4.1	Pair cross-sections	158
4.4.2	p_{out} and j_T	160
4.5	Propagating uncertainties	164

5 Extracting the fragmentation photon signal	166
5.1 Estimating the decay photon yield	167
5.1.1 Testing the method	168
5.2 Tagging π^0 and η decay photons	172
5.2.1 Tagging efficiencies	175
5.2.2 The false-tagged background	179
5.2.3 Minimum bias event mixing	181
5.3 Tagging probabilities	191
5.3.1 Testing the method	195
5.3.2 Tagging probabilities in the data	198
5.3.3 Tagging efficiency revisited	200
5.3.4 Hadron trigger effects	202
5.3.5 Full method in PISA	205
5.3.6 Systematic Uncertainties	213
6 Results	215
6.1 Correlated per-trigger yields	215
6.2 Hadron- γ_{frag} pair cross-section	216
6.3 Relative pair yield	219
6.4 Associated photon p_{out}	225
6.5 $\sqrt{\langle p_{out}^2 \rangle}$ and $\sqrt{\langle j_T^2 \rangle}$	227
7 Conclusions	232

Bibliography	238
A h-γ $\Delta\phi$ dependent per-trigger yields	251
A.1 π^0 and η decay photons	251
A.2 Inclusive, decay, and fragmentation photons	254
B Distributions to go from p_{out} to j_T	257
B.1 $p_{out,h}$	257
B.2 x_h	259
B.3 x_h^{-1}	260
C Data Tables	261
C.1 Pair cross sections and ratios of yields	261
C.2 Associated photon p_{out}	263
C.3 Associated photon $\sqrt{\langle p_{out}^2 \rangle}$ and $\sqrt{\langle j_T^2 \rangle}$	266

List of Figures

1.4	Elliptic flow parameter v_2 as a function of n_{ch}/n_{max} , a measure of the amount the colliding nuclei overlap, where v_2 is extracted from measurement of the correlation between particle pairs. The different points correspond to different ways of pairing particles: randomly chosen pairs (circles), opposite signs of charge (crosses), same signs of charge (triangles), and opposite signs of pseudorapidity (squares) [14].	8
1.5	The Nuclear modification factor, R_{AA} , for π^0 s (open red boxes) and charged hadrons (solid blue boxes), as a function of p_T for different centrality classes.[21]	12
1.6	Illustration of the two particle correlation distribution resulting from jets.[30]	14
1.7	Jet yields from two-particle correlations in $\Delta\phi$ for various p_T ranges ($p_T^a \otimes p_T^b$), arranged by increasing pair energy, for p + p in open circles and Au + Au in solid black circles. The solid red and blue lines indicate the uncertainties associated with subtracting the elliptic flow contribution [30].	16
1.8	R_{AA} for direct photons (black squares), neutral pions (blue circles) and η s (red triangles) for central Au + Au collisions [32].	18

1.9	Invariant cross section ($p + p$) and invariant yield ($Au + Au$) of direct photons vs p_T . The dashed curves show a modified power-law fit to the $p + p$ data scaled by N_{coll} and the black curves are an exponential plus the scaled fit. The curves on the $p + p$ data come from pQCD calculations [35].	20
1.10	Calculation of the total direct photon cross-section for central $Au + Au$ collisions, with each of the contributions shown separately as well, and compared to the measured cross section (0 – 10% centrality) [37].	21
1.11	Calculations of direct photon R_{AA} as a function of p_T in central $Au + Au$ (solid lines) and $Cu + Cu$ (dashed lines) and comparison with data. For $Au + Au$, the solid green line includes induced photon radiation and jet conversion, without suppression through parton energy loss, and the solid red line includes energy loss suppression as well as the medium-induced sources [41].	22
1.12	Calculation of the R_{AA} , as a function of p_T , for fragmentation photons (including induced emission), both with (solid line) and without (dashed line) energy-loss suppression [40].	23
2.1	QCD Feynman vertices. (a) illustrates gluon absorption/emission by a quark. (b) illustrates gluon absorption/emission by another gluon. (c) illustrates direct gluon-gluon interaction.	29

2.2	The pQCD prediction for the dependence of the QCD coupling α_s , on the momentum scale, Q , compared to values of α_s extracted using data for several different observables. The open and closed symbols correspond to the determination of α_s from data at different orders in the perturbative expansion [52].	32
2.3	The QCD potential as a function of distance, R (in units of the lattice spacing), calculated from lattice QCD [54]. The solid line shows a fit to the numerical values of the given form.	34
2.4	Free energy of a heavy quark pair as a function of the separation in lattice units calculated from the lattice at several different temperatures [55].	35
2.5	Leading order Feynman diagrams for the deep inelastic scattering of a lepton on a hadron with the corresponding four-momenta assigned to the particles in parentheses.	37
2.6	The <i>Bjorken x</i> dependence of the F_2 structure function for several values of Q^2 , from SLAC-MIT, BCDMS, H1 and ZEUS [57]. . . .	39
2.7	The proton structure function $F_2(x)$ for two values of Q^2 (3.5 GeV^2 and 90 GeV^2). Here the breaking of scaling can be seen at $x \sim 0.14$ with one set of pQCD predictions shown to be in good agreement [63].	42
2.8	Distributions of x times the parton distributions, denoted $f(x)$, for several partons in the proton at two energy scales, 20 GeV^2 (left) and 10,000 GeV^2 (right) [63].	43

2.9	Leading order Feynman diagrams for $e^+e^- \rightarrow q\bar{q}$	45
2.10	World data on total cross-section of $e^+e^- \rightarrow hadrons$ as a function of the center-of-mass collision energy, \sqrt{s} . The dashed-line curve (green) is a naive quark-parton model prediction and the solid-line curve (red) is the 3-loop pQCD prediction [63].	46
2.11	e^+e^- fragmentation functions as a function of x at several energy scales [69].	48
2.12	Feynman-diagram-like picture of hadron-hadron collisions decomposed into the initial soft and final soft processes and the underlying parton scattering.	49
2.13	The inclusive jet cross-section as a function of jet E_T measured by CDF and compared to NLO pQCD calculations. Only statistical errors are shown. Data and theory agree within quoted systematic uncertainties [89].	56
2.14	The thrust distribution measured at LEP by DELPHI with predicted distributions at leading-order for vector (solid line) and scalar (dashed line) gluon theories [57].	57
2.15	On the left is the mean (right axis) and RMS (left axis) k_T as a function of trigger p_T using two independent methods for extracting $\langle k_T \rangle$ from the correlated away-side, for different \sqrt{s} . On the right is the mean and RMS j_T vs. trigger p_T (top) and \sqrt{s} (bottom). Both are from two-particle correlations with ISR data [91].	59

2.16 Jet profile for jet $E_T = 100$ GeV, reconstructed using a cone algorithm with $R = 1$ [57].	62
2.17 (a) Example of a parton shower diagram. (b) Clustering of shower components into final state hadrons.	63
2.18 Measured $1 - \psi(0.3/R)$, as a function of jet p_T for jets with a rapidity from 0.1 to 0.7, compared to various simulations (see text for descriptions) [93].	65
2.19 Leading order Feynman diagrams for direct photon production in QCD hard scatterings. The two quark-gluon Compton diagrams are shown on the top, and the two annihilation diagrams are on the bottom.	67
2.20 The ratio of the measured γ -jet cross-section to NLO QCD predictions, as a function of photon p_T . Here y^{jet} is the rapidity of the jet opposite the direct photon. The yellow band represents the uncertainty in the initial PDFs, and the dotted and dashed lines represent theoretical scale uncertainties [106].	70
2.21 The ratios of data to theory for a range of collider and fixed target data as a function of x_T . The CDF and D0 data are for isolated direct photons only [109].	71
2.22 Two next-to-leading order Feynman diagrams for direct photon production in QCD hard scatterings.(a) is an example of gluon radiation by hard scattered quark. (b) is an example of photon radiation by the hard scattered quark.	72

2.23 Ratio of fragmentation photons to inclusive direct photons as a function of photon p_T calculated using a next-to-leading order simulation [110].	73
2.24 The photon energy spectrum measured by OPAL compared to several predictions including various orders in the perturbative expansion (LO and HO) as well as non-perturbative corrections (HOPL and BLL) [112].	74
2.25 The cross-section for photons in jets as a function of their fractional jet energy measured by ALEPH compared to BLL predictions [111].	75
2.26 The direct photon cross-section as a function of photon p_T at $\sqrt{s} = 200$ GeV compared to an NLO pQCD calculation. The bottom panel shows the relative difference between data and theory, with the range for the uncertainties on both [115].	77
3.1 The RHIC ring with the original four detectors [117].	83
3.2 The PHENIX Detector. Side view (left). Beam view (right) [118]. .	84
3.3 The PHENIX Magnetic Field. Side View (left). Total field strength $B_{Mod}(R)$ vs. R for the three field configurations available [125]. . . .	86
3.4 The Drift Chamber. Left: A side-view layout of the wire position in a sector of the drift chamber with a close-up of one group of wires. Right: A top-view diagram of the stereo wire orientation [124]. . . .	87
3.5 Diagram of a single pad chamber [124].	88

3.6	Illustration of an electromagnetic cascade. As indicated, the radiation length X_0 is the distance an electron or photon will travel in the material before interacting.	91
3.7	Diagrams of the electromagnetic calorimeters. Left: A module of Pb-scintillator towers. Right: A supermodule of Pb-glass towers [126].	92
3.8	Schematic of the full PHENIX DAQ and triggering system.	100
3.9	The path a track takes through the PHENIX central arm. Hits used for reconstruction are indicated by white stars. Hits matched with track projection (blue arrow) are indicated by red stars.	102
3.10	χ^2 distributions for showers produced by 2 GeV/c electrons (solid line) and pions (dashed line) in the Pb-scintillator.	104
3.11	Example of the invariant mass distribution for photon pairs showing the clear peak at an invariant mass equal to the mass of a π^0 .[126] . .	106
4.1	BBC z vertex distribution (cm). Events analyzed are required to have $ z < 30$ cm.	110
4.2	Average track p_T vs. run number (left). Average cluster p_T vs. run number (right).	112
4.3	Average track multiplicity vs. run number (left). Average photon multiplicity vs. run number (right).	113

4.4	π^0 mass peak position (top) and width (bottom) vs. run number for Run 6 prior to run-dependent recalibrations. The red line demonstrates the non-zero slope of the data for both the peak position and width.	114
4.5	π^0 mass peak positions (top) and widths (bottom) vs. run number for Runs 5 and 6.	116
4.6	ϕ vs. z distribution of tracks in the drift chamber, with fiducial cuts marked by the red lines, for Run 5 (left) and Run 6 (right)	119
4.7	Track pair Δz vs. $\Delta\phi$ for good tracks.	120
4.8	Radial distance between clusters and the closest track projected into the EMCal.	122
4.9	Distribution of the radial distance (in radians) between cluster pairs in the EMCal.	124
4.10	Cluster pair asymmetry vs. ΔR in four bins in leading photon p_T : 0.4 – 1.5 GeV/c (top left), 1.5 – 2.5 GeV/c (top right), 2.5 – 3.5 GeV/c (bottom left), and 3.5 – 15 GeV/c (bottom right).	125
4.11	Cluster pair asymmetry vs. ΔR with a cut of $m < 0.05$, as defined in 4.3, in four bins in leading photon p_T : 0.4 – 1.5 GeV/c (top left), 1.5 – 2.5 GeV/c (top right), 2.5 – 3.5 GeV/c (bottom left), and 3.5 – 15 GeV/c (bottom right).	126

4.12 Run 6 cluster time-of-flight(ns) vs. p_T is plotted on the left. Two projection of the two-dimensional distribution in the specified momentum range are plotted on the right: $0.4 < p_T < 1.5$ GeV/c (top) and $5.0 < p_T < 15.0$ GeV/c (bottom).	128
4.13 Distribution for central towers of photons from $1.5 - 3.5$ GeV/c for each sector in the EMCAL as a function of the z and y index of the tower. The data shown was taken during Run 6, for events required to fire an ERT trigger.	129
4.14 Distribution of the number of hits in central tower clusters from $1.5 - 3.5$ GeV/c for each EMCAL sector, fit with a Gaussian. The blue line indicates the 4σ cut used to identify hot towers. The data shown was taken during Run 6 for events required to fire an ERT trigger.	130
4.15 Distribution for central towers, after hot tower rejection, of photons from $1.5 - 3.5$ GeV/c for each sector in the EMCAL as a function of the z and y index of the tower. The data shown was taken during Run 6, for events required to fire an ERT trigger.	131
4.16 Example of the PHENIX acceptance for hadron-photon pairs within a fixed p_T range for each, as determined from event mixing.	134
4.19 Example of the multiplicity ratios for hadrons (left), with conditional photons p_T from $1.5-2$ GeV/c, (left) and photons (right), with hadron p_T from $2-2.3$ GeV/c : inclusive vs conditional.	146

4.20 (a) The $\Delta\phi$ distribution for hadron-photon pairs, $2 < p_{T,h} < 2.3$ GeV/c and $2.5 < p_{T,\gamma} < 3.5$ GeV/c (black), and event background (blue), with the scale (f) applied shown. The scaled background level and ZYAM background level are shown, as well as the % difference. (b) The $\Delta\phi$ distribution with the scaled background subtracted, with a blue dashed line showing zero yield.	147
4.26 p_{out}	160
5.1 The top plot shows the $h - \gamma$ distributions for all PYTHIA generated decay photons in black and scaled π^0 photons (equation (5.3)) in blue. The ratio of the distributions is plotted bellow it.	169
5.2 $\Delta\phi$ distributions for $h - \gamma$ pairs, for π^0 decay photons in black and η decay photons in blue.	170
5.3 The top plot shows the $h - \gamma$ distributions for all PYTHIA generated decay photons in black and the combined π^0 and scaled η photons (Equation (5.2)) in blue. The ratio of the distributions shown is plotted bellow.	171
5.4 Left: π^0 peak position (GeV/c ²) vs. the π^0 p_T (GeV/c). Right: π^0 peak width vs. the π^0 p_T (GeV/c). Each of the trigger hadron p_T bins is shown.	173
5.5 Left: η peak position (GeV/c ²) vs. the η p_T (GeV/c). Right: η peak width vs. the η p_T (GeV/c). Each of the trigger hadron p_T bins is shown.	174

5.6	2-D tagging efficiency for γ_{π^0} 's for the full PISA statistics, with the ϕ (top) and η (bottom) projected efficiencies on the right.	177
5.7	2-D tagging efficiency for γ_{η} 's for the full PISA statistics, with the ϕ (top) and η (bottom) projected efficiencies on the right.	178
5.8	Left: Integrated tagging efficiency for γ_{π^0} 's for each hadron trigger bin, and the full PISA statistics (purple). Right: Integrated tagging efficiency for γ_{η} 's for each hadron trigger bin, and the full PISA statistics (purple).	179
5.9	Invariant mass distribution for same-event (black) and mixed (red) pairs with the mixed pair distribution scaled by the number of events used for mixing.	180
5.10	Left: Invariant mass distributions for photon pairs from the same event (black) and different events (red). Right: Fit to remaining distribution after subtraction of the mixed yield from the real pair yield, with correlated background fit component shown in red. . . .	183
5.11	Left: Invariant mass distributions for photon pairs from the same event (black) and different events (red). Right: Fit to remaining distribution after subtraction of the mixed yield from the real pair yield, with correlated background fit component shown in red. . . .	184
5.12	False tagged background correction due to correlated background, for the four trigger p_T bins. The correction for the π^0 is shown on the left, and for the η on the right.	186

- 5.13 Left: The invariant mass distribution in PYTHIA for all photon pairs, around the π^0 mass peak (black) and the background invariant mass distribution for photons in the filtered event mixed with photons from an unfiltered PYTHIA event (red). Right: The mixed background subtracted invariant mass, fit with a Gaussian plus linear function, and the linear background fit result (red dashed line). . 187
- 5.14 Left: The invariant mass distribution in PYTHIA for all photon pairs, around the η mass peak (black) and the background invariant mass distribution for photons in the filtered event mixed with photons from an unfiltered PYTHIA event (red). Right: The mixed background subtracted invariant mass, fit with a Gaussian plus linear function, and the linear background fit result (red dashed line). . 188
- 5.15 $h\gamma\Delta\phi$ distributions used to test the false-tagging estimate. In black is the same-event(fg) tagged yield (raw counts), in red is the false-tagged background yield, in blue is the true decay yield, and in green is the correction for lost decay photons. The case for π^0 photons is shown on the left, and for η photons on the right. 189
- 5.16 In black is the true $h\gamma\Delta\phi$ distribution generated in PYTHIA, and in blue is the (fg-bg+lost) tagged photon distribution. The ratio of the two distributions is shown in the lower plot. The case for π^0 tagging is shown on right and for η tagging on the left. 190

5.17 Top left: tagging probability for π^0 photons - from PISA (black), using Eq. (5.13) with inputs directly from PISA (red) or obtaining p_a and p' from fits to $p_{tag}(n)$ (blue). Top right: probabilities from PISA - p , true pair (black); p^π , photon is from a π^0 (blue); p_a , pair photon is accepted (includes all cuts) (red), and p_a determined from fit (magenta). Bottom left: p' from Eq. (5.16) (blue) and from fit (black). Bottom right: % difference between tagging probability from PISA and from the equation with the different inputs. All vs.

$p_{T,\gamma}$ 196

5.18 Top left: tagging probability for η photons - from PISA (black), using Eq. (5.13) with inputs directly from PISA (red) or obtaining p_a and p' from fits to $p_{tag}(n)$ (blue). Top right: probabilities from PISA - p , true pair (black); p^π , photon is from a η (blue); p_a , pair photon is accepted (includes all cuts) (red), and p_a determined from fit (magenta). Bottom left: p' from Eq. (5.16) (blue) and from fit (black). Bottom right: % difference between tagging probability from PISA and from the equation with the different inputs. All vs.

$p_{T,\gamma}$ 197

5.19 In black is the true $h\gamma\Delta\phi$ distribution generated in PYTHIA, and in blue is the $(\frac{p_{true}}{p_{tag}} \cdot \text{fg+lost})$ tagged photon distribution. The ratio of the two distributions is shown in the lower plot. The case for π^0 tagging is shown on right and for η tagging on the left. 198

5.20 The probability of tagging a photon with momentum from 1.5 to 2 GeV/c vs. the number of photons in the event, fit using Eq. (5.12) with input from PISA.	199
5.21 The pair acceptance probability vs. $p_{T,\gamma}$ is shown on the left and the false tagging probability vs. $p_{T,\gamma}$ is shown on the right, extracted from fits to data (black) and determined from PISA (blue). The case for π^0 photons is shown on the top, and for η photons on the bottom.	200
5.22 The final average tagging probability for π^0 (top) and η (bottom) photons, as a function of photon p_T , comparing data and the value for p_{tag} determined from Eq. (5.13).	201
5.23 Near-side $\Delta\phi$ variation in the tagged photon probability for π^0 photons (left) and η photons (right).	203
5.24 Various probabilities that go into tagging π^0 photons. Top left: The pair acceptance probability, p_a , vs. $p_{T,\gamma}$ for the different hadron trigger bins obtained from fits to $p_{tag}(n)$. Top right: The false tagging probability, p' , vs. $p_{T,\gamma}$ for the different hadron trigger bins. Bottom left: the resulting tagging efficiency determined using the p_a shown. Bottom right: the resulting f_{false} correction determined using the p_a and p' shown.	204

5.25 Various probabilities that go into tagging η photons. Top left: The pair acceptance probability, p_a , vs. $p_{T,\gamma}$ for the different hadron trigger bins obtained from fits to $p_{tag}(n)$. Top right: The false tagging probability, p' , vs. $p_{T,\gamma}$ for the different hadron trigger bins. Bottom left: the resulting tagging efficiency determined using the p_a shown. Bottom right: the resulting f_{false} correction determined using the p_a and p' shown. 205

5.26 The final scale correction for π^0 tagged photons (left) and η tagged photons (right) and the percent difference between the estimated total tagging probability and the tagging probability in the data (bottom panels) as a function of photon p_T for each hadron trigger bin. 206

5.27 The total scale correction for simulated π^0 tagged photons (left) and η tagged photons (right) and the percent difference between the estimated total tagging probability and the tagging probability in the PISA (bottom panels) as a function of photon p_T for each hadron trigger bin. 207

5.28 The total scale correction for simulated π^0 tagged photons (left) and η tagged photons (right) and the percent difference between the estimated total tagging probability and the tagging probability in the PISA (bottom panels) as a function of photon p_T with different minimum p_T cuts for the pair photon. 208

5.29 True $h - \gamma_{\pi^0}$ (left) and $h - \gamma_{\eta}$ (right) $\Delta\phi$ dependent pair yield (black) and the estimated yield (blue) using the three sets of corrections. 209

5.30 Ratio of all non- π^0 decay photons to η decay photons, when paired with trigger hadrons of several p_T ranges on the near-side.	209
5.31 True total $h - \gamma_{decay}$ $\Delta\phi$ dependent pair yield (black) and the estimated $\pi^0 + \eta$ yield (blue).	210
5.32 The final scale correction for π^0 tagged photons (left) and η tagged photons (right), with fits to get the p_T dependence - and the percent difference between the estimated total tagging probability and the tagging probability in the data (bottom panels) as a function of photon p_T for each hadron trigger bin in data.	211
5.33 Top: the decay photon p_{out} for photons from 1.5 – 15.0 GeV/c, for trigger hadrons from 2.0 – 2.3 GeV/c for true decay photons (black) and the estimate from tagging π^0 and η photons (blue) in PISA. The integrated percent difference between the two distributions is shown, as well as the average point-to-point difference. Bottom: the ratio of the true distributions to the estimated, as a function of p_{out}	212

5.34 Hadron-photon $\Delta\phi$ per trigger yield for hadrons with p_T from 2.0 – 2.3 GeV/c and photons with p_T from 1.5 – 2.0 GeV/c. Shows the fully corrected distributions for π^0 photons when tagging included pair photons with p_T above 0.4 GeV/c (black circles), 0.5 GeV/c (blue circles), and 0.6 GeV/c (red circles); and for η photons with the same pair p_T cuts (magenta circles, blue triangles, and red triangles respectively). Also shows inclusive photons (solid black) for comparison.	213
6.1 Decay photon per-trigger yields, $\frac{1}{N_{trig}} \frac{dN^{h-\gamma}}{d\Delta\phi}$, for trigger hadrons with p_T from 2.0 – 2.3 GeV/c and associated γ_{π^0} (black) and γ_{η} (blue) photons with p_T from 1.5 – 2.0 GeV/c.	216
6.2 $\frac{1}{N_{trig}} \frac{dN^{h-\gamma}}{d\Delta\phi}$ for trigger hadrons with p_T from 2.0 – 2.3 GeV/c and associated photons in six p_T bins ranging from 1.5-2.0 GeV/c to 8.0 - 15.0 GeV/c. $h - \gamma_{inc}$ is shown in black, $h - \gamma_{decay}$ in blue, and $h - \gamma_{frag}$ in red.	217
6.3 Top: Integrated near-side ($-0.7 < \Delta\phi < 0.7$) $h - \gamma_{inc}$ pair cross-section sum over all hadron bins, as a function of photon p_T , for Run 5 (black) and Run 6 (blue). Bottom: ratio of the cross-sections for the two data sets for comparison, with $< 5\%$ variation between the Runs across the full p_T range.	218

6.4	Integrated near-side ($-0.7 < \Delta\phi < 0.7$) $h - \gamma_{frag}$ pair cross-section for each trigger hadron p_T bin, as well as for the sum over all hadron bins, as a function of photon p_T . Left: differential in terms of both hadron and photon momentum. Right: integrated over hadron momentum.	219
6.5	Left: ratio of integrated $h - \gamma_{frag}$ to $h - \gamma_{inc}$ yields, integrated from -0.7 to 0.7 in $\Delta\phi$, summed over all hadron trigger p_T bins, as a function of photon p_T for Run 5 (black) and Run 6 (blue) separately. Right: ratio of integrated $h - \gamma_{frag}$ to $h - \gamma_{inc}$, integrated from -0.5 to 0.5 in $\Delta\phi$ from Run 5 with the old method, for hadrons with $2.0 < p_T < 5.0$ GeV/c as a function of photon p_T	220
6.6	Ratio of integrated $h - \gamma_{frag}$ to $h - \gamma_{inc}$ yields, with an integration window from -0.7 to 0.7 in the $\Delta\phi$ for each trigger hadron p_T bin, as well as for the sum over all hadron bins, as a function of photon p_T	221
6.7	Ratio of isolated direct photons to all direct photons as a function of photon p_T (solid points) as well as several theoretical NLO pQCD predictions. Also shown is the same ratio for decay photons (shaded points) which shows the reduction in decay photon background achieved by applying isolation cuts.[115]	222
6.8	Ratio of direct photons to all photons as a function of photon p_T . Plotted from values published in [115], with an approximate polynomial fit to extrapolate between points.	223

- 6.9 Ratio of integrated $h - \gamma_{frag}$ to $h - \gamma_{inc}$ yields, with an integration window from -0.7 to 0.7 in the $\Delta\phi$, summed over all hadron trigger p_T bins, as a function of photon p_T (solid black circles), compared with the estimated fragmentation photon yield using the ratio of isolated direct photons to inclusive direct photons (open red circles) from [115]. 224
- 6.10 p_{out} distribution for photons with p_T from $1.5 - 8.0$ GeV/c, within $|\Delta\phi| < 0.7$ of a trigger hadron, for each of the four trigger p_T bins: $2.0 - 2.3$ GeV/c (top left), $2.3 - 2.8$ GeV/c (top right), $2.8 - 3.6$ GeV/c (bottom left), and $3.6 - 5.0$ GeV/c (bottom right). Inclusive photons are shown in black (circles), decay photons in blue (up triangles), and fragmentation photons in red (down triangles). For fragmentation photons, in the case where the point is more than one σ below zero, the 2σ limit is indicated with an arrow. 225
- 6.11 p_{out} distribution for photons with p_T from $1.5 - 8.0$ GeV/c, within $|\Delta\phi| < 0.7$ of a trigger hadron, over the full hadron p_T range of $2.0 - 5.0$ GeV/c. Inclusive photons are shown in black (circles), decay photons in blue (up triangles), and fragmentation photons in red (down triangles). For fragmentation photons, in the case where the point is more than one σ below zero, the 2σ limit is indicated with an arrow. 226

- 6.16 $\sqrt{\langle j_T^2 \rangle}$ versus trigger hadron p_T , for photons with p_T from 1.5 – 8.0 GeV/c, within $|\Delta\phi| < 0.7$ of a trigger hadron. The case for inclusive photons is shown in black (circles), decay photons in blue (up triangles), and fragmentation photons in red (down triangles). 231
- 7.1 Effective ratio of integrated $h - \gamma_{frag}$ to $h - \gamma_{direct}$ yields, integrated within $|\Delta\phi| < 0.7$ and summed over all hadron trigger p_T bins, as a function of photon p_T (solid black points) - errors from R_γ are not shown. A comparison to a prediction based on an NLO pQCD simulation is shown by the solid line, with theoretical uncertainties set by varying the renormalization scale shown by the dashed lines [110]. 234
- 7.2 Left: $\sqrt{\langle j_T^2 \rangle}$ versus trigger hadron p_T , for photons with p_T from 1.5 – 8.0 GeV/c, within $|\Delta\phi| < 0.7$ of a trigger hadron, for inclusive (black circles), decay (blue up triangles), and fragmentation (red down triangles) photons. Right: $\sqrt{\langle j_T^2 \rangle}$ versus π^0 trigger p_T , for associated hadrons with p_T from 1.4 – 5.0 GeV/c [138]. 235
- 7.3 p_{out} distribution for inclusive (black) and fragmentation (blue) photons generated using PYTHIA 6.4. [140] 236
- A.1 Decay photon per-trigger yields, $\frac{1}{N_{trig}} \frac{dN^{h-\gamma}}{d\Delta\phi}$, for trigger hadrons with p_T from 2.0 – 2.3 GeV/c and associated photons in six p_T bins ranging from 1.5 – 2.0 GeV/c to 8.0 – 15.0 GeV/c. $h - \gamma_{\pi^0}$ is shown in black, $h - \gamma_\eta$ in blue. 251

A.2 Decay photon per-trigger yields, $\frac{1}{N_{trig}} \frac{dN^{h-\gamma}}{d\Delta\phi}$, for trigger hadrons with p_T from $2.3 - 2.8$ GeV/c and associated photons in six p_T bins ranging from $1.5-2.0$ GeV/c to $8.0 - 15.0$ GeV/c. $h - \gamma_{\pi^0}$ is shown in black, $h - \gamma_{\eta}$ in blue.	252
A.3 Decay photon per-trigger yields, $\frac{1}{N_{trig}} \frac{dN^{h-\gamma}}{d\Delta\phi}$, for trigger hadrons with p_T from $2.8 - 3.6$ GeV/c and associated photons in six p_T bins ranging from $1.5-2.0$ GeV/c to $8.0 - 15.0$ GeV/c. $h - \gamma_{\pi^0}$ is shown in black, $h - \gamma_{\eta}$ in blue.	252
A.4 Decay photon per-trigger yields, $\frac{1}{N_{trig}} \frac{dN^{h-\gamma}}{d\Delta\phi}$, for trigger hadrons with p_T from $3.6 - 5.0$ GeV/c and associated photons in six p_T bins ranging from $1.5-2.0$ GeV/c to $8.0 - 15.0$ GeV/c. $h - \gamma_{\pi^0}$ is shown in black, $h - \gamma_{\eta}$ in blue.	253
A.5 $\frac{1}{N_{trig}} \frac{dN^{h-\gamma}}{d\Delta\phi}$ for trigger hadrons with p_T from $2.0 - 2.3$ GeV/c and associated photons in six p_T bins ranging from $1.5-2.0$ GeV/c to $8.0 - 15.0$ GeV/c. $h - \gamma_{inc}$ is shown in black, $h - \gamma_{decay}$ in blue, and $h - \gamma_{frag}$ in red.	254
A.6 $\frac{1}{N_{trig}} \frac{dN^{h-\gamma}}{d\Delta\phi}$ for trigger hadrons with p_T from $2.3 - 2.8$ GeV/c and associated photons in six p_T bins ranging from $1.5-2.0$ GeV/c to $8.0 - 15.0$ GeV/c. $h - \gamma_{inc}$ is shown in black, $h - \gamma_{decay}$ in blue, and $h - \gamma_{frag}$ in red.	255

B.3 $x_h^{-1} = p_{T,h}/p_{T,\gamma}$ distribution for photons with p_T from $1.5 - 8.0$ GeV/c, for each of the four hadron p_T bins: $2.0 - 2.3$ GeV/c (top left), $2.3 - 2.8$ GeV/c (top right), $2.8 - 3.6$ GeV/c (bottom left), and $3.6 - 5.0$ GeV/c (bottom right), when the pair has $|\Delta\phi| < 0.7$. Inclusive photons are shown in black (circles), decay photons in blue (up triangles), and fragmentation photons in red (down triangles).²⁶⁰

List of Tables

4.1	ϕ_{DC} acceptance for Runs 5 and 6	119
4.2	Event background scale for all $p_{T,h}(\text{GeV}/c)$ and $p_{T,\gamma}(\text{GeV}/c)$, and the relative difference between the background level from this method and ZYAM (Z).	148
4.3	Minimum Bias BBC inputs to determining the invariant hadron- photon pair cross-section	160
C.1	Invariant pair cross section (mb GeV/c^{-4}) for fragmentation pho- tons associated with hadrons with p_T from $2.0 - 2.3 \text{ GeV}/c$	261
C.2	Invariant pair cross section (mb GeV/c^{-4}) for fragmentation pho- tons associated with hadrons with p_T from $2.2 - 2.8 \text{ GeV}/c$	262
C.3	Invariant pair cross section (mb GeV/c^{-4}) for fragmentation pho- tons associated with hadrons with p_T from $2.8 - 3.6 \text{ GeV}/c$	262
C.4	Invariant pair cross section (mb GeV/c^{-4}) for fragmentation pho- tons associated with hadrons with p_T from $3.6 - 5.0 \text{ GeV}/c$	262
C.5	Invariant pair cross section (mb GeV/c^{-4}) for fragmentation pho- tons associated with hadrons with p_T from $2.0 - 5.0 \text{ GeV}/c$	263

C.6 p_{out} (GeV/c) for photons with p_T from $1.5 - 8.0$ GeV/c associated with hadrons with p_T from $2.0 - 2.3$ GeV/c and $ \Delta\phi < 0.7$	263
C.7 p_{out} (GeV/c) for photons with p_T from $1.5 - 8.0$ GeV/c associated with hadrons with p_T from $2.3 - 2.8$ GeV/c and $ \Delta\phi < 0.7$	264
C.8 p_{out} (GeV/c) for photons with p_T from $1.5 - 8.0$ GeV/c associated with hadrons with p_T from $2.8 - 3.6$ GeV/c and $ \Delta\phi < 0.7$	264
C.9 p_{out} (GeV/c) for photons with p_T from $1.5 - 8.0$ GeV/c associated with hadrons with p_T from $3.6 - 5.0$ GeV/c and $ \Delta\phi < 0.7$	265
C.10 p_{out} (GeV/c) for photons with p_T from $1.5 - 8.0$ GeV/c associated with hadrons with p_T from $2.0 - 5.0$ GeV/c and $ \Delta\phi < 0.7$	265
C.11 Inclusive photon $\sqrt{\langle p_{out}^2 \rangle}$ and $\sqrt{\langle j_T^2 \rangle}$ for each trigger hadron bin. Pairs required to have $ \Delta\phi < 0.7$ and photons restricted to p_T from $1.5 - 8.0$ GeV/c.	266
C.12 Decay photon $\sqrt{\langle p_{out}^2 \rangle}$ and $\sqrt{\langle j_T^2 \rangle}$ for each trigger hadron bin. Pairs required to have $ \Delta\phi < 0.7$ and photons restricted to p_T from $1.5 - 8.0$ GeV/c.	266
C.13 Fragmentation photon $\sqrt{\langle p_{out}^2 \rangle}$ and $\sqrt{\langle j_T^2 \rangle}$ for each trigger hadron bin. Pairs required to have $ \Delta\phi < 0.7$ and photons restricted to p_T from $1.5 - 8.0$ GeV/c.	266

Acknowledgments

I must first thank my research advisor, Brian Cole, for encouraging the great attention to detail and use of innovative techniques that makes challenging and detailed measurements possible. The lessons I have learned through his guidance will continue to make me a better scientist, and ultimately a better teacher for future scientists. I would also like to thank both Brian Cole and Bill Zajc for encouraging independence while providing their guidance and wisdom.

I would like to thank my mom, who always encouraged me to pursue my interests in math and science as a child, and gave me the sense that nothing was outside my grasp if I put my mind to it. I would also like to thank my step father for providing support and stability, without which I could not have made it to this point. I am lucky to have had parents who encouraged me so freely at every stage of my education, even when it involved great personal sacrifice. Their questions about my work have also helped me to find ways of putting the physics I've studied into laymen's terms, always a useful exercise for developing one's own understanding. Additionally, my mom devoted considerable time and attention to proof reading this thesis, a task I am very appreciative of, especially considering the length and technical detail in an area of study far outside her own experience.

The Columbia Physics department as a whole deserves credit for encouraging a helpful and friendly atmosphere between all the graduate students. However, Lalla Grimes must get special thanks for making the students feel at home and looked after in a way that makes a huge difference for people just starting out on a very

long and challenging adventure. She especially deserves my thanks for rescuing me from homelessness my first week and setting the tone for my time as a student.

I would like to thank Dave Winter and Nathan Grau for day to day feedback and guidance through out my time with the group at Columbia. Their mentorship was a great help to me as a new and developing student in the field of heavy ion physics. I would also like to thank my friends and colleagues Eric Vazquez, Yue Shi Lai, and early on Jiamin Jin, for many useful physics discussions. And of course they and all the other students in the group provided a friendly and supportive atmosphere that greatly improved my own experience as a student.

I would like to thank all of my colleagues from the PHENIX experiment for making up a collaboration with a truly collaborative atmosphere. Most especially I would like to thank Mike Tannenbaum, Gabor David, Justin Franz, Stephan Bathe, Anne Sickles, just to name a few of the many members of the collaboration that mate an effort to provide useful feedback and help when needed. Many who were students with me that I interacted with along the way deserve mention as well, most noteably Matt Nyugen, Megan Connors and John Chen.

Finally, I would like to thank Joanna Atkin. The many physics and math discussion we had as graduate students provided a unique insight and perspective I could not have gotten from somebody in my own sub-field. I can only hope I retain much of that perspective as I move forward. Additionally, her support as a friend and fellow graduate student has been key to my own success.

For Mom and Sam

Chapter 1

Introduction - Motivation from the Quark-Gluon Plasma

The results presented in this thesis will focus on the production of fragmentation photons within high energy proton-proton collisions. Fragmentation photons are produced at higher orders in perturbative Quantum Chromodynamics (pQCD) or as part of the non-perturbative fragmentation of partons (quarks and gluons) into highly correlated clusters of composite particles (jets). As a measurement able to further our limited understanding of parton showering, such results are interesting from a purely high-energy particle physics perspective. However, the primary motivation for these particular measurements is as a proof of principle for further such measurements in the much more complex environment of high energy heavy-ion collisions, as well as a comparison for understanding modifications to the production of fragmentation photons in the heavy-ion environment.

1.1 A new state of matter

The interaction of particles produced in the high energy collisions of nuclei is governed primarily by the strong force, the force which binds quarks and gluons together to form hadrons, and described by QCD. There are two key features of QCD which make it rather unique, as well as providing an indication that it is the correct theory for describing strong force interactions. The first feature is asymptotic freedom, which causes the interactions between particles to become arbitrarily weak at high enough energies, or short enough distances [1; 2]. That is, the coupling constant describing the strength of particle interactions is energy dependent, becoming smaller as energy increases. The second feature follows directly from this energy scaling of the coupling constant, which leads to an arbitrarily large coupling at low energies and large distances that suggests the confinement of quarks and gluons within nuclei. Conceptually, this confinement results from the force between quarks remaining constant at any distance and implies that an infinite amount of energy would be needed to split them apart. There is no formal proof for confinement, however all numerical calculations of QCD and QCD-inspired models indicate confinement and are consistent with seeing no free quarks or gluons.

The concept of asymptotic freedom led to predictions that at extremely high densities, where composite hadrons will begin to overlap, long range effects would be screened, and quarks and gluons would become deconfined [3], producing a new state of matter. It was then realized that there are two ways of achieving these high densities, either with a system of high baryon density - large densities of quarks - or

with high temperatures - which yield a high density of both quarks and gluons [4]. The screening of long range interactions in such hot, dense environments is similar to the Debye screening of electromagnetic plasmas, which led to dubbing such a state the Quark-Gluon Plasma (QGP).

With this proposed new state of matter came the task of predicting the properties of such matter. The logical first step is the description of the phase transition from confinement to deconfinement, including the temperature at which such a transition will occur and the energy density required. However, such a phase transition, like the property of confinement itself, is not calculable analytically. Nor is it calculable through the use of perturbation theory, which only becomes applicable at large enough energies that the coupling constant is sufficiently small. Instead, such calculations are done using Lattice QCD, where the discrete nature of the theory makes it well defined mathematically and there is no need to rely on perturbation theory [5].

Lattice QCD is an important theoretical tool for overcoming limitations to analytical methods in QCD; however, it is ill-defined at high baryon densities. Therefore the high temperature limit is more easily related to things calculable using lattice techniques. Fortunately, it is also unclear that the necessary high baryon densities would be achievable experimentally, while as we will see in the discussion that follows, the high temperature case can be achieved by colliding heavy ions at high energies, motivating the development of the RHIC accelerator. Additionally, lattice calculations provide a natural framework for calculating the thermodynamics of QCD which can then be related to what is observed experimentally.

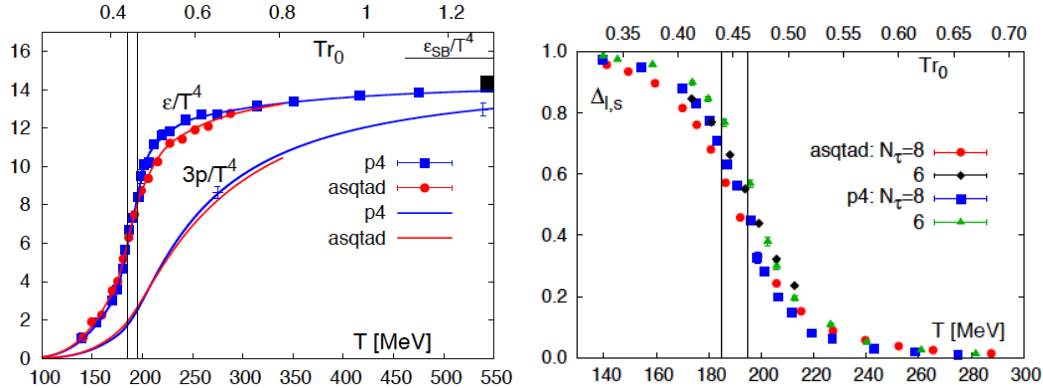


Figure 1.1: Left: QCD energy density/ T^4 from lattice calculations as a function of temperature with a horizontal black line indicating the Stefan-Boltzmann limit. Right: The chiral condensate (parameter for chiral symmetry breaking), normalized to the zero temperature value, as a function of temperature. The different colors compare calculations using two choices of action, with different temporal extent (right). The vertical bands indicate the range for the transition temperature [6].

The results from lattice calculations are shown in Figure 1.1. The arrows show the Stefan-Boltzmann limit, which corresponds to a gas of non-interacting quarks and gluons. At four times the critical temperature the energy density is still below the Stefan-Boltzmann limit, indicating that the matter is strongly interacting and implying that it is more fluid-like than gas-like. This result suggests two main features of the QGP expected experimentally: a large energy density at formation time, and strong collective motion of the bulk particles produced at low transverse momentum rather than as part of a hard scattering.

These lattice calculations demonstrate the phase transition from confinement to de-confinement, as indicated by the rapid change in energy density resulting from a change in the degrees of freedom from bound quarks to free quarks. A transition temperature within the range $180 \lesssim T \lesssim 200$ MeV is predicted, and the observation

of chiral symmetry restoration in the same temperature range indicates that this transition occurs in a region of the QCD phase diagram where the transition is a crossover rather than a true phase transition [6].

Based on these lattice calculations, the phase transition to the QGP occurs at a critical temperature of $T_C \approx 190$ MeV, and the energy density required is $\epsilon_C \approx 1$ GeV/fm³ [7; 8], similar to what is expected from basic order of magnitude estimates [9]. Energy densities this large are 10 times larger than densities observed in ordinary nuclear matter. While it is thought that such conditions were present μ s after the Big Bang, they are not thought to occur naturally, with the possible exception of the lower temperature (high baryon density) case of Neutron Stars [3].

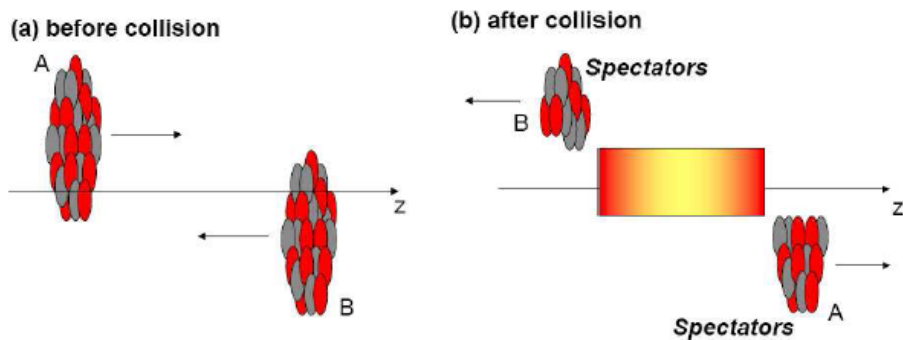


Figure 1.2: Illustration of a relativistic heavy ion collision, (a) shows the Lorentz contracted incoming nuclei, (b) shows an example of the matter remaining in the overlap region after the two nuclei collide.[10]

Experimentally, heavy ion collisions at high enough energies, i.e., relativistic speeds, will be highly Lorentz contracted. When two such ions collide, the overlapping region of the two nuclei will contain an extremely dense collection of matter

that releases a large amount of energy in a small volume to produce extremely high energy densities. Attempts to understand the initial particle production indicate that at these energies and higher the physics is dominated by gluons and not describable at the hadronic level. This idea is illustrated by the schematic shown in Figure 1.2, and makes such Relativistic Heavy Ion (RHI) collisions prime candidates for the production and study of the QGP.

1.2 The heavy ion environment

The first question one must ask experimentally is whether the energy densities needed to produce a QGP have indeed been reached. Again following the schematic shown in Figure 1.2, one can consider the incoming nuclei as Lorentz contracted disks that interact and then move apart. The resulting cylindrical region is the origin of the particles produced. This idea gives the Bjorken energy density [11]

$$\epsilon_{Bj} = \frac{1}{\pi R^2} \frac{1}{\tau_0} \frac{dE_T}{dy} \quad (1.1)$$

where R is the nuclear radius, τ_0 is the formation time of the plasma, and y is the rapidity - a measure of the longitudinal velocity of the particle. The energy density can then be calculated using the final state transverse energy and using the nominal value of 1 fm/c for τ_0 as an order-of-magnitude estimate. In Au + Au collisions at 200 GeV, for example, this gives an estimated energy density of about 5.4 GeV/fm³, well above that required for QGP production [12].

This type of description of the medium in terms of energy density and temperature, as well as more rigorous descriptions using lattice QCD, are only accurate if the medium exhibits hydrodynamic or collective behavior, where pressure and thermalization are meaningful concepts. The anisotropy in the shape of the overlap of the two colliding nuclei should translate to an azimuthal anisotropy in the distribution of final state hadrons if such collective behavior is present.

1.2.1 Elliptic flow

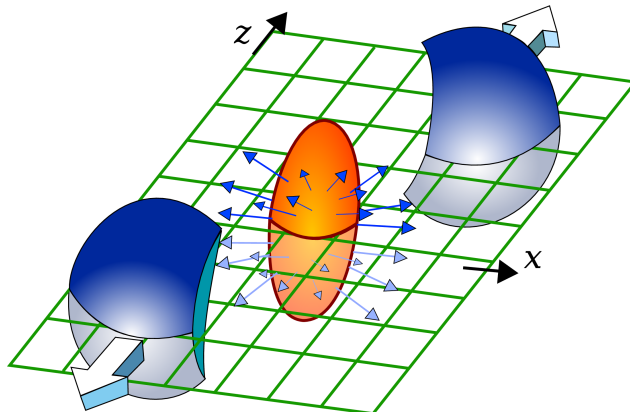


Figure 1.3: Diagram illustrating the almond shaped overlap region resulting from the collision of two nuclei, as well as the elliptic flow produced as a result of the anisotropy. The plane shown corresponds to the reaction plane.[13]

In most heavy ion collisions, the two nuclei will not overlap completely, instead leaving an almond shaped distribution of matter, or an ellipsoid, as illustrated in Figure 1.3. As long as strong scattering occurs within the produced matter in the early stages, this spatial anisotropy translates into a momentum anisotropy, which is then observable as an elliptic flow of the final state hadrons. If we define the

short axis of the overlap region as the reaction plane, elliptic flow will lead to an anisotropic azimuthal distribution of particles with respect to this plane, which can be measured experimentally. Measured single particle spectra can be written as a Fourier expansion in terms of azimuthal angle with respect to the reaction plane, Eq. (1.2). Elliptic flow corresponds to the second Fourier coefficient, v_2 , and should be the dominant term, (allowing both the first coefficient and higher order coefficients to be neglected), giving an experimental measure of this flow parameter.

$$\frac{dN}{d\phi dp_T} = \frac{N}{2\pi} (1 + 2v_2(p_T)\cos(2\Delta\phi)) \quad (1.2)$$

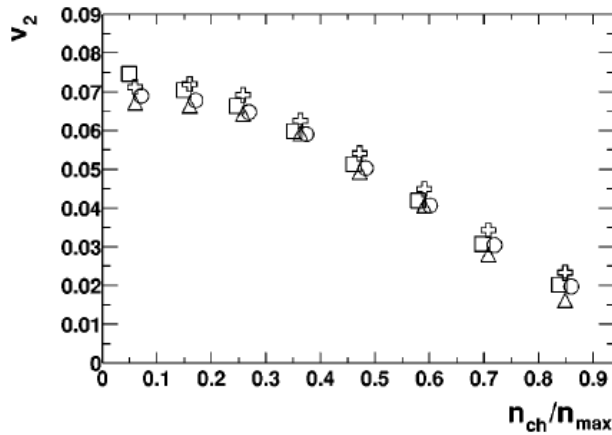


Figure 1.4: Elliptic flow parameter v_2 as a function of n_{ch}/n_{max} , a measure of the amount the colliding nuclei overlap, where v_2 is extracted from measurement of the correlation between particle pairs. The different points correspond to different ways of pairing particles: randomly chosen pairs (circles), opposite signs of charge (crosses), same signs of charge (triangles), and opposite signs of pseudorapidity (squares) [14].

Figure 1.4 shows how the extracted v_2 varies with the number of final state charged particles relative to the maximum number of charged particles. This ratio,

n_{ch}/n , is a measure of the ellipticity of the overlap region, as the more overlap (and less asymmetry) between the nuclei, the more particles will be produced from the collision. As the figure shows, more overlapping nuclei will have a lower v_2 modulation, as expected if v_2 arises as a result of the ellipticity of the collision region. Before drawing any conclusions based on the measured v_2 , it is important to verify that v_2 is indeed related to the initial asymmetry of the collision. The observation that at low p_T v_2 scales with the spatial eccentricity of the reaction zone provides good confirmation [15].

The theoretical framework for describing elliptic flow comes from hydrodynamic calculations, which describe this collective flow as the result of an initial pressure gradient. The observed v_2 are large enough that - for such calculations to successfully reproduce data - a very early thermalization time is required [16]. The longer equilibration takes, the weaker the remaining spacial anisotropy and the weaker the pressure gradient producing flow. Additionally, the success of ideal hydrodynamics, which assumes zero viscosity, has led to the argument that the QGP is in fact a strongly interacting near-perfect fluid [17]. However, relating hydrodynamic models to the observed v_2 is complex, involving not only a choice of initial conditions and thermalization time, but also some consideration of when hadronization occurs.

1.3 Energy loss and jets

Examination of bulk properties such as elliptic flow is key to understanding the properties of the QGP, but that is not the only tool available. Further understanding can be gained from the study of high momentum probes of the medium. Particles produced through an initial hard scattering, in which a large momentum transfer occurs between two partons in the incoming nucleons, will then traverse the medium prior to their fragmentation into observable hadrons. One of the key signatures expected for the QGP was that these high p_T partons would experience substantial energy loss through interactions with the medium, which would lead to a suppression of high p_T final state hadrons [18]. The first test of this prediction was done through the study of single hadron spectra.

If hard scattering products remained unmodified by the nuclear medium, one would expect the total cross-section for single particles to scale with the number of hard scatterings, or binary (nucleon-nucleon) collisions (N_{coll}). Practically speaking, N_{coll} will fluctuate from collision to collision, but the average will depend on the size of the overlap region of the two heavy ions, determined by the impact parameter b which is defined as the transverse distance between the centers of the two nuclei. A collision with more overlap, often referred to as more central, corresponds to a smaller centrality percentage.

The estimated number of binary collisions for a given centrality, or impact parameter, can be determined using the Glauber Model [19; 20]. This model first

defines the nuclear thickness function for a nucleus as

$$T_A(b) = \int \rho_A(r) dz \quad (1.3)$$

where $\rho(r)$ is the nuclear density function, typically a *Woods-Saxon* distributions with a characteristic radius $R_A \approx 1.2A^{1/3}$ fm. The thickness function for the nuclear overlap region, T_{AB} , can be defined as a function of the impact parameter in terms of the thickness functions for the two nuclei, A and B:

$$T_{AB}(b) = \int db_A T_A(b_A) T_B(b - b_A) \quad (1.4)$$

The probability of having a single p + p-like hard scattering, within a cross-sectional area db , is then given by $db T_{AB}(b) \sigma_{hard}^{pp}$.

A measure of how far the observed particle cross sections deviate from what would be expected through trivial binary scaling can therefore be obtained by taking a ratio - the nuclear modification factor - of the form:

$$R_{AA} = \frac{\frac{1}{N_{evt}} \frac{d^2N_{AA}}{dp_T dy}}{\langle T_{AB} \rangle \frac{1}{N_{evt}} \frac{d^2\sigma_{pp}}{dp_T dy}}. \quad (1.5)$$

If $R_{AA} = 1$, this would mean particle production in A + A collisions is simply an incoherent superposition of p + p collisions. Deviation from unity is then an indication of nuclear effects, with $R_{AA} > 1$ indicating enhanced production and $R_{AA} < 1$ indicating suppression.

Figure 1.5 shows the observed R_{AA} for Au + Au collisions with a center-of-

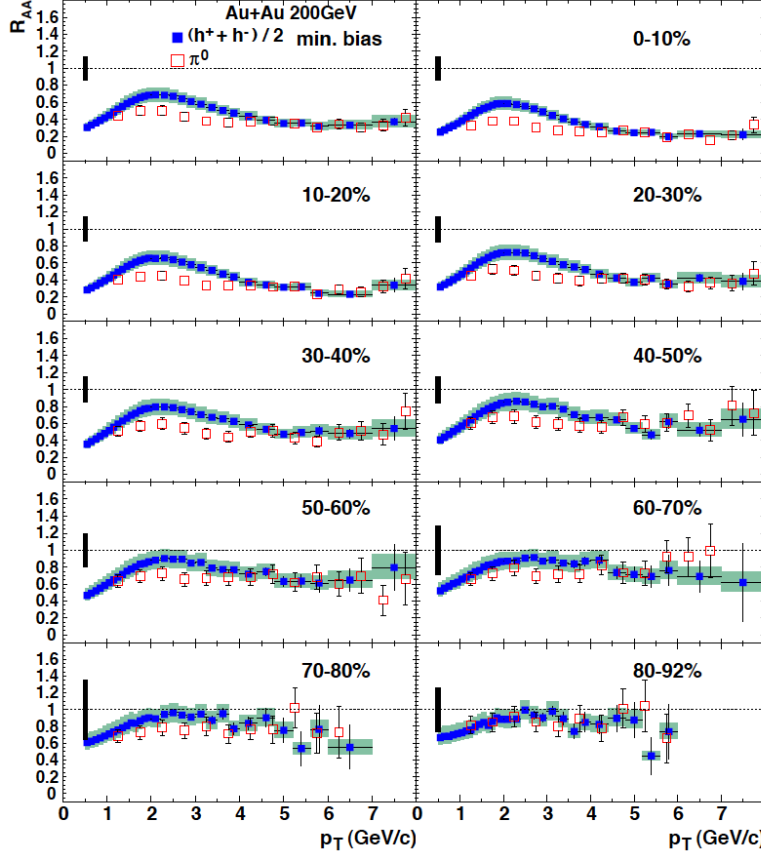


Figure 1.5: The Nuclear modification factor, R_{AA} , for π^0 s (open red boxes) and charged hadrons (solid blue boxes), as a function of p_T for different centrality classes.[21]

mass energy of $\sqrt{s} = 200$ GeV. For the most central collisions hadrons are found to be suppressed by almost a factor of five at high p_T . It is possible that cold nuclear matter, or initial state, effects could lead to a nuclear modification factor not equal to one simply as a result of the more complex nuclear structure in which the scattering takes place. However, similar measurements of the modification factor for d + Au collisions, where no QGP formation is expected, show no such suppression. Such measurements verify that the observed suppression is a final state effect [22].

The suppression of high p_T hadrons measured confirmed predictions based on the energy loss of the initial hard scattered partons. Such energy loss can occur either through elastic scattering with quarks and gluons in the QGP [18] as originally predicted, or through induced radiation, gluon bremsstrahlung [23]. Radiative energy loss is now considered the dominant source, and many models go so far as to neglect elastic energy loss for simplicity. There are many competing models for describing the energy loss process which have been relatively successful in reproducing the observed single particle suppression [24–28], despite starting from qualitatively different descriptions of the medium.

The strongly coupled nature of the QGP complicates questions of parton energy loss, as it raises the question of whether the observed suppression results from weakly or strongly coupled processes, and therefore whether the energy loss can be described perturbatively. More discerning probes such as photons, which are more directly sensitive to the interaction of quarks with the medium, are needed if one is to gain further insight into the properties of the QGP and gain insight into the coupling strength.

1.3.1 Jet modification

As a result of confinement, once a parton is produced through a hard scattering it will fragment into a shower of hadrons, called a jet, strongly correlated around the original parton trajectory. To measure the jet, a way of determining which detected particles belong to the jet is required. In $p + p$ collisions, where virtually all particles produced are part of a jet, measurements are made using algorithms that

apply some well defined method for identifying clusters of particles and grouping them into jets. However, in the high multiplicity environment of heavy ion collisions, where most of the particles produced are not the result of a hard scattering, there is a large background of non-jet particles that makes it difficult to identify and measure jets accurately with such algorithms [29]. The narrow distribution of jet products around the parton axis means that jets should be observable through two particle correlations that measure the angle separating the two particles. Figure

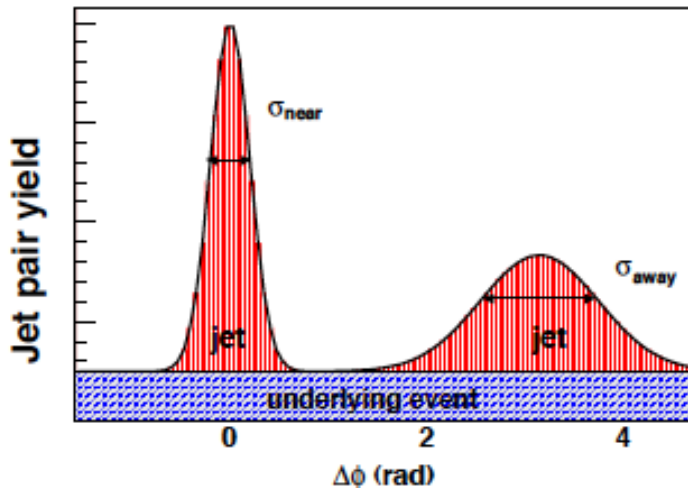


Figure 1.6: Illustration of the two particle correlation distribution resulting from jets.[30]

1.6 shows an example of how jet signals appear in two particle correlation measurements. In $p + p$ collisions, jets are typically produced in back-to-back pairs (di-jets) resulting from a $2 \rightarrow 2$ hard scattering. These di-jets are the source of the two peak structure seen in the figure. The peaks are roughly Gaussian, with the width of the peak at $\Delta\phi$, the near-side, relating to the shape of the jet. The two jets will not be exactly back-to-back as a result of an intrinsic transverse momentum,

k_T , which contributes and additional Gaussian smearing, and causes a broadening of the peak at $\Delta\phi = \pi$, the away-side. Particles not produced as part of a jet will contribute to a background of uncorrelated pairs, collectively termed the underlying event, which must be estimated and subtracted because they should not contribute to the jet yield. In heavy-ion collisions, this background is much larger, with the additional complication of elliptic flow leading to a correlated modulation that also requires correction.

One key result of two-particle measurements in heavy-ion collisions has been the strong suppression of the away-side peak at high momentum [31]. As with the suppression of high momentum single hadrons, the explanation is thought to be the energy loss of the initial parton as it traverses the medium. In the simplest view, this energy loss is shifting the energy of produced hadrons down. The power of two-particle correlations is that they provide the tools for looking deeper into such explanations. By varying the momentum of both hadrons in the pair, one would expect to be able to probe a region where the away-side peak is recovered. Basically, if the two hadrons are representative of the energy of the initial parton producing them, choosing one parton at a relatively high momentum and then looking for pair hadrons of much lower momentum should recover remnants of the parton undergoing energy loss. In addition, using asymmetric pairs makes it possible to probe the medium response to the initial parton.¹

An example of one such study is shown in Figure 1.7, where significant modification to the away-side, as well as some broadening of the near-side, was observed.

¹There is an assumption made here that the act of requiring the first high p_T hadron leads to a surface bias, meaning the parton producing the near-side peak undergoes minimal energy loss.

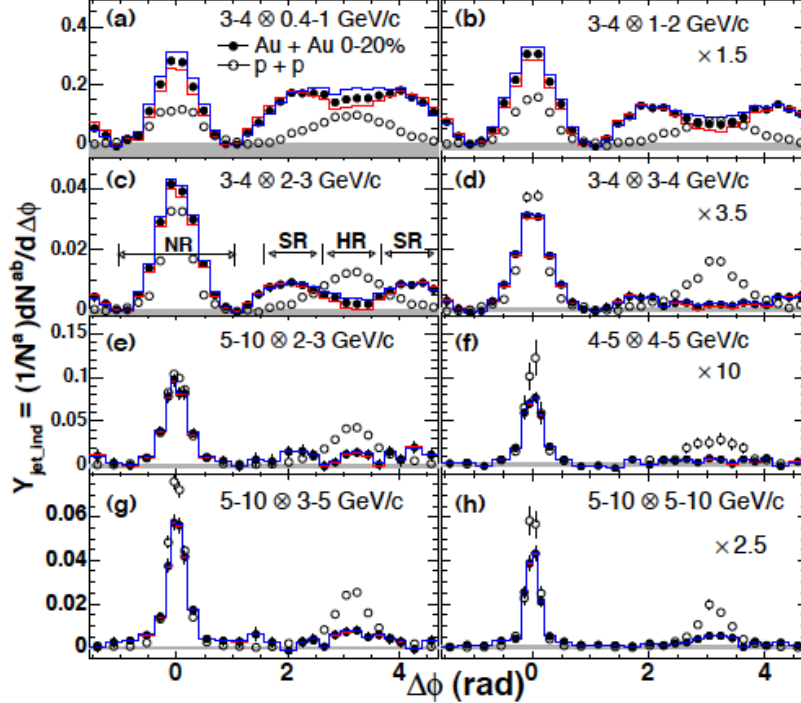


Figure 1.7: Jet yields from two-particle correlations in $\Delta\phi$ for various p_T ranges ($p_T^a \otimes p_T^b$), arranged by increasing pair energy, for $p + p$ in open circles and $Au + Au$ in solid black circles. The solid red and blue lines indicate the uncertainties associated with subtracting the elliptic flow contribution [30].

The surprising result is the emergence of two peaks on the away-side, offset from π , rather than the reemergence of a single, broadened peak. There has been much speculation about the explanation for this observation, along with many others that have yielded similarly unexpected results. From these studies, it is clear that correlations provide a plethora of information, however there are inherent limitations in our ability to interpret what is seen. The indirectness of two-particle correlations, as measures of the initial parton momentum and subsequent fragmentation, makes it difficult to quantify what is measured in terms of modifications to the parton.

1.4 Direct photons

Up to now, our discussion has been focused on the studies of the modification of hadronic production as a way of understanding the medium produced in heavy-ion collisions. It is clear that while much is learned through such studies, there are limitations in our ability to interpret and explain observations resulting from the complexities of hadron production. Photons are a useful tool in this sense because once produced, their interaction with the medium is minimal. While the photons themselves remain unmodified by the medium, there are several new production mechanisms that result in some modification to their total production cross-section and can provide additional information about the hot, dense environment.

Most photons are not directly produced in the collision but are instead the product of the decay of other particles. The distinction is drawn by denoting all photons not produced as part of a decay *direct* photons. In $p + p$ collisions, the majority of direct photons are produced as a result of a hard scattering, primarily through what is called a quark-gluon Compton scattering. This Compton-like process contributes to leading order (LO) photon production, meaning the cross-section can be estimated using only the first order in perturbative QCD calculations. At higher order, one can think of the initial hard scattering producing a quark which then goes on to radiate a photon as it fragments. Such processes contribute to the yield of fragmentation photons, and are expected to be modified in a heavy-ion environment. The next chapter presents a more detailed discussion of photon production as understood in pQCD.

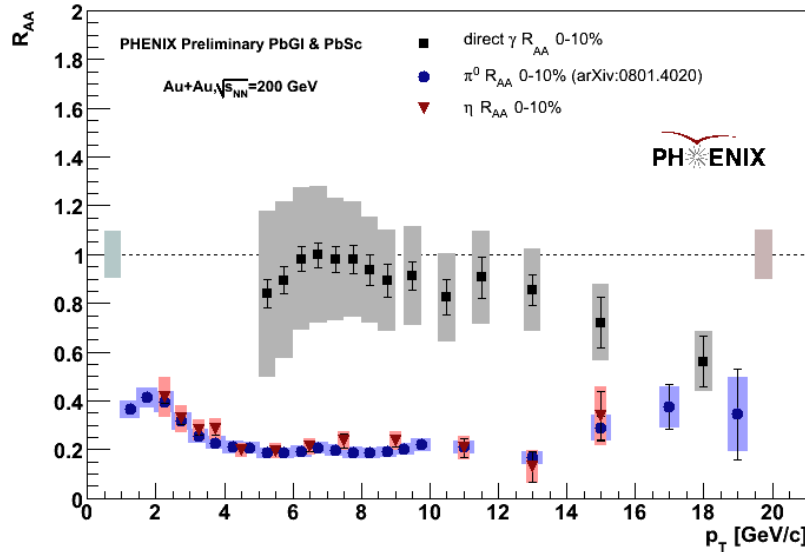


Figure 1.8: R_{AA} for direct photons (black squares), neutral pions (blue circles) and η s (red triangles) for central Au + Au collisions [32].

Because most direct photons are produced at leading order, as the result of a hard scattering, the medium produced in heavy ion collisions should have relatively little impact on the total cross-section, at least at momenta where hard scattering is expected to dominate. Therefore, photons are a good check that the observed modification to the hadronic cross-section is a result of the medium produced, rather than cold nuclear matter effects. The R_{AA} for photons in Au + Au collisions is found to be consistent with unity for all centralities [33], and as shown in Figure 1.8, direct photons remain largely unsuppressed in the region where hadrons are being suppressed by a factor of five. This lends further evidence to the claim that hadron suppression is a final state effect, resulting from the energy loss of the initial parton. The figure also shows that the R_{AA} of photons does not remain one out to the highest p_T currently accessible, which suggests that nuclear effects do play a role in direct

photon production, and opens the door for more detailed investigations.

1.4.1 Thermal photons

The presence of a thermalized medium would introduce an additional source of photons in the form of thermal photons, produced directly by the medium and dependent on its temperature [34]. Thermal photons are expected to dominate for $1 < p_T < 3 \text{ GeV}/c$, a region that is difficult to access experimentally given the large background of decay photons. Measurements using the reconstruction of virtual photons from e^+e^- pairs have proven successful, however, and do find an enhancement of photon production in this momentum range over that expected without thermal emission [35].

The measured cross-section is shown in Figure 1.9, where an exponential added to a scaled fit to $p + p$ data is fit to the Au + Au data. If the source of this observed enhancement is indeed thermal emission of photons from the QGP, the inverse slope of the exponential is directly related (less by a factor of 1.5 to 3) to the initial temperature of the thermalized medium. The relationship between them depends on the space-time evolution of the medium, but the fit yields a value for the inverse slope of approximately 200 MeV which is in qualitative agreement with hydrodynamic models predicting an initial temperature of 300 to 600 MeV [34; 36], well above the critical temperature required according to lattice calculations [7].

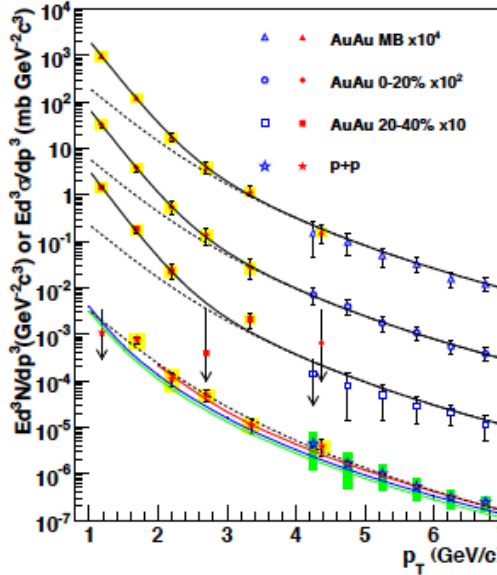


Figure 1.9: Invariant cross section ($p + p$) and invariant yield ($Au + Au$) of direct photons vs p_T . The dashed curves show a modified power-law fit to the $p + p$ data scaled by N_{coll} and the black curves are an exponential plus the scaled fit. The curves on the $p + p$ data come from pQCD calculations [35].

1.4.2 Direct photons from jets

As discussed previously, beyond-leading-order photons can be produced through the radiation of a photon by the initial hard scattered quark, or more generally as part of the quark fragmentation. In the heavy-ion environment there are two additional sources of photons that are related to hard scatterings. The first is jet conversion, a process by which a hard scattered parton rescatters with the medium in a Compton-like process to produce a photon [38; 39]. Experimentally there is no clear way of distinguishing such photons from LO, but they will contribute to the total direct photon cross section. The second is induced Bremsstrahlung emission. In this case partons traversing the medium will radiate photons through interaction with the

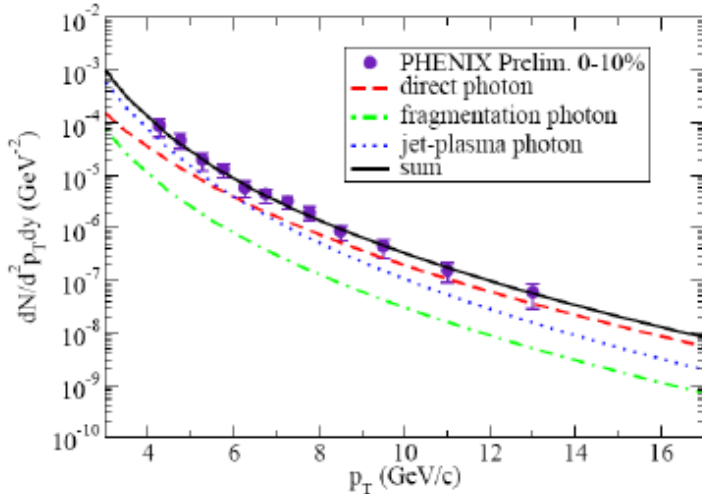


Figure 1.10: Calculation of the total direct photon cross-section for central Au + Au collisions, with each of the contributions shown separately as well, and compared to the measured cross section (0 – 10% centrality) [37].

medium, just as they radiate gluons [40]. Bremsstrahlung photons can be expected to maintain some spatial correlation with the parton producing them, and therefore with the resulting jet. This expected correlation gives us some hope of a direct measurement, provided jet-associated direct photons can be cleanly identified. The full set of photon sources is shown in Figure 1.10 and compared to the measured cross-section, with good agreement.²

These medium-induced sources are estimated to contribute significantly to the total photon cross-section, contributing as much as half of the photons measured at lower momentum, for $p_T \approx 3 - 6$ GeV[37]. Such a large contribution should lead to a significant enhancement in R_{AA} , which is not observed. However, p + p-like production of fragmentation photons is expected to be suppressed as a result

²In the figure, fragmentation photon describes both p + p-like production and medium-induced radiation.

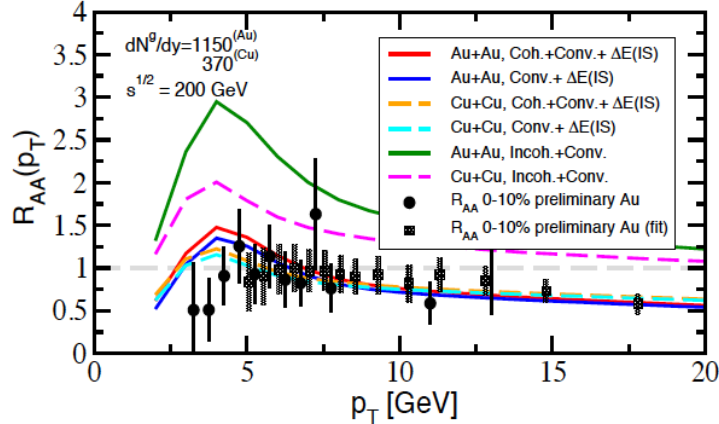


Figure 1.11: Calculations of direct photon R_{AA} as a function of p_T in central $Au + Au$ (solid lines) and $Cu + Cu$ (dashed lines) and comparison with data. For $Au + Au$, the solid green line includes induced photon radiation and jet conversion, without suppression through parton energy loss, and the solid red line includes energy loss suppression as well as the medium-induced sources [41].

of the energy loss of the parton. This energy loss is a competing factor that would instead lead to a slight suppression of R_{AA} , as well as suppressing the expected contribution of induced radiation[40–42]. Figure 1.11 illustrates this point, showing the significantly enhanced R_{AA} expected if energy loss is not included (solid green line for $Au + Au$), as well as the case including suppression due to energy loss (solid red line), which shows that some enhancement remains around 5 GeV/c. However, at higher p_T the combined effect is an overall suppression. It is important to note that a large contributor to the suppression seen at the highest momenta is actually a cold nuclear matter effects [41].

The competing factors of fragmentation photon suppression through parton energy loss and induced emission through medium interaction make fragmentation (Bremsstrahlung) photons highly sensitive to the details of the description of the

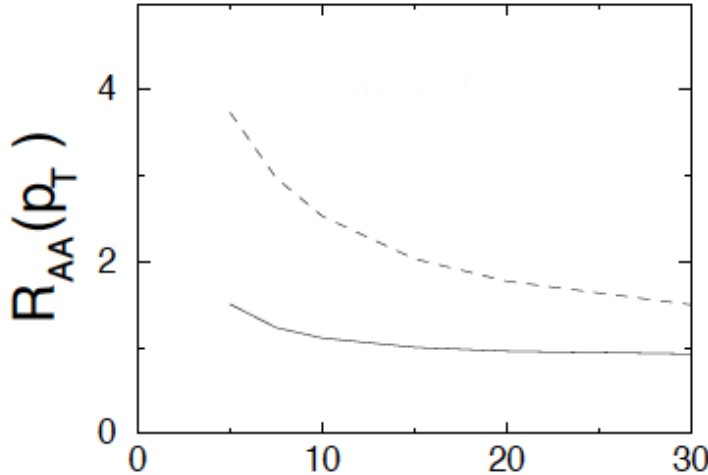


Figure 1.12: Calculation of the R_{AA} , as a function of p_T , for fragmentation photons (including induced emission), both with (solid line) and without (dashed line) energy-loss suppression [40].

medium. At the same time, they provide a picture of the radiation spectrum unencumbered by the further medium interactions that the radiated gluons undergo. The sensitivity of the total direct photon R_{AA} to these energy-loss effects is limited by the relatively small contribution that fragmentation photons make to the total yield, as well as by the relatively large systematic uncertainties resulting from the difficulty of identifying direct photons amid the large decay photon background. As Figure 1.12 shows, the fragmentation photon R_{AA} alone remains enhanced by as much as 50% at 5 GeV/c even with suppression. This result suggests that a direct measurement of fragmentation photons, even with somewhat large uncertainties, would provide more sensitivity to theoretical predictions. This sensitivity to the details of parton-medium interactions is the primary motivation for the analysis presented here.

1.4.3 Direct photon correlations

It has now been shown that single photon studies can provide information about the medium produced in heavy ion collisions beyond what is learned from studies of hadrons. It naturally follows that two-particle correlation studies involving direct photons can again improve our understanding of what is observed in hadron-hadron correlations. Recall that the key features of di-hadron measurements are energy-loss of the initial parton leading to a suppression of away-side yield and modification to the shape of both the near- and away-side resulting from multiple scattering and medium response, and that these features were hampered by the indirectness of the measurements as they relate to the initial parton and its fragmentation.

The primary way photons are able to elucidate observations from di-hadrons is through γ_{dir} -hadron correlations, which serve as a proxy for γ -jet measurements. Again considering the Compton-like processes responsible for most direct photons, the hard scattering will result in a direct photon back-to-back with a quark which will then produce a jet. Unlike with hadron-hadron correlations, here the outgoing photon will remain unmodified by the medium, with the same momentum as the recoiling parton. This overcomes two aspects of di-hadron measurements which make interpretation difficult. First, the initial energy of the parton producing the away-side distribution is equivalent to the energy of the photon, making it possible to measure the parton energy loss directly, generally in the form of a modified fragmentation function [43; 44]. And second, the photon will not experience a surface bias, as is generally thought to be the case when studying the near-side in di-hadron measurements. The lack of surface bias suggests that γ_{dir} -hadron measurements are

a more complete probe of the full path-length dependence of energy loss.

Fragmentation photons, which will be correlated with jets, can also be measured using two particle correlations involving direct photons. Modification to the shape of such correlations relative to $p + p$ would provide further insight into parton radiation and fragmentation without the complication of further interaction with the medium or hadronization. Discussions of γ -hadron measurements typically neglect the near-side since, when considering only the leading order Compton process, there should be no hadrons associated with the outgoing photon. However, fragmentation photons should contribute to the near-side yield. Thus far, both the high momentum ranges for photons used in γ -hadron studies - where the fragmentation photon signal is most suppressed - as well as the large uncertainties associated with the measurements, lead to near-side yields consistent with a negligible yield of fragmentation photon [45]. However, the most recent results show small non-zero yields in some momentum ranges, suggesting that studies of fragmentation photons using two-particle correlations are within reach [46].

1.5 Statement of purpose

From the perspective of Heavy Ion physics, fragmentation photons provide a unique probe of parton energy loss, as they are highly sensitive to the radiation spectrum of the parton while remaining unmodified after production, unlike the radiated gluons. The competing effects of induced emission through interaction with the medium and suppression resulting from the stimulated emission of gluons make inclusive di-

rect photons less sensitive to modification to the already small fragmentation photon component. The direct measurement of fragmentation photons can be done through the identification of direct photons associated with jets, and in the high multiplicity environment of heavy ion collisions, where full jet reconstruction is very challenging, the use of two particle correlations is likely to be the most straightforward way of attempting such a measurement. As it is the modification to the fragmentation photon yield one hopes to study, similar measurements in $p + p$ collisions are necessary. Further, establishing the success of the method in the much less complicated $p + p$ environment is an important first step to performing such measurements in heavy ion collisions.

The next chapter presents a general overview of the underlying theory of Quantum Chromodynamics which describes nuclear interactions will be given, with special attention paid to direct photons, and more specifically fragmentation photons. Chapter 3 describes the RHIC accelerator and PHENIX detector, with a more detailed discussion of the parts of the detector used for the analysis that follows. Chapters 4 details the steps taken for constructing two particle correlations between hadrons and photons, and extracting universal physics quantities from them. Chapter 5 describes the development and careful testing of a method for accurately identifying and removing the large decay photon background. Finally, the first results from RHIC for the direct measurement of fragmentation photons and their properties in $p + p$ collisions will be presented and discussed in Chapters 6 and 7, with some comments on the possibilities for similar measurements in heavy ion collisions.

Chapter 2

QCD and the photon

The previous chapter presented the motivation for studying photons produced as part of the fragmentation of partons into jets from the perspective of understanding parton energy loss in the hot, dense color medium produced in relativistic heavy-ion collisions. Given that motivation, it is important to establish some of the fundamental ideas related to the underlying physics of strong interactions. We will now lay out the development of QCD as the theory for the strong force and some of the building blocks for understanding the more basic proton-proton collisions used as a baseline for studying medium modification. Of particular interest is the description of jets and direct photon production, as this will further motivate the study of fragmentation photons in the p + p environment.

2.1 Quantum Chromodynamics

QCD is a quantum field theory described by the Lagrangian [47],

$$\mathcal{L} = \bar{\Psi}_{f,i} [i\gamma^\mu \partial_\mu - m_f] \Psi_{f,i} - g \bar{\Psi}_{f,i} \gamma^\mu A_\mu^a T_{ij}^a \Psi_{f,j} - \frac{1}{4} F_a^{\mu\nu} F_{\mu\nu,a} , \quad (2.1)$$

which is a function of the spin-1/2 fermionic quark fields, ψ_f , and the spin-1 bosonic gluon vector fields, A_μ , with the parameters m_f - the mass of the quark - and g - the coupling constant defining the strength of strong force interactions. The label f distinguishes the six quark flavors - up, down, strange, charm, bottom, and top. The quark fields each have three components, i , for the three (N_c) 'color' charges - red, green, and blue - associated with the strong force. The gluon vector fields describe the vector potential used to determine the field strength, defined by the tensor $F_{\mu\nu}$ as

$$F_{\mu\nu}^a = \partial_\mu A_\nu^a - \partial_\nu A_\mu^a - g C^{abc} A_\mu^b A_\nu^c, \quad (2.2)$$

where C^{abc} are the structure constants of the SU(3) symmetry group defining the QCD Lagrangian; $a, b, c = 1 \dots N_c^2$ are the group components of A_μ ; and T_a are a set of $N_c \times N_c$ (3×3) matrices which define the Lie algebra for the group through their commutation relations [48],

$$[T_a, T_b] = i C_{abc} T_c. \quad (2.3)$$

This Lagrangian describes three basic kinds of interactions that occur as a result of the strong force. The first, which arises from the $-g \bar{\Psi}_{f,i} \gamma^\mu A_\mu^a T_{ij}^a \Psi_{f,j}$ term, describes interactions between quarks and gluons through the emission or absorption of a gluon by a quark. This type of interaction is analogous to the fermion-photon interactions described by QED and reflects the idea that fundamental particles interact through the exchange of a "force-carrier" - the photon or gluon. The fundamental difference between QCD and QED comes from the third term in the field strength

tensor, $-gC^{abc}A_\mu^b A_\nu^c$, which gives rise to two types of gluon self-interaction: the emission or absorption of a gluon by a gluon, and the direct interaction of two gluons. These additional types of interactions can occur as a result of gluons carrying color charge, while in QED photons are neutral, so do not interact with themselves, and are responsible for the non-Abelian nature of QCD [49].

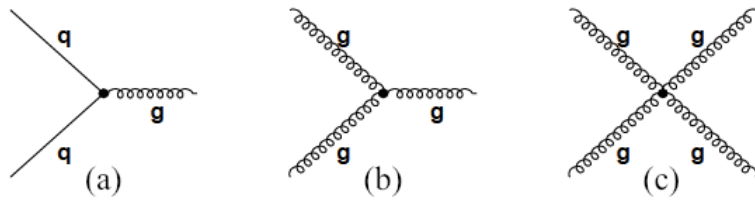


Figure 2.1: QCD Feynman vertices. (a) illustrates gluon absorption/emission by a quark. (b) illustrates gluon absorption/emission by another gluon. (c) illustrates direct gluon-gluon interaction.

In perturbation theory, using Feynman rules, each of these interactions can be represented graphically by a vertex, as shown in Figure 2.1. These are essentially visual representations of the mathematical components that go into calculating the probability for a given interaction [50]. A measurable interaction is represented by the connection of two or more vertices to form Feynman diagrams, with an infinite number of diagrams contributing to the total probability of the interaction occurring. Each diagram corresponds to an order in the perturbative expansion of the total probability as a power series in $\alpha_s = g^2/4\pi$. The number of vertices in the diagram corresponds to the order in the expansion the diagram represents.

As a method for making calculations in QCD, this is only valid if the perturbative expansion converges, in other words when $\alpha_s \ll 1$. Higher order diagrams are inherently harder to calculate, so in the first perturbative QCD (pQCD) calculations,

only the lowest order (tree level) diagrams were included. Current predictions have gone further, to include next-to-leading order (NLO; one-loop) diagrams, but do not typically go beyond NLO (multi-loop). Although there has been an impressive amount of success with such calculations, as we will see, there are many limitations to the applicability of pQCD as a result of the requirement that α_s be small.

An unfortunate consequence of including orders in pQCD involving loop diagrams is that this inclusion introduces divergences associated with infinite loop momenta, called ultraviolet (UV) divergences. These divergences are handled through the introduction of an arbitrary momentum cut-off in the form of an additional parameter μ - the renormalization scale. In other words, if we were to calculate the cross-section σ for some interaction involving particles at a momentum scale Q , the best we could hope to obtain is

$$\sigma(Q^2, \mu^2) = \alpha_s A_1(Q^2, \mu^2) + \alpha_s^2 A_2(Q^2, \mu^2) + \dots , \quad (2.4)$$

where A_n are the results of computing the diagrams at each order. As μ is an arbitrary parameter, nothing physically observable should depend on the value chosen. However, α_s is already a free parameter of the theory, and by making a measurement at a fixed momentum, α_s at that scale can be determined as a function of μ . Predictions for a given physical quantity can then be made for all energy scales independent of μ by requiring

$$\mu^2 \frac{d}{d\mu^2} \sigma(Q^2, \mu^2) = (\mu^2 \frac{\partial}{\partial \mu^2} + \mu^2 \frac{\partial \alpha_s}{\partial \mu^2} \frac{\partial}{\partial \alpha_s}) \sigma(Q^2, \mu^2) = 0 , \quad (2.5)$$

and keeping the μ dependence in α_s . Since μ is just an arbitrary energy scale, this basically defines the energy dependence of α_s to be

$$\mu^2 \frac{\partial \alpha_s(\mu^2)}{\partial \mu^2} = \beta(\alpha_s(\mu^2)) \quad (2.6)$$

where this *beta function* can be expressed perturbatively as

$$\beta(\alpha_s(\mu^2)) = \beta_0 \alpha_s^2(\mu^2) + \beta_1 \alpha_s^3(\mu^2) \dots \quad (2.7)$$

Neglecting β_1 and higher order terms, this can then be used to obtain an approximate form for α_s at some momentum scale, Q , of

$$\alpha_s(Q^2) = \frac{\alpha_s(\mu^2)}{1 - \alpha_s(\mu^2) \beta_0 \ln \frac{Q^2}{\mu^2}}. \quad (2.8)$$

As Eq. (2.5) suggests, the terms in the expansion of β can be evaluated through the calculation of any physical observable requiring renormalization. The leading order term was found to be

$$\beta_0 = -\frac{33 - 2n_f}{12\pi}, \quad (2.9)$$

where n_f is the number of active quark flavors¹[2; 51]. The demonstration that the beta function for QCD is negative (as long as the number of flavors remains small) leads to $\alpha_s(Q^2)$ decreasing asymptotically to zero as Q^2 becomes large - the property of asymptotic freedom. As shown in Figure 2.2, once α_s has been measured at

¹The large variation in quark mass requires that the number of quarks considered in the calculation will depend on the energy scale.

some reference scale², Eq. (2.8) provides a prediction for $\alpha_s(Q^2)$ that agrees well with values extracted from data [52] and illustrates this asymptotic behavior.

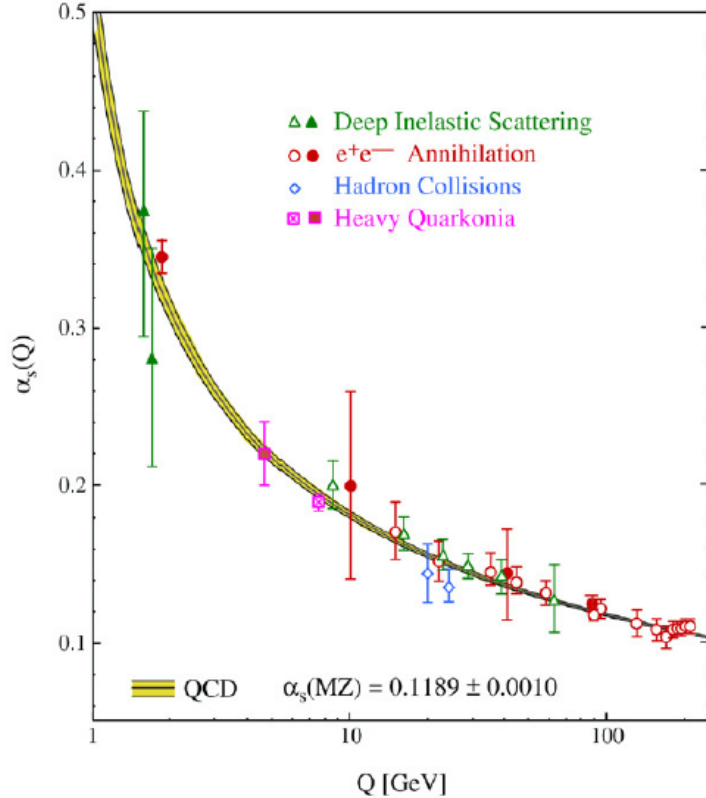


Figure 2.2: The pQCD prediction for the dependence of the QCD coupling α_s , on the momentum scale, Q , compared to values of α_s extracted using data for several different observables. The open and closed symbols correspond to the determination of α_s from data at different orders in the perturbative expansion [52].

In contrast to the behavior at large energies, according to this perturbative form for α_s as Q approaches zero α_s diverges to infinity. This is a result of the breakdown of pQCD, which is not expected to work as α_s approaches unity, and reflects the

²In the figure shown the reference scale chosen was the mass of the Z^0 boson.

onset of confinement. If we define another energy scale,

$$\Lambda^2 = \mu^2 e^{-\beta_0 \alpha_s(\mu^2)}, \quad (2.10)$$

Eq. (2.8) can be rewritten as

$$\alpha_s(Q^2) = \frac{1}{\beta_0 \ln(Q^2/\Lambda^2)}. \quad (2.11)$$

Λ , often labeled Λ_{QCD} , sets the momentum scale at which QCD becomes non-perturbative and is found experimentally to be 100-200 MeV/c, although the exact value depends on the scheme used for renormalization. This energy scale defines the separation between the long-range low- p_T (soft) physics not describable by pQCD, and the short-range high- p_T (hard) physics where pQCD is applicable.

The trend that $\alpha_s(Q^2)$ becomes large as the momentum transfer for a given interaction becomes small reflects the increasingly strong coupling of quarks and gluons as energy scales get small, or length scales get large, that leads to confinement. Essentially by definition, because a small coupling is required for perturbative methods to work, confinement cannot be shown through perturbative calculations. The limited applicability of perturbation theory to QCD leads us to search for non-perturbative formulations of the theory, the most developed of these being lattice QCD, in which quarks are described as points on a lattice, with a characteristic separation defined by the lattice spacing, and gluons act as the links connecting neighboring sites [53].

The lattice approach approximates QCD by discretizing Euclidean space-time

into hypercubes with sides of length a . The continuum limit is recovered as a goes to zero. The lattice spacing also naturally introduces a momentum cut-off of order $1/a$, removing the ultraviolet divergences that plague pQCD, although it is necessary for a to be much smaller than the scale associated with whatever observable is being estimated. Calculations are then done using numerical simulations at a specific lattice spacing, where a major practical limitation of the theory arises as a result of the rapid increase in computing power needed as a decreases.

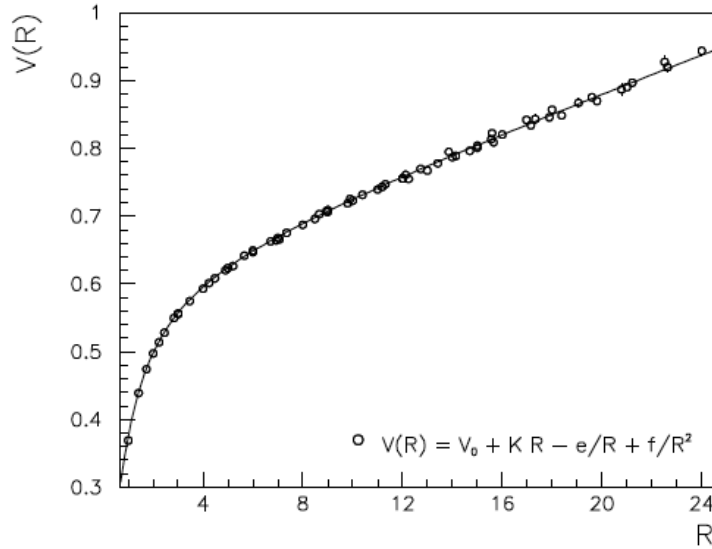


Figure 2.3: The QCD potential as a function of distance, R (in units of the lattice spacing), calculated from lattice QCD [54]. The solid line shows a fit to the numerical values of the given form.

One example of the success of lattice QCD is the description of the QCD potential through the calculation of the static potential for a quark-antiquark pair. The resulting form for the potential is shown in Figure 2.3, which demonstrates the linear behavior of the potential as the distance between the pair becomes large [54].

This behavior results in the force between the pair remaining constant, rather than decreasing with distance, as is the case for other forces seen in nature. As the pair separation increases, it will at some point become energetically favorable to produce an additional quark-antiquark pair. At the point where there is sufficient energy, the original pair splits and two new colorless bound states are created. This result is essentially a theoretical description of confinement, with the caveat that the calculation was done at finite lattice spacing and would have to be extended to the continuum limit to claim that confinement had been fully demonstrated.

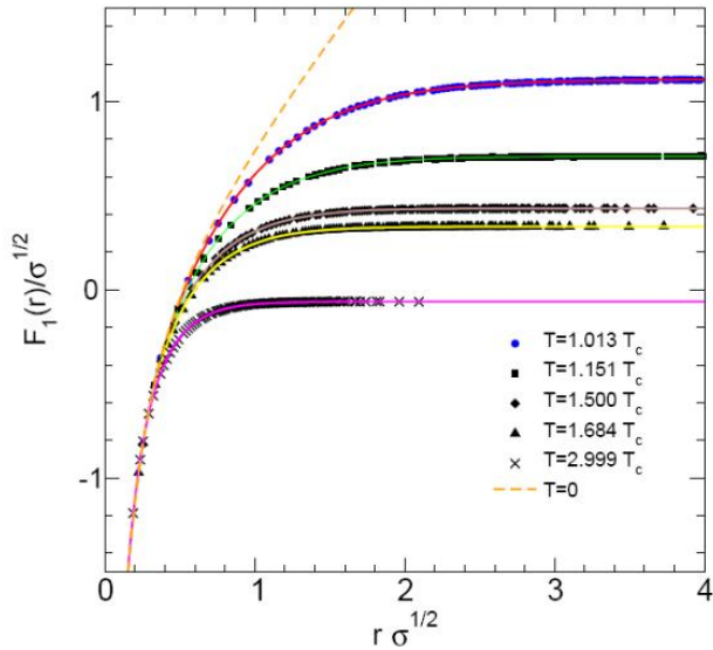


Figure 2.4: Free energy of a heavy quark pair as a function of the separation in lattice units calculated from the lattice at several different temperatures [55].

When considering the motivation for studying the heavy ion environment described in Chapter 1, it is of interest to note that the potential shown in Figure 2.3

is calculated at zero temperature. At high temperatures the potential is modified as shown in Fig. 2.4, where the free energy of a heavy quark pair is plotted as a function of separation for different temperatures [55]. The dashed line indicates the free energy at zero temperature. As the temperature increases the asymptotic behavior begins to change. That is, the linear slope begins to decrease and turn over. At a temperature of about T_c the QCD potential at large distances has a slope of zero, resulting in zero force between the heavy quark pair. This is one way of demonstrating the prediction that at high enough temperatures quarks and gluons become deconfined.

2.2 Perturbative QCD in practice

The asymptotic states considered in pQCD are the quarks and gluons, which are treated as free particles that undergo high momentum (hard) interactions. These are not the particles measured, however, confinement requiring that they instead form into color-neutral bound states: baryons, which contain three quarks with each of the three colors; and mesons, which are quark anti-quark pairs. The application of pQCD to measurements made experimentally requires developing ways of understanding or modeling the inherently non-perturbative process of going between observable hadrons and the quarks and gluons the theory describes. Despite these limitations, there are several key predictions made by pQCD that motivate its use even when input from data is required.

2.2.1 Deep inelastic scattering and factorization

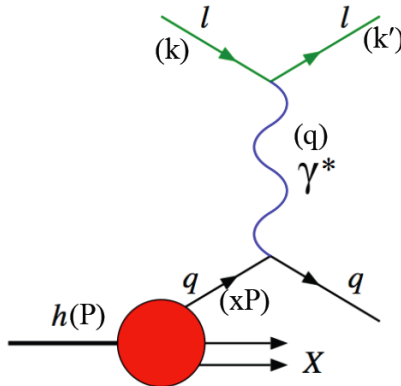


Figure 2.5: Leading order Feynman diagrams for the deep inelastic scattering of a lepton on a hadron with the corresponding four-momenta assigned to the particles in parentheses.

The first and still one of the most powerful quantitative tests of pQCD is the breaking of Bjorken scaling in deep-inelastic lepton-hadron scattering (DIS). Deep inelastic structure function analyses not only provide some of the most precise tests of the theory, but also determine the momentum distributions of partons in hadrons. The underlying perturbative process is the elastic scattering of a lepton and one of the quarks in the hadron, through the exchange of a virtual photon³, as illustrated in Figure 2.5. This type of scattering is sensitive to the kinematics of the quark structure of the proton, giving a direct measure of the proton interior.

If we take the incoming and outgoing lepton to have momenta k and k' respectively, the target hadron to have momentum p , and the momentum transfer carried

³Here the photon is virtual because it acts simply as the force carrier for the electromagnetic interaction and would never be measurable in this context.

by the photon to be q , the scattering cross-section will be defined by

$$Q^2 = -q^2 = (k - k')^2 ; \quad (2.12)$$

the Bjorken scaling variable x , which is the fraction of the proton momentum carried by the quark

$$x = \frac{p_q}{P} = \frac{Q^2}{2P \cdot q} ; \quad (2.13)$$

and the inelasticity, the ratio of the energy transferred to the hadronic system to the total leptonic energy (in the hadron rest frame),

$$y = \frac{P \cdot q}{P \cdot k} . \quad (2.14)$$

At a fixed center-of-mass energy \sqrt{s} , these satisfy the condition

$$Q^2 = (s - m_p^2) \cdot xy , \quad (2.15)$$

leaving the cross-section dependent only on x and Q^2 .

At lowest order the cross-section can be considered as the product of the leptonic and hadronic tensors [56]

$$\sigma \sim L_j^{\mu\nu} W_{\mu\nu}^j . \quad (2.16)$$

$L_{\mu\nu}$ is the leptonic tensor, which describes the vertex $l \rightarrow \gamma* + l$ associated with the coupling of the exchange boson - in this case a virtual photon - to the leptons, and

is determined from QED. $W_{\mu\nu}$ is the hadronic tensor defining the vertex $\gamma^* + h \rightarrow X$ describing the interaction of the vector boson - in this case a photon - with the target nucleon. The hadronic tensor can be expressed as an expansion in terms of scalar structure functions, coefficients of vector products in the expansion, that can be parameterized in terms of x and Q^2 . In the case of electro-proton scattering, imposing Lorentz invariance and the known discrete symmetries of QED reduces the set of structure functions to two, $F_1(x, Q^2)$ and $F_2(x, Q^2)$, which define the partonic content of the proton.

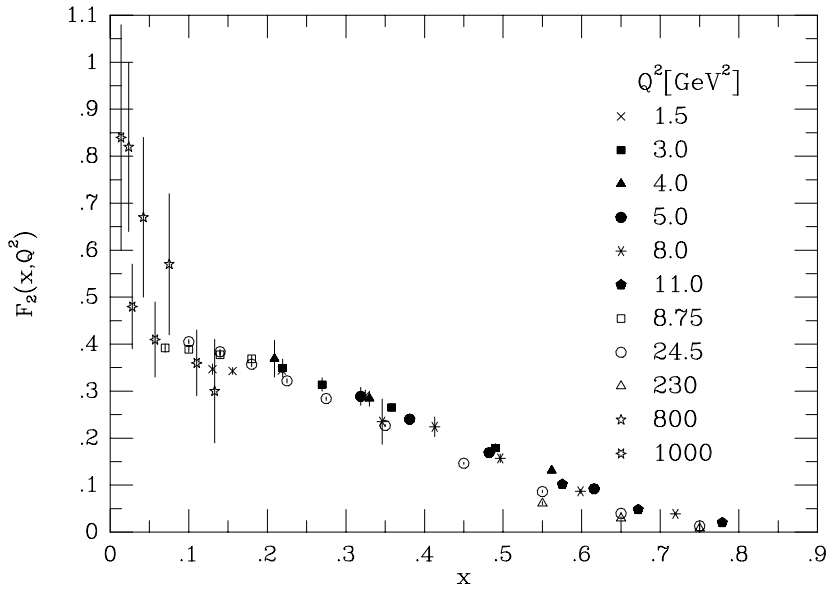


Figure 2.6: The Bjorken x dependence of the F_2 structure function for several values of Q^2 , from SLAC-MIT, BCDMS, H1 and ZEUS [57].

Early measurements of the DIS cross-section [56; 58] revealed the proton structure functions to be approximately independent of the collision energy, a property

referred to as *scaling*. Further measurements have only served to support this, as illustrated in Figure 2.6. F_2 as a function of x , obtained from data taken at a range of experiments, at Q^2 values ranging over three orders of magnitude, shows that to a good approximation the data lie on a single curve. It was this observation that originally led to the development of the parton model [59; 60].

If the proton is taken to be a composite of point-like parton constituents, in the Bjorken limit that $Q^2, P \rightarrow \infty$ with x fixed, it was found that $F_i(Q^2, x) \rightarrow F_i(x)$, giving an approximate scaling law that predicted what was seen in data [61]. If a further assumption is made that the constituents are spin-1/2 particles, i.e. quarks, it can be shown that the structure functions obey the Callan-Gross relation [62]

$$F_2(x, Q^2) = 2x F_1(x, Q^2) . \quad (2.17)$$

This suggests that the structure function $F_2(x)$ directly probes a quark constituent of the proton with momentum fraction x , where the quark constituent can carry a range of values for x .

In the parton model, the total electron-proton scattering cross-section is simply a weighted sum over the possible elastic hard-scatterings of the electron and a constituent quark:

$$\sigma_{ep} = \sum_a \phi_{a/p}(x) \sigma_{ea \rightarrow ea} , \quad (2.18)$$

where $\phi_{a/h}(x)$ is the probability of finding a parton a with momentum fraction x of the proton, typically called the parton distribution function (PDF). The proton

structure function is then simply a sum over quark structure functions:

$$F_2(x) = \sum_a q_a^2 x \phi_a(x) , \quad (2.19)$$

where q_a is the electromagnetic charge of the scattered quark.

This "naive" picture of the proton relies on the assumption that the transverse momentum of the parton is small in the infinite-momentum frame of the proton. In QCD this assumption does not hold, since the quark can radiate a hard gluon, giving rise to a large transverse momentum k_T , with a probability proportional to $\alpha_s dk_T^2/k_T^2$ at large k_T . The result is the appearance of logarithmic scaling violations which become large at small x . This scaling violation is a key prediction of QCD, and was verified as very low- x results came out. An example of this agreement is shown in Figure 2.7, where the low- x behavior of F_2 is highlighted for two very different values of Q^2 . The radiation of gluons will grow as Q^2 increases, as there will be more energy in the system, and these gluons can in turn split into $q\bar{q}$ pairs, creating a 'sea' of pairs that becomes large at low- x and breaking the scaling of the structure function.

This process leads to the distinction between the 'valence' quarks, which are thought to be the main constituents of hadrons (the only constituents considered in the simple parton model), and 'sea' quarks, which come in the form of $q\bar{q}$ pairs produced by radiated gluons and are a largely non-perturbative effect. The parton-model-like behavior of the theory is restored with the theorem of factorization, which states that the long-distance (non-perturbative) and short-distance (pertur-

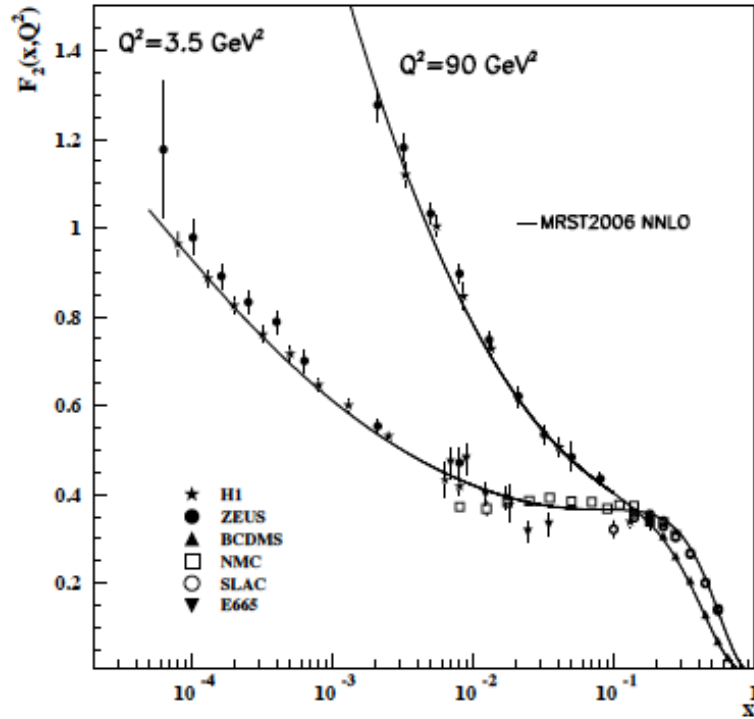


Figure 2.7: The proton structure function $F_2(x)$ for two values of Q^2 (3.5 GeV^2 and 90 GeV^2). Here the breaking of scaling can be seen at $x \sim 0.14$ with one set of pQCD predictions shown to be in good agreement [63].

bative) dependence of hadronic interactions can be considered completely independently [64].

The factorization process requires the introduction of a new scale, μ_f , to define the separation of short-distance and long-distance effects. The proton structure function can then be described in terms of scale-dependent parton density functions:

$$F_2(x, Q^2) = \sum_{a=q,\bar{q},g} \int_x^1 dz C_2^a \left(\frac{x}{z}, \frac{Q^2}{\mu^2}, \frac{\mu_f^2}{\mu^2}, \alpha_s(\mu^2) \right) \phi_{a/h}(z, \mu_f, \mu^2). \quad (2.20)$$

The coefficient function C_2^a is dependent only on the short-distance hard scattering of the virtual photon with the parton, a , and can be calculated in perturbation theory. Although it will depend on the renormalization and factorization scales chosen, it is independent of the long-distance effects. The parton distribution, $\phi_{a/h}(z, \mu_f, \mu^2, \alpha_s(\mu^2))$, on the other hand, contains all the non-perturbative effects and cannot be predicted with pQCD. It is specific to the hadron and depends on μ_f . However it is thought to be universal, meaning it is independent of the hard-scattering process being considered.

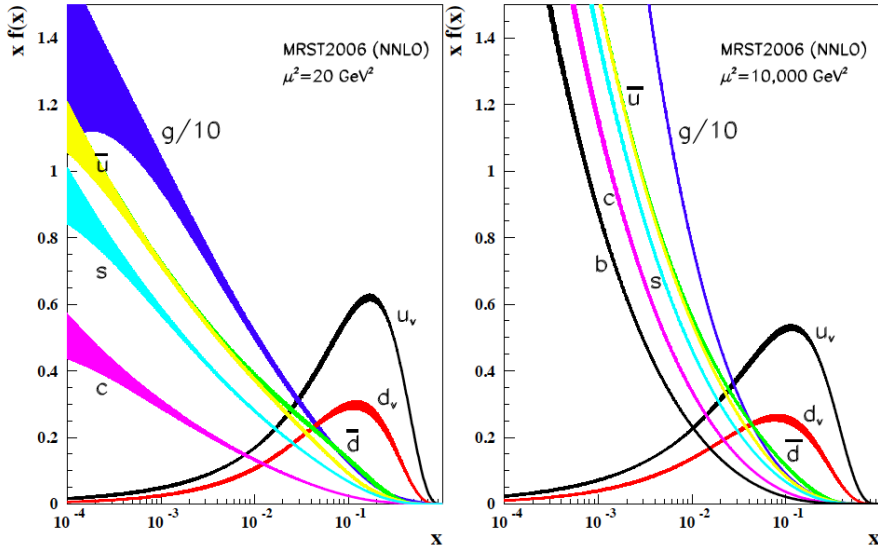


Figure 2.8: Distributions of x times the parton distributions, denoted $f(x)$, for several partons in the proton at two energy scales, 20 GeV^2 (left) and $10,000 \text{ GeV}^2$ (right) [63].

Although the PDFs cannot be predicted *a priori*, as with α_s , the arbitrariness of the factorization scale μ_f allows for the derivation of DGLAP equations - named after Dokshitzer, Gribov, Lipatov, Altarelli, and Parisi - that describe the evolution of the distribution functions in terms of the momentum scale of the interaction [65–

68]:

$$\frac{\partial \phi_a}{\partial \ln Q^2} \sim \frac{\alpha_s(Q^2)}{2\pi} \sum_b \int_x^1 \frac{dz}{z} P_{ab}\left(\frac{x}{z}\right) \phi_b(z) , \quad (2.21)$$

where P_{ab} are the splitting functions describing the parton splitting process $b \rightarrow a$, which are also calculable perturbatively. In this way, once the parton distribution functions have been measured at one energy scale they can be predicted for all other Q^2 scales, provided $Q^2 \gg \Lambda_{QCD}$. Typically the determination of the PDFs from data is done through a global analysis using coefficient functions and splitting functions calculated to next-to-leading order (NLO) or next-to-next-to-leading order (NNLO) the pQCD. The resulting distributions are shown in Figure 2.8 for two different energy scales. From the figure it is clear that the valence quarks, u and d, dominate the proton structure at high- x , while at low- x the gluons and sea quarks start to dominate.

2.2.2 e^+e^- annihilation and fragmentation functions

The underlying hard scattering of an electron and parton in DIS studies can be directly probed by measuring the scattered electron. The recoiling parton, however, cannot be measured directly, as a result of deconfinement. The process by which the parton ultimately forms into hadrons is within the realm of soft, long-range physics, and therefore non-perturbative. To make predictions for the production of hadrons in collisions requires first developing a way of modeling parton \rightarrow hadron process. The cleanest environment for studying this process is through e^+e^- collisions, where the only non-perturbative component is the formation of hadrons, and

the initial parton energy is well understood.

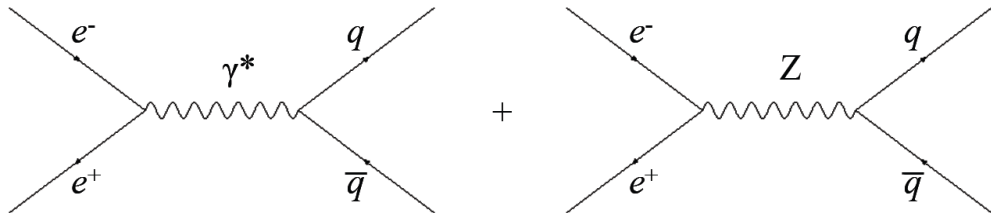


Figure 2.9: Leading order Feynman diagrams for $e^+e^- \rightarrow q\bar{q}$.

One of the fundamental processes of QED is the production of muon pairs in electron-positron collisions, $e^+e^- \rightarrow \mu^+\mu^-$. The mechanism for this process is the combination of an electron and positron to form a photon (or Z), with a momentum Q equal to the energy of the collision \sqrt{s} . The photon can then fluctuate into any particle-antiparticle pair, as long as the pair is kinematically accessible, that is, the condition $m < Q/2$ is satisfied. Thus, the same annihilation process can produce a quark-antiquark pair, with a cross-section calculable using pQCD as long as $Q \gg \Lambda_{QCD}$. The lowest order Feynman diagrams contributing to this interaction cross-section are shown in Figure 2.9.

As a result of confinement, the produced quark-antiquark pair will subsequently form themselves into hadrons through a process called hadronization. Hadronization occurs at a much later time scale, meaning long-distance, non-perturbative dynamics govern the process, putting it outside the domain of pQCD. This process is often referred to as parton fragmentation, as it involves the splitting of the parton into many final state hadrons with only a fraction of the parton energy. Despite this difficulty, at lowest order the total hadronic cross-section can be obtained simply by

summing over all of the kinematically accessible quark-antiquark pairs. Including higher order gluon-loop corrections, the agreement between pQCD and data, shown in Figure 2.10, is very good at sufficiently high energies.

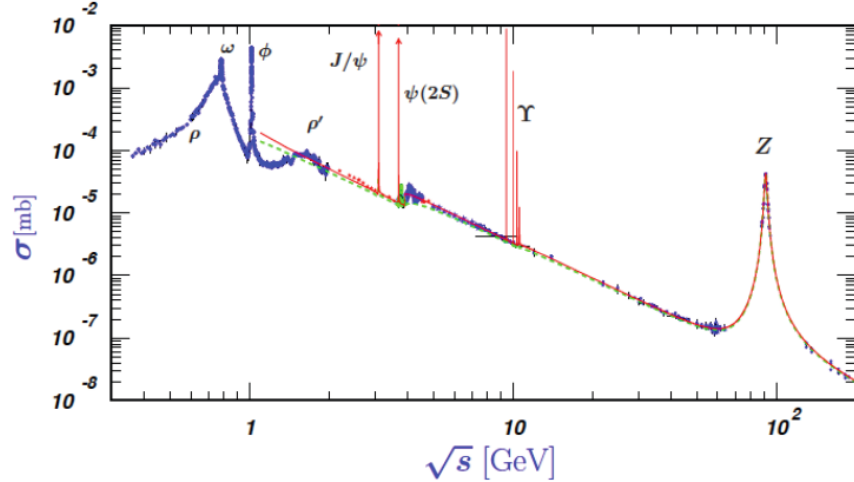


Figure 2.10: World data on total cross-section of $e^+e^- \rightarrow \text{hadrons}$ as a function of the center-of-mass collision energy, \sqrt{s} . The dashed-line curve (green) is a naive quark-parton model prediction and the solid-line curve (red) is the 3-loop pQCD prediction [63].

The ability of pQCD to reproduce the total hadronic cross-section is an important success of the theory. However, as a prediction it is fairly limited in scope, saying nothing about the single-hadron cross-sections or the kinematic distribution of hadrons in the final state⁴. The non-perturbative nature of hadronization implies that rather than using a direct calculation, we must rely once again on a parameterization of the fragmentation process that can be fit to data in the form of fragmentation functions. e^+e^- annihilation, where all of the center-of-mass energy, \sqrt{s} , goes into the final state, is especially useful for defining fragmentation functions since

⁴The later depends on details of parton fragmentation discussed in Section 2.4

the initial quark momentum is known through momentum conservation to be $\sqrt{s}/2$.

Therefore, the fractional energy of a produced hadron is well defined as

$$x = \frac{2E_h}{\sqrt{s}}. \quad (2.22)$$

The factorization theorem again tells us that the cross-section for specific hadron type h can then be written as

$$\frac{1}{\sigma_{tot}} \frac{d\sigma_{e^+e^-}^h}{dx} = \sum_a \int_x^1 \frac{dz}{z} C_a(s; \frac{x}{z}, \alpha_s) D_{h/a}(z, s), \quad (2.23)$$

where

$$C_a = \frac{d\sigma_{e^+e^-}^a}{dx} \quad (2.24)$$

is the cross-section for the underlying perturbative $e^+e^- \rightarrow q\bar{q}$ process. Once again, as part of factorization, the fragmentation functions are assumed to be universal, meaning that once determined at a fixed energy scale, they can be predicted for all other energy scales and used to make predictions about hadronic cross-sections in any hard scattering process.

As with PDFs, in the naive parton model the fragmentation functions are predicted to be scale-independent functions of x , and this scaling is predicted to be violated in the same way when the QCD formalism is applied. The fragmentation functions have an implicit dependence on the factorization scale chosen, which

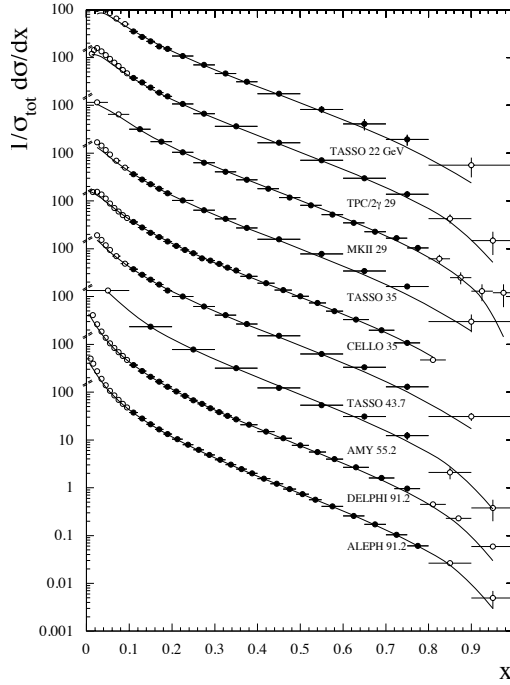


Figure 2.11: e^+e^- fragmentation functions as a function of x at several energy scales [69].

leads to a DGLAP evolution equation [65],

$$t \frac{\partial}{\partial t} D_a(x, t) = \sum_b \int_x^1 \frac{dz}{z} \frac{\alpha_s}{2\pi} P_{ba} \left(\frac{x}{z}, \alpha_s \right) D_b(z, t) , \quad (2.25)$$

which describes the scale dependence of D_a . The splitting functions are again calculable perturbatively, and are similar to those of DIS (the same at lowest order), although the function is now P_{ba} rather than P_{ab} since here we are describing the fragmentation of the final-state parton rather than the distribution of the initial-state parton. Complications arising from the poorly understood hadronization process lead to corrections to purely perturbative calculations of the order $1/Q$ [70].

Nonetheless, with the inclusion of a simple parameterization of these corrections, NLO evolution of the fragmentation functions gives good agreement with data, as shown in Figure 2.11. The curves deviate slightly in the low- x region, where $\ln(1/x)$ terms become large and the parton density saturates, making additional corrections to NLO calculations necessary [71–73].

2.3 QCD in hadronic collisions

A major advantage of both DIS and e^+e^- annihilation is that the point-like nature of the leptons involved gives precise information about the energy of the underlying hard scattering. In the case of e^+e^- annihilation, all of the beam energy goes into the final state, and in $e^- + p$ collisions the recoil electron can be measured to directly determine the Q^2 of the hard scattering. In purely hadronic collisions the dominant processes will be governed by the strong force such that the exact energy of the partons involved in the hard scattering is not known.

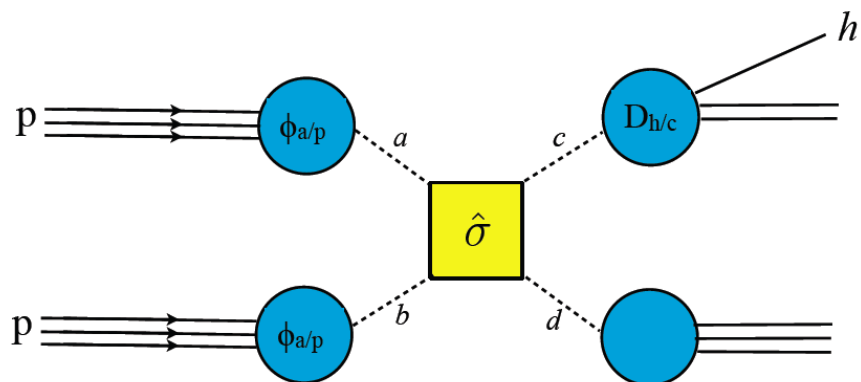


Figure 2.12: Feynman-diagram-like picture of hadron-hadron collisions decomposed into the initial soft and final soft processes and the underlying parton scattering.

As with the previous interactions discussed, based on the parton picture the final state measured from hadronic collisions is the result of an underlying parton-parton hard-scattering [74]. However, as we saw from DIS, the initial scattered constituent parton will not contain the exact momentum of the colliding hadron. In addition, the scattered parton be directly measurable, instead producing a jet, as in e^+e^- annihilation. More accurately, hadronic collisions can be thought of as a combination of the effects seen in the previously discussed interactions. That is, the partonic structure of the hadron must first be resolved using PDFs and the final state hadrons are determined by the fragmentation functions for a specified parton fragmenting into the measured hadron, as illustrated in Figure 2.12.

The total cross-section, for example to produce a hadron h from a $p + p$ collision, is then a convolution over these elements⁵:

$$E_h \frac{d\sigma_{pp \rightarrow hX}}{d^3 p} = \sum_{a,b,c,d} \int dx_a dx_b \phi_{a/p}(x_a, Q^2) \phi_{b/p}(x_b, Q^2) d\hat{\sigma}_{ab \rightarrow cd} \frac{1}{\pi z_c} D_{h/c}(z_c, Q^2) \quad (2.26)$$

where x_a , x_b , and z are, respectively, the fractional momentum carried by initial partons a and b , within each proton, and of the hadron fragmented to the produced parton c . This again assumes the factorization of the soft, long-distance processes described by the PDFs and fragmentation functions and the hard, short-distance process, $\sigma_{ab \rightarrow cd}$. The universality of the PDFs and fragmentation functions is also assumed; that is, these functions can be determined from DIS and annihilation measurements at different energies and then included in pQCD predictions for hadronic

⁵This form is actually only accurate to leading-logarithm as it assumes a single momentum scale characterizes the process

cross-sections in $p + p$ collisions. The relative success of pQCD in hadronic collisions is considered a confirmation of this universality.

Although early comparisons of data with QCD were in good agreement at high p_T , that agreement broke down at lower p_T in two key ways. First, predictions consistently fell below the data. Second, they failed to predict the correct scaling law. Above ~ 1 GeV/c, where pQCD is expected to work, data are observed to exhibit power-law-like behavior [75; 76] which takes the form

$$E \frac{d^3\sigma}{d^3p} = p_T^{-n} f(x_T) , \quad (2.27)$$

where $x_T = \frac{2p_T}{\sqrt{s}}$. QCD calculations predicted an n of 5-6; however, at $\sqrt{s} \sim 60$ GeV for $p_T < 7.5$ GeV/c the data were best described with $n = 8$. The discrepancy was not reconciled until experiment motivated the inclusion of a non-zero transverse momentum, k_T , of the partons within the colliding hadrons.

2.3.1 k_T smearing

More detailed analysis of the final state hadrons was first done through two particle correlations, as described in Section 1.3.1. These correlations are sensitive to details of both the parton distributions within the initial hadron and the fragmentation process of the scattered parton that single particle spectra are not. When developing the form for Eq. (2.26), it was essentially assumed - incorrectly - that the initial state scattering partons were collinear with their hadron, that is, that they had no transverse momentum with respect to the hadron direction. This *intrinsic* trans-

verse momentum, k_T , is observed through the broadening of the away-side peak in two-particle correlation. Further, the already Gaussian-like near-side distribution is a result of a similar transverse momentum spread in the fragments of the final-state parton, j_T .

Although direct observation of k_T comes from two-particle correlations, as will be described in Section 2.4.2, it can play an important role in the single particle spectra. Initially, k_T effects were ignored in calculations of single particle spectra because uncertainty arguments suggested the magnitude of k_T should be on the order of only a few hundred MeV [74]. However, early two particle correlation measurements were more consistent with $\langle k_T \rangle \sim 500$ MeV[77].

The inclusion of k_T effects helped to explain early discrepancies between perturbative calculations and data [78]. The basic idea is that if the initial partons have some initial transverse momentum, at a specific p_T for the final hadronic cross-section, a less-hard scattering is required to produce the same p_T hadron, which will enhance the cross-section. When considering these effects in QCD, complications arise as a result of the fact that higher order corrections involving gluon radiation processes will lead to essentially the same effect, making it difficult to separate them theoretically.

Including k_T effects in predictions for single particle spectra then requires additional integrals of the form $\int d^2k_T$ of the initial parton distribution functions such that

$$\phi(x, Q^2) \rightarrow f(k_T) \phi(x, Q^2) , \quad (2.28)$$

assuming the transverse distribution can be factored out of the longitudinal distribution. Generally $f(k_T)$ is assumed to have an exponential form with a unit integral, for example [79],

$$f(k_T) = \frac{e^{-k_T^2/\langle k_T^2 \rangle}}{\pi \langle k_T^2 \rangle}. \quad (2.29)$$

The mean k_T is essentially a free parameter, although attempting to fit cross-sections at multiple energy scales can put constraints on the theoretically allowed values. When smearing with a $\langle k_T \rangle$ consistent with data is included, the discrepancy for x_T scaling between data and theory can be reconciled.

The improvement in comparisons of data and theory with the inclusion of a large k_T supported the idea that this k_T effect comes from both the expected intrinsic k_T resulting from the finite size of the photon and the soft gluon radiation in the initial state [80]. While the true intrinsic k_T remains outside the realm of QCD calculations, and must be included in the way described above, effects from gluon radiation should in principle be included as one aspect of the QCD dynamics. However, there are logarithmic divergences associated with the soft nature of this radiation which make higher order terms significant. To include such effects at all orders in α_s , calculations applying a resummation of the leading logarithm terms were developed [81] and later extended to beyond leading logarithm [82; 83].

Despite this progress, it is not possible to fully separate the effects of intrinsic k_T and gluon radiation. This is not surprising, since they basically come from the same underlying physics - the interaction of quarks and gluons. However, it does lead to ambiguities in the theory, which result in some amount of instability. This

difficulty arises especially in conjunction with uncertainties associated with NLO sensitivity to the various arbitrary scales introduced to separate the perturbative and non-perturbative scales. More detailed studies of the kinematic structure of the hadronic final state provide one way of further constraining theory.

2.4 Jets and parton showering

Hadronization is an inherently soft process, suggesting that the hadron fragments will have limited transverse momentum relative to the parent parton (collinear fragmentation), appearing as part of a jet of parallel-moving particles. Therefore, at lowest order the contribution to $e^+e^- \rightarrow q\bar{q}$ can be thought of as two back-to-back jets, with the next order corresponding to the hard emission of a gluon by one of the quarks and resulting in three distinct jets, and so on. However, this parton level fragmentation of the initial quark can occur at all energy scales; therefore, non-perturbative effects will contribute. The hardness of the gluon radiation is related to the gluon j_T relative to the initial quark, such that the gluon emission becomes collinear as it becomes non-perturbative, and indistinguishable from later fragmentation into hadrons. As a result, the final jet shape results from a combination of parton splitting and hadronization, requiring more sophisticated modeling. For simple jet cross-section predictions, though, straightforward perturbative methods can be applied.

2.4.1 Jet rates

The total jet cross-section in e^+e^- annihilations is in principle equivalent to the total hadronic cross-section discussed in 2.2.2 . However, for studies of jets to be quantitative, it is first necessary to develop a procedure for defining jets in terms of the final state hadrons measured experimentally. The general requirements for such a definition are that it be consistent with a theoretical definition in terms of final state quarks and gluons that is well described by pQCD, and that it have minimal sensitivity to the non-perturbative hadronization process.

Consistent jet definitions are obtained through the development of algorithms for the clustering of measured particles into jets which are well motivated from theory. There are a few standard types of algorithms that are now well developed [84–88]. The first, and most widely used, is the cone algorithm⁶, where particles are grouped within a cone of fixed size with a jet axis, defined by the p_T weighted sum of the positions of all the particles in the cone and required to line up with the cone axis.

With a consistent definition of a jets, predictions for the total jet cross-section can be made straightforwardly perturbatively. Figure 2.13 shows the total jet cross-section measured using the cone algorithm compared to an NLO calculation, with good agreement between theory and experiment. Here the cross-section is plotted as a function of the transverse energy, $E_T = E \sin \theta$, as it is typically energy, rather than p_T , that is measured experimentally.

⁶There are actually several variations on this basic idea in use.

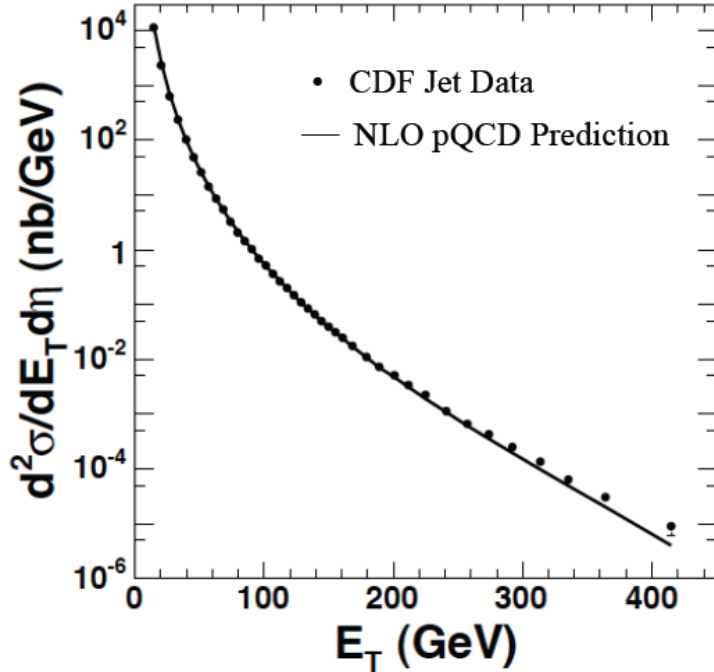


Figure 2.13: The inclusive jet cross-section as a function of jet E_T measured by CDF and compared to NLO pQCD calculations. Only statistical errors are shown. Data and theory agree within quoted systematic uncertainties [89].

2.4.2 Jet shape

While jet rates are a good test of pQCD, more can be learned through studies of the jet shape, which provide a much more stringent test of the theory. At the most basic level, the idea that the hard scattered partons will fragment into near-collinear streams of particles suggests a highly non-uniform structure to the distribution of hadrons in the final state. There are a number of ways the kinematics of the final state can be investigated, ranging from basic studies of the p_T -dependent distribution of particles in the event to those involving detailed analysis of fully reconstructed jets.

2.4.2.1 Event shape

Testing the uniformity of the hadron distribution can be done most simply through the use of event shape parameters, without requiring the jets to be defined. One such widely used parameter is thrust [90]:

$$T = \max_n \frac{\sum_i |\vec{p}_i \cdot \hat{n}|}{\sum_i |\vec{p}_i|} . \quad (2.30)$$

Here \vec{p}_i are the final-state hadron momenta and \hat{n} is an arbitrary unit vector such that, after the maximization of \hat{n} , it will represent the approximate jet axis. If \vec{p}_i form an almost collinear jet the thrust will tend towards one, and if the hadron distribution is more uniform, it will tend towards zero.

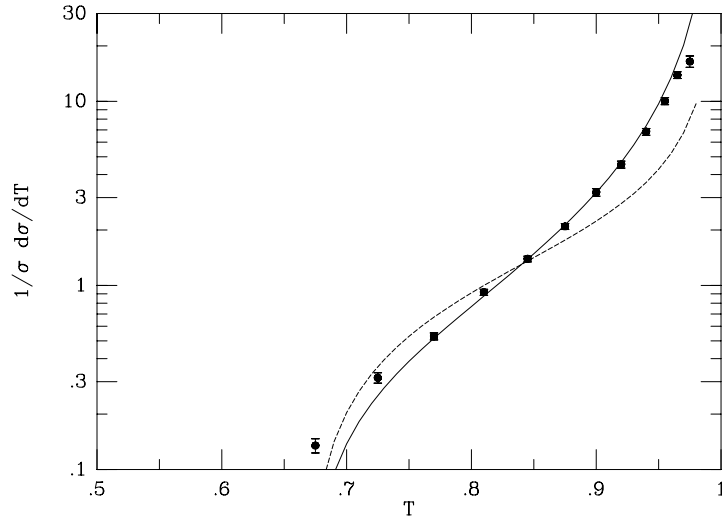


Figure 2.14: The thrust distribution measured at LEP by DELPHI with predicted distributions at leading-order for vector (solid line) and scalar (dashed line) gluon theories [57].

Variables of these types were chosen because of their invariance under the branching $\vec{p}_i \rightarrow \vec{p}_j + \vec{p}_k$, which makes them well defined in pQCD. In fact, early comparisons of calculations with thrust distributions provided the first evidence that gluons were vector particles. An early comparison of thrust (T) is shown in Figure 2.14, with pQCD predictions using scalar and vector gluons, which rules out the scalar gluon theory. The vector gluon prediction does well for intermediate T , but deviates slightly at both large and small T where higher order contributions become important as will be discussed in more detail in Section 2.4.

2.4.2.2 Two particle correlations

Two particle correlations also provide descriptions of the jet shape, since the p_T -dependent angular distribution of hadron pairs is directly related to the kinematics of the jet fragmentation. In correlation measurements of this type, the leading particle selected is defined as the ‘trigger’ particle, which is then correlated with other particles produced in the same collisions, ‘associated’ particles. The relationship between jet kinematics and two-particle kinematics can be described using two basic parameters. The first is the fraction of the associated particle p_T in the direction of the trigger particle,

$$x_E = -\frac{\vec{p}_{T,trig} \cdot \vec{p}_{T,assoc}}{|\vec{p}_{T,trig}^2|}, \quad (2.31)$$

which is indirectly related to the fraction of the jet energy carried by the associated particle. The second is the component of associated particle momentum perpendic-

ular to the direction of the trigger particle,

$$p_{out} = \frac{|\vec{p}_{T,trig} \times \vec{p}_{T,assoc}|}{|p_{T,trig}|}. \quad (2.32)$$

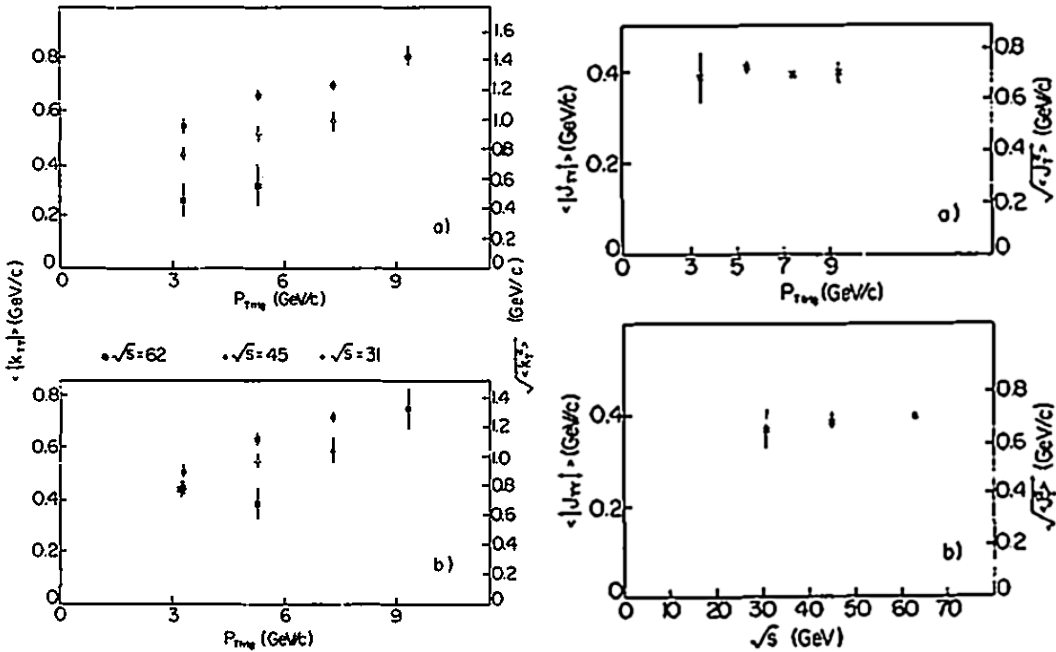


Figure 2.15: On the left is the mean (right axis) and RMS (left axis) k_T as a function of trigger p_T using two independent methods for extracting $\langle k_T \rangle$ from the correlated away-side, for different \sqrt{s} . On the right is the mean and RMS j_T vs. trigger p_T (top) and \sqrt{s} (bottom). Both are from two-particle correlations with ISR data [91].

The measured p_{out} distribution is then thought to be related to the two underlying effects mentioned in Section 2.3.1: the transverse momentum of the initial scattering partons (k_T), and the transverse momentum of the measured hadrons rel-

ative to the jet axis (j_T). An approximate form for this relationship is [92]

$$\langle p_{out} \rangle^2 = (2\langle k_{Ty} \rangle^2 + \langle j_{Ty} \rangle^2)x_E^2 + \langle j_{Ty} \rangle^2. \quad (2.33)$$

Using fits to the $\langle p_{out} \rangle^2$ distributions as a function of x_E^2 , both the mean k_T and j_T as a function of trigger (or associated) p_T and collision energy, \sqrt{s} , can be determined. Figure 2.15 shows some of the first measurements of these quantities. It was found that j_T was independent of collision energy and of trigger p_T , as expected if the parton fragmentation is in fact universal and therefore independent of the underlying hard scattering.

These measurements also demonstrate the discovery that k_T was larger than originally expected and proportional to both the trigger p_T and \sqrt{s} . The dependence of k_T on trigger p_T is expected, as a form of ‘trigger bias’, since a trigger hadron of a given p_T will be more likely to come from a hard scattering at lower Q^2 with some initial k_T than from higher Q^2 . Predictions for the measured p_{out} distributions were made and found to be in good agreement with data [78] - however, only with the inclusion of effective k_T and j_T smearing motivated by the measured values from data. Even so, the ability to match these distributions supports the parton model, and QCD in general, and it provided early measures that helped to further develop the theory.

2.4.2.3 Reconstructed jets

Full jet reconstruction provides a way of more directly accessing information about the distribution of particles in the jet. With knowledge of the jet axis and momentum, which corresponds to that of the original hard scattered parton, as well as the full set of fragmented hadrons⁷, it is possible to directly measure both the fractional parton energy carried by each hadron fragment (z) and the component of the hadron momentum perpendicular to the parton (j_T). The ability to measure the z distribution this way implies that reconstructed jets provide an independent measure of the parton→hadron fragmentation functions previously determined, for example, in e^+e^- annihilations. The j_T distribution is a direct determination of the kinematic distribution of hadrons in the jet, like that previously determined indirectly through measurements of thrust or the mean j_T from two-particle correlations.

Rather than j_T , the jet shape is typically described in terms of the parameter, $\psi(r)$, defined as the average fraction of the jet transverse momentum lying inside a cone of radius r , where r is defined as

$$r = \sqrt{\Delta\eta^2 + \Delta\phi^2} \quad (2.34)$$

and η is the pseudorapidity defined in terms of the polar angle as

$$\eta = -\ln \left[\tan \left(\frac{\theta}{2} \right) \right]. \quad (2.35)$$

⁷At least within the constraints for the jet definition placed by the specific algorithm used.

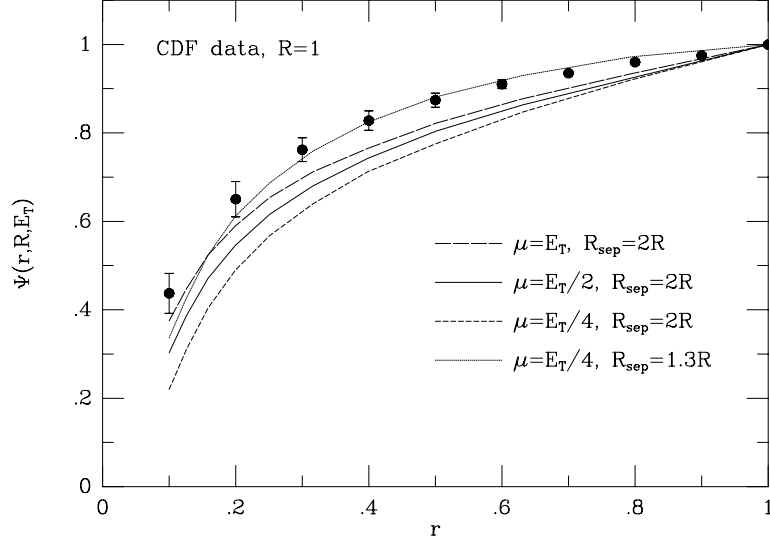


Figure 2.16: Jet profile for jet $E_T = 100$ GeV, reconstructed using a cone algorithm with $R = 1$ [57].

$\psi(r)$ is often called the jet profile, and has the form,

$$\psi(r) = \frac{1}{N_{jet}} \sum_{jets} \frac{P_T(0, r)}{P_T(0, R)} , \quad 0 \leq r \leq R , \quad (2.36)$$

where $P_T(0, r)$ is the integrated transverse momentum in the range specified, N_{jet} is the total number of jets, and R is the jet size defined by the algorithm [93]. In general, ψ will also depend on the specific value for R used by the algorithm, as well as the total transverse jet energy, E_T . Figure 2.16 shows the r dependence of $\psi(r)$ for jets defined by the cone algorithm with $R = 1$, at $E_T = 100$ GeV, along with several NLO predictions. As with attempts to determine thrust, the theoretical predictions have some difficulty reproducing the data, especially for small values

of r , which correspond to the region where collinear divergences will become an issue.

2.4.3 Parton showering

Although we have seen that pQCD does quite well with single particle cross-sections, descriptions of the kinematics of the final state have proven more difficult, particularly in limits where higher order terms in the perturbative expansion become more significant due to logarithmic divergences. Essentially, these higher order enhancements come about as a result of the radiation of very soft gluons, either through collinear emission leading to discrepancies near the jet axis, or soft emission at all angles leading to wide angle low- p_T discrepancies.

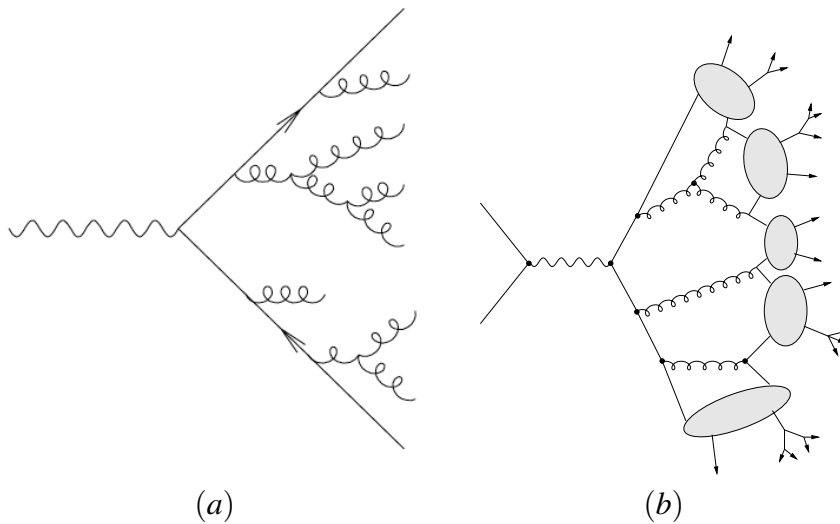


Figure 2.17: (a) Example of a parton shower diagram. (b) Clustering of shower components into final state hadrons.

The rapidly increasing difficulty of pQCD calculations as we go to higher orders

- due to the growing number of diagrams needed - makes attempting to include such effects with fixed order calculations difficult. Instead, what is typically done is to include only the leading logarithmic terms - coming from parton splitting - to all orders [81]. This means that at a given order in α_s , no loop diagrams are included in the calculation; only the $2 \rightarrow n$ process is calculated. An example of the type of diagram this would involve is shown in Figure 2.17(a). The parton splitting continues until the remaining partons reach some minimum p_T below which the non-perturbative soft regime takes effect. This is basically the same formalism applied to the initial state described in Section 2.3.1.

The details of the showering include a choice in how the stages in the shower are ordered in the summation. The most commonly used way is motivated by the hard-soft factorization, where the hardest interactions are included first [94]. The only complication to this ordering is that it involves the inclusion of interference diagrams, where soft emission is reabsorbed, complicating the calculations somewhat. The other option is what is called angular ordering, where splittings are included in order of emission angle, omitting the need for interference graphs but requiring the introduction of a low p_T cut-off for each graph [95].

These types of parton shower models are implemented using simulations, where in the case of hadronic collisions splitting is included both for the initial state partons and for the final parton fragmentation. The final step required for comparison with data is to then implement a model for the hadronization of all the final state partons produced in the shower, with a variety of models to choose from [96–100]. An illustration of this process is shown in Figure 2.17(b), where the final partons

are clustered together to form hadrons which can then decay into the particles ultimately measured experimentally[99; 100].

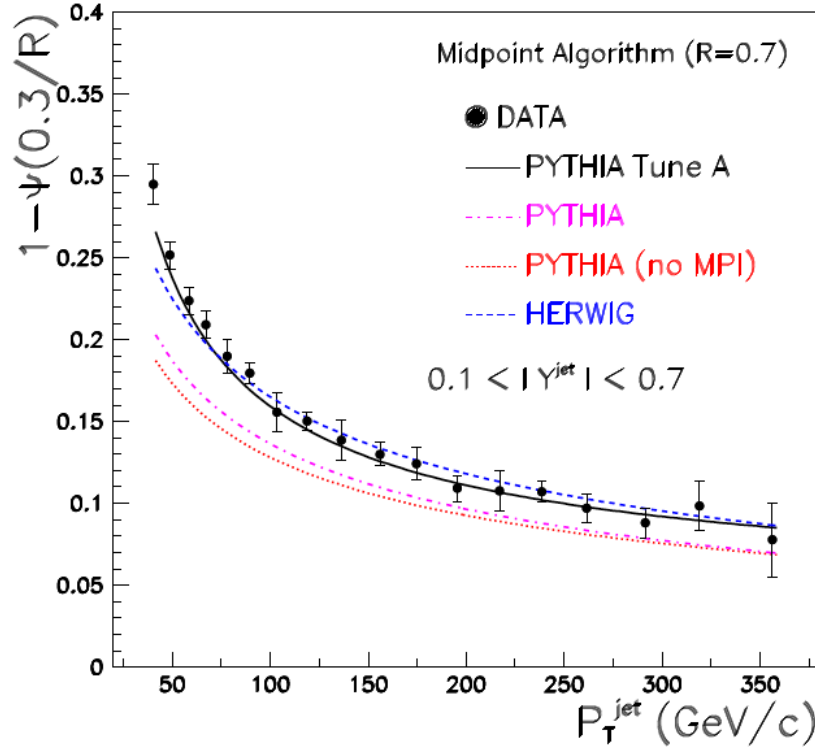


Figure 2.18: Measured $1 - \psi(0.3/R)$, as a function of jet p_T for jets with a rapidity from 0.1 to 0.7, compared to various simulations (see text for descriptions) [93].

Several Monte Carlo simulation programs have been developed over the years that implement parton showering, often coupled with a few choices for the modeling of the fragmentation into hadrons. In general, these simulations do a much better job of reproducing details of jet shape and kinematics than fixed order pQCD calculations, although it is important to note that they often include the ability to adjust the details of the parton showering in order to obtain good agreement. For example, Figure 2.18 shows a measure of the jet profile as a function of jet p_T

with the predictions of various simulations. The two simulation types shown here represent the two choices mentioned for the ordering of diagrams included in the parton shower, with PYTHIA [101] implementing a momentum (virtuality) ordering and HERWIG [102] implementing an angular ordering. The PYTHIA Monte Carlo agreement with data was obtained by including enhanced contributions from initial-state gluon radiation and secondary parton interactions between remnants (PYTHIA-Tune A) along with multi-parton interactions (MPI) [93].

2.5 Direct photons

The production of high- p_T direct⁸ photons is closely related to the production of jets, with several advantages from both an experimental and theoretical perspective. As the point-like QED vector boson, photons are not subject to any non-perturbative fragmentation process. Therefore, there is less theoretical uncertainty in describing photon production, even in hadronic collisions. In addition, the small number of parton-level hard scatterings contributing to the production of photons further simplifies theoretical calculations. Experimentally, the photon energy and direction relative to the production point are straightforward to measure directly. The only draw-back is the low production rate - $O(\alpha\alpha_s)$ ⁹ as opposed to $O(\alpha_s^2)$ for jets - coupled with the large background from neutral hadron decays - mostly from $\pi^0 \rightarrow \gamma\gamma$.

⁸Generally, direct photons at leading-order are referred to as ‘prompt’ and those at higher orders as ‘fragmentation’

⁹ α is the QED coupling constant and is roughly equal to 1/137.

2.5.1 Photons at leading order

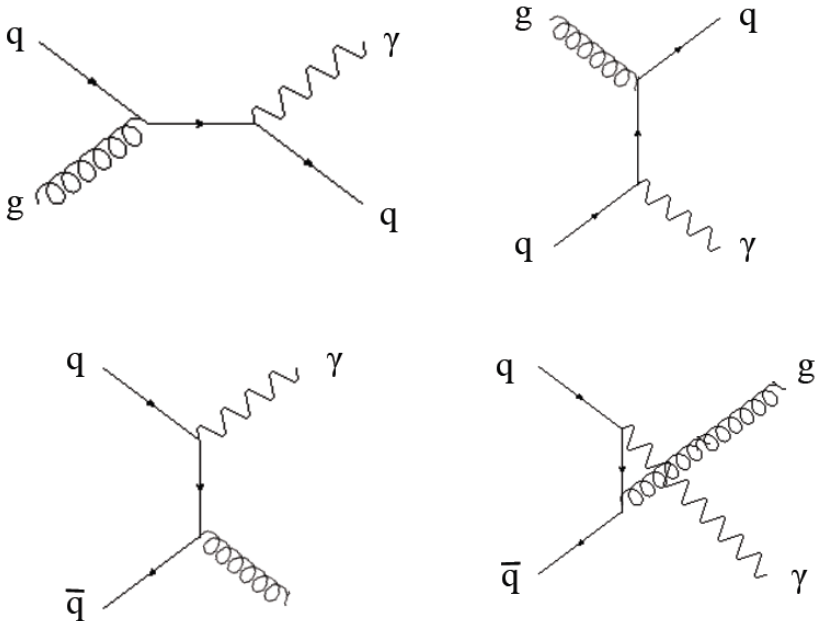


Figure 2.19: Leading order Feynman diagrams for direct photon production in QCD hard scatterings. The two quark-gluon Compton diagrams are shown on the top, and the two annihilation diagrams are on the bottom.

At leading order in pQCD photons are produced through two subprocesses: quark-antiquark annihilation $q\bar{q} \rightarrow \gamma g$, and QCD Compton scattering $qg \rightarrow \gamma q$. The diagrams contributing to these processes are shown in Figure 2.19. In $p + p$ collisions, the Compton process dominates the direct photon cross-section by roughly an order of magnitude over the annihilation process because of the low probability for anitquarks. For this reason, in $p + \bar{p}$ collisions the annihilation process will become significant in certain kinematic ranges. There are several aspects to these processes which make measurements of direct photons at leading order extremely useful in further understanding the details of QCD.

The photon will be produced approximately back-to-back with the final state quark or gluon, which will then fragment into a jet. As a result, in the kinematic range where either the Compton or annihilation process dominates, the tagging of jets that are back-to-back with high p_T direct photons (γ -jet) directly probes quark jets or gluon jets respectively. When considering the Compton process, the presence of the gluon in the initial state indicates that the process is sensitive to the gluon distribution function, which is generally poorly understood.

It is also possible to determine which LO process is dominant, as well as probe the quark flavor of the recoiling jet in the case of the Compton process, using studies of the charge ratio for hadrons opposite a direct photon. The idea with respect to the Compton process is that the relative abundance of up quarks (2:1), combined with the relative charge coupling of up and down quarks to the photon $((2/3)^2 : (1/3)^2$, suggests the up quark is 8 times more likely to participate in the production of a photon than the down quark. This increased probability should lead to a $(+/-)$ charge ratio larger than one opposite a direct photon. Alternatively, if the recoiling parton is a gluon, the charge ratio should be one. Early measurement of direct photon-hadron correlations did in fact reveal a charge ratio larger than one and consistent with NLO calculations [103].

Despite the powerful ability of direct photon measurements - and in particular γ -jet measurements - to probe the gluon distribution function, with past theoretical calculations it has been a struggle to accurately reproduce direct photon cross-section measurements [104]. As a result, direct photons have yet to prove useful in our understanding of the gluon structure of protons [105]. There are essentially

two key ambiguities in calculations of the inclusive direct photon cross-section that lead to the larger theoretical uncertainties not originally expected for such point-like interactions.

One ambiguity results from poorly constrained NLO contributions, as we will see in Section 2.5.2. When studying γ –jet measurements, where the photon is required to be back-to-back with a jet, the desire is to study the dominant leading order processes. NLO contributions are typically minimized through the application of an isolation cut where the photons are required to be separated from any hadronic activity by some well defined radius. However, even with such cuts, theory has struggled to describe the cross-section for photons found back-to-back with jets over the full kinematic range [106]. This is shown in Figure 2.20, where the γ –jet cross-section was measured over a large p_T range and a variety of jet rapidities and compared to several NLO QCD predictions.

The second ambiguity result from the initial k_T effect. As mentioned in Section 2.3.1, in hadronic collisions the finite size of the proton coupled with initial-state gluon radiation leads to an initial k_T in the hard scattering which can modify the final-state p_T distribution measured. This k_T effect can contribute in the processes leading to direct photon production as well, leading to similar ambiguities in theoretical predictions for the cross-section. The inclusion of k_T smearing, again as described in Section 2.3.1, has been shown to improve agreement between theory and earlier direct photon measurements [107; 108]. On the other hand, claims have also been made that applying similar resummation techniques, without additional k_T smearing, is able to reconcile theory and data in most cases [104]. As Figure

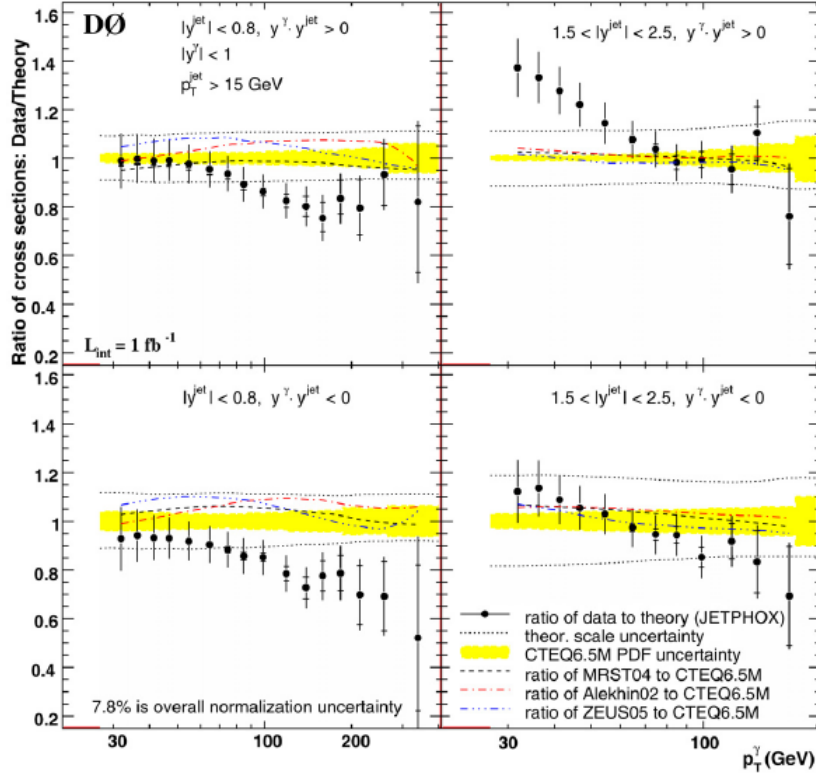


Figure 2.20: The ratio of the measured γ –jet cross-section to NLO QCD predictions, as a function of photon p_T . Here y^{jet} is the rapidity of the jet opposite the direct photon. The yellow band represents the uncertainty in the initial PDFs, and the dotted and dashed lines represent theoretical scale uncertainties [106].

2.21 demonstrates, where the ratio of data to theory for inclusive and isolated direct photons is compared across two orders of magnitude in x_T and nine orders of magnitude in the cross-section, the agreement between data and theory is extremely good, with one unresolved exception [109]. However, the discrepancies shown in Figure 2.20 persist, and the issue of intrinsic k_T is far from resolved.

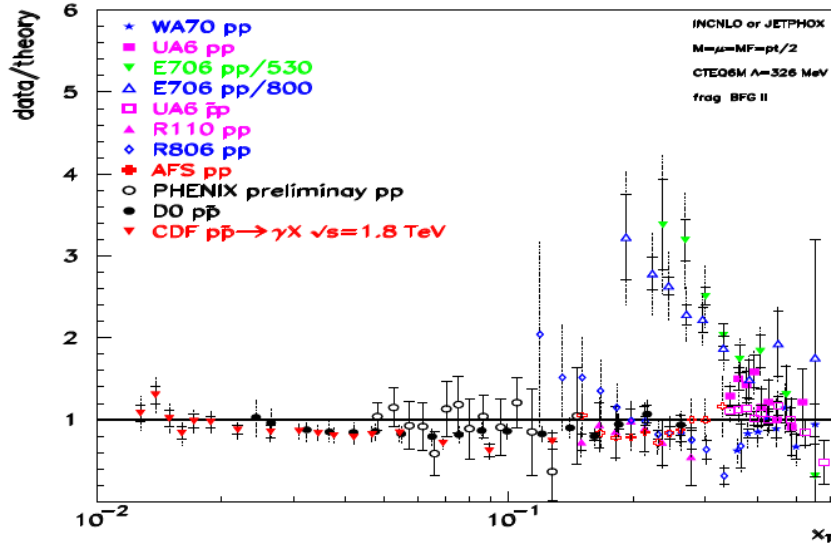


Figure 2.21: The ratios of data to theory for a range of collider and fixed target data as a function of x_T . The CDF and D0 data are for isolated direct photons only [109].

2.5.2 Photons beyond leading order

Figure 2.22 shows two NLO diagrams that will contribute to calculations of the total direct photon cross-section. The first is an example of diagrams that are higher order, while contributing to the cross-section for prompt photons produced in the initial hard scattering. In the discussion of jets in Section 2.4, gluon radiation by quarks participating in hard scattering played an important part in the development of the parton shower. In a similar fashion, quarks have some probability of radiating photons as a result of their electric charge, a case illustrated in the second diagram in Figure 2.22. In this case the point-like vertex is the same as in QED, meaning in principle the effective fragmentation function for obtaining a photon from a quark can be calculated (it will be zero for gluons, which are electrically neutral). How-

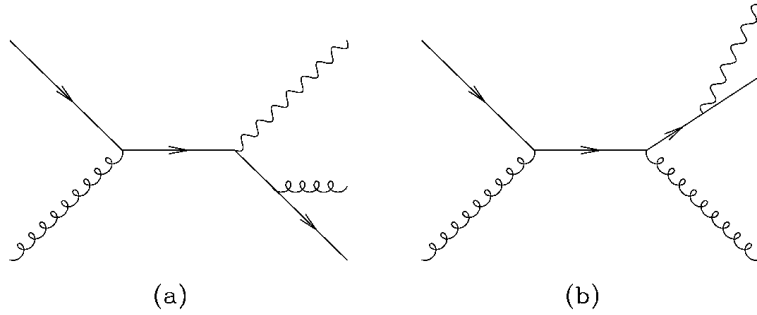


Figure 2.22: Two next-to-leading order Feynman diagrams for direct photon production in QCD hard scatterings. (a) is an example of gluon radiation by hard scattered quark. (b) is an example of photon radiation by the hard scattered quark.

ever, the details of the calculation involve integrating over the full range of photon j_T , which will diverge as the photon becomes parallel to the quark.

A leading-logarithm (LL) approximation is often used, which can be written as [79]

$$zD_{\gamma/a}(z, Q^2) = q_a^2 \frac{\alpha}{2\pi} [1 + (1-z)^2] \ln(Q^2/\Lambda_{QCD}^2), \quad (2.37)$$

where q_a is the fractional charge of the a quark. As with the hadronic fragmentation functions, the photon fragmentation functions will evolve with Q^2 , again because of parton splitting. This leads to a softening of $D_{\gamma/q}$ and a non-zero $D_{\gamma/g}$.

Solutions to the evolution equations reveal that the fragmentation functions are proportional to $\alpha/\alpha_s(Q^2)$, a result of their logarithmic growth with Q^2 . When one then convolutes the $O(\alpha_s^2)$ parton-parton subprocess with the fragmentation function, the resulting contribution is of order $\alpha\alpha_s$, the same order as the LO direct photon processes. Surprisingly, it is therefore possible that these fragmentation photons can be produced at a rate comparable to prompt photon production. For example, Figure 2.23 shows an NLO calculation for the ratio of fragmentation pho-

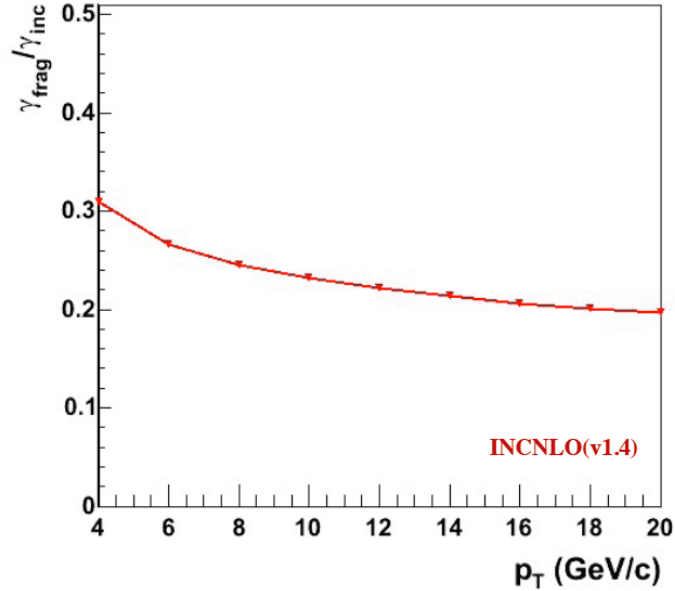


Figure 2.23: Ratio of fragmentation photons to inclusive direct photons as a function of photon p_T calculated using a next-to-leading order simulation [110].

tons to inclusive direct photons, which predicts a contribution of as much as 30% [110].

At leading order, solutions have a form similar to Eq. (2.37); however, for a complete solution, a non-perturbative component is required. This non-perturbative input is generally estimated using the Vector Meson Dominance Model (VDM) [111], in which the photon is described by a superposition of vector mesons. The photon fragmentation function is then directly related to the vector meson fragmentations functions, which are constrained by data in the standard way (see Section 2.2.2).

As with hadrons, the quark-to-photon fragmentation function can be tested experimentally most directly through e^+e^- annihilations. One way such collisions

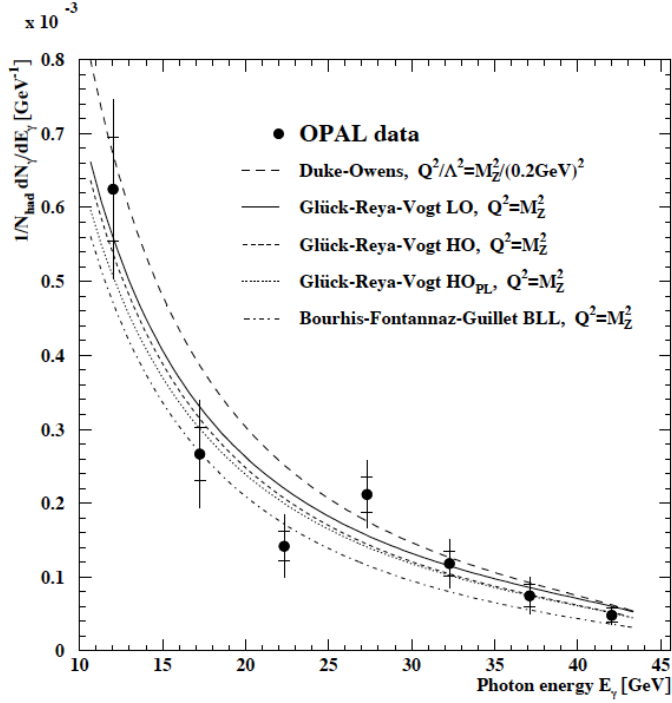


Figure 2.24: The photon energy spectrum measured by OPAL compared to several predictions including various orders in the perturbative expansion (LO and HO) as well as non-perturbative corrections (HO_{PL} and BLL) [112].

have been used is through the measurements of high- p_T photons from Z^0 decays, which are attributed to radiation from one of the primary quarks[112]. In this case the photon cross-section can be directly related to the fragmentation function using [113]

$$\frac{1}{\sigma_h} \frac{d\sigma(E_\gamma)}{dE_\gamma} = \frac{4}{\sqrt{s}} \sum_q \omega_q D_{\gamma/q} . \quad (2.38)$$

A comparison of data with theoretical calculations for $D_{\gamma/q}$ using this relation is shown in Figure 2.24. There are several predictions shown, including leading order, higher order (HO), and beyond-leading-logarithm (BLL) - which includes non-

perturbative components using VMD. While the data shows good agreement in general, it is not sensitive to the theoretical details, and therefore unable to constrain the non-perturbative component.

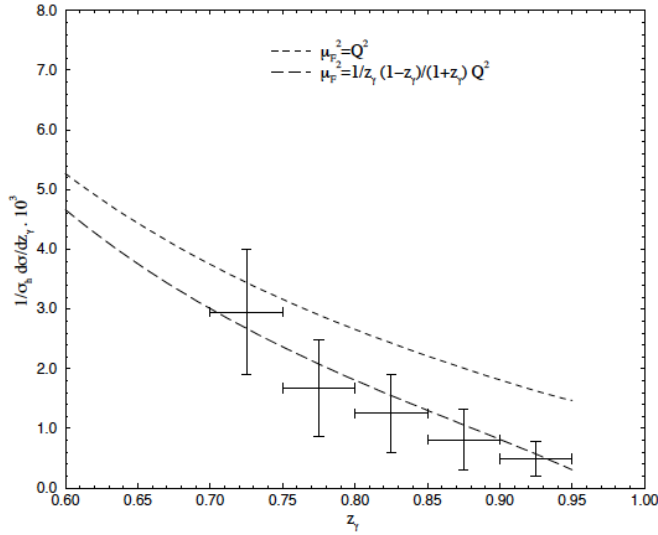


Figure 2.25: The cross-section for photons in jets as a function of their fractional jet energy measured by ALEPH compared to BLL predictions [111].

Another way of measuring the fragmentation function was through the selection of hadron jets containing a photon with $z > .7^{10}$ [114]. This measurement can be directly compared to predictions for $D_{\gamma/q}(z)$, as shown in Figure 2.25. In the case shown, the comparison is not direct because of kinematic restrictions on the data as a result of the requirement that they be in an algorithmically defined jet [111]. Even so, the relatively good agreement between data and theory is encouraging.

¹⁰Here z is the fraction of the total jet energy, which should be equivalent to the initial parton energy.

2.5.2.1 Fragmentation photons in $p + p$

The prediction for direct photon production has somewhat larger uncertainties than might be expected for what is essentially a QED process. The larger uncertainties result from the combination of the poorly understood initial state k_T effect, which leads to uncertainties in the total direct photon cross-section similar to those for hadronic cross-sections, and the non-perturbative component of the fragmentation function. In hadronic collisions, when coupled with experimental limitations resulting from the large background of photons produced through the decay of neutral hadrons, the result is that while pQCD calculations at NLO are able to reproduce the measured inclusive direct photon cross-section¹¹, the agreement leaves room for large variations in the underlying approximations made. Figure 2.26 illustrates this point, showing the cross-section for direct photons in $p + p$ collisions at $\sqrt{s} = 200$ GeV, compared with NLO pQCD calculations [115], where - at lower p_T - variations of as much as a factor of two are permitted.

The method mentioned in Section 2.5.1 - applying an isolation cut around high- p_T photons to remove the contribution from fragmentation photons to γ -jet measurements - suggests that comparisons between inclusive direct photon productions and isolated direct photon production could help to constrain predictions for the relative yield of fragmentation photons. However, isolation cuts do not provide a clean separation between leading-order and higher order photon production¹². Ad-

¹¹This statement applies specifically at energies currently accessible to heavy-ion collisions for studying medium modification.

¹²It is estimated that there is an approximate 10% contamination from fragmentation photons remaining after these cuts are applied [106].

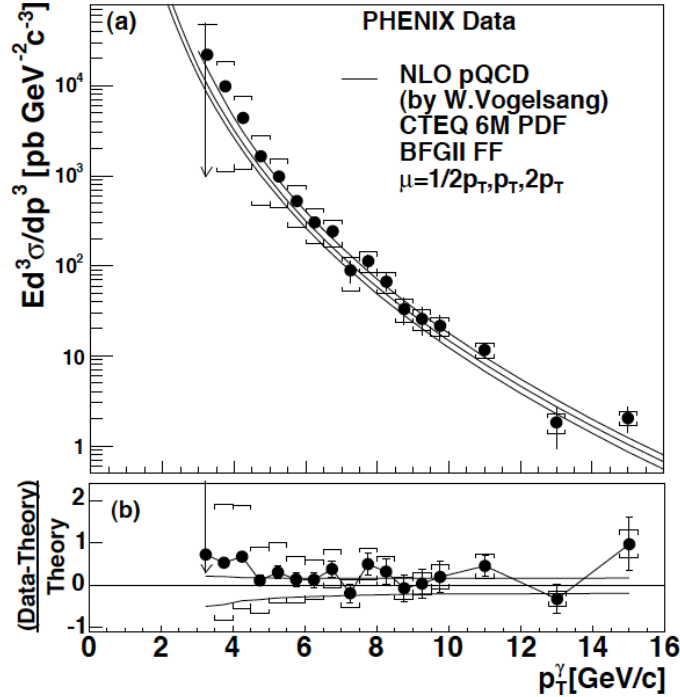


Figure 2.26: The direct photon cross-section as a function of photon p_T at $\sqrt{s} = 200 \text{ GeV}$ compared to an NLO pQCD calculation. The bottom panel shows the relative difference between data and theory, with the range for the uncertainties on both [115].

ditionally, given the large uncertainties (Figure 2.26) for inclusive direct photon measurements and the expectation that the yield of fragmentation photons is not more than $\sim 30\%$, it is not realistic to expect such a method to provide much constraint on the quark-to-photon fragment function.

The early measurements of photons in jets shown in Figure 2.25 suggest that an alternative is to identify the jet signal and then identify direct photons associated with the jet, which will naturally suppress the ‘background’ from leading-order. We have seen the use of two-particle correlations serve as a good proxy for full jet measurements. Therefore, with some consideration for the hope to compare any

measurement of fragmentation photons to a similar study in heavy-ion collisions, these correlations seem a likely candidate for a successful direct measurement of fragmentation photons that may be extendible to further studies of nuclear effects.

An additional advantage to using correlations to measure fragmentation photons is that, as described in Section 2.4.2.2, correlations provide information about the jet shape inaccessible from inclusive cross-section measurements. When considering models of parton showering, such photons have the unique ability to directly probe the showering of the initial parton without the complication of hadronization.

Chapter 3

Detection

As discussed in chapter 2, the study of QCD and jet physics requires collisions between particles at energies high enough to probe the structure of the proton. To go further and study the properties of deconfined quarks and gluons, these collisions must be at high enough energy, and density, to pass the critical temperature for the QGP phase transition. Therefore, these investigations require the use of large particle accelerators, typically spanning several kilometers in length and able to manipulate large numbers of particles (on the order of $10^{11} - 10^{12}$ per bunch) simultaneously, to ensure a high rate of collisions. There are several options available in terms of particle accelerator technology, most notable being linear, cyclotron, and synchrotron accelerators [116]. The limitations of linear and cyclotron accelerators in terms of size, as well as the ability of synchrotrons to accelerate and store particle beams for an extended period of time, make synchrotrons the obvious choice.

The work of this thesis is based on data collected at the synchrotron at Brookhaven National Laboratory (BNL), the Relativistic Heavy Ion Collider (RHIC) [117], by the Pioneering High Energy Nuclear Interaction eXperiment (PHENIX). There

were originally four experiments operating at RHIC, PHENIX [118], STAR [119], BRAHMS [120], and PHOBOS [121], with physics programs that were both competitive and complementary in their goals, allowing for the comparison of results across experiments, as well as a wider range of possible measurements. PHOBOS and BRAHMS were smaller more specialized collaborations that have completed their goals and are no longer in operation. The specific design features of PHENIX, discussed in detail in Section 3.2, are ideal for measuring direct photons, as well as those found in coincidence with jets. In addition, the range of collision systems available at RHIC make extensions of the work described in this thesis possible.

3.1 RHIC

The RHIC facility consists of two storage rings each acting as an independent particle accelerator (see Figure 3.1). The two rings, labeled “blue” and “yellow” for clockwise and counter-clockwise particle beams, respectively, are housed in an approximately circular 3.8 km long tunnel. There are six interaction points, relatively straight sections of the tunnel where the rings cross, enumerated by clock positions, with PHENIX sitting at 8 o’clock (see Figure 3.1). Particle bunches are steered through each ring using a series of niobium-titanium superconducting magnets, with a separate set of dipole magnets used to steer the beams into collinear paths at the interaction points, and quadrupole magnets to focus the beam for high luminosities. The beams are timed such that, at the interaction points where there are detectors, bunches in each beam will cross at the same time, and collisions can occur.

At the relativistic energies achieved at RHIC, particles in the beam will be moving near the speed of light, with a relatively constant frequency of 78 kHz (f_{rev}). The design of RHIC allows for up to 120 bunches per ring (b), with 2×10^{11} particles in each bunch for p + p, or 10^9 for Au + Au. The corresponding luminosities, determined by

$$\mathcal{L} = \frac{b}{4\pi} \frac{N^2}{\sigma_x \sigma_y} f_{rev}, \quad (3.1)$$

where N is the number of particles per bunch, and σ_x and σ_y are the cross-section of the bunches, are $2 \times 10^{32} \text{ cm}^{-2} \text{s}^{-2}$ and $2 \times 10^{26} \text{ cm}^{-2} \text{s}^{-2}$ respectively. Even at these high luminosities a collision, generally referred to as an event, will not occur with every beam crossing, making it necessary to apply a trigger condition to determine if an event has occurred. The method employed by PHENIX is described in detail in Section 3.6.

3.1.1 Accelerating to RHIC

As a synchrotron accelerator, RHIC is able to stores particle beams for as long as 10+hrs (in theory), and can accelerate proton and Au-ion beams up to 250 GeV and 100 GeV, respectively. As with similar accelerators, however, it is not able to accelerate particles from rest, instead relying on a chain of accelerators with successively higher maximum energies to then feed the beam into the RHIC tunnel. In the case of p + p, the primary objective for RHIC is to study polarized proton collision - both longitudinal and transverse - to further our understanding of spin physics rather than simply for comparison with heavy ion results. To that end,

while not relevant to the work presented here, many of the details of the operation of RHIC during p + p running focus on the ability to produce and maintain highly polarized proton beams [122].

As shown in figure 3.1, the process starts with a pulse of polarized hydrogen(H^-) ions that get accelerated up to 200 MeV by a linear accelerator (LINAC), then stripped of their electrons and injected as a single bunch into the Alternating Gradient Synchrotron (AGS) Booster. In the AGS Booster the bunch is accelerated to 1.5 GeV and transferred to AGS proper, where it can then be accelerated up to 25 GeV. Finally, bunches are injected into RHIC one at a time, through a transfer line designed to steer beams within a certain energy range; 20.58 – 28.3 GeV in the case of p + p. This effectively fixes the minimum energy collisions RHIC is able to produce without decelerating the beam.

Once injected into the main RHIC ring, each bunch is captured and accelerated by a radiofrequency(RF) system operating at 28 MHz, the harmonic number $h = 360$ of the particle rotation frequency. This design allows for fixed numbers of evenly spaced bunches of 60, 72, 90, or 120, which are then accelerated through the RF pulse and finally stored at the maximum energy. An additional RF system, operating at 197 MHz, is then used for shortening the bunches to keep the longitudinal cross-section ($\sigma_L \approx 25$ cm) reasonable. The challenge is then the maintenance of the proton polarization. While not relevant for the results discussed here, it is important to note that polarized protons beams were used to generate the data used; averaged over polarizations, the data should be equivalent to unpolarized data.

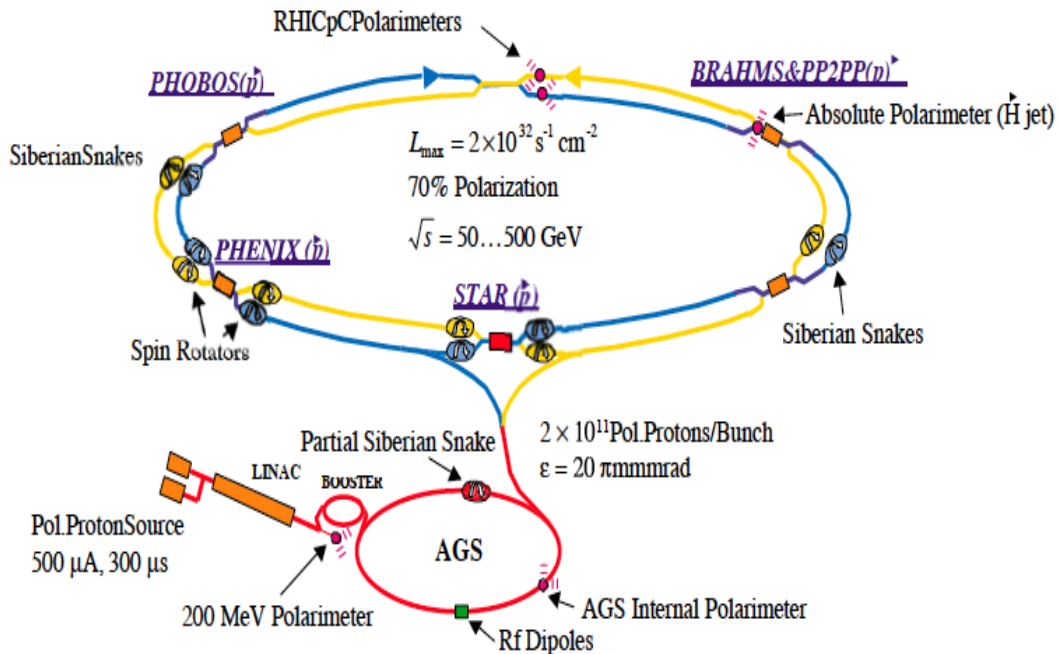


Figure 3.1: The RHIC ring with the original four detectors [117].

3.2 PHENIX Overview

The PHENIX detector is designed to specialize in the measurement of processes such as photon, lepton, and high- p_T hadron production, making use of high resolution particle identification capabilities and a sophisticated triggering system for selecting such rare events. The design of the PHENIX detector began as the merger of multiple physics programs leading to the development of two relatively independent detector systems: the central spectrometer at mid-rapidity ($|\eta| < 0.35$), and the forward spectrometer arms [123] extending over $1.8 < |\eta| < 2.2$ in pseudorapidity ($\eta = -\tan \frac{\theta}{2}$). The central spectrometer consists of an east and west arm, each with a limited ($\frac{\pi}{2}$) ϕ acceptance, while the forward spectrometer arms have full azimuthal

coverage. Both a side view and beam view image showing the arrangement of the various detector subsystems are shown in Figure 3.2.

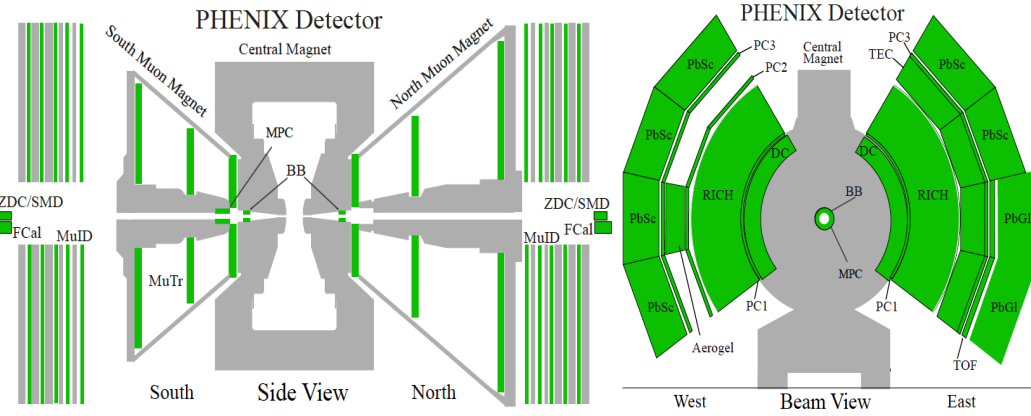


Figure 3.2: The PHENIX Detector. Side view (left). Beam view (right) [118].

The forward spectrometer arms specialize in the detection of muons, featuring prominently in measurements related to heavy quark production, as well as measurements involving rapidity dependent variations in particle production. The central spectrometer arms are instead designed for a variety of uses over a much more limited rapidity range, such as identifying and tracking electrons, tracking charged hadrons, and detecting photons with enough precision to reconstruct neutral mesons (π^0 s) to very high p_T . This thesis focuses on correlations between hadrons and direct photons, making use of the full range of detection capabilities of the central arms, with the exception of the ability to identify charged hadron species. Each of the relevant subsystems will be discussed in further detail in the sections that follow.

3.3 PHENIX Central Tracking

Charged particles produced at mid-rapidity when a collision occurs are tracked through the PHENIX detector by combining information from almost all of the detectors in the central arms. Looking at the beam view of the full PHENIX detector shown in Figure 3.2, as it moves away from the collision vertex, a charged particle will first pass through the central magnetic field, bending along the ϕ direction, then passing into the detector system, producing a series of interactions, or hits, in the Drift Chamber (DC) and inner Pad Chambers (PC1) [124]. These detectors provide information about the three dimensional position of charged particles as they pass through used to reconstruct their full trajectory. Electrons will then also produce Čerenkov light in the Ring Imaging Čerenkov Counter (RICH). Charged particles will also produce hits in the outer Pad Chambers (PC2 and PC3) and sometimes the Electromagnetic calorimeter (EMCal), which can provide further position information. The remaining detectors aid in the identification of particle type. Further details of how individual hits in these various detectors are combined to form the final tracks are discussed in Section 3.7.1.

In the central region of PHENIX, a uniform axial magnetic field is maintained, which causes charged particles to bend in the ϕ direction. An example of the type of field configuration used is shown in Figure 3.3. The dependence of the field strength on the radial distance from the beam pipe is shown on the right for three possible field configurations [125]. During the time the data used for this analysis was taken, the field was in the Outer+Inner configuration indicated by the squares.

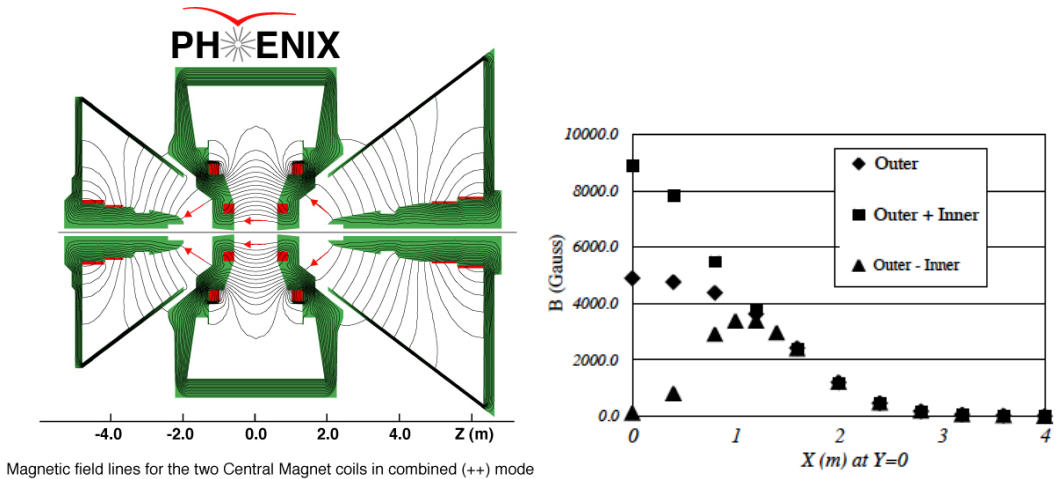


Figure 3.3: The PHENIX Magnetic Field. Side View (left). Total field strength $B_{Mod}(R)$ vs. R for the three field configurations available [125].

The tracking detectors sit just at the tail end of this field, so once the particle reaches the detectors it will again be moving in a relatively straight line. The amount a particle bends while passing through this magnetic field provides the information necessary for determining momentum during track reconstruction.

3.3.1 The Drift Chamber

The Drift Chamber (DC) sits at a radius of $2.0 - 2.4$ m from the beam pipe, and extends two meters along the beam direction. The DC detects a track through the ionization of gas held within the main volume of the detector. The electrons ionized by the charged particle are collected by anode wires that stretch across the chamber, with the drift time of the electrons providing information about the location of the track relative to the anode. Each arm is divided in half, with each half being made up of 20 sections, or “keystones”, one of which is shown in Figure 3.4 (left). From the

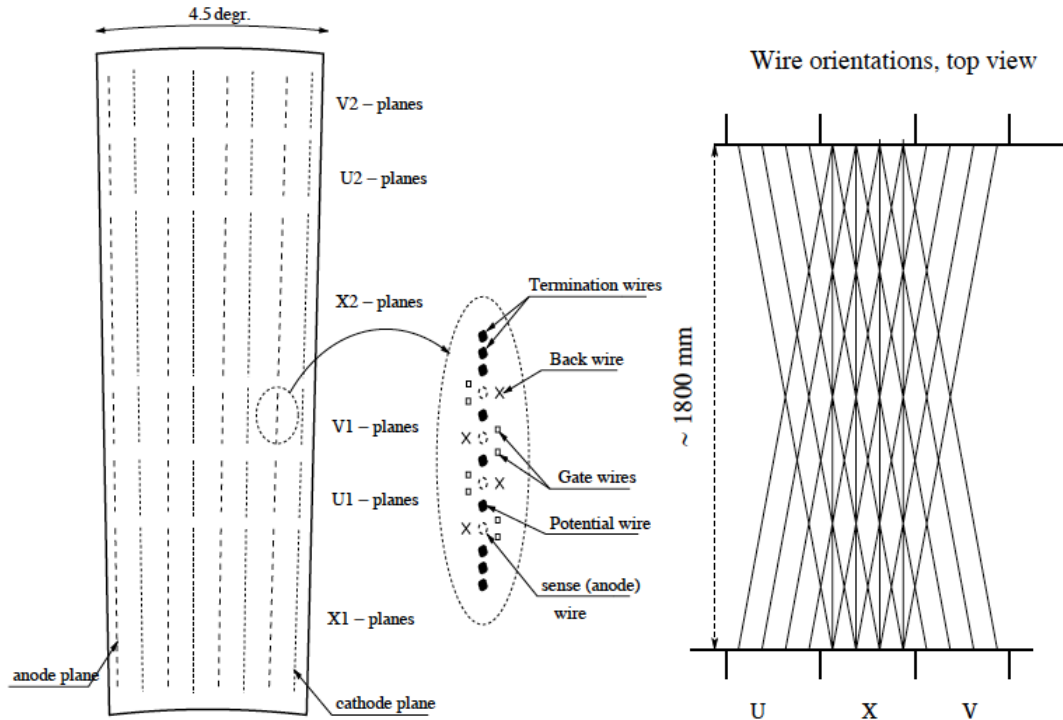


Figure 3.4: The Drift Chamber. Left: A side-view layout of the wire position in a sector of the drift chamber with a close-up of one group of wires. Right: A top-view diagram of the stereo wire orientation [124].

figure we see that each section is 4.5° in ϕ . Within each section there are six sets of wire configurations particles will pass through as they move outward radially: X1, U1, V1, and X2, U2, V2. These are called modules, and within each module there are four sets of anode/cathode planes that form cells spaced 2-2.5 cm apart in ϕ . The X wire cells, each containing 12 anode wires, run parallel to the beam, providing precise $r - \phi$ measurements. The U and V cells, each with 4 anode wires, act as stereo wires, with a 6° angle relative to the beam axis to provide the z position of the track, illustrated by the top view shown in Figure 3.4 (right). All together

each ϕ cell therefore contains 40 drift cells at different radii able to record position information for charged particles as they pass through the detector.

The drift chamber implements a controlled geometry design; in which wires placed around the anode hold voltages designed to improve the two-track resolution by lowering the track sampling length and to distinguish between tracks falling on the left or right of the anode plane. From the inset shown in Figure 3.4 we see that a set of two gate wires and a back wire surround each anode, on alternating sides of consecutive anodes. The voltage applied to the gate wires can then be used to adjust the boundary of the anode sensitivity to a track, while the back wires act as a shield, keeping the anode sensitive only to tracks passing on the other side. The potential wires then produce the electric field, which separates the individual anode wires. This design results in a final spatial track resolution of better than 2 mm.

3.3.2 The Pad Chambers

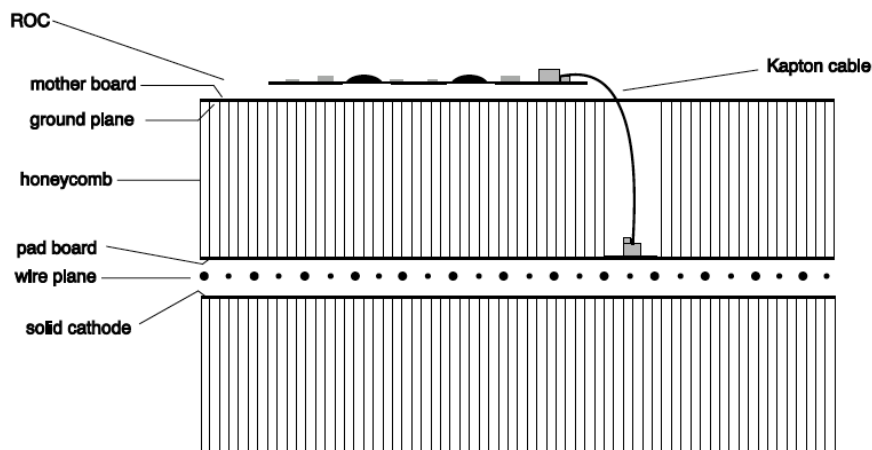


Figure 3.5: Diagram of a single pad chamber [124].

The other key players in tracking the path of charged particles through PHENIX are the three Pad Chamber (PC) layers. Each PC layer is a multi-wire proportional chamber composed of a single plane of anode wires bounded by cathode planes with one of the cathode planes divided into pixels to provide better resolution. Figure 3.5 shows a cross-sectional view of a single chamber. The innermost PC plane, PC1, which sits directly behind the drift chamber. In this position, PC1 provides high resolution 3D position measurements (1.7 mm in z), which primarily improve on the z information available from the DC alone. The second and third layers, PC2 and PC3, sit behind the RICH and in front of the EMCal and are used for rejecting secondary tracks produced through decays and conversions. Because PC2 is present only in the West arm, here only PC3 is used here for such rejection to maintain the full statistics available.

3.4 The Electromagnetic Calorimeter

Photons - the other particles of interest here - are measured using an electromagnetic calorimeter. The EMCal is positioned outside the tracking system (see Figure 3.2), making charged hadron and electron identification possible and thereby providing additional tracking information, as well as the ability to eliminate them as photon candidates. It was designed primarily for measuring the energies and positions of individual photons and electrons and is capable of reconstructing π^0 decays ($\pi \rightarrow \gamma\gamma$) up to 15 GeV/c [126]. This capacity also makes it well suited for identifying and rejecting photons from mesonic decays order to make direct photon mea-

surements. Two independent detector technologies are employed, lead scintillator sampling calorimeters (Pb-scintillator) and lead glass Čerenkov calorimeters (Pb-glass), each with very different characteristics, providing a valuable cross-check on photon measurements.

3.4.1 Electromagnetic showering

Particles that pass through the EMCal will deposit some or all of their energy through an interaction with the material of the detector. In the case of photons, this begins with an initial electron-positron pair production, resulting from the interaction of the photon with the nucleus of an atom in the detector material. Electrons, instead, will produce Bremsstrahlung radiation when accelerated, again as a result of the passing through atomic material. In both cases, the product of these initial interactions will be electrons and photons, which can then undergo a further interaction with the material, and so on. Each particle interaction doubles the total number of particles, resulting in a cascade of particles, or electromagnetic (EM) shower, with exponentially smaller fractions of the original particle energy. Figure 3.6 shows an example of this process where X_0 - the radiation length - is the distance the particle will travel through the detector material before interacting.

As pair production requires the photon to have a minimum energy of $2m_e$, the cascade will end when the generation of photons produced no longer has enough energy to produce an electron-positron pair. For electrons, the process ends when the electron energy drops to the critical energy, E_C , meaning it is equivalent to the ionization energy loss in one radiation length, at which point it will be absorbed by

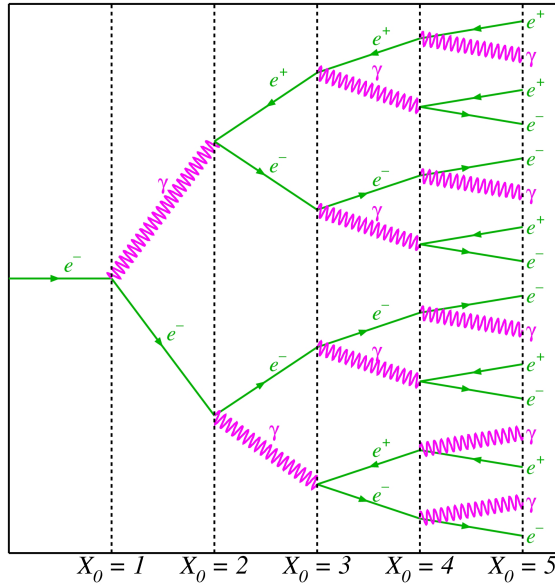


Figure 3.6: Illustration of an electromagnetic cascade. As indicated, the radiation length X_0 is the distance an electron or photon will travel in the material before interacting.

the material. This is clearly a property of the material, and has the general form,

$$E_C = \frac{610 \text{ MeV}}{Z + 1} . \quad (3.2)$$

The transverse size of the shower can then be parameterized by the Moliere radius R_m , a simple function of X_0 , containing approximately 90% of the EM shower energy. Along with the shower depth, this radius is only weakly dependent on the energy of the initial particle, and is empirically found to have the form:

$$R_M = 21 \text{ MeV} \frac{X_0}{E_C} . \quad (3.3)$$

As a result, showers produced by photons and electrons are easily identifiable, and the full energy of the incident particle can be contained within the calorimeter.

Some fraction of the time, hadrons may also interact with calorimeter material, colliding with a nucleus and producing hadronic fragments, resulting in a hadronic shower. The most common fragments in such showers are pions. In cases where the hadronic fragment is a neutral pion, this will then decay into two photons, producing an EM shower. In these cases the shower produced can be mistaken for a photon or electron. In such cases only a fraction of the hadronic process is detectable in this way, a fact that will aide greatly in distinguishing between different sources of showers.

3.4.2 Pb-scintillator vs. Pb-glass

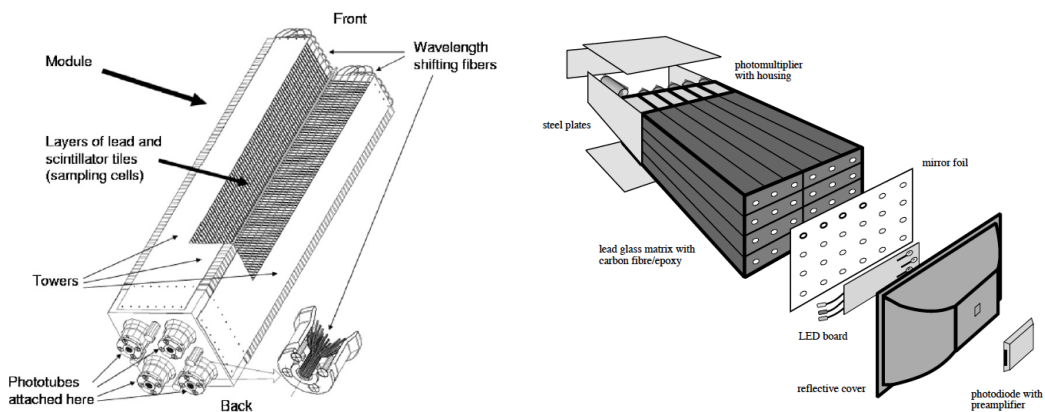


Figure 3.7: Diagrams of the electromagnetic calorimeters. Left: A module of Pb-scintillator towers. Right: A supermodule of Pb-glass towers [126].

Practically speaking, the challenge is now to measure the energy produced in the EM shower. The first method used in PHENIX is the Pb-scintillator, made of

alternating layers of Pb absorber and scintillating plastic. In this case, when charged particles pass through a scintillation layer, they will excite molecules in the material, which then release some of that energy as light. The light produced can then be read out of via wavelength shifting fibers into phototubes. In this way, each layer is collecting a fraction, or sample, of the total shower energy. It is important to note that while charged hadrons will not produce an EM shower, they can still produce light in the scintillator through ionization which can be mistaken for a low energy photon or electron. Structurally, the calorimeter is constructed of individual cells called towers, each with a $5.5 \times 5.5 \text{ cm}^2$ face, which are optically isolated and collected into groups of four called modules, shown in Figure 3.7 (left). Modules are then held together in larger groups of 36 called supermodules (SM). Eighteen SMs make up a sector, and there are six sectors in all. These groupings are important beyond the simple structural design of the detector, featuring prominently in the details of most photon analyses.

The Pb-glass, by contrast, is a homogenous calorimeter; a mixture of Pb, glass, and Pb Oxide. In this case, the energy absorption and signal generation take place in the same material, where the light output is read out by phototubes. However, instead of scintillation, the source of light is now Čerenkov radiation, produced as a result of charged particles traveling faster than the speed of light in the material. Typically only electrons will produce this Čerenkov light, making this detector much less sensitive to hadrons. Structurally this is similar to the Pb-scintillator, segmented into towers with $4 \times 4 \text{ cm}^2$ faces, which are grouped directly into SMs of 24 towers. There are a total of two Pb-glass sectors, each with 196 SMs. The struc-

tural segmentation currently differs some from the groupings used at the analysis stage; SMs are then combined further into groups of six with these larger groupings referred to as super modules as well.

In both detector types, individual towers are optically isolated from each other, meaning the measured light is a result of the energy deposited in that tower alone. However, the EM shower produced by the incident particle will cross multiple towers. This is clear once we revisit Equations (3.2) and (3.3), noting that an X_0 of 2 cm for the Pb-scintillator and 2.8 cm for the Pb-glass leads to an R_M of 3-4 cm. Fully reconstructing the original particle energy, then, requires an algorithm for clustering together towers likely to have come from the same shower. Details of the clustering, as well the calibration of the detector, are discussed in Section 3.7.2.

3.5 Electron identification

While the focus of the work discussed here is on measurements involving charged hadrons and photons, so an important detail in that process is correctly identifying those types of particles. As the previous sections describing the detection of charge hadron tracks and EM showers produced by photons suggest, electrons will mimic the behavior of both charged hadrons passing through the central tracking detectors and photons depositing energy in the calorimeter. This means both the momentum and energy of electrons is measurable, providing a well defined E/p , which should be approximately one and making them useful for calibrating the EMCAL. To correctly identify these electrons, an independent detector designed specifically

for electron detection is necessary. In PHENIX the RICH serves that purpose.

The RICH sits just behind PC1 (see Fig. 3.2) and covers a volume of 40 m^3 . It is filled with Ethane gas, chosen both because it has a high photon yield for electrons passing through and because it is thin, minimizing photon conversions within the detector. This gas acts as a Čerenkov radiator, with segmented intersecting spherical mirror panels focusing this light into arrays of photomultiplier tubes on either end of the detector. Below the pion Čerenkov threshold of just under $4 \text{ GeV}/c$, only electrons will produce radiation - in the form of a light ring with a radius of 7 cm. Above the pion threshold, distinguishing between hadrons and electrons becomes more challenging but can be done using more sophisticated analysis cuts.

3.6 Event and Vertex detectors

Before the measurement of hadrons and photons produced in a collision can begin, it is necessary to develop a system for determining when such events occur. A precise determination of where the collision occurred, defining the event vertex, is also crucial. Naïvely it might seem that an event could simply be defined as occurring each time bunches cross in the interaction region; however, there is not actually the case that there is a collision with each crossing. Therefore, attempting to read out all the information stored in the full PHENIX detector each time the beams cross could result in leaving the detector busy reading out an empty event when a collision does occur. The obvious disadvantage is the loss of real physics, but perhaps just as problematic is the poorly defined efficiency with which true

events are measured as a result. It is therefore necessary to have a well defined way of determining when an event occurs, ideally with an equally well defined efficiency for identifying events.

There are two detectors in PHENIX with the primary purpose of event determination, as well as measurement of the vertex of such events: the Beam-Beam Counters (BBC) [127] and the Zero Degree Calorimeters (ZDC) [128]. They are shown in Figure 3.2. Both have a north and south portion, acting as multiplicity detectors, with high precision timing capabilities (100 ps for the ZDC, and 50 ps for the BBCs). In either case, an event is defined as the occurrence - during a bunch crossing - of simultaneous signals in the North and South portions of the detector. The timing difference between the two signals can then be used to determine the vertex location along the beam axis. The BBC and ZDC therefore provide independent event determinations and event vertex measurements. However, the higher timing resolution of the BBC makes it the primary detector for both. Additionally, in $p + p$ the ZDC sees only a small fraction of interactions, so is not practical for determining when a collision occurs.

Each portion of the BBC is an array of quartz Čerenkov counters surrounding the beam pipe, and attached to photomultiplier tubes (PMT) for readout. The counters cover a pseudorapidity range from $3.0 < |\eta| < 3.9$, putting them in place to detect charged particles produced in the collision with a large deflection from the vertex. In the heavy-ion environment this is ideal for measuring the full range of centralities while keeping possible correlations with the central arm detectors to a minimum, an important feature when determining bulk properties of the collision.

Their primary role, however, applies in both $p + p$ and $A + A$ and is to provide high precision timing; for both synchronizing the rest of the detector to signal the PHENIX triggering system and more importantly for time-of-flight measurements. For triggering, the precise definition of an event is the requirement that a minimum of one PMT in each of the BBCs fires with the collision vertex falling within the PHENIX central arm acceptance - more specifically, that $|z_{vertex}| < 30$ cm, where z runs along the beam axis. This requirement will exclude some classes of events, so is not a zero bias selection criterion and is instead referred to as a minimum-bias (MB) trigger. In $p + p$, this results in approximately 50% of the total inelastic cross-section being measured, while in $Au + Au$ - where the multiplicity is much higher - this goes up to 92%.

3.6.1 Triggering on rare physics

As mentioned previously, the primary focus of PHENIX is on rare processes and high- p_T probes. Even with the remarkable readout rate achievable with the PHENIX data acquisition system, the luminosities achievable at RHIC make reading out every event impractical, if not impossible. In the case of $p + p$, the raw event rate is on the order of 10MHz, while the data acquisition capabilities of PHENIX are typically 6-7 kHz. Thus, rejection rates of as high as 50,000 are necessary to record large numbers of events containing a hard scattering, which are rare. To achieve these rates of rejection, a sophisticated triggering system is implemented. At the hardware level this is done with a Level-1 trigger (LVL1) able to communicate directly with the detectors used in triggering, as well as combine data from several

detectors to make more selective trigger decisions. Higher level triggering, implementing algorithms to calculate more advanced selection criteria (LVL2), has also been developed, but so far has not been needed beyond filtering for more efficient analysis of the data.

Section 3.6 describes the first step in the triggering process, the definition of the MB trigger and signaling of the LVL1 system by the BBC. The more selective triggering implemented includes trigger applied as a high- p_T photon trigger, or as an electron trigger when both the EMCal and RICH are used - the EMCal-RICH trigger (ERT). The logic of the trigger takes groups of EMCal towers, called tiles, and performs a sum on the energy deposited on each tile. An energy threshold is set to determine whether the event should be recorded based on that sum. There are two tile configurations used: non-overlapping 2x2 sets of towers, used for the electron trigger; and overlapping 4x4 sets of towers used for high- p_T photon triggering. For the purposes of analysis, events that fire these triggers are only recorded if the MB trigger condition has also been satisfied, to ensure that it was not simply noise in the detector causing the trigger to fire.

There are several other selective triggers available with PHENIX, but the ERT 4x4 tile triggers are ideally suited for the work discussed here. The trigger condition for the 4x4 tiles compares the tower sum with three separate energy thresholds of successively higher values, ~ 1.4 GeV (4x4c), ~ 2.1 GeV (4x4a), and ~ 2.8 GeV (4x4b). The higher energy thresholds allow for further optimization of data recording and analysis, and potentially enhance the statistics for the highest p_T physics. Obviously, any event that fires the 4x4a or 4x4b triggers, will also fire the 4x4c.

However, at the highest luminosities available at RHIC, during p + p running, it is necessary to record only a subset of events that fire the 4x4c. This practice, called scaling down the trigger, is also used for recording only a small fraction of the full MB trigger sample and means that for a scale down of n , only every $(n + 1)^{th}$ event firing the trigger will be recorded. For the ERT 4x4c trigger, this scale-down is never more than 2, meaning at least every 3rd event firing the trigger will be recorded.

3.7 Data acquisition and event reconstruction

Once it has been established that an event has occurred, the next task is reading out the data generated in the full range of detector subsystems and reconstructing this raw data into the individual particles produced in the collision. The level 1 triggering already described is just one part of the full system of data acquisition (DAQ), shown in Figure 3.8, which itself relies on some subset of the full event information being assimilated in raw form.

This process begins with the Granule Timing Modules (GTMs), which provide the clock signal which then triggers the Front-End Modules (FEMs). The FEMs are the collection of Front-End Electronics (FEE), which collect from all the detectors, sampling from the detectors each time the GTMs send a signal - and store the data in memory cells called AMUs. The various LVL1 triggers then rely on fast calculations done locally (LL1) on single FEMS using this raw data to determine if the relevant trigger condition is met. A single board, the global level 1 board (GL1), collects this information, determines if the event should be recorded, and sends a

signal back through the GTMs to the FEMs, initiating a readout of the full event. The next step is to assimilate all the information being sent by the FEMs. The first step in that process is to format the digitized FEM data into compressed packets, including suppressing data from empty detector channels (zero suppression), a job done for groups of FEMs by Data Collection Modules (DCMs).

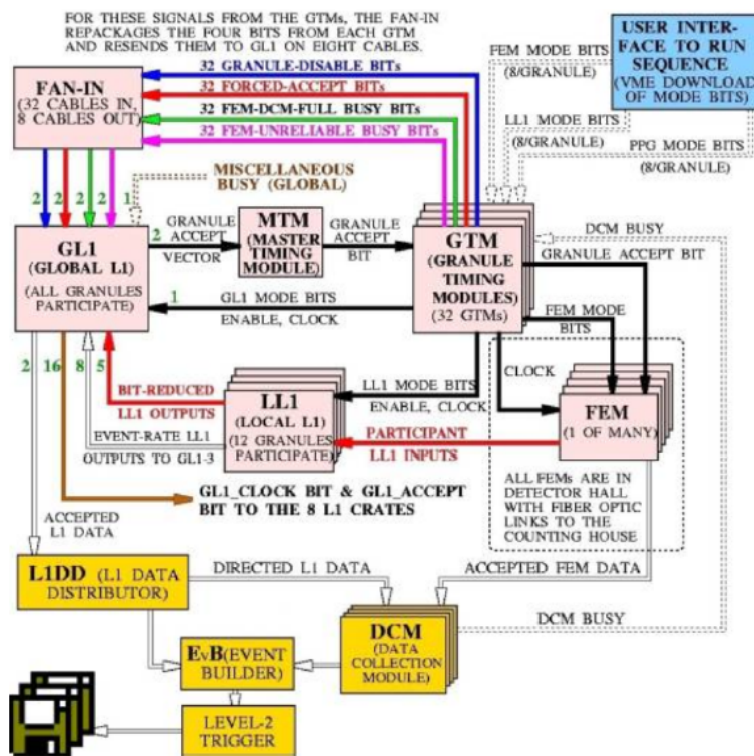


Figure 3.8: Schematic of the full PHENIX DAQ and triggering system.

The repacking - and later combining - of data from all the detector subsystems takes time, while new events are constantly ready to be read out. It is therefore necessary to provide some buffering and a sophisticated way of keeping track of how the buffered data should subsequently be combined. This combining process is

performed by a large computer cluster, the Event Builder (EvB), starting with a set of computers called Sub Event Buffers (SEBs) which store the output from a given DCM group. The job of combining packets from all the different SEBs is done with another set of computers called Assembly Trigger Processors (ATPs). Once events are assembled, they are temporarily stored on a small array of machines (buffer boxes) with very fast hard drives capable of buffering many millions of events - so as to keep up with the event rate - prior to transfer to a more permanent storage facility. Although this has not occurred in PHENIX yet, this final data storage step could create a bottle neck as well, in which case the more advanced LVL2 triggering would be necessary. LVL2 algorithms would operate on the assembled events in the ATPs to provide further rejection prior to the buffering and storage of full events.

The data stored in the final assembled events is still in a raw form, not yet ready for final analysis. Reconstruction of the raw data then involves decompressing the data read-out from the detectors to extract information, such as position of the hit within the detector, as well as the energy recorded in the case of the EMCal. Once the full set of hits within each detector is available, the process of combining those likely to have come from the same particle begins.

3.7.1 Track reconstruction

The process of tracking an individual charged particle through the central arms relies on first being able to determine which hits in the tracking detectors were produced by that particle. Figure 3.9 illustrates the hits typically used for track reconstruction. Hits in the DC (shown as white stars) are formed into track candidates

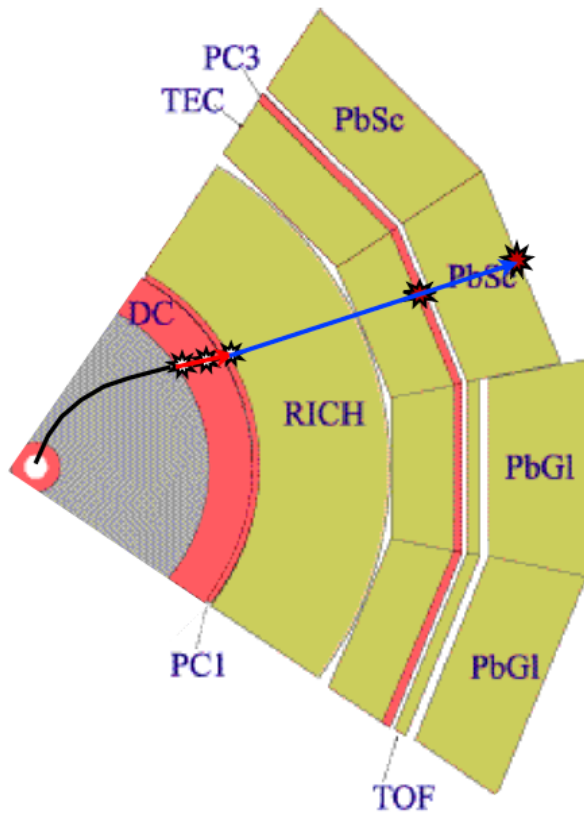


Figure 3.9: The path a track takes through the PHENIX central arm. Hits used for reconstruction are indicated by white stars. Hits matched with track projection (blue arrow) are indicated by red stars.

using Hough transform pattern recognition procedure, which determines the most likely set of r - ϕ hit positions from a single particle. Although there is some z information available from the DC, in practice the charged particle trajectory through the DC is measured in the $r - \phi$ direction. Pointing the track back to the vertex then provides a measure of its curvature, and corresponding p_T . However, determination of the full momentum vector requires more information on the longitudinal direction of the track than the DC alone can provide.

These track candidates can then be projected into other central arm detectors and matched with hits in those systems. In the figure, this is indicated by the blue arrow showing the projection of the DC track into the outer detectors. This additional information mainly helps to reduce the rate of fake tracks; however, in the case of PC1 - best because it sits just behind the DC, the high-resolution z information can be used to get the full track momentum. The resulting momentum resolution is $\delta p/p \simeq 0.7\% \oplus 1.0\%p$ (GeV). The first term is due to multiple scattering prior to the track reaching the drift chamber, and the second results from the intrinsic angular resolution of the detectors. Tracks reconstructed using the DC and PC1 information alone then form the set of track candidates used for analysis, with projection into the PC3 and EMCal aiding in further rejection of fake tracks.

In an ideal environment, one would be able to determine that a track candidate correctly reflects the path of a charged particle through the detector by requiring that it have hits in each layer of the DC and a matching hit in the PC1, as well as that those hits are unique to that track. In other words, none of the hits are shared with another track candidate. In practice, however, there will be instances where two particles are close enough to have overlapping hits or where one DC layer did not correctly record a hit when a charged particle passed through. For this reason, a parameter called the track quality is defined. This parameter includes information about which DC layers the track has hits in, whether they are unique, and whether there is a matching PC1 hit. Then it is left to individual analyst to determine how selective their analysis should be.

3.7.2 Cluster reconstruction and calibration

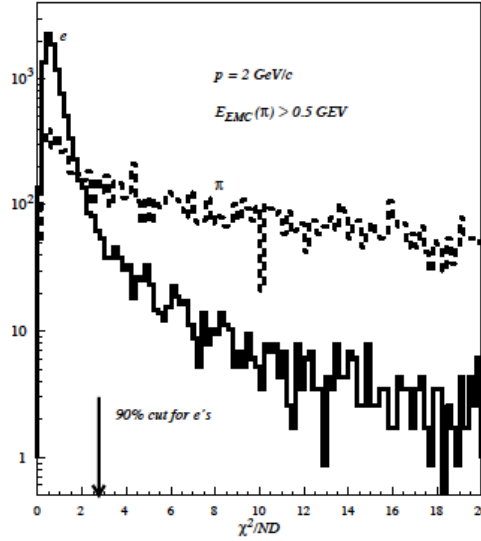


Figure 3.10: χ^2 distributions for showers produced by 2 GeV/c electrons (solid line) and pions (dashed line) in the Pb-scintillator.

As mentioned in Section 3.4.1, the EM showers produced by photons and electrons will generally span multiple towers, making it necessary to group towers into clusters for identifying particles. The obvious first step is to simply group together contiguous towers; however, there is the possibility of multiple particles producing overlapping clusters, as with high $p_T \pi^0$ photon pairs. Thus, it is necessary to look more closely at the energy distribution within the cluster. Local energy maxima within grouped towers are found and fit with a function parameterizing the EM shape, which is basically an exponential in tower distance from the central maximum tower.

This fit also produces a χ^2 used to determine how likely the cluster is to have

come from an EM source - an electron or photon - or a hadronic source, such as a pion. An example of what the χ^2 distribution looks like for different particles is shown in Fig. 3.10, which compares the fit of the χ^2 distribution for electron showers versus pion showers. As one can see from the figure, not all hadrons will be rejected with a shower shape cut of this type. Similarly, electron showers are indistinguishable from photon showers. In both cases, matching cuts can be used to further distinguish between photonic clusters and those produced by charged particles (see Section 4.1.3.1).

3.7.2.1 Calibration

As described in Section 3.4.1, the energy deposited in the EMCal is determined using PMTs to measure the light produced - either through scintillation or Čerenkov radiation - in the detector. The PMTs produce an analog voltage signal which then gets converted to a digitized signal - a discretized number of counts - by an Analog to Digital Converter (ADC). Getting from these discrete counts to a corresponding energy requires calibrating the detector so the correct conversion factor, or gain factor, is known. This can be done, even in testing situations, by exposing the detector to single particles - typically electrons - of a known energy and measuring the shower response. However, during regular data taking, the response of the detector will fluctuate, so a more accurate approach is to collect a statistical sampling of calibration measurements over time, as the detector is running. This is done in PHENIX by firing a laser of known intensity at the PMTs frequently during running - but not during bunch crossings, to monitor fluctuations in the gain.

Additional calibrations, or re-calibrations, can be done during the analysis stage using recorded data. There are three methods that have been used in PHENIX: π^0 reconstruction, electron E/p , and the slope method - that is, the assumption of a uniform slope to the energy spectrum for photons at low p_T . This last method has been used in the past at PHENIX, but was not used for the data discussed in this thesis.

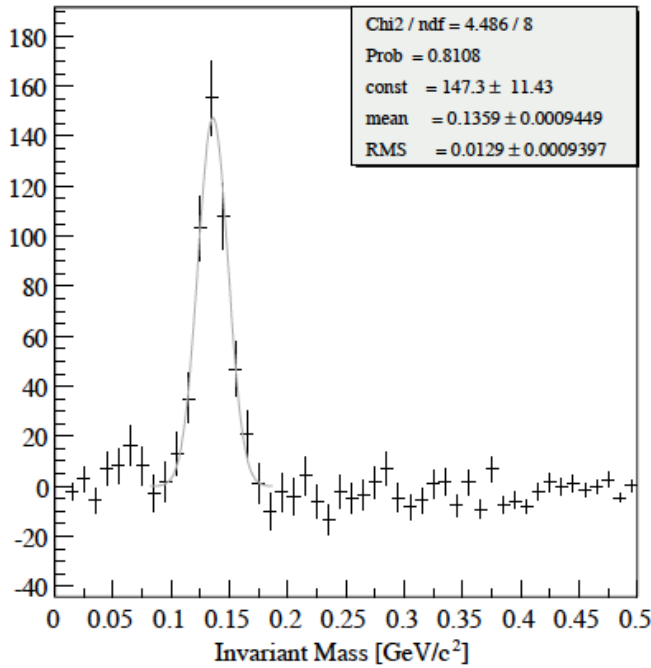


Figure 3.11: Example of the invariant mass distribution for photon pairs showing the clear peak at an invariant mass equal to the mass of a π^0 .[\[126\]](#)

The first method uses reconstructed π^0 decays. The invariant mass distribution for photon pairs, shown in Fig. 3.11, shows a clear peak at the mass of the π^0 , as indicated by the mean value for the fit parameters. The invariant mass is proportional to the product of the photon energies. Therefore, for symmetric pairs, the

correction to the photon energy can be directly determined by the ratio of the true π^0 mass to the invariant mass of the measured pairs. This correction can be applied to the central tower of each photon cluster or as a more global energy scale correction to entire sectors. This type of re-calibration is used for most EMCAL-centered analyses in PHENIX. During the reconstruction of raw data an iterative procedure is applied in which individual towers are re-calibrated. Then, the cluster energy is recalculated with the new tower energies and used again to construct π^0 peaks tower-by-tower, and so on. Typically, four iterations are used.

The second method for correcting calibrations makes use of fully reconstructed electrons. In this case, the E/p distribution for electron clusters can be generated, again either tower-by-tower or, on a larger scale, for each sector. The E/p distribution for electrons should be centered around one, so the shift from one provides the correction to the cluster energy. The advantage of this method is that it does not require input from multiple clusters; however, adjacent towers will contributing to the electron energy. An additional complication is that in reality the average E/p will not be exactly one, as many electrons will come from conversions in the beam pipe. Their reconstructed momentum assumes they were produced by the primary collision, reducing the measured E/p . Careful studies using simulations of these conversion electrons can be used to understand how much the E/p mean will shift. Again, to apply such a recalibration correctly, the optimal method is an iterative procedure involving recalculation of cluster energies after towers are rescaled. However, the single-cluster nature of this method makes it a good candidate for any analysis level recalibrations [129].

Chapter 4

Hadron-Photon correlations and jets

As discussed in Section 2.5.2.1, two-particle correlations can be used to directly measure the properties of fragmentation photons. The first step is to construct the pair distributions for hadrons and inclusive photons, where we consider the hadron as the “trigger” particle and the photon as the “associated” particle. The total pair yield is related to the pair cross-section:

$$\frac{d^2N^{h-\gamma}}{d\Delta\phi d\Delta\eta} \propto \frac{d\sigma_{pp}^{h\gamma}}{d^3p_{trig} d^3p_{assoc}}. \quad (4.1)$$

When considering the yield of fragmentation photons, it is also useful to measure the conditional yield,

$$\frac{1}{N_{trig}} \frac{d^2N^{h-\gamma}}{d\Delta\phi d\Delta\eta}, \quad (4.2)$$

also referred to as the per trigger yield. In PHENIX, where the η acceptance is small, this is further simplified by integrating over the $\Delta\eta$ dependence and considering the one-dimensional $\Delta\phi$ distributions. Discussion of how the decay photon background is removed to go from these inclusive photon distributions to those for

fragmentation photons will take place in Chapter 5. Even before correlation measurements can be made, it is necessary to verify the quality of the data, both globally - by ensuring that detector as a whole was in a good state while events were being recorded - and on an individual track and cluster level.

4.1 Data and event selection

Data from two years of RHIC operations producing $p + p$ collisions at $\sqrt{s} = 200$ GeV, during 2005 (Run 5) and 2006 (Run 6), was used for the analysis presented here. The data was analyzed separately and combined after all efficiency corrections were applied, with similar procedures for selecting good events and evaluating efficiencies used for both data sets. As discussed in Section 3.6.1, when analyses are focused on events where a high p_T process has occurred, it is necessary to employ a more selective trigger than the MB trigger to define an event. In this analysis we require the event to have fired the ERT4x4c trigger in combination with the MB trigger as a way of selecting events that involved a hard scattering. The MB trigger is included to eliminate background from random high energy particles such as cosmic rays. In addition to the trigger requirement, only events with a BBC vertex between ± 30 cm along the beam axis are used. Figure 4.1 shows the vertex distribution measured by the BBC, where we see that outside ± 30 cm the distribution drops off rapidly. Therefore, this range is chosen to ensure that the central arm acceptance is relatively flat. A slowly varying acceptance is especially important when doing correlations, which will depend intrinsically on the acceptance of the detector (see Section 4.2).

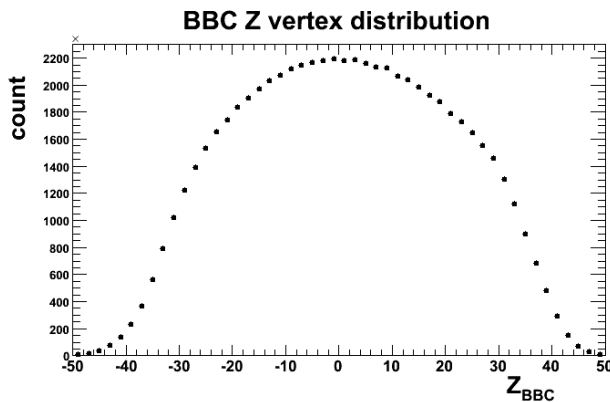


Figure 4.1: BBC z vertex distribution (cm). Events analyzed are required to have $|z| < 30$ cm.

4.1.1 Run quality

While RHIC is operating and collisions are being produced, events are recorded continuously for periods of up to an hour. Each set of data taken is labeled as a separate "run", and these groupings are used for evaluating the time dependence of the data quality. There are then hundreds of such short runs recorded throughout the year. The state of the detector, such as dead or noisy regions in various subsystems, does change over the course of data taking; however, this is generally a slow process, leading to variation in detector response on the scale of many hours. Segmenting the data recorded into runs no longer than an hour, along with regular daily calibrations, helps to maintain consistency in the data and monitor fluctuations resulting from transient problems in the detector. The first step in any analysis is therefore to check the quality of all runs and reject those that appear anomalous.

Most problematic (bad) runs are identified as such during data taking or during

the initial calibration process. Bad runs are removed during Production - the process described in Section 3.7 of reconstructing the raw data into analyzable information about full tracks and clusters. To further identify bad runs, for the purposes of measuring hadrons and photons produced in the central arm region, the mean multiplicity and mean p_T of good tracks and clusters for each run, defined as those that passed the cuts described in 4.1.2 and 4.1.3 respectively, was compared across runs. Figure 4.2 shows the per event mean p_T , and Figure 4.3 shows mean multiplicity, as a function of run number, for both hadrons and photons. The figures show both the Run 5 and Run 6 distributions, with red bands indicating the upper and lower bounds used for rejected runs. The bounds were chosen simply to reject any runs that fell well outside the variation seen across the full data set.

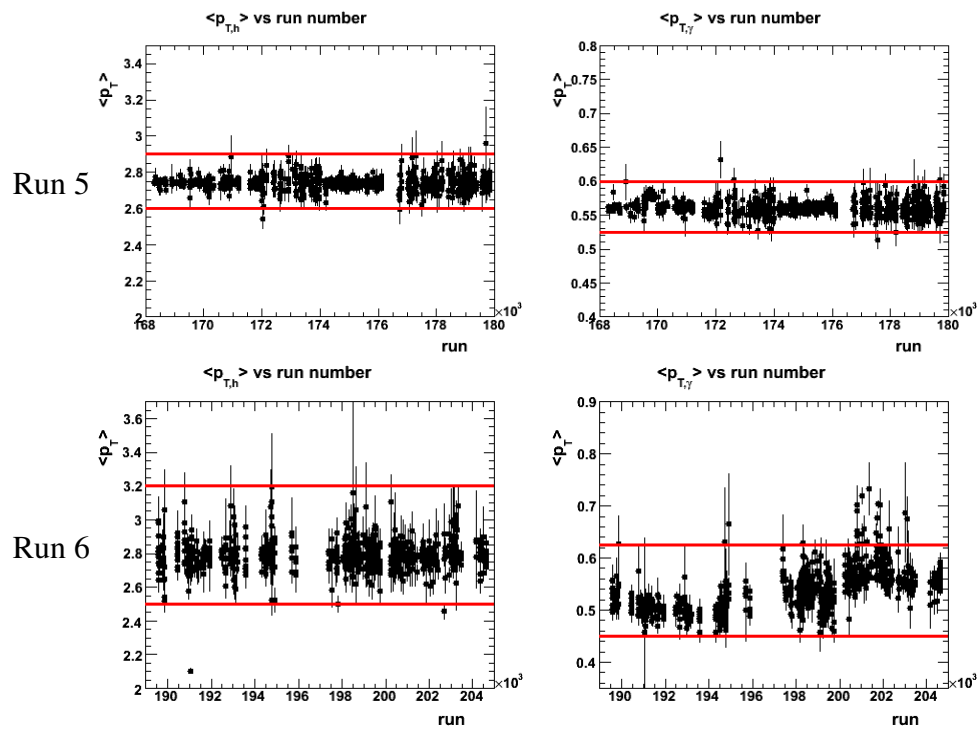


Figure 4.2: Average track p_T vs. run number (left). Average cluster p_T vs. run number (right).

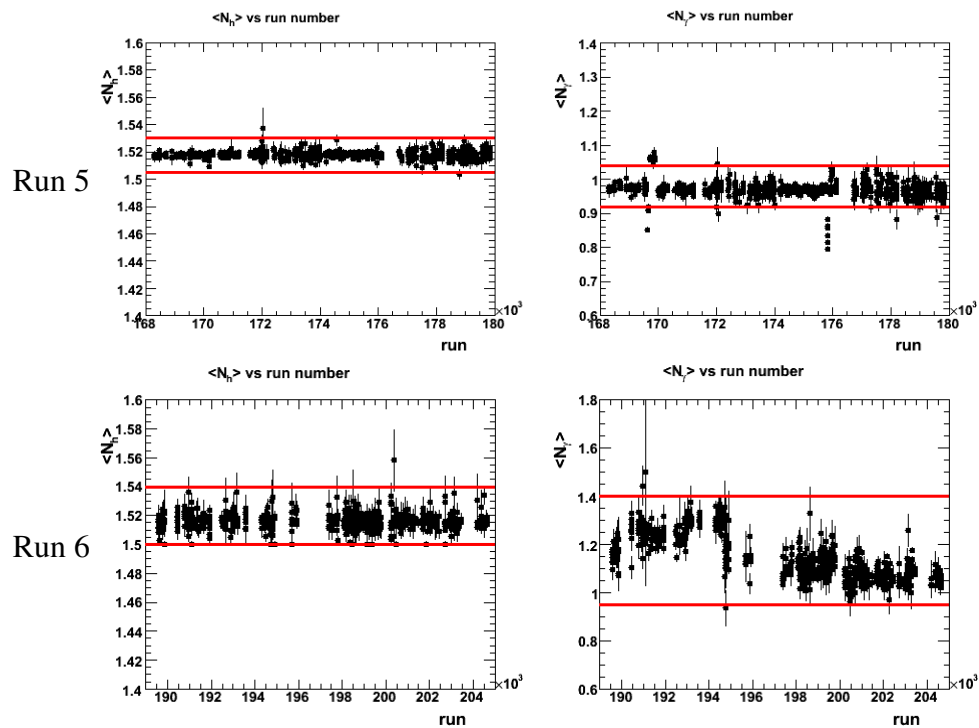


Figure 4.3: Average track multiplicity vs. run number (left). Average photon multiplicity vs. run number (right).

4.1.1.1 Run dependent calibrations

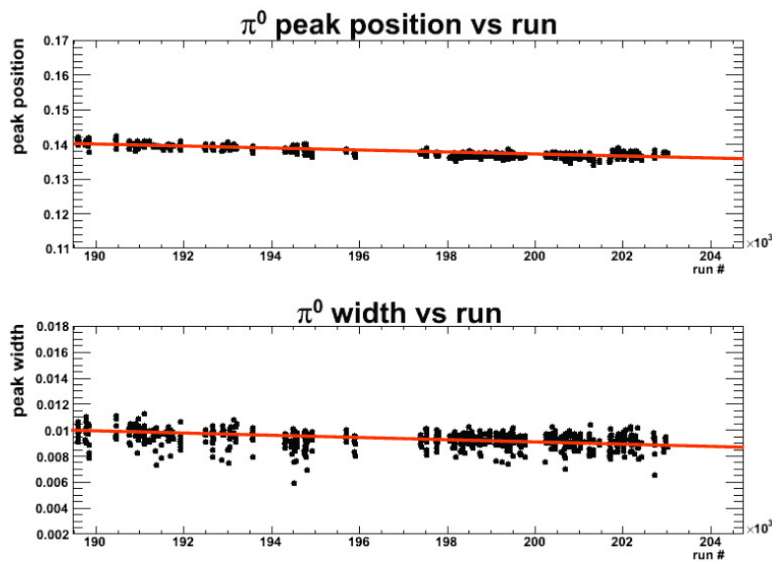


Figure 4.4: π^0 mass peak position (top) and width (bottom) vs. run number for Run 6 prior to run-dependent recalibrations. The red line demonstrates the non-zero slope of the data for both the peak position and width.

An additional check of the run dependence of the EMCAL calibrations was performed by comparing the reconstructed π^0 mass peak positions and widths as a function of the run number. This comparison was done as a way of checking for badly calibrated or problematic runs, and also to check the consistency of the calibrations across the whole data-set. For the Run 6 data especially, this revealed a large run-dependent variation in the π^0 peak position, as shown in Figure 4.4. This is indicative of energy scale variations as the run progressed, which can lead to systematic effects in cross-section measurements, although typically quite small. The more important issue is the effect such variations may have on the ability to correctly estimate the efficiency with which π^0 s can be reconstructed, which will be

come important in the next chapter. Tower-by-tower re-calibrations, using electron E/p , would be the ideal method for resolving this variation. However, the statistics needed to apply single tower calibrations require large sets of runs, making careful run-dependent calibrations difficult. Given that single tower calibrations are already done during event reconstruction, for resolving the run dependence it should be sufficient to apply an additional energy scale correction (see Section 3.7.2.1).

Recalibration based on the E/p distribution for electrons was used to correct for the run dependence. For each run¹ and within each sector, cluster energies are rescaled based on a fit to the measured E/p peak position for tracks that point to the clusters and are identified as electrons with $1.0 < p_T < 1.5$ GeV/c. The cuts used to identify electron tracks will be described in Section 4.1.2.2.

A significant fraction of electrons detected come from conversions in the beam pipe, which leads to a slightly mis-reconstructed p_T for the electron, as the p_T is determined assuming the track came from the collision vertex. A simulation in which the beam pipe conversions were enhanced was done to determine the effect this has on the mean electron p_T as a function of p_T and based on the electron ID cuts used. The peak position also depends on the sector, as each has a slightly different response. For electrons with $1.0 < p_T < 1.5$ GeV/c, it was found that the E/p distribution should peak at 0.957 in the West arm, 0.965 in the East Pb-scintillator, and 0.905 in the Pb-glass [130].

The final run dependence of the mass peak position and width for both Run 5 and Run 6 is shown in Figure 4.5, with further rejection of bad runs indicated by

¹Often small groups of adjacent runs were used rather than individual runs, due to low statistics.

the red bands.

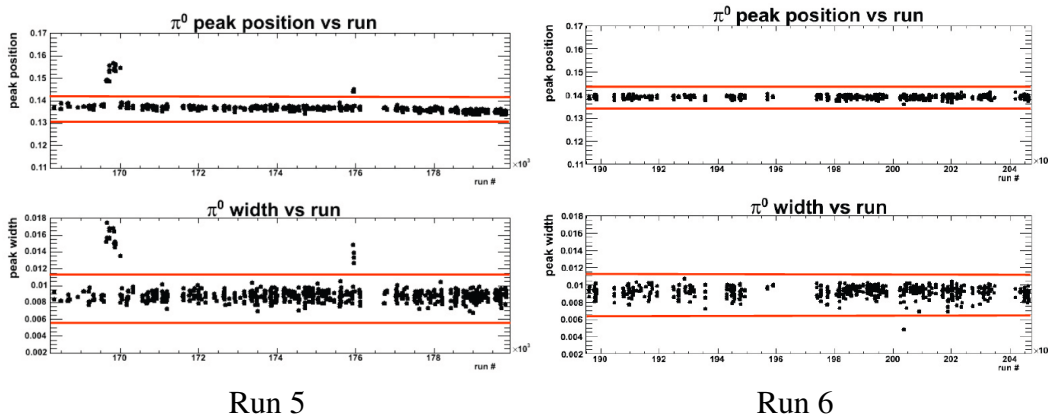


Figure 4.5: π^0 mass peak positions (top) and widths (bottom) vs. run number for Runs 5 and 6.

4.1.2 Hadron cuts

To minimize contamination from reconstructed tracks not coming from charged hadrons produced during the collision, such as conversions in the detector or miss-reconstructed tracks, cuts are applied based on the DC and PC information. For the momentum range used in this analysis, the rejection of electrons using the RICH also helps to reduce the background. Additional fiducial cuts, determined based on the acceptance in the DC and PC3, are applied to reduce fluctuations in the acceptance and improve agreement between data and simulation when determining hadron efficiencies.

4.1.2.1 Track quality and matching

The first step in identifying tracks coming from hadrons is to minimize contamination from mis-reconstructed tracks. The likelihood that a track came from a charged particle produced at the primary vertex is determined by the quality of the track. As discussed in Section 3.3, track quality is defined based on hits in the various layers of the drift chamber - and their uniqueness, as well as matching hits in PC1 and PC3. More specifically, the quality is based on the presence of a hit in the X1 and X2 layers, the uniqueness of hits in the UV layers, and the presence and uniqueness of a matching hit in the PC1. Typically in the most restrictive analyses, only tracks with hits in all DC layers and the PC1 - where the PC1 hit was not required to be unique - are considered good quality. However, to reduce holes in the drift chamber acceptance due to dead wires in the X1 and X2 layers, this requirement was relaxed for the results shown here, allowing for a missing hit in X1 or X2. Although this can increase the rate of background from conversions inside the drift chamber, the RICH sits behind the DC and should be able to aid in minimizing the effect. To further reduce background contamination, tracks are projected into the PC3 and matched with a hit. By plotting the Δz (beam axis) and $\Delta\phi$ between tracks and PC3 hits, one can construct an approximately Gaussian distribution which is calibrated to be centered around zero. Generally tracks are then required to be within 3σ of a PC3 hit. At higher momentum, where background from conversions and other random sources begins to dominate, this cut is often tightened to 2σ . However, these backgrounds are typically less correlated with other particles in the event. Therefore, for correlation analysis this is not a major source of signal contamination. Also, for this

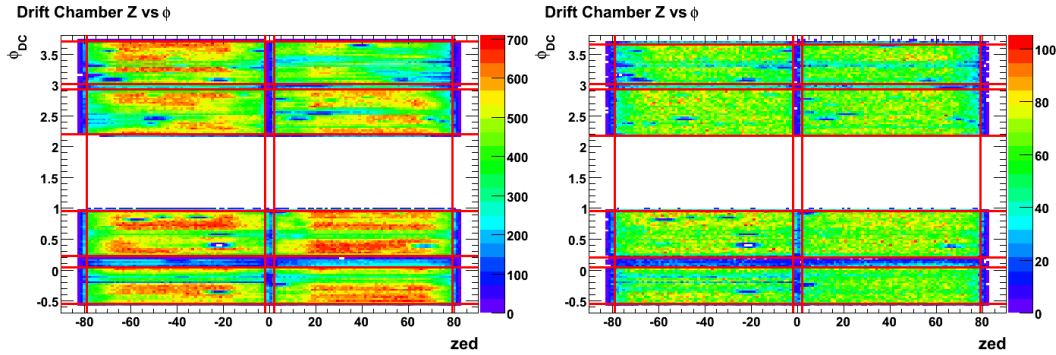
analysis hadrons above 5 GeV are not included, meaning background contamination is already minimal. Nonetheless, the dependence of the correlation results on this cut can be used to estimate the sensitivity to background contamination [131].

4.1.2.2 Electron identification and rejection

In addition to charged hadrons, electrons will produce good quality tracks through the drift chamber. Though most of these tracks will be due to electrons produced by the primary collision, there will also be background electrons produced through conversions in the beam pipe and inner detectors. Electrons traveling through the Central Arms will produce Čerenkov light in the RICH, and they can be identified and rejected. The parameter $n0$ gives the number of phototubes that fired in the RICH within the expected ring area for an electron. Using this parameter, requiring that there be no light in the RICH that matches to a track is done by applying an $n0 < 0$ cut. Similarly, for $p + p$ analyses good electrons are generally defined as those with $n0 > 2$. Above p_T of about 4.5 GeV/c charged pions will begin to produce Čerenkov light as well, making electron rejection cuts too restrictive. Therefore, these cuts are only applied to tracks with $p_T < 4.5$ GeV/c to keep the reconstruction efficiency constant. For this reason, the RICH is not effective as a means for rejecting background to hadronic cross-sections above 5 GeV/c, a major reason for tighter PC3 matching requirements at high p_T .

Table 4.1: ϕ_{DC} acceptance for Runs 5 and 6

Run	ϕ_{DC} acceptance			
	5	$-0.55 - 0.05$	$0.23 - 0.95$	$2.2 - 2.93$
6	$-0.55 - 0.04$	$0.2 - 0.95$	$2.18 - 2.93$	$3.02 - 3.65$

**Figure 4.6:** ϕ vs. z distribution of tracks in the drift chamber, with fiducial cuts marked by the red lines, for Run 5 (left) and Run 6 (right)

4.1.2.3 Fiducial cuts

Finally, there are regions within the DC where the track reconstruction efficiency is very low or even zero. In these regions as well as near the edge of the detector, the rapidly changing efficiency can lead to discrepancies both when using simulations to estimate the efficiency and when correcting for the track acceptance in two-particle correlation. Fiducial cuts around the worst of these regions are applied to minimize this effect. Figure 4.6 shows the cuts applied in both ϕ and z used for Run 5 and Run 6. In the figure the two-dimensional ϕ_{DC} vs. z_{DC} (zed) hit distributions within the DC are plotted for each Run, with the color grade indicating the hit rate. In both cases tracks are required to have $|z_{DC}| > 2$ cm and $|z_{DC}| < 79$ cm. The cuts on ϕ_{DC} are listed in Table 4.1.

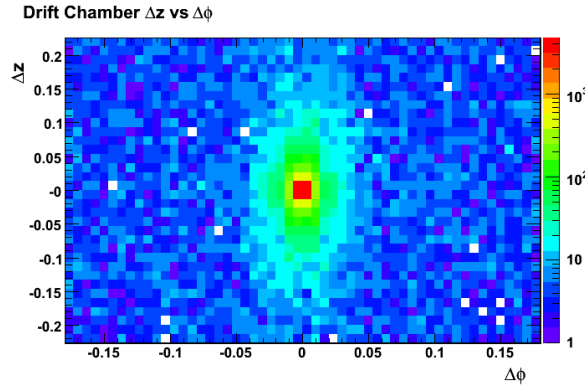


Figure 4.7: Track pair Δz vs. $\Delta\phi$ for good tracks.

4.1.2.4 Ghost cuts

Allowing the use of tracks where not all hits included in the reconstruction are required to be unique, because other tracks may share a hit or due to noise in the detector, can lead to the possibility of ghost tracks. In other words, a single track can get reconstructed twice as separate tracks. These ghost tracks can be identified by looking at the $\Delta\phi$ vs. Δz for all track candidates. This $\Delta\phi$ vs. Δz distribution is shown in Figure 4.7, with the color grade indicating number of hits. A clear peak at very small $\Delta\phi$ and Δz can be seen, indicating the presence of ghost tracks, which are identified by pairs with $|\Delta\phi| < 0.01$ and $|\Delta z| < 0.05$. Occasionally conversions produced by the track in the detector will also appear as very closely correlated tracks, which would also be labeled ghost tracks. Typically one of the tracks in the pair will be rejected by the cuts already discussed, and the track that passes these cuts will be kept. However, some good tracks can still be reconstructed as multiple tracks if there are nearby hits from other tracks or noise in the detector. In this case,

it is likely that a real particle from the primary vertex produced the hits. Therefore, it is not necessary to reject both tracks in the pair and instead one track in the pair is rejected randomly.

4.1.3 Photon cuts

In the discussion of clustering in Section 3.7.2, it was shown that electromagnetic particles produce a distinct cluster shower shape that can then be used to identify clusters likely to be from photons (or electrons). The χ^2 and probability of fits to the shower shape are generally used for rejecting non-photons (or electronic) clusters. Here clusters are required to have a $\chi^2 < 3$ and a probability > 0.1 . The next step is to apply further rejection cuts using track matching to eliminate the background from electrons, which produce the same shower shape, and hadrons, which have some probability of producing showers that pass these cuts.

4.1.3.1 Track-photon matching cuts

As part of the general reconstruction of raw data in PHENIX, good track candidates are projected into the EMCal, and the distance to the nearest cluster is recorded for both the track and cluster. Hits in the PC3 are also projected, assuming the hit came from a particle that originated at the collision vertex, and distance to the nearest projection is recorded for clusters. This information serves primarily as a way of identifying those clusters produced by charged particles rather than photons, but it can also be used as an additional measure of the quality of tracks, which can be applied in the same way as the PC3 cuts discussed in Section 4.1.2. To reject track

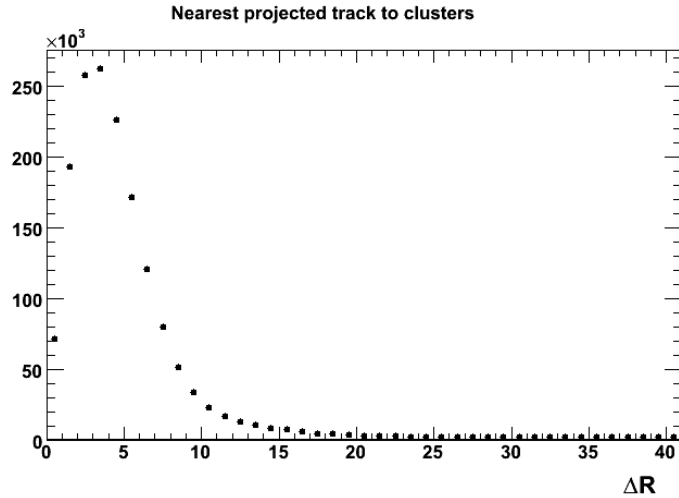


Figure 4.8: Radial distance between clusters and the closest track projected into the EMCAL.

clusters we require that there be no track or PC3 projections within 7cm in z and 0.01 in ϕ of a cluster.

It was found that these cuts alone, limited by holes in the PC3 and the requirement that tracks be of the highest quality, were not sufficient to remove all non-photonic clusters. As a further rejection, track candidates were projected from the DC and PC3 into the EMCAL. Plotted in Figure 4.8 is the distance (in cm) between clusters and the closest projected track. The peak seen at small distance indicates clusters that were most likely produced by a charge particle rather than a photon. If a track was found to fall within a 12cm radius around the photon candidate, the cluster was rejected. A projection of this kind is also important when attempting to understand the two-particle acceptance for hadron-photon pairs, since a cut of this type will artificially reduce the real pair yield at small hadron-photon $\Delta\phi$ (see Section 4.2.1).

In principle this type of cut should be momentum dependent, and one would expect hadronic sources to dominate at low momentum, as they typically only deposit a fraction of their energy in the EMCAL. While the correlation measurements discussed here involve photons with $p_T > 1.5$ GeV/c, where a p_T independent cut is sufficient, this analysis is also concerned with identifying photons coming from π^0 decays, where one of the photons in the decay can have a p_T as low as 400 MeV/c (see Chapter 5). At these low momenta it was found that the tracks are responsible for producing clusters at much larger projection distances (~ 20 cm). However, it was determined that increasing the minimum track-matching distance to accommodate this effect leads to a complicated $\Delta\phi$ dependence in the efficiency with which π^0 photons could be identified. This is because of the steeply falling and strongly $h\gamma$ $\Delta\phi$ dependent efficiency for low p_T photons resulting from such a wide cut. Further investigation revealed that these cases were most likely arising as a result of hadrons showering in the EMCAL being reconstructed as multiple clusters, which could be eliminated by not allowing pairs of clusters to fall too close together.

4.1.3.2 Cluster splitting

It can happen that the clustering algorithm used to group towers miss-reconstructs very oddly shaped tower distributions into multiple clusters, one or both of which may then have shower profiles that look like photons and pass the preliminary cuts applied. This effect is called cluster splitting. Splitting is typically produced by hadronic showers and is therefore mostly an issue at lower p_T , although photons or electrons hitting the detector at oblique angles at any p_T can get split as well. An

example of the effect can be seen in Figure 4.9, which shows the radial distance (in radians) between all cluster pairs in an event. The lack of pairs at very small ΔR comes from the fact that clusters cannot overlap. Because such measurements will be sensitive to the resolution - or tower size - of the detector, a study of the sector dependence was done to ensure that the Pb-glass and Pb-scintillator were behaving in similar ways. The smaller tower size of the Pb-glass was found to have a small effect, but one that would not significantly change how split clusters are cut.

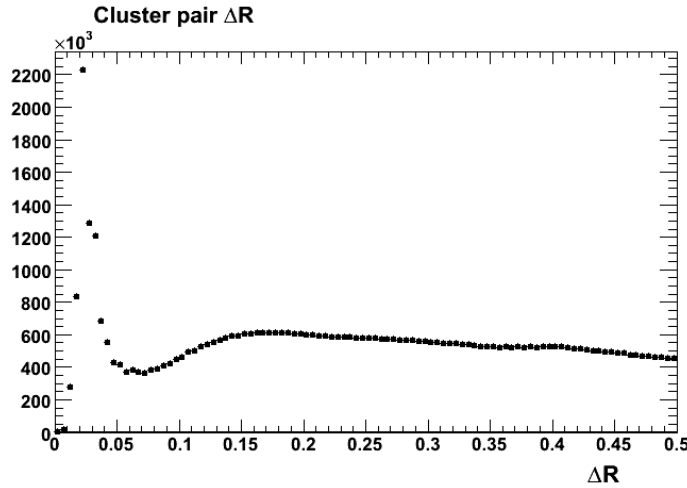


Figure 4.9: Distribution of the radial distance (in radians) between cluster pairs in the EMCal.

Based on Figure 4.9, it appears that removing split clusters can be achieved using a cut rejecting cluster pairs with $\Delta R < 0.05$. However, at higher p_T , as the opening angle for π^0 decays becomes small, a flat ΔR cut will begin to overlap with real π^0 pairs, leading to a large drop in reconstruction efficiency. A simple p_T dependent cut is not sufficient, however, as highly asymmetric pairs will have different behavior, with the lower p_T cluster in the pair being more susceptible to contam-

ination. Figure 4.10 shows two-dimensional plots of the pair asymmetry versus ΔR , in different leading photon p_T bins, where both the π^0 peak and the splitting peak can be seen clearly. This splitting peak persists for the most asymmetric pairs even at high p_T , where a flat ΔR cut would clearly reject most symmetric π^0 pairs - emphasizing the need for a more sophisticated cut if one hopes to keep the π^0 reconstruction efficiency high at high p_T .

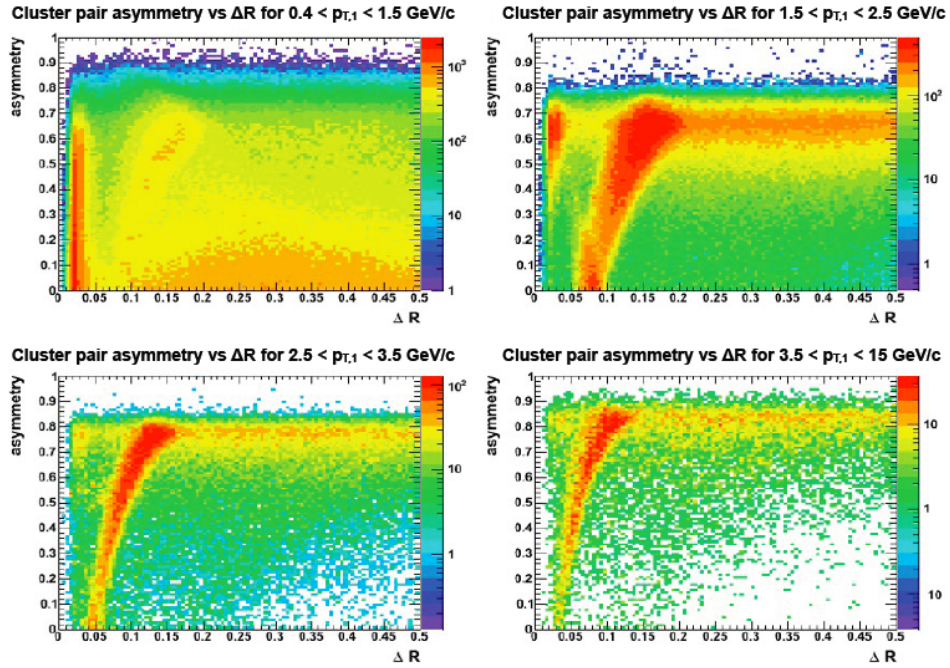


Figure 4.10: Cluster pair asymmetry vs. ΔR in four bins in leading photon p_T : $0.4 - 1.5$ GeV/c (top left), $1.5 - 2.5$ GeV/c (top right), $2.5 - 3.5$ GeV/c (bottom left), and $3.5 - 15$ GeV/c (bottom right).

ΔR is basically the opening angle for the pair, projected onto the EMCAL, and with a little bit of algebra, one can express the invariant mass of the pair as:

$$m = p_T \Delta R \sqrt{\frac{1 - A}{1 + A}} \quad (4.3)$$

where p_T is for the cluster of interest and the signed asymmetry for the pair is $A = (p_{T,1} - p_{T,2})/(p_{T,1} + p_{T,2})$. With the pair determined by scanning over all cluster pairs and finding the minimum pair ΔR for each photon. Using the mass parameterized in this way, one can apply a cut that falls well outside the π^0 mass range while still removing split clusters. Figure 4.11 shows the same pair asymmetry versus ΔR distribution described above, with a cut of $m < 0.05$ applied to the pairs. It is clear from these plots that such a cut leaves π^0 pairs intact, while completely removing split clusters.

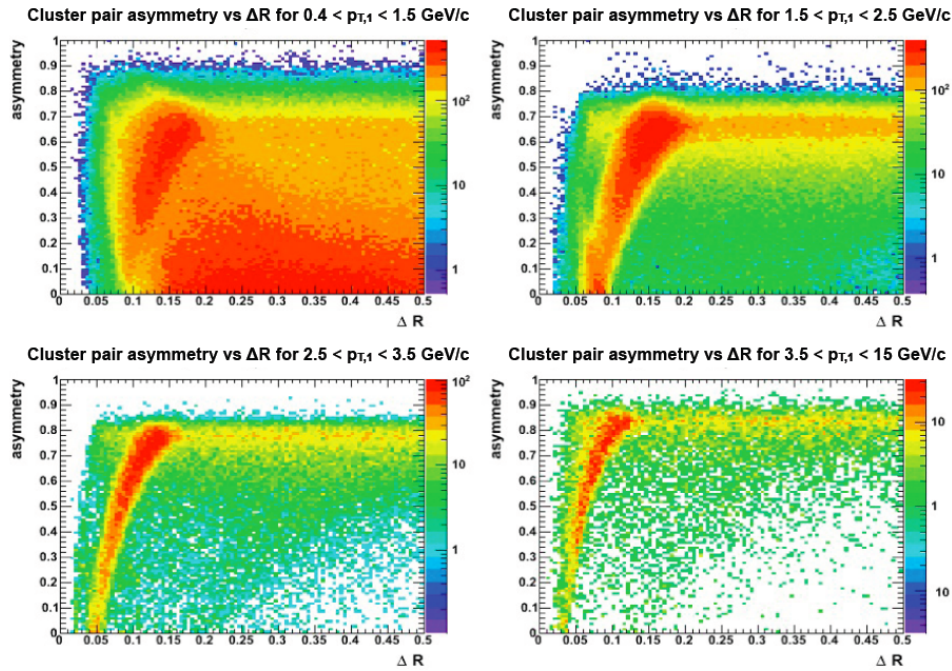


Figure 4.11: Cluster pair asymmetry vs. ΔR with a cut of $m < 0.05$, as defined in 4.3, in four bins in leading photon p_T : $0.4 - 1.5$ GeV/c (top left), $1.5 - 2.5$ GeV/c (top right), $2.5 - 3.5$ GeV/c (bottom left), and $3.5 - 15$ GeV/c (bottom right).

4.1.3.3 Time of Flight

The cuts described so far are primarily for the rejection of background from charged particles produced in collisions, which will deposit energy in the EMCal and can therefore be mistaken for photons. The remaining background comes from noise and other random sources that cannot be removed with such cuts. However, these sources will generally not produce showers in a way that is well timed with the event. Based on the event time - determined by the BBC - and the time a shower is produced in the EMCal, the time-of-flight (ToF) for clusters can be determined. Photons should of course have a very small ToF. Therefore, cutting out clusters with a large ToF can remove any random background, as well as further reducing hadronic background, as hadrons - which have mass - will not have the same ToF distribution as photons. The two-dimensional plot on the left in Figure 4.12 shows the ToF distribution (in nano-seconds) from Run 6 for clusters passing all other cuts. The photon peak at small ToF is clear, as is the background at large ToF. On the left are two slices in photon p_T for a smaller range of ToF values. As the momentum slices shown illustrate, the ToF peak varies with p_T . The requirement that clusters be within 10ns of the event time was made to remove most of the background without cutting into the tail of the signal peak.

4.1.3.4 Bad towers

Although most clusters measured in the EMCal will come from real particles, there are a small set of individual towers with faulty electronics, or some other issue, that causes them to produce fake hits unrelated to a real particle or hinders their ability

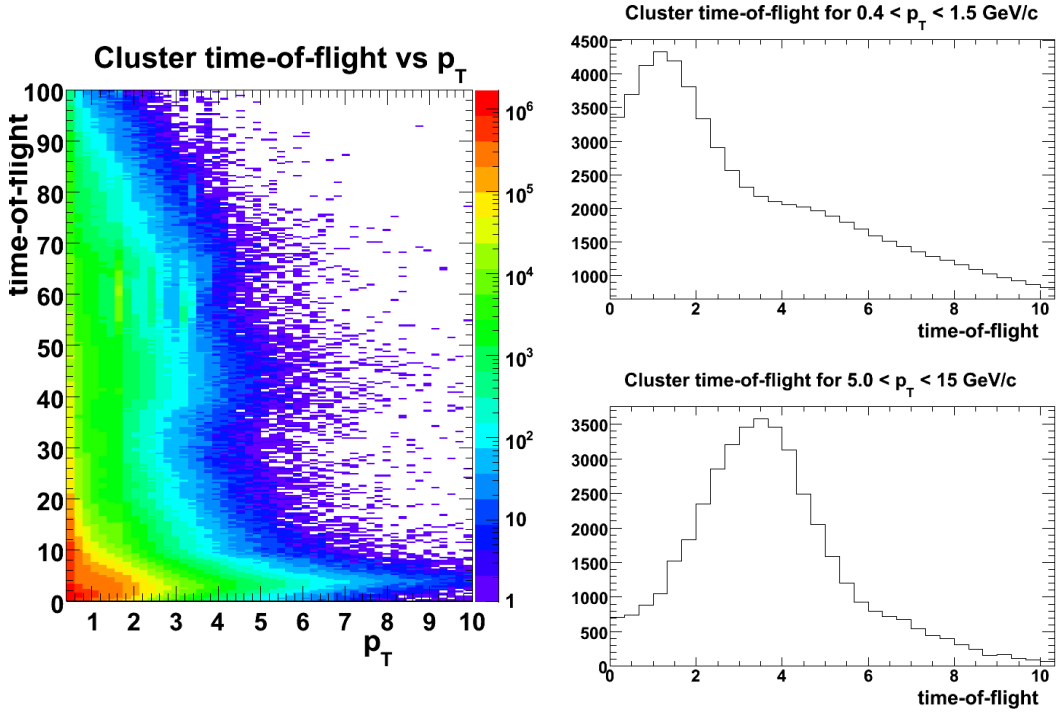


Figure 4.12: Run 6 cluster time-of-flight(ns) vs. p_T is plotted on the left. Two projection of the two-dimensional distribution in the specified momentum range are plotted on the right: $0.4 < p_T < 1.5$ GeV/c (top) and $5.0 < p_T < 15.0$ GeV/c (bottom).

to detect anything at all. Generally these will show up as noisy (hot), or dead towers producing far more, or far fewer, hits than measured from real data. Here a tower has a hit if it is identified as the central tower for a reconstructed cluster. Figure 4.13 shows the two-dimensional distribution of tower hits in each EMCAL sector for Run 6, using clusters with p_T from $1.5 - 3.5$ GeV/c. In most sectors, the worst hot towers are clearly visible in this figure. Identifying all hot towers requires looking more closely at the hit distribution for towers.

One can determine the mean number of hits a tower can be expected to receive throughout the Run by looking at the frequency of hits for all towers in a sector, and

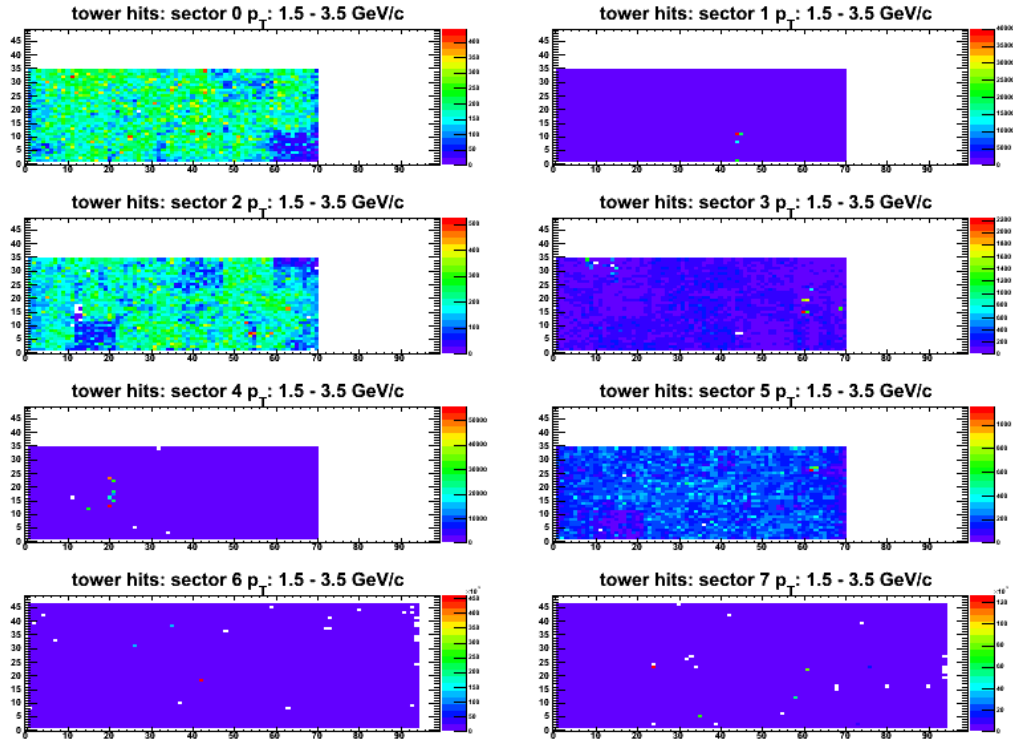


Figure 4.13: Distribution for central towers of photons from $1.5 - 3.5$ GeV/c for each sector in the EMCAL as a function of the z and y index of the tower. The data shown was taken during Run 6, for events required to fire an ERT trigger.

the hit distribution should have an approximate Gaussian shape. Towers that have a number of hits well above this mean are considered hot. Towers that fall well below the mean can be considered cold, although generally only completely dead towers are identified as cold. For this analysis a tower is considered hot if it records hits at least 4σ above the mean. Because clusters generally include several adjacent towers, towers in a 3×3 block around each hot tower are also rejected to avoid including bad towers as part of any cluster. There are generally more noisy towers at low p_T , as well as some towers that become noisy at higher p_T , so hot towers

were identified for three p_T ranges: $0.4 - 1.5$ GeV/c, $1.5 - 3.5$ GeV/c, and > 3.5 GeV/c. The hit distribution for the central tower of clusters with p_T from $1.5 - 3.5$ GeV/c is shown in Figure 4.14 as an example. The blue line indicates where the 4σ cut falls for rejecting hot towers.

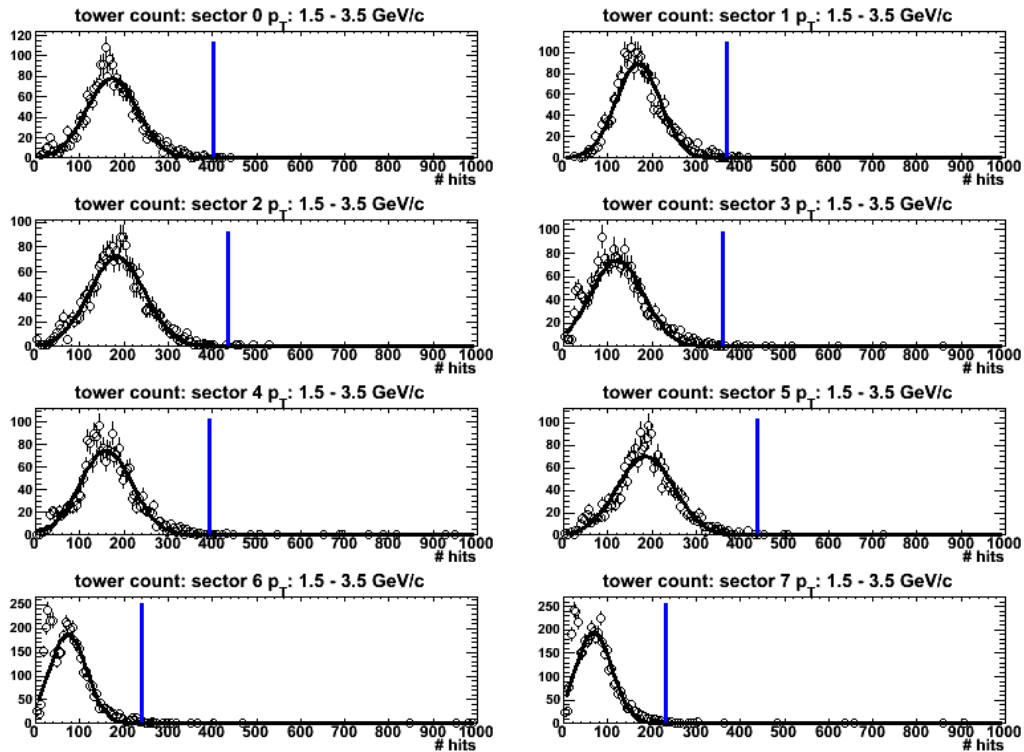


Figure 4.14: Distribution of the number of hits in central tower clusters from $1.5 - 3.5$ GeV/c for each EMCal sector, fit with a Gaussian. The blue line indicates the 4σ cut used to identify hot towers. The data shown was taken during Run 6 for events required to fire an ERT trigger.

In addition to hot towers, a two tower fiducial cut is applied around the edges of each sector. As with the 3×3 block around hot towers, this cut ensures the cluster energy remains accurate, as clusters near the edge often do not deposit all of their

energy inside the detector. Similar cuts are placed around any dead towers found. Once all bad towers are identified and removed, the hit distribution for good towers is generated as a map for the detector acceptance which can then be used as input to simulations needed to determine the detector efficiency. Figure 4.15 shows an example of the hit distribution for towers in each sector after hot tower and fiducial cuts are applied, again for clusters with p_T from 1.5 – 3.5 GeV/c. The remaining non-uniformity is a result of the triggered data set, where some SMs are masked off during the run if they begin firing too frequently due to faulty electronics.

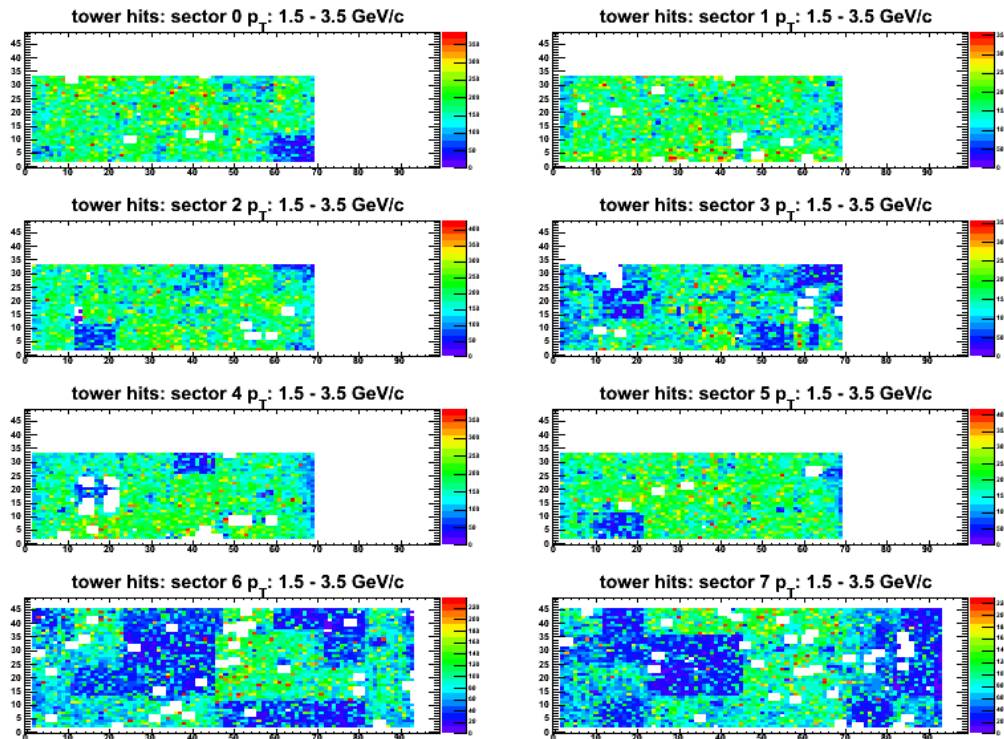


Figure 4.15: Distribution for central towers, after hot tower rejection, of photons from 1.5 – 3.5 GeV/c for each sector in the EMCAL as a function of the z and y index of the tower. The data shown was taken during Run 6, for events required to fire an ERT trigger.

4.2 Two particle correlations

Once good hadrons and photons have been selected, measurements of hadron-photon pairs being produced as part of a jet can be made. While it is most natural to think of such spatial correlations in terms of the opening angle between the two particles, it is often more straightforward to look instead at the difference in azimuthal angle between the pair, $\Delta\phi$, integrating over η . In general this will increase the uncorrelated background measured under the jet peak. However in the case of PHENIX, where the central arms cover only a small range in η , the effect is minimal. As discussed in Section 2.4.2.2, particles produced from jets will be strongly correlated, producing a Gaussian distribution around $\Delta\phi = 0$, and a similar structure around $\Delta\phi \approx \pi$ from di-jets, where the p_T and $\Delta\phi$ dependence can be directly related to properties of the jets. In the analysis presented here, the focus will be on hadrons and photons produced in the same jet, the near-side correlation signal.

Unlike full jet reconstruction, which can distinguish jets on an event-by-event basis, correlation measurements are statistical, summing over many events, with no guarantee that there is actually a jet in every event. To keep the background from non-jet sources to a minimum, the particles used are generally required to be high- p_T and are assumed to carry most of the jet energy. In this analysis we first determine those events likely to have a jet in them by defining a *trigger* particle a hadron with p_T from $2 - 5$ GeV/c with finer binning introduced in the course of the analysis and measure the $\Delta\phi$ distributions between these triggers and associated photons over a large range of photon p_T .

4.2.1 Detector acceptance and event mixing

Two particle azimuthal correlations begin with a raw $\Delta\phi$ distribution for all pairs. This will include a combinatoric background from uncorrelated pairs not produced as part of the same hard scattering, which can contribute to the total pair yield if not removed. Additionally, a non-uniform detector acceptance will lead to a non-flat distribution for such uncorrelated pairs, causing a distortion in the correlation signal which can bias jet measurements. A common technique for determining the combinatoric background - as well as any effects of a non-flat acceptance - is to use event mixing, i.e. combining pairs where each particle came from a different event. Using different events ensures the pairs have no real correlations, while accurately reflecting the effect holes in the acceptance have on the underlying combinatoric distribution. Consistency in the number of particles used when mixing and particle rates contributing to real pairs can help to determine the scale of the underlying uncorrelated background, which will be discussed in Section 4.2.2.

In PHENIX, while dead regions within the detector will have an impact, the most obvious effect on the two-particle acceptance is the limited azimuthal acceptance, which leads to a $\Delta\phi$ acceptance that is, even in the ideal case, a convolution of two flat acceptance functions with limited ϕ ranges ($-\frac{3\pi}{16} < \phi < \frac{5\pi}{16}$ and $\frac{11\pi}{16} < \phi < \frac{19\pi}{16}$). As shown in Figure 4.16, the probability distribution for a random hadron-photon pair will be highest for $\Delta\phi$ around 0 and π and have a minimum at $|\Delta\phi| \approx \frac{\pi}{2}$. In fact, it is only because the gap between the east and west arms is asymmetric that the two-particle acceptance does not go to zero at $\pi/2$.

When evaluating the two-particle acceptance in this way, careful attention must

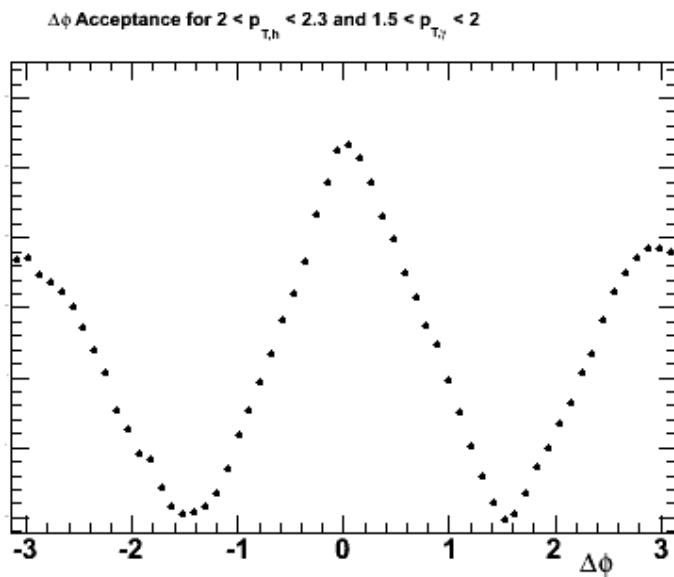


Figure 4.16: Example of the PHENIX acceptance for hadron-photon pairs within a fixed p_T range for each, as determined from event mixing.

be paid to how the acceptance varies based on the properties of both the event and the particles used to construct the pair probability distribution. The first important detail which goes into this mixing method is how the acceptance varies in time. The assumption made is that within a given run - or even small numbers of consecutive runs - the detector acceptance will not change, or at least will not change enough to cause distortions. This is a safe assumption as long as changes in the acceptance - for example, regions of the detector becoming noisy or being masked out - occur gradually such that mixing between events within the same or near-by runs will accurately reflect the two-particle acceptance.

It is also important to incorporate how the pair acceptance will vary based on the z-vertex of an event. Hadrons and photons from events produced near the edge

of the detector acceptance will not be distributed in the same way as those coming from events near the center of the detector, leading to a different probability of being randomly correlated. It is therefore necessary to only mix events with a similar z-vertex to accurately determine the uncorrelated pair distribution in that class of events. This effect is accounted for by keeping events in z-vertex bins of 6cm and only mixing events within the same vertex bin.

Finally, it is important to note how the acceptance depends on the p_T of the particles in the pairs themselves. For charged hadrons there is an obvious p_T dependent ϕ acceptance, resulting from the p_T dependent bending of hadrons in the magnetic field prior to their passage through the central arms. Calculating the hadron-photon acceptance in small hadron p_T bins keeps this effect to a minimum. However, the p_T dependence of the particle efficiencies can also distort the acceptance. To understand how the particle efficiencies contribute the acceptance, we will consider the full functional form for the correlated two particle yields in a specific hadron-photon p_T bin (neglecting η):

$$\frac{dN^{h-\gamma}}{d\Delta\phi} = \int dp_{T,h} \int dp_{T,\gamma} \int d\phi_h \int d\phi_\gamma \frac{d^4N^{h-\gamma}}{dp_{T,h} dp_{T,\gamma} d\phi_h d\phi_\gamma} \delta(\Delta\phi - (\phi_h - \phi_\gamma)) . \quad (4.4)$$

This is related to the measured yields by

$$\frac{d^4M^{h-\gamma}}{dp_{T,h} dp_{T,\gamma} d\phi_h d\phi_\gamma} = \epsilon^{h\gamma}(\phi_\gamma, p_{T,\gamma}, \phi_h, p_{T,h}) \frac{d^4N^{h-\gamma}}{dp_{T,h} dp_{T,\gamma} d\phi_h d\phi_\gamma} , \quad (4.5)$$

where

$$\epsilon^{h\gamma}(\phi_\gamma, p_{T,\gamma}, \phi_h, p_{T,h}) = \text{Acc}(\Delta\phi)\epsilon^h(\phi_h, p_{T,h})\epsilon^\gamma(\phi_\gamma, p_{T,\gamma}). \quad (4.6)$$

Generally it is then assumed that the single particle efficiency can be further factorized as $\epsilon(\phi, p_T) = \epsilon(\phi)\epsilon(p_T)$, in other words, that the spatial variation in detector efficiency is independent of the momentum dependent variation. The spatial efficiency, $\epsilon(\phi)$ can then be absorbed into $\text{Acc}(\Delta\phi)$, measured from mixing, and the final efficiency corrections can simply be made using $\epsilon(p_T)$, integrated over the full acceptance, and determined from simulation as described in Section 4.3.

The assumption that the single particle efficiencies can be factorized in this way is often relatively safe, since there is no obvious reason to expect different regions of the detector to have a different p_T dependent response to particles. This is especially true if the efficiency does not vary rapidly with p_T ; however, when using triggered data more care must be taken. When considering the ERT triggers, it is important to note that a photon is considered to have fired the trigger if it falls within a super-module where a set of tiles had a combined energy above the trigger threshold. As a result, there will be a spatial dependence to the trigger efficiency related to the response within each SM that is coupled to the p_T dependent turn on of the trigger. If only photons well above the trigger threshold were analyzed, this would not be a problem. However, this analysis is also interested in photons with p_T as low as 1.5 GeV/c - which is just at the ERT 4x4c trigger threshold - and therefore lies in the region where the trigger efficiency is rapidly varying. An example of this variation as a function of SM is shown in Figure 4.23, in Section 4.3, where the efficiency

corrections are discussed in more detail.

The complexity of the ERT trigger efficiency means that the efficiency is not factorizable, so we instead have

$$\epsilon^{h\gamma}(\phi_\gamma, p_{T,\gamma}, \phi_h, p_{T,h}) = \text{Acc}(\Delta\phi) \epsilon^h(p_{T,h}) \epsilon^\gamma(p_{T,\gamma}) \epsilon^{ERT}(\phi_{SM}, \eta_{SM}, p_{T,\gamma}) . \quad (4.7)$$

This final two-particle efficiency \times acceptance is corrected for pair-by-pair using a weight for each pair of $1/\epsilon$.

To determine $\text{Acc}(\Delta\phi)$, hadrons from MinBias events satisfy the analysis-based trigger requirements are mixed with photons from ERT events that fire the ERT 4x4c trigger - the requirement applied to photons in real pairs. Using ERT photons is necessary to accurately correct for the acceptance of the ERT trigger, which photons in the pair are required to fire. It is important to use a minimum bias sample of hadrons, however, so as not to introduce distortions in the underlying distribution of hadrons resulting from the non-uniform ERT efficiency. The same pair-by-pair ERT efficiency corrections applied to the real pairs must be applied to the mixed pairs, as those efficiency affects should not contribute to the definition of $\text{Acc}(\Delta\phi)$.

So

$$\text{Acc}(\Delta\phi) = \frac{2\pi \frac{dN_{mix}^{h-\gamma}(\Delta\phi)}{d\Delta\phi}}{\int \Delta\phi \frac{dN_{mix}^{h-\gamma}(\Delta\phi)}{d\Delta\phi}} . \quad (4.8)$$

Applying the acceptance correction pair-by-pair, along with the other efficiency corrections, automatically corrects for acceptance in any kinematic variable being measured, allowing us to measure properties such as p_{out} directly. This weighting

is also applied to the mixed background to obtain the underlying event background distribution. In the case of $\Delta\phi$ correlations, this gives the flat combinatoric background. However, for other pair distributions, such as p_{out} , the Jacobian between p_{out} and the $\Delta\phi$ of the combinatoric pairs means the background is not flat, making proper subtraction even more important for an accurate measure of the p_{out} of jet pairs.

When subtracting the non-jet background, the assumption is often made that there is no jet yield at large $\Delta\phi$ - zero yield at the minimum (ZYAM). In this case, a simple scale based on matching the real and mixed $\Delta\phi$ distributions can be applied to the background for any pair yield before subtraction. However, this is an approximation that has the potential to bias the physics towards more tightly correlated jet results, and it is highly sensitive to statistical fluctuations in the pair yield in the region of the PHENIX acceptance where the statistics are poorest. For this reason, this method was not employed in this analysis. Instead, a method was developed to estimate the background level directly from the data; it is described in the next section.

4.2.2 The underlying event

We can express the per-event yield for particles of type a , or b , as a sum of the contribution from correlated sources, i.e. jets, and from an uncorrelated combinatorial background. In other words $n_a = n_a^{\text{fg}} + n_a^{\text{bg}}$. The number of pairs is then $n_{ab} = n_a n_b = (n_a^{\text{fg}} + n_a^{\text{bg}})(n_b^{\text{fg}} + n_b^{\text{bg}})$. As with previous absolute normalization methods, we will estimate the uncorrelated background using pairs combined from dif-

ferent events. Rather than using full event mixing, as has been done previously, a pool of particles from different events is sampled. The number of particles used is a multiplicative factor (N_{mix}) times the number used to produce the same event pairs, ensuring that $n_{ab}^{\text{real}} = n_{ab}^{\text{mix}}$.

The final average per event yields for real pairs can be written as:

$$\begin{aligned}
 \langle n_{ab}^{\text{real}} \rangle &= \langle (n_a^{\text{fg}} + n_a^{\text{bg}})(n_b^{\text{fg}} + n_b^{\text{bg}}) \rangle \\
 &= \langle n_a^{\text{fg}} n_b^{\text{fg}} \rangle + \langle n_a^{\text{fg}} n_b^{\text{bg}} \rangle + \langle n_a^{\text{bg}} n_b^{\text{fg}} \rangle + \langle n_a^{\text{bg}} n_b^{\text{bg}} \rangle \\
 &= \underbrace{\langle n_a^{\text{fg}} n_b^{\text{fg}} \rangle}_{\langle n_{ab}^{\text{corr}} \rangle} + \underbrace{\langle n_a^{\text{fg}} \rangle \langle n_b^{\text{bg}} \rangle + \langle n_a^{\text{bg}} \rangle \langle n_b^{\text{fg}} \rangle + \langle n_a^{\text{bg}} \rangle \langle n_b^{\text{bg}} \rangle}_{\langle n_{ab}^{\text{comb}} \rangle}. \tag{4.9}
 \end{aligned}$$

For mixed pairs, where everything is uncorrelated, this becomes:

$$\begin{aligned}
 \langle n_{ab}^{\text{mix}} \rangle &= \langle n_a^{\text{fg}} + n_a^{\text{bg}} \rangle \langle n_b^{\text{fg}} + n_b^{\text{bg}} \rangle \\
 &= \langle n_a^{\text{fg}} \rangle \langle n_b^{\text{fg}} \rangle + \langle n_a^{\text{fg}} \rangle \langle n_b^{\text{bg}} \rangle + \langle n_a^{\text{bg}} \rangle \langle n_b^{\text{fg}} \rangle + \langle n_a^{\text{bg}} \rangle \langle n_b^{\text{bg}} \rangle. \tag{4.10}
 \end{aligned}$$

The mixed pairs include an additional term, $\langle n_a^{\text{fg}} \rangle \langle n_b^{\text{fg}} \rangle$, which is not part of the combinatorial background, $\langle n_{ab}^{\text{comb}} \rangle$. As noted previously in [132], this leads to an overestimate of the background level. Note that if the correlated yield is small relative to the underlying event background, this term will be negligible, as is generally the case in minimum bias A + A events. However, in the case of p + p, and more specifically a high p_T trigger data set, correlated pairs from jets are the dominant source of pairs. Therefore, to use mixed pairs to subtract the background, a correction factor is necessary to avoid over-subtraction. This correction can be determined

by requiring $\langle n_{ab}^{\text{comb}} \rangle = f(\langle n_{ab}^{\text{mix}} \rangle)$:

$$\begin{aligned}
 f(\langle n_a \rangle \langle n_b \rangle) &= \langle n_a^{\text{fg}} \rangle \langle n_b^{\text{bg}} \rangle + \langle n_a^{\text{bg}} \rangle \langle n_b^{\text{fg}} \rangle + \langle n_a^{\text{bg}} \rangle \langle n_b^{\text{bg}} \rangle \\
 \Rightarrow f &= \frac{\langle n_a^{\text{fg}} \rangle \langle n_b^{\text{bg}} \rangle + \langle n_a^{\text{bg}} \rangle \langle n_b^{\text{fg}} \rangle + \langle n_a^{\text{bg}} \rangle \langle n_b^{\text{bg}} \rangle}{\langle n_a \rangle \langle n_b \rangle} \\
 &= \frac{\langle n_a \rangle \langle n_b^{\text{bg}} \rangle + \langle n_a^{\text{bg}} \rangle \langle n_b \rangle - \langle n_a^{\text{bg}} \rangle \langle n_b^{\text{bg}} \rangle}{\langle n_a \rangle \langle n_b \rangle} \\
 &= \frac{\langle n_a^{\text{bg}} \rangle}{\langle n_a \rangle} + \frac{\langle n_b^{\text{bg}} \rangle}{\langle n_b \rangle} - \frac{\langle n_a^{\text{bg}} \rangle}{\langle n_a \rangle} \frac{\langle n_b^{\text{bg}} \rangle}{\langle n_b \rangle}. \tag{4.11}
 \end{aligned}$$

With this scale factor, we can then use mixed events to estimate the background level, and subtract to extract the correlated yield:

$$\langle n_{ab}^{\text{corr}} \rangle = \langle n_{ab}^{\text{real}} \rangle - f(\langle n_{ab}^{\text{mix}} \rangle). \tag{4.12}$$

4.2.2.1 Determining f from data

In the previous section we derived the scale factor needed to use the absolute normalization method in $p + p$. Determining this scale factor in a specific physical case requires knowing the ratio of uncorrelated background particles as well as the total particle multiplicities used in the measurement. The contribution to the pair yields from background is not directly measurable; however, it may be possible to estimate from quantities that can be measured. Because jets are rare, in a minimum bias sample the contribution to single particle per event multiplicities will be dominated by soft, uncorrelated sources. It is therefore possible to estimate the background contribution to conditional particle yields using the measured minimum bias per event

yields:

$$\frac{\langle n_a^{\text{bg}} \rangle}{\langle n_a \rangle} \approx \frac{\langle n_a^{\text{MB}} \rangle}{\langle n_a^{\text{cond}} \rangle} . \quad (4.13)$$

Here n_a^{cond} is the multiplicity of particles of type a in events where there was also a particle of type b present within the momentum range used to determine the pair yields:

$$\langle n_a^{\text{cond}} \rangle = \frac{N_a(\text{b in event})}{N_{\text{evt}}(\text{b in event})}$$

. While it is true that the minimum bias sample is dominated by soft physics, there will still be a contribution from jets, although small, that is not really part of the background. This can be roughly estimated by measuring the multiplicity for particles tagged as part of a pair within the angular range where the jet yield dominates, $n_{a,\text{tag}}^{\text{MB}}$, and subtracting this contribution:

$$\langle n_a^{\text{bg}} \rangle \approx \langle n_a^{\text{MB}} \rangle - \langle n_{a,\text{tag}}^{\text{MB}} \rangle . \quad (4.14)$$

There will be an efficiency associated with the ability to tag such particles, in principle calculable from simulation, as well as some amount of uncertainty associated with the definition of what qualifies as a correlated pair that will be part of any systematic uncertainty applied to the method. The efficiency for tagging a type a particle as coming from a correlated pair should depend only on whether the pair particle, b , is detected along with a . This can be determined by measuring the pair

efficiency, and dividing out the single particle efficiency for a :

$$\epsilon_a^{tag} = \frac{\epsilon_{ab}}{\epsilon_a} \quad (4.15)$$

and

$$\Rightarrow \frac{\langle n_a^{bg} \rangle}{\langle n_a \rangle} \approx \frac{\langle n_a^{MB} \rangle - \frac{\epsilon_a}{\epsilon_{ab}} \langle n_{a,tag}^{MB} \rangle}{\langle n_a^{cond} \rangle} \quad (4.16)$$

Because the final scale factor, f , involves only ratios of particle yields, all other particle efficiencies will cancel, so it is not necessary to include them when using measured data.

4.2.2.2 p_T Dependence and Binning

When assembling a pool of pair particles to mix for determining the uncorrelated background, it is necessary to ensure that the average number of particles used reflects the particle multiplicities going into the real pair distributions. This is done by always mixing with the same number of pair particles present in the real event, modulo a constant multiplicative factor N_{mix} . Especially in the case of charged particles, the pool of particles being sampled from must contain particles within the same p_T range as the real events; otherwise, the p_T dependence of the detector acceptance will not match between real and mixed pairs. If the type of events used to build the particle pools does not have the same p_T dependence as events used for real pairs, and the p_T range of the mixing pool does not exactly match the range used to estimate f , a p_T dependent bias would be introduced in the resulting values for f .

An illustration of this point can be seen in Figure 4.19, which shows the ratio of background MB hadrons per MB event to hadrons per event when it is required that there be a photon with p_T from 1.5 - 2 GeV/c, as a function of hadron p_T . This ratio shows the p_T spectrum for MB hadrons will be softer than that of ERT hadrons because the ERT data by definition applies the condition that there be a cluster above a p_T of 1.5 GeV/c. If we track the momentum dependence of the event averages used to obtain f , assuming the p_T dependence of the non-jet particles alone will be the same in both samples, we have:

$$f = \frac{\langle n_\gamma(p_T^{ERT}) \rangle \langle n_h^{\text{bg}}(p_T^{ERT}) \rangle + \langle n_\gamma^{\text{bg}}(p_T^{ERT}) \rangle \langle n_h(p_T^{ERT}) \rangle + \langle n_\gamma^{\text{bg}}(p_T^{ERT}) \rangle \langle n_h^{\text{bg}}(p_T^{ERT}) \rangle}{\langle n_\gamma(p_T^{ERT}) \rangle \langle n_h(p_T^{MB}) \rangle} \\ = \frac{\langle n_\gamma^{\text{bg}} \rangle \langle n_h(p_T^{ERT}) \rangle}{\langle n_\gamma \rangle \langle n_h(p_T^{MB}) \rangle} + \frac{\langle n_h^{\text{bg}}(p_T^{ERT}) \rangle}{\langle n_h(p_T^{MB}) \rangle} - \frac{\langle n_\gamma^{\text{bg}} \rangle \langle n_h^{\text{bg}}(p_T^{ERT}) \rangle}{\langle n_\gamma \rangle \langle n_h(p_T^{MB}) \rangle}. \quad (4.17)$$

From this it is clear that if the particle pools sampled from for mixing are not binned in momentum to match those used for the correlations, it will not be the case that the average number of hadrons used for mixing is equivalent to the average number used for real pairs. For the purposes of mixing with this method, therefore, multiple hadron pools - each containing only hadrons within one of the specified trigger bins - were sampled. Similarly, the scale corrections are determined within each p_T bin used for forming the correlations to ensure that averaging over momentum is done consistently throughout.

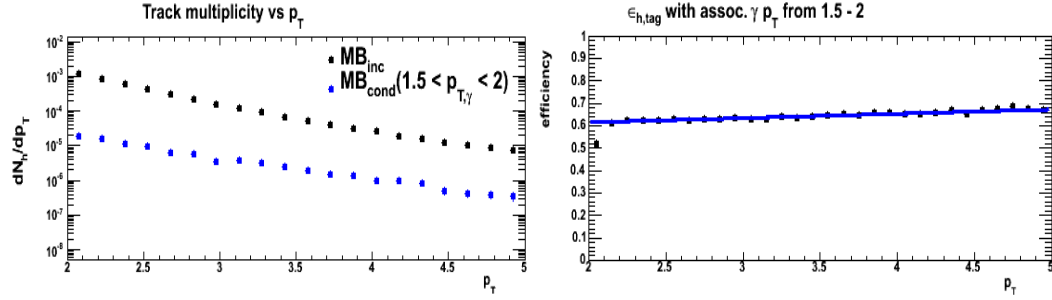


Figure 4.17: MB per event yields for hadrons, inclusive in black, hadron-photon pair tagged in blue, with photon p_T from 1.5-2 GeV/c (left). Corresponding tagging efficiency (right).

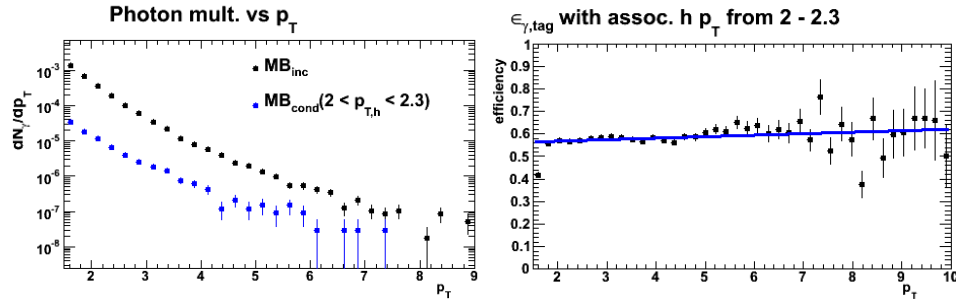


Figure 4.18: MB per event yields for photons, inclusive in black, hadron-photon pair tagged in blue, with hadron p_T from 2-2.3 GeV/c (left). Corresponding tagging efficiency (right).

4.2.2.3 Input to estimate f for hadron-photon pairs

The obtain the input for Eq. (4.16), the raw MB per event yields for hadrons and photons are measured, as well as for hadrons and photons tagged as coming from a pair with an associated photon or hadron within each momentum range of interest. The plots on the left in Figures 4.17 and 4.18 show examples of these multiplicity distributions for hadrons and photons respectively. In these examples, the lowest associated partner p_T ranges used in the full analysis, stated in the figure, have been

applied to obtain the tagged yields shown in blue. The inclusive minimum bias yields will not change for other cases, but the tagged yields will decrease as the p_T range of the associated particle increases.

The final input needed for determining the multiplicity ratio is the efficiency for tagging pairs. This efficiency is found using PYTHIA generated events, run through a simulation of the PHENIX detector response (PISA). For hadrons, and similarly for photons, the conditional efficiency is calculated by taking the rate of detected hadrons with an associated reconstructed photon compared to the rate of production of such hadrons measured in PYTHIA, within the nominal PHENIX acceptance. This gives the pair efficiency, which is then divided by the single particle efficiency for the hadron or photon to get the tagging efficiency. Here, associated hadrons and photons are required to be within the same p_T range used in the data, with the restriction that $|\Delta\phi| < 1.0$, to limit pairs to those within the signal region. These efficiencies, for one partner p_T bin, are shown on the right in Figures 4.17 and 4.18, and are used as input to obtaining the tagged yields shown in the plots on the left.

Explicitly including the binning applied to the pair particle, Eq. (4.16) can be written:

$$\frac{\langle n_h^{\text{bg}} \rangle}{\langle n_h \rangle}(p_{T,h}, [p_T]_{\gamma}^{\text{bin}}) \approx \frac{\langle n_h^{\text{MB}} \rangle - \frac{\epsilon_h(p_{T,h})}{\epsilon_{h\gamma}(p_{T,h}, [p_T]_{\gamma}^{\text{bin}})} \langle n_{h,\text{tag}}^{\text{MB}}(p_{T,h}, [p_T]_{\gamma}^{\text{bin}}) \rangle}{\langle n_h^{\text{cond}}(p_{T,h}, [p_T]_{\gamma}^{\text{bin}}) \rangle} . \quad (4.18)$$

This shows the case for hadrons, as a function of hadron p_T , with binning based on the p_T of the conditional photon; a similar form for photons applies. The resulting multiplicity ratios for hadrons and photons, again for one of the partner p_T bins, are

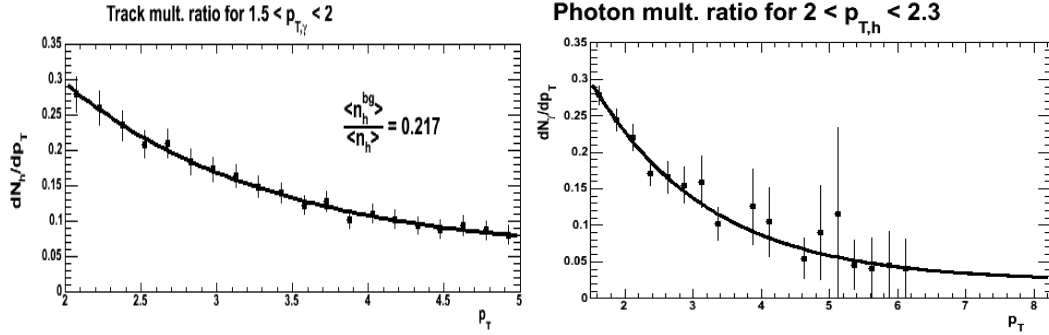


Figure 4.19: Example of the multiplicity ratios for hadrons (left), with conditional photons p_T from 1.5–2 GeV/c, (left) and photons (right), with hadron p_T from 2–2.3 GeV/c : inclusive vs conditional.

shown in Figure 4.19.

These ratios can now be used to determine the scale factor, f , applied to the mixed background. Figure 4.20 shows an example of the acceptance and efficiency corrected $\Delta\phi$ distributions for hadron-photon pairs, for hadrons with p_T from 2.0 – 2.3 GeV/c and photons from 1.5 – 2.0 GeV/c with the scaled mixed background shown in blue. The value for f , as well as the deviation from the assumption that there is zero jet yield at the $\Delta\phi$ correlation minimum (ZYAM), is stated along with the raw background levels measured by the two methods. While this method will be much less sensitive to fluctuations in the real pair background, used to estimate the ZYAM scale, it relies on assumptions about our ability to estimate the level of the background directly.

Table 4.2 shows the values for f for each hadron and photon p_T bin used in this analysis, as well as the relative difference, $|\text{Abs} - \text{ZYAM}|/\text{Abs}$, when compared with ZYAM. The good agreement between this absolute normalization method and

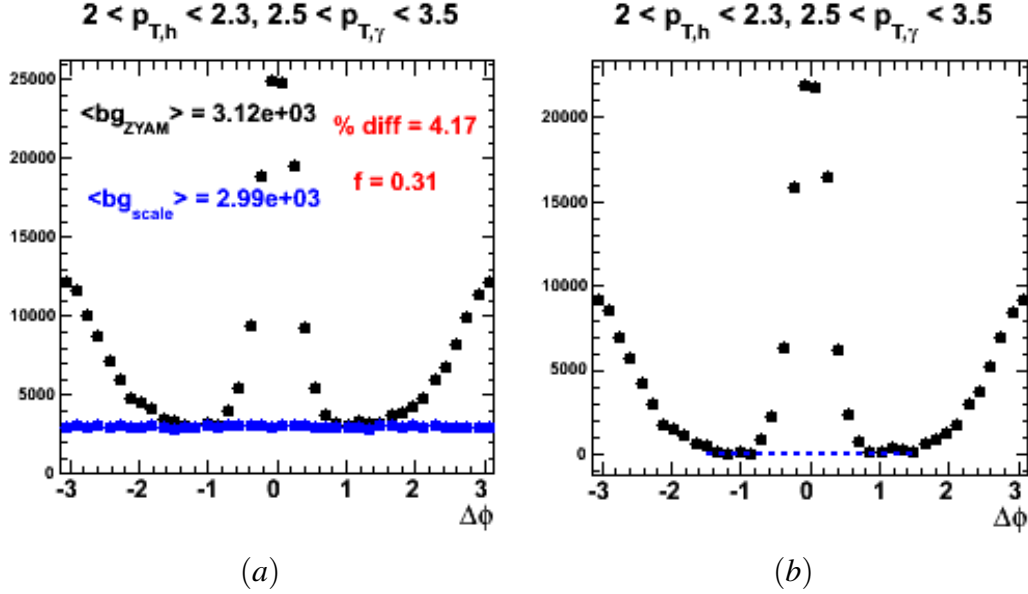


Figure 4.20: (a) The $\Delta\phi$ distribution for hadron-photon pairs, $2 < p_{T,h} < 2.3$ GeV/c and $2.5 < p_{T,\gamma} < 3.5$ GeV/c (black), and event background (blue), with the scale (f) applied shown. The scaled background level and ZYAM background level are shown, as well as the % difference. (b) The $\Delta\phi$ distribution with the scaled background subtracted, with a blue dashed line showing zero yield.

ZYAM, in the region where there are good statistics for estimating the ZYAM background level, both suggests that the ZYAM assumption does not introduce a significant bias in estimates of the background and gives some confidence that absolute normalization can work in the low background environment of $p + p$ collisions. It is important to note that while the difference in the two methods does become large at higher p_T , this is the region where the ZYAM assumption has a large uncertainty due to fluctuations in the limited statistics background in real events. In fact, this increase in the ZYAM uncertainty is one of the motivating factors for the development

$p_{T,\gamma}$ (GeV/c)	$p_{T,h}$ (GeV/c)							
	2 – 2.3		2.3 – 2.8		2.8 – 3.6		3.6 – 5	
	f	diff _Z	f	diff _Z	f	diff _Z	f	diff _Z
1.5 – 2.0	0.465	0.010	0.395	0.038	0.307	0.087	0.206	0.170
2.0 – 2.5	0.395	0.014	0.331	0.01	0.235	0.035	0.144	0.160
2.5 – 3.5	0.310	0.042	0.251	0.030	0.158	0.110	0.084	0.250
3.5 – 5.0	0.228	0.087	0.163	0.083	0.082	0.240	0.038	0.450
5.0 – 8.0	0.142	0.049	0.085	0.087	0.035	0.380	0.013	0.610
8.0 – 15	0.092	0.160	0.046	0.090	0.021	0.360	0.006	0.330

Table 4.2: Event background scale for all $p_{T,h}$ (GeV/c) and $p_{T,\gamma}$ (GeV/c), and the relative difference between the background level from this method and ZYAM (Z).

of the Absolute Normalization method.

Understanding systematic uncertainties in such a method is challenging, given the nature of the method. However, as with the ZYAM method, the validity of the assumptions that go into the determination of the background does not define the systematic uncertainty. Nevertheless, many of the steps for estimating the non-jet background, such as the removal of the jet yield from the Minbias sample, as well as determining the conditional yield from triggered data, can lead to systematic variations in the final result. The jet yield in MB within the hadron trigger p_T range used, as well as for photons in the p_T range with good statistics, is never more than 10%. Therefore, the 10% uncertainty on the estimate of the tagging efficiency (based on the uncertainty in the single particle efficiency) will lead to a < 1% uncertainty in f . An additional uncertainty resulting from the use of ERT data for the foreground comes from the fact that the p_T and SM dependent trigger efficiency can distort the mean p_T within a given bin, most notably at low photon p_T . Comparing the results for f using Minbias data to determine the conditional

yield with and without also requiring the ERT 4x4c trigger to fire leads to a total variation in f of 5% in the lowest photon p_T bins, which drops to 1% above $p_{T\gamma} \approx 2.5$ GeV/c. Because the low p_T points determine the form for the fits to the background scale, the total systematic uncertainty for f is set at 5% independent of p_T .

4.3 Efficiency corrections

Determining either the per-event yields for jet pairs, or associated photon yields per hadron trigger, requires first correcting for the detector efficiency. In the case of per trigger yields, in principle only the photon efficiency corrections are necessary, as the hadron efficiency will cancel when normalized by the number of hadron triggers. However, for combined Run 5 and Run 6 data sets, where the hadron efficiencies will not be identical, the hadron efficiencies are still necessary:

$$N_{h,total} = \int \frac{N(p_{T,h})_{h,Run\,5}}{\epsilon(p_{T,h})_{h,Run\,5}} + \int \frac{N(p_{T,h})_{h,Run\,6}}{\epsilon(p_{T,h})_{h,Run\,6}}. \quad (4.19)$$

Single particle efficiencies are determined using PISA, which is a PHENIX specific application of GEANT, to simulate charged particles propagating through the detector, as well as particles showering in the EMCAL. The input for PISA, in the case of hadron efficiencies, is single charged pions, protons and kaons separately run through the simulation and recombined to obtain the final efficiency. For photons the single particle efficiency was determined along with the tagging efficiency for decay photons, described in 5, where simulations of the full event were neces-

sary. In both cases, the full reconstruction process for real data is applied to the PISA output, as well as to all analysis cuts described in Section 4.1. The resulting efficiencies are the ratio of reconstructed hadrons or photons that pass all the analysis cuts to the total number of hadrons or photons generated initially, in the same η range. To ensure that the reconstructed hadrons and photons really came from the original input, the additional requirement is made that reconstructed tracks match an input hadron with $\Delta p/p = 20\%$ and clusters match a photon within a radius of 0.1 rad .

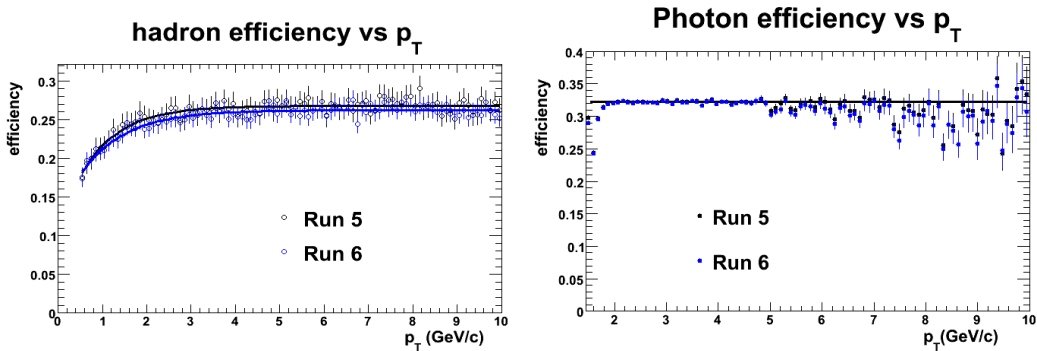


Figure 4.21: Single particle efficiencies for hadrons(right) and photons(left) as a function of particle p_T (GeV/c) for Run 5 (black) and Run 6(blue).

Comparisons of calibration parameters for both hadrons and photons between simulation and data are made to ensure that the simulation is accurately reproducing the data. In the case of hadrons, the distribution for matching variables, such as the projection of reconstructed tracks in the PC3, are compared. The distribution of track projections around the PC3 hit in data is fit with a Gaussian - or often the sum of two Gaussians - which is then used to recalibrate the PC3 hit position and the

width of the distribution, such that two or three sigma cuts on the distance between the hit and the track projection can be applied. It was found that some recalibration of the PC3 matching in PISA was also necessary to reproduce the same behavior seen in the data [133; 134]. In the case of photons, comparisons were made of the reconstructed π^0 peak position and width for each sector. An additional energy smearing of 3% in the Pb-scintillator and 5% in the Pb-glass was required to match simulation with data. Although this smearing has almost no impact on the single cluster efficiency in the p_T range used for this analysis, it is important when using PISA to determine the efficiency for reconstructing π^0 and η decays.

Those efficiencies are plotted in Figure 4.21 as a function of p_T . For hadrons the fit used was of the form $A + Be^{Cp_T}$. For photons the dip seen below p_T of about 2 GeV/c is an artifact of a filter applied to the PYTHIA data used; therefore, a flat line fit was applied. The fits shown are used to make the final efficiency corrections, to minimize the effect of statistical fluctuations. In both cases a scale uncertainty of $\sim 10\%$ is applied based on variations between PISA and data in the local particle distribution within the DC, PC3 [134] for hadrons, and the EMCAL for photons.

4.3.1 Triggered data sets

As discussed previously, the ERT4x4c trigger condition is used to increase the rate of recorded jet events while data are taken. Using triggered data introduces a bias associated with the behavior of the trigger that must be corrected to obtain invariant physics results. In the case of the ERT4x4c trigger, the bias is primarily in p_T distribution for particles that fire the trigger, but dead or masked off trigger tiles can

also lead to differences in overall event rates.

4.3.1.1 Photon p_T corrections

The hardware threshold for the ERT4x4c trigger is 1.4 GeV, meaning that the trigger will fire if that much energy is deposited in a 4x4 tower block. In practice, the trigger information is maintained on a super module (SM) level, so any clusters falling with a SM containing a 4x4 tower block that fired the trigger are considered to have fired the trigger. In practice, there will be a turn on curve for the trigger around the nominal threshold energy, leading to a strong momentum dependence for the trigger efficiency until well above that threshold value. The efficiency is determined using MB data, comparing the p_T distribution for MB photons that also fire the 4x4c trigger to that of all MB photons:

$$\epsilon_{\text{ERT}}(p_{T,\gamma}) = \frac{N_{\text{MB\&ERT4x4c}}^{\gamma}(p_{T,\gamma})}{N_{\text{MB}}^{\gamma} \cdot (p_{T,\gamma})} \quad (4.20)$$

Figure 4.22 shows the resulting ERT4x4c efficiency, fit using a fermi function. As expected, the efficiency at the threshold energy is about 50%, and it plateaus near 2.0 GeV/c. If this efficiency measurement is restricted to only those SMs that were not masked out during data taking, the plateau should be at 100%. In this case that restriction is not made, and one can see that unused SMs lead to a 20% loss in overall trigger efficiency.

The efficiency with which a given SM fires the trigger will also vary, as a result of dead areas as well as noisy regions that cannot be used for the trigger condition.

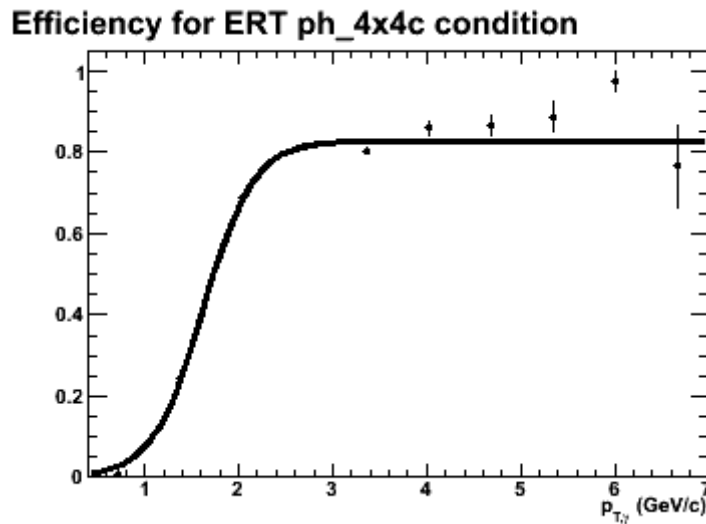


Figure 4.22: ERT4x4c efficiency for photons vs. $p_{T,\gamma}$ (GeV/c).

Generally this SM dependence is averaged, although, the EMCAL sectors are often studied separately. In the case of single particle measurements, averaging is sufficient; however as discussed previously, the variations between super modules can affect the acceptance for ERT photons in ways that distort the $\Delta\phi$ acceptance for hadron-photon pairs. Again, if the variation were in overall efficiency alone, this effect should be minor. However, for photons with $p_T \lesssim 2.5\text{GeV}/c$ the turn on for the trigger leads to a significant p_T dependence in the efficiency which is not constant between SMs. This effect is shown in Figure 4.23, where variation in trigger turn on of as much as $\sim 20\%$ between super-modules. There is also large variation in the steepness of the turn on curve. The masked off SMs show up as cases where no fit was made; correcting for the total p_T independent ERT efficiency accounts for these cases. The total ERT efficiency is determined by determining the average

p_T integrated SM efficiency after the p_T dependent correction is applied, including masked off SMs; it was found to be 95% for both runs.

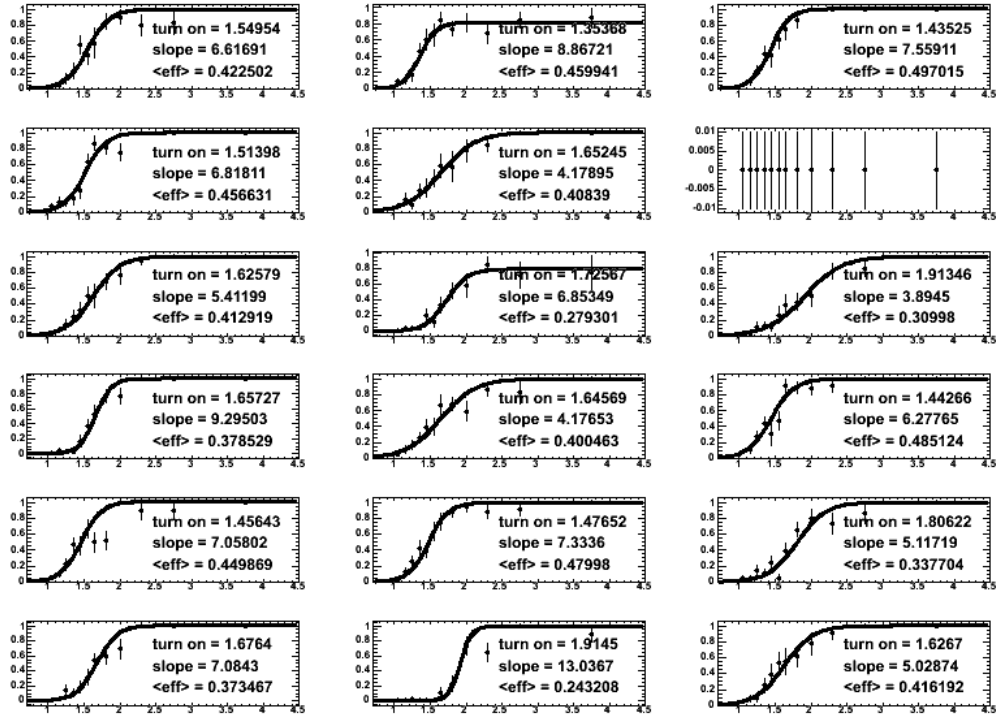


Figure 4.23: ERT4x4c efficiency for all super-modules in sector 0 vs. $p_{T,\gamma}$ (GeV/c).

4.3.1.2 Hadron trigger corrections

For this analysis, where the analysis trigger is not the same as the hardware trigger, quantities such as per-trigger yields will include an additional trigger bias. The firing of the ERT4x4c trigger, which most often occurs as the result of a high p_T photon, will artificially enhance the rate of photons per trigger hadron as a result of the much higher probability of a photon being in the event relative to a true mini-

mum bias sample of events. To correct for this bias, the rates of hadron triggers are compared in MB events, with and without the condition that the ERT4x4c trigger fire. Figure 4.24 shows the p_T dependent yield of hadrons in MB events with (red) and without the ERT4x4c trigger also firing. The figure also shows the p_T dependent ratio, as well as the ratio of the average number of trigger hadrons within the full p_T range (2.0 - 5.0 GeV/c) in ERT4x4c events versus MB events.

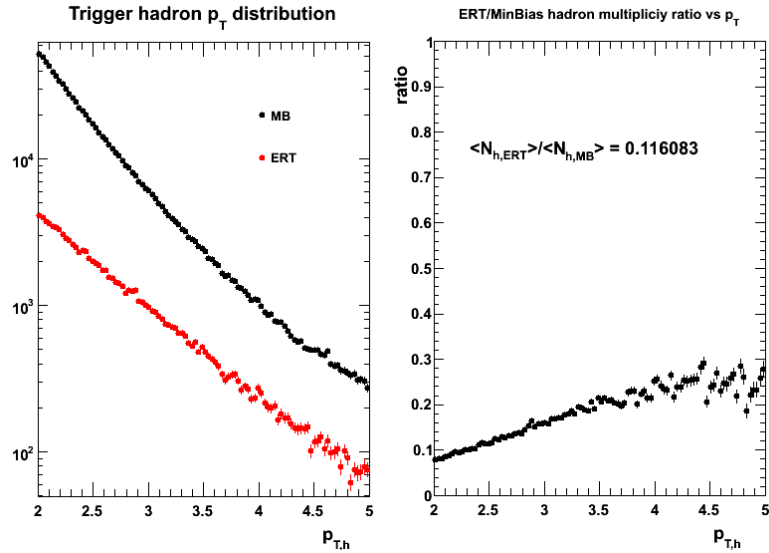


Figure 4.24: Left: ERT4x4c (red) and MB (black) hadron p_T distribution. Right: Ratio of total count of ERT4x4c to MinBias hadrons as a function of hadron p_T and the ratio of the total number of hadrons integrated over p_T within the range shown.

Scaling the number of ERT trigger hadrons by the inverse of $\frac{\langle N_{h,ERT} \rangle}{\langle N_{h,MB} \rangle}$ gives the unbiased number of trigger hadrons for obtaining the invariant per-trigger yields for each trigger p_T bin. The values determined for $\frac{\langle N_{h,ERT} \rangle}{\langle N_{h,MB} \rangle}$ for each hadron trigger bin are listed in table 4.3.1.2 for both Run 5 and Run 6, differences in the ERT efficiency between the two runs leading to a slight difference in the relative rate of

ERT trigger hadrons.

$p_{T,h}$ (GeV/c)	2.0 - 2.3	2.3 - 2.8	2.8 - 3.6	3.6 - 5.0
Run 5 $\frac{\langle N_{h,ERT} \rangle}{\langle N_{h,MB} \rangle}$	0.1135	0.1475	0.2032	0.2674
Run 6 $\frac{\langle N_{h,ERT} \rangle}{\langle N_{h,MB} \rangle}$	0.0861	0.1152	0.1650	0.2096

4.3.1.3 Test of correlated bias

The use of the ERT4x4c trigger for correlated pair measurements introduces the possibility of an additional trigger bias that can distort the $\Delta\phi$ distribution for hadron-photon pairs. The possibility that both the hadron and photon deposit energy in the EMCAL within the same supermodule makes it possible for the hadron to effectively enhance the rate for the trigger firing for photons with p_T below 2.5 GeV, where the trigger has not yet saturated. Figure 4.25 shows a comparison of the near-side ($|\Delta\phi| < 0.7$) ERT4x4c and MB $\Delta\phi$ dependent per-trigger yields for photons with p_T from 1.5 - 2.0 GeV/c associated with trigger hadrons from 2.0 - 2.3 GeV/c with all the efficiency and trigger bias corrections applied. This comparison shows that any trigger effects on the shape are negligible.

4.4 Extracting physics beyond per-trigger yields

The assumption that by triggering on high- p_T hadrons a jet is being selected suggests that after subtraction of the underlying event background, normalizing the yield of hadron-photon pairs by the total number of trigger hadrons is similar to

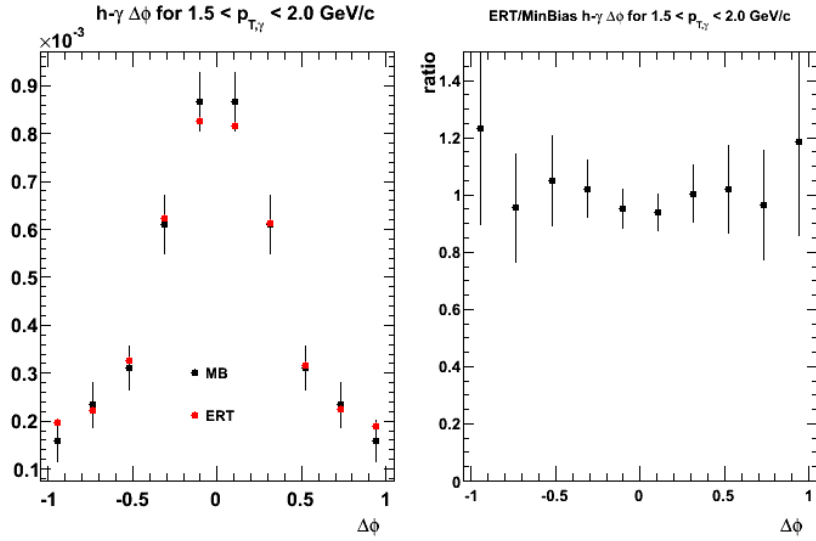


Figure 4.25: Left: ERT4x4c (red) and MB (black) hadron-photon $\Delta\phi$ dependent per-trigger yields for hadrons from 2.0-2.3 GeV/c and photons from 1.5-2.0 GeV/c. Right: Ratio of ERT4x4c to MinBias hadron-photon per-trigger yields.

obtaining the yield of photons in jets. The per-trigger distribution of photons is therefore an invariant quantity that should describe the physics of photons produced as part of a jet, both in terms of the jet shape measured through $\Delta\phi$ and p_{out} distributions, and the total per-trigger yields. To obtain the full per trigger yield for associated photons from the same jet as the hadron, the near-side $\Delta\phi$ yield is integrated over. Ideally this integral would cover the full near-side range, from $-\pi/2$ to $\pi/2$. However limiting the integral to $|\Delta\phi| < 0.7$ reduces the uncertainty in the final yield due to the fluctuations near $\pi/2$, where the acceptance is worst. Although such yields are a proxy for the per-jet yields, there is not a direct one-to-one mapping between trigger hadrons and jets, as the hadron is also an individual fragment of the original parton.

4.4.1 Pair cross-sections

Per trigger yields are a good first step, and in the case of heavy-ion analyses, comparisons of such yields between $p + p$ and $A + A$ are rich with information about the underlying physics. However, such measures are generally more comparable with theory, in the case of di-jet studies, when focusing on the away-side yields. A more theoretically meaningful quantity, although still complex since it involves the fragmentation function for both the trigger hadron and associated photon, is the jet-pair cross-section. Starting with the per event pair yields rather than per trigger photon yields, this again involves defining a range in $\Delta\phi$ for the pair over which to integrate.

Going from a per-event yield to the invariant cross-section requires determining both the efficiency of the triggers used to record events and the fraction of the full inelastic cross-section those triggers identify. The per event yields are determined simply by multiplying per trigger yields by the number of trigger hadrons per event. This calculation already includes the single particle efficiency corrections for photons and hadrons, as well as the ERT trigger efficiency correction for the photons, described in more detail in Section 4.3. What remains is to correct for the minimum bias trigger efficiency for events containing hadron-photon pairs from jets, as the MB trigger (BBCLL1) is required in coincidence with the ERT. During running the BBCLL1 trigger is scaled down so not every event is recorded. The scale-down factor is determined by the luminosity for a given run, so when determining cross-section using the number of minimum bias events, the average scale-down must be included. The ERT triggers are generally not scaled down; however, for the high-

est beam intensities the 4x4c trigger, which has the lowest energy threshold, was scaled down such that only one out of every two or three events that fired the trigger were recorded. Therefore, although the correction is small, an additional ERT scale-down correction must be included. The final step is to determine the fraction of the inelastic cross-section measured by the BBCLL1, which is estimated separately using Vernier scans [135] and was determined to be about $23 \text{ mb} \pm 5\%$ in Run 5 and Run 6 [136]. The final pair cross-section for hadron-photon pairs is then:

$$\frac{1}{(2\pi)^2 p_{T,\gamma} p_{T,h}} \frac{d^4\sigma}{dp_{T,\gamma} dp_{T,h} d^2\eta} = \frac{\sigma_{BBCLL1}}{\epsilon_{BBCLL1} \langle S_{BBCLL1} \rangle N_{evt,BBCLL1}} \frac{\langle S_{ERT4x4c} \rangle d^4 N_{pairs}}{(2\pi)^2 p_{T,\gamma} p_{T,h} dp_{T,\gamma} dp_{T,h} d^2\eta}. \quad (4.21)$$

The efficiency for the BBCLL1 depends on the type of events being selected. Thus, in the case of this analysis it is determined using events that yield a hadron-photon pair that passes all analysis cuts. The possibility that the pair was not part of a jet is reduced by requiring $|\Delta\phi| < 1.0$, and the effect of residual background was studied by varying this angular cut. Applying these requirements, along with the 30cm vertex cut, to events firing the ERT4x4c trigger alone and comparing with events where the ERT4x4c and BBCLL1 triggers both fired gives the BBCLL1 efficiency:

$$\epsilon_{BBCLL1} = \frac{N_{evt}(ERT4x4c \& BBCLL1)}{N_{evt}(ERT4x4c)}. \quad (4.22)$$

As with the fractional BBCLL1 cross-section, this efficiency was determined separately for Runs 5 and 6 and found to be 81% and 78%, respectively. This result

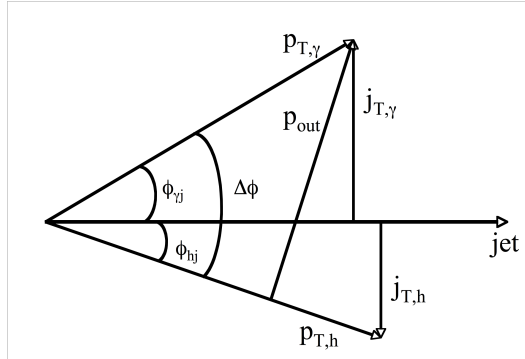


Figure 4.26: p_{out}

is consistent with efficiency measurements for events with high $p_T \pi^0$ s and η s [134].

The dependence of these on event selection, based on the angular restriction applied to pairs, as well as on the p_T of the pair, was estimated by varying the $\Delta\phi$ restriction from 1 to 0.5, as well as by studying the hadron and photon p_T dependence. It was found that the efficiency varied $\approx 5\%$, which is then included as an overall scale uncertainty on the final result. Table 4.3 shows each of the compiled each of the inputs from Run 5 and 6 that went into the final pair cross-section.

Table 4.3: Minimum Bias BBC inputs to determining the invariant hadron-photon pair cross-section

	σ_{BBCLL1}	$\langle S_{BBCLL1} \rangle$	$N_{evt,BBCLL1}$	ϵ_{BBC}	$\langle S_{ERT4x4c} \rangle$
Run 5	$23.0 \text{ mb} \pm 10\%$	32.19	1749944617	$0.81 \pm 5\%$	1.0
Run 6	$22.9 \text{ mb} \pm 5\%$	423.27	421437207	$0.78 \pm 5\%$	1.04

4.4.2 p_{out} and j_T

As Section 2.4.2.2 described, when using two-particle correlations, parameters such as p_{out} help to quantify information about the jet shape. For this analysis, p_{out} is

defined as the component of the associated photon p_T perpendicular to the trigger hadron p_T , projected along the azimuth for simplicity:

$$p_{\text{out}} = p_{T,\gamma} \sin \Delta\phi_{h-\gamma}, \quad (4.23)$$

as illustrated in Figure 4.26. This figure also illustrates j_T , the component of a particle's momentum perpendicular to the actual jet axis. To measure p_{out} directly in PHENIX, we use the method described in 4.2.1 of applying an acceptance weighting to each hadron-photon pair.

For pairs coming from the same jet, so correlated on the near-side in $\Delta\phi$, p_{out} is often considered to be equivalent to j_T , which is the observable more directly related to the jet, and comparable with theory. However, this is an approximation. In general, we will see that while this is true for the special case of identical particles, it relies on either the assumption of equivalence of the j_T for the two particle types or a large p_T imbalance between the trigger and associated particles. Even when attempting to be more explicit about the true relationship between p_{out} and j_T , the assumption that j_T is small compared to p_T - that is, that the angle between the particle and the jet axis is small - is necessary to obtain a simple relationship. Eq. (4.24) derives the relationship to first order in j_T/p_T .

$$\begin{aligned}
p_{\text{out},\gamma} &= p_{\text{T},\gamma} \sin(\Delta\phi) \\
&= p_{\text{T},\gamma} \sin(\phi_{hj} + \phi_{\gamma j}) \\
&= p_{\text{T},\gamma} \left(\sin(\phi_{hj}) \cos(\phi_{\gamma j}) + \cos(\phi_{hj}) \sin(\phi_{\gamma j}) \right) \\
&= p_{\text{T},\gamma} \left(\frac{j_{\text{T},h}}{p_{T,h}} \cos(\phi_{\gamma j}) + \frac{j_{\text{T},\gamma}}{p_{\text{T},\gamma}} \cos(\phi_{hj}) \right) \\
&= j_{\text{T},h} \frac{p_{\text{T},\gamma}}{p_{T,h}} \sqrt{1 - \left(\frac{j_{\text{T},\gamma}}{p_{\text{T},\gamma}} \right)^2} + j_{\text{T},\gamma} \sqrt{1 - \left(\frac{j_{\text{T},h}}{p_{T,h}} \right)^2} \\
&\approx j_{\text{T},h} \frac{p_{\text{T},\gamma}}{p_{T,h}} \left(1 - \frac{1}{2} \left(\frac{j_{\text{T},\gamma}}{p_{\text{T},\gamma}} \right)^2 \right) + j_{\text{T},\gamma} \left(1 - \frac{1}{2} \left(\frac{j_{\text{T},h}}{p_{T,h}} \right)^2 \right) \\
&\approx j_{\text{T},h} \frac{p_{\text{T},\gamma}}{p_{T,h}} + j_{\text{T},\gamma}, \tag{4.24}
\end{aligned}$$

Giving

$$j_{\text{T},\gamma} \approx p_{\text{out},\gamma} - j_{\text{T},h} \frac{p_{\text{T},\gamma}}{p_{T,h}}. \tag{4.25}$$

If the j_{T} distribution for hadrons is known, by applying unfolding techniques similar to those used in full jet reconstruction measurements, the j_{T} for photons could be obtain. In the absence of the full hadron j_{T} distribution, it is still possible to obtain the $\sqrt{\langle j_{\text{T}}^2 \rangle}$ of photons directly, applying the same approximations. Again starting with the definition of p_{out} :

$$\begin{aligned}
p_{\text{out},\gamma} &= p_{\text{T},\gamma} \sin(\Delta\phi) \\
&= p_{\text{T},\gamma} \left(\sin(\phi_{hj}) \cos(\phi_{\gamma j}) + \cos(\phi_{hj}) \sin(\phi_{\gamma j}) \right).
\end{aligned}$$

Therefore the rms can be approximated as

$$\begin{aligned}
 \langle p_{\text{out},\gamma}^2 \rangle &= \left\langle p_{\text{T},\gamma}^2 \left(\underbrace{\sin^2(\phi_{hj})}_{\frac{j_{\text{T},h}^2}{p_{\text{T},h}^2}} \underbrace{\cos^2(\phi_{\gamma j})}_{\left(1 - \frac{j_{\text{T},\gamma}^2}{p_{\text{T},\gamma}^2}\right)} + \cos^2(\phi_{hj}) \sin^2(\phi_{\gamma j}) \right) \right\rangle \\
 &= \left\langle \frac{p_{\text{T},\gamma}^2}{p_{\text{T},h}^2} j_{\text{T},h}^2 \left(1 - \frac{j_{\text{T},\gamma}^2}{p_{\text{T},\gamma}^2} \right) + \left(1 - \frac{j_{\text{T},h}^2}{p_{\text{T},h}^2} \right) j_{\text{T},\gamma}^2 \right\rangle \\
 &= \left\langle j_{\text{T},h}^2 \frac{p_{\text{T},\gamma}^2}{p_{\text{T},h}^2} + j_{\text{T},\gamma}^2 + O(j_{\text{T}}^4) \right\rangle \\
 &\approx \left\langle j_{\text{T},\gamma}^2 \right\rangle + \left\langle j_{\text{T},h}^2 \right\rangle \left\langle \frac{p_{\text{T},\gamma}^2}{p_{\text{T},h}^2} \right\rangle. \tag{4.26}
 \end{aligned}$$

The corresponding equation for the relationship between p_{out} of the hadron with respect to the photon and the hadron j_{T} is

$$\langle p_{\text{out},h}^2 \rangle \approx \left\langle j_{\text{T},h}^2 \right\rangle + \left\langle j_{\text{T},\gamma}^2 \right\rangle \left\langle \frac{p_{\text{T},h}^2}{p_{\text{T},\gamma}^2} \right\rangle. \tag{4.27}$$

Defining $x_h \equiv \frac{p_{\text{T},\gamma}}{p_{\text{T},h}}$, with a little algebra we find that we can express the photon $\sqrt{\langle j_{\text{T}}^2 \rangle}$ in terms of directly measurable quantities

$$\langle j_{\text{T},\gamma}^2 \rangle = \frac{\langle p_{\text{out},\gamma}^2 \rangle - \langle p_{\text{out},h}^2 \rangle \langle x_h^2 \rangle}{1 - \langle x_h^2 \rangle \cdot \langle 1/x_h^2 \rangle} \tag{4.28}$$

Using this - and measurable hadron-photon pair properties - the photon $\sqrt{\langle j_{\text{T}}^2 \rangle}$ can be measured directly.

4.5 Propagating uncertainties

As discussed in Section 4.2.1, hadron-photon pair yields are corrected for detector acceptance and efficiency by applying a pair-by-pair weight, w . These weights are determined using acceptance histograms calculated from the mixed $\Delta\phi$ distribution and single particle efficiencies determined from fits to data. Thus, in the case where there is only one efficiency correction,

$$w = \frac{1}{\epsilon(p_T)Acc(\Delta\phi)}$$

. Each of these will have a corresponding uncertainty that must be included as part of the resulting uncertainty on the pair distribution. The acceptance histograms will have a small non-negligible statistical error, while any efficiency corrections coming from fits will include an uncertainty on the fit.

In general for histograms, where the contents of a single bin are defined as

$$N = \sum_i w_i$$

where w_i is the weight of a single entry, the statistical uncertainty is then just the square root of the sum of the weights squared. If the weights have their own uncertainty than the total variance for a given bin is

$$\sigma^2 = \sum_i w_i^2 + \sum_i (\delta w_i)^2 , \quad (4.29)$$

assuming the uncertainties on the weights themselves are uncorrelated. This is

a reasonable assumption in this case, because these uncertainties come from independent inputs. The uncertainty on a given weight is

$$\begin{aligned} (\delta w)^2 &= \sum_i \left(\frac{dw}{d\epsilon_i} \delta \epsilon_i \right)^2 + \left(\frac{dw}{d(Acc)} \delta (Acc) \right)^2 \\ &= \sum_i \left(\frac{w}{\epsilon_i} \delta \epsilon_i \right)^2 + \left(\frac{w}{Acc} \delta (Acc) \right)^2 \end{aligned} \quad (4.30)$$

Chapter 5

Extracting the fragmentation photon signal

The details for measuring correlated pairs of hadrons and photons from jets described in the previous chapter comprise the first step toward direct measurements of fragmentation photons. Inclusive hadron-photon pair measurements contain a combination of photons produced through mesonic decays and the fragmentation photons we are interested in studying. Eq. (5.1) demonstrates this point for the $\Delta\phi$ -dependent per-trigger yields, and the relations will be the same for the per-event pair yields and p_{out} distributions.

$$\frac{1}{N_{\text{trig}}^h} \frac{dN^{h-\gamma_{\text{inc}}}}{d\Delta\phi} = \frac{1}{N_{\text{trig}}^h} \frac{dN^{h-\gamma_{\text{dec}}}}{d\Delta\phi} + \frac{1}{N_{\text{trig}}^h} \frac{dN^{h-\gamma_{\text{frag}}}}{d\Delta\phi} \quad (5.1)$$

To extract the fragmentation photon signal, the yield from decay photons must be estimated and subtracted from the inclusive measurements. Almost all photons produced will be from these mesonic decays, making it very important to have a precise determination of this decay yield. This chapter will focus on the steps

necessary for identifying decay photons, as well as the inherent uncertainties in the method. Many of the details of determining the full decay photon yield depend not only on the momentum of the associated photon, but also on that of the trigger hadron - as will become clear in the discussion that follows. For clarity, much of the discussion and evaluation of the various steps involved will focus on the example of a single hadron-photon p_T bin.

5.1 Estimating the decay photon yield

Most decay photons ($\sim 80\%$) will come from the lightest meson, the π^0 . As discussed in 3.4, the EMCal in PHENIX is well suited for directly reconstructing π^0 s, making it possible to identify (tag) photons produced from such decays with a reasonable level of efficiency (see Section 5.2.1). Using tagging, then, to determine the contribution from π^0 photons is the first step to estimating the total decay yield. Many direct photon measurements find this sufficient, estimating the remaining decay background by applying a p_T dependent multiplicative factor to the π^0 decay. However, as will be discussed in more detail in Section 5.1.1, with correlation measurements this approach leads to a large systematic effect on the shape of the decay photon distributions. Instead, photons from η decays are tagged separately, and inclusion of the remaining decay contribution is done by applying a multiplicative factor to the γ_η yield. The final decay yield is then:

$$\frac{1}{N_{trig}^h} \frac{dN^{h-\gamma_{decay}}}{d\Delta\phi} = \frac{1}{\epsilon_{\pi^0-tag}} \frac{1}{N_{trig}^h} \frac{dN^{h-\gamma_{\pi^0-tag}}}{d\Delta\phi} + (1 + R_{h/\eta}) \frac{1}{\epsilon_{\eta-tag}} \frac{1}{N_{trig}^h} \frac{dN^{h-\gamma_{\eta-tag}}}{d\Delta\phi}, \quad (5.2)$$

where $R_{h/\eta}$ is the ratio of heavier mesonic decay photons to η photons. For inclusive decay photons, the ratio determined from PYTHIA is 0.3 and constant in photon p_T . However, a full study of the method ultimately found that for near-side hadron-photon pairs, $R_{h/\eta}$ depends on both the trigger hadron and associated photon, as will be described in detail in Section 5.3.5.

5.1.1 Testing the method

Fragmentation photons are expected to comprise only a very small portion of the inclusive photon yield. As a result, whatever method is used to remove the decay background must be carefully tested. Using the PYTHIA event generator, we can compare the generated decay yield with what is estimated. The first attempt was based on the assumption that photons identified as coming from π^0 decays could be used to estimate the full decay background. In this case,

$$\frac{1}{N_{trig}^h} \frac{dN^{h-\gamma_{decay}}}{d\Delta\phi} = (1 + R_{h/\pi^0}) \frac{1}{\epsilon_{\pi^0-tag}} \frac{1}{N_{trig}^h} \frac{dN^{h-\gamma_{\pi^0-tag}}}{d\Delta\phi}, \quad (5.3)$$

where R_{h/π^0} is determined from PYTHIA and depends on the p_T of the decay photon. This relation can then be applied to π^0 photons in PYTHIA and compared to the full decay yield. Figure 5.1 (left) shows the $\Delta\phi$ distribution for hadron-photon pairs for all decay photons (black) and the estimate obtained using π^0 decay photons (blue), for the lowest photon p_T bin used in the full analysis. Also quoted in the

figure is the systematic difference between the two distributions within $|\Delta\phi| < 1.0$:

$$\frac{\left| \int_{-1.0}^{1.0} \gamma_{decay} - \int_{-1.0}^{1.0} R_{h/\pi^0} \gamma_{\pi^0} \right|}{\int_{-1.0}^{1.0} \gamma_{decay}}. \quad (5.4)$$

From this we find that the integrated yield measured for decay photons by this method would differ from the true yield by only 1%, making it clear why this is generally considered sufficient. However, looking at the ratio of the two $\Delta\phi$ distributions, the bottom plot in figure 5.1, we find that the variation between the estimated yield and the true yield is actually more than 10% as a function of $\Delta\phi$. This level of systematic effect would make it impossible to resolve the fragmentation photon signal, and would destroy any ability to determine further pair properties dependent on the shape of these distributions.

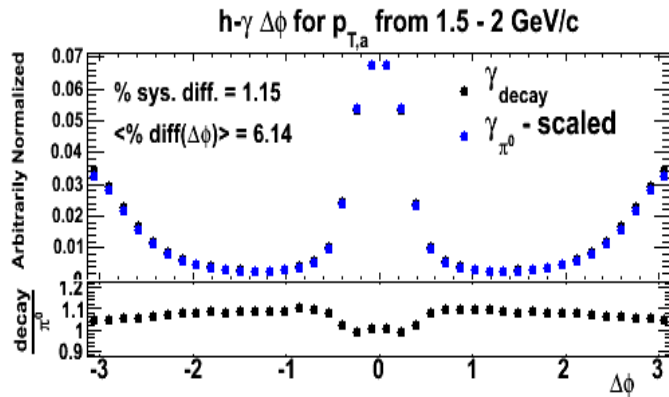


Figure 5.1: The top plot shows the $h - \gamma$ distributions for all PYTHIA generated decay photons in black and scaled π^0 photons (equation (5.3)) in blue. The ratio of the distributions is plotted below it.

To move forward it is therefore necessary to reexamine the choice to identify

only π^0 photons. Looking at Figure 5.2, which shows the $\Delta\phi$ distributions for $h - \gamma$ pairs for π^0 photons (black) and η photons (blue), it is clear that the η photon distribution is more broad than that of π^0 photons. The γ_η distribution is scaled up for easier visual comparison. The wider opening angle for η decays suggests that this is not surprising; however, the method described above would fail to account for this difference, resulting in the larger systematic effect in $\Delta\phi$ dependent measurements.

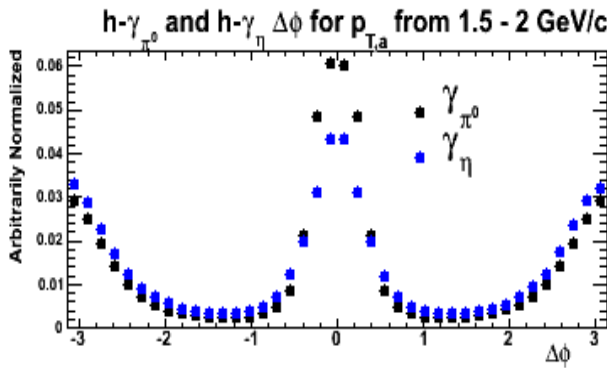


Figure 5.2: $\Delta\phi$ distributions for $h - \gamma$ pairs, for π^0 decay photons in black and η decay photons in blue.

After the π^0 , the next largest source of decay photons, 10%, is from $\eta \rightarrow \gamma\gamma$. As with π^0 decays, it is possible to identify such photons to estimate the γ_η decay contribution. We can then use the η decay photon distributions to estimate heavier decays, effectively going a step closer to an exact measurement of all decay photons. This leads us to Eq. (5.2) for estimating the decay photon yield. Again, this estimate of the decay yield can be compared with the full decay yield generated by PYTHIA. Figure 5.3 (left) shows the $\Delta\phi$ distribution for hadron-photon pairs for all decay photons (black) and the estimate obtained using π^0 and η decay photons (blue), again for the lowest photon p_T bin used, as well as the systematic difference

((5.4)). The difference in the integrated yields is now much less than 1%, a clear improvement. However, the real test comes from again looking at the ratio of the yields, the lower plot in the same figure, where the $\Delta\phi$ dependent variation is now $< 1\%$.

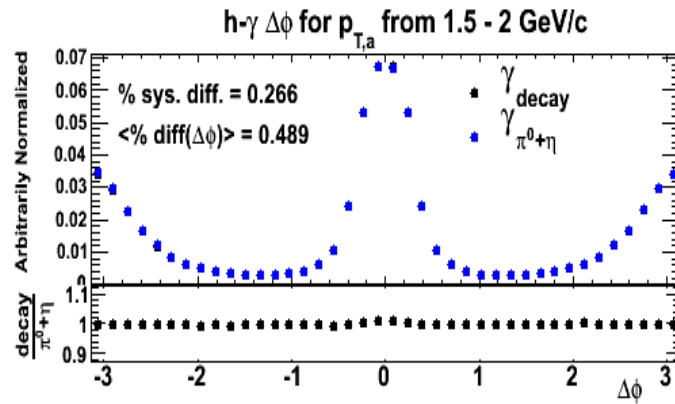


Figure 5.3: The top plot shows the $h - \gamma$ distributions for all PYTHIA generated decay photons in black and the combined π^0 and scaled η photons (Equation (5.2)) in blue. The ratio of the distributions shown is plotted below.

In principle, one could continue along in this vein, directly tagging photons produced from the less common heavier mesonic decays. However, the decay channels become more complex, and the decay opening angles wider, making the efficiency with which these decay photons are identified much lower. Therefore, practically speaking there is no gain in such attempts, as the uncertainties related with identifying such photons will dominate over any improvement in the method itself.

5.2 Tagging π^0 and η decay photons

Identifying photons produced from $\pi^0 \rightarrow \gamma\gamma$ and $\eta \rightarrow \gamma\gamma$ decays begins with the determination of the invariant mass distributions for photon pairs. Pairs produced from a π^0 or η decay will produce a peak in the invariant mass at the mass of the parent particle, and they can be tagged as coming from that decay. For this analysis, pairs of photons are made by combining photons that fire the ERT trigger with all other photons in the event that pass the quality cuts described in 4.1.3. The distinction must be made here between the ERT photon being correlated with the trigger hadron, and the photon with which it is being paired, which we will call the pair photon for clarity. These pair photons are required to be above some minimum energy, or in practice some minimum p_T , which is 400 MeV/c in this case. How the results vary based on this minimum p_T restriction is a useful measure of the inherent uncertainties in this tagging method.

As most photons in an event will come from π^0 decays, the distribution of pair masses will be dominated by the peak around the mass of the π^0 , ~ 135 MeV/c². The width of the measured peak, as well as the precise mass it centers around, result from the energy resolution of the EMCAL. To tag π^0 photons, the mass peak is fit with a Gaussian (see Figure 5.10), and photon pairs that fall within 3σ of the mean are identified as π^0 pairs. The energy resolution of the detector will depend on the p_T of the clusters, translating into a p_T -dependence in the peak position and width. Figure 5.4 shows both the mass peak positions (left) and peak width (right) as a function of the reconstructed π^0 p_T . When determining how to apply the 3σ mass

window used for identifying π^0 pairs, this p_T dependence is crucial.

To help reduce the combinatoric background (section 5.2.2), additional restrictions on the pair are used. The most basic requirement is that all photon pairs must come from the same arm of the EMCal. In the case of η pairs, where the background from random photon pairs is large, an additional restriction is made that the energy asymmetry between the photons be less than 0.7, as most non-decay pairs will have larger asymmetries. These restrictions, combined with the minimum energy cut on pair photons and the 2 or 3 σ restrictions on the pair mass, comprise the complete list of cuts placed on photon pairs. These, as well as the single photon reconstruction efficiency, will limit the ability to correctly tag a photon as coming from a decay, meaning there will be a $< 100\%$ efficiency with which decay photons are tagged.

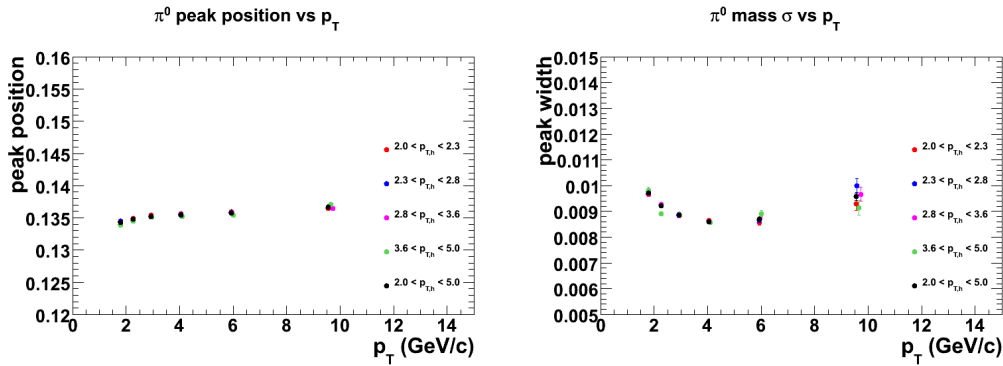


Figure 5.4: Left: π^0 peak position (GeV/c^2) vs. the π^0 p_T (GeV/c). Right: π^0 peak width vs. the π^0 p_T (GeV/c). Each of the trigger hadron p_T bins is shown.

To tag decay photons, the cut on the invariant mass of the pairs must be determined. While the actual mass of the π^0 is fixed, the measured pair mass will not be exact and will vary as a function of the pair p_T , as a result of the detector

resolution. Figure 5.4 measures the dependence of the observed π^0 peak position (invariant mass) and width on the p_T of the reconstructed π^0 . Photons in pairs that fall within a 3σ window of the measured peak position are tagged as coming from π^0 .

The condition that there be a trigger hadron of a certain momentum will bias the event sample towards higher energy hard scatterings, which will result in a harder π^0 and η spectrum. When using relatively large momentum ranges for studying the p_T dependent mass distributions, this has the potential to change the average peak position and width in a given π^0 p_T bin, although the effect should be small. Therefore, the dependence of the peak position and width was studied as a function of the hadron trigger p_T as well as π^0 p_T , as shown in Figure 5.4, to ensure that any variation was accounted for when tagging photons. A similar study was done for the η , and is shown in Figure 5.5.

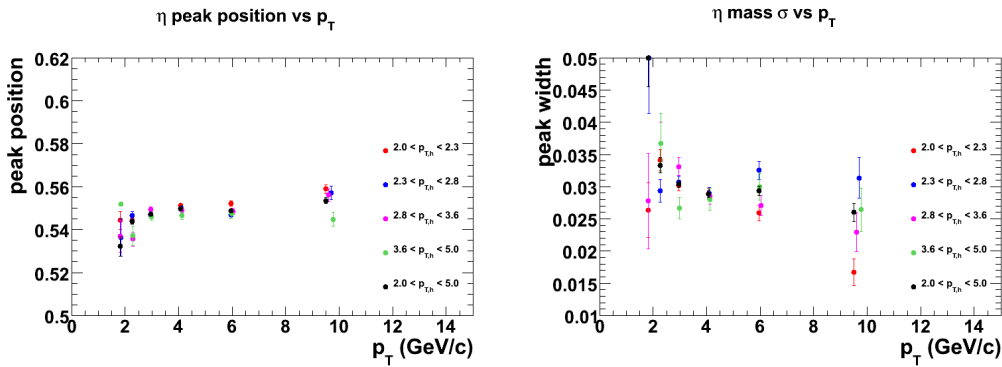


Figure 5.5: Left: η peak position (GeV/c^2) vs. the η p_T (GeV/c). Right: η peak width vs. the η p_T (GeV/c). Each of the trigger hadron p_T bins is shown.

There are two fundamental corrections that need to be applied to any tagged

photon yield. First, there is an efficiency with which photons from a decay can be correctly tagged based on the detector efficiency, acceptance, and various cuts applied to the data. One must estimate and correct for this efficiency to get the true decay yield. Second, when using combinations of all photon pairs in an event to reconstruct those pairs coming from a decay, there is a combinatoric background of random pairs that will fall within the invariant mass range chosen to tag the decay photons which will lead to falsely-tagged decay photons. These two somewhat competing effects contain all the details that make precise measurement of the decay photon yield a challenge.

5.2.1 Tagging efficiencies

To obtain the full decay photon yields, it is necessary to correct for the efficiency with which π^0 and η photons can be identified. There are many contributors to this tagging efficiency, including the cuts applied to photon pairs before they are tagged, as well as the cuts applied to individual photons. Most important is the loss of one photon in the pair if it falls outside the PHENIX acceptance or gets missed as a result of dead areas in the detector. For hadron-photon pairs, the requirement that the leading photon be associated with a trigger hadron, and the extent to which they are correlated, can affect the efficiency with which a pair photon is found. Determining the tagging efficiency in terms of both the position of the photon in the detector and the position relative to the trigger hadron ($\Delta\phi$), and then applying that efficiency as part of the pair-by-pair weight that corrects for any localized fluctuations in the overall p_T dependent efficiency could lead to systematic effects in the shape of the

decay distributions being measured.

The tagging efficiency is determined using full PISA simulations and applying efficiency corrections within each of the associated photon p_T bins used in the analysis as a function of the η and ϕ of the cluster. We use PYTHIA events as the input to PISA, rather than single particles with a flat p_T (which would obviously help with statistics at high p_T), because the p_T of the decaying π^0 and η , as well as the p_T of the hadron can all affect the tagging efficiency. In principle, weighting a flat input by the known p_T spectrum could correct for this. However, the added complication of the hadron trigger, which leads to a harder π^0 and η spectrum, as discussed previously, makes this approach non-trivial. Therefore, despite larger statistical fluctuations at high p_T that result, full events are used. To improve the available statistics as much as possible, only PYTHIA events containing a hadron with $p_T > 2$ GeV/c and a photon with $p_T > 1.5$ GeV/c are used. Again, this is in some sense applying the same trigger condition to the simulated data as is applied when using ERT trigger data.

The full 2-dimensional efficiency distributions for the lowest photon p_T bin, for both π^0 and η tagging, are shown in Figures 5.6 and 5.7 respectively. To maximize the PISA statistics available, initially no requirement is placed on the event that there be a detected trigger hadron. The effect of the hadron trigger, for each p_T bin used, is then studied and applied as an overall scale correction to the 2D tagging efficiency. Figure 5.8 shows the overall tagging efficiency as a function of photon p_T , for both the η and π^0 . Shown is the efficiency for each trigger hadron p_T range, as well as the efficiency when no requirement is made that a hadron be detected.

The effect of the hadron trigger requirement is small, but significant, resulting from the hardening of the p_T spectrum for π^0 s and η s.

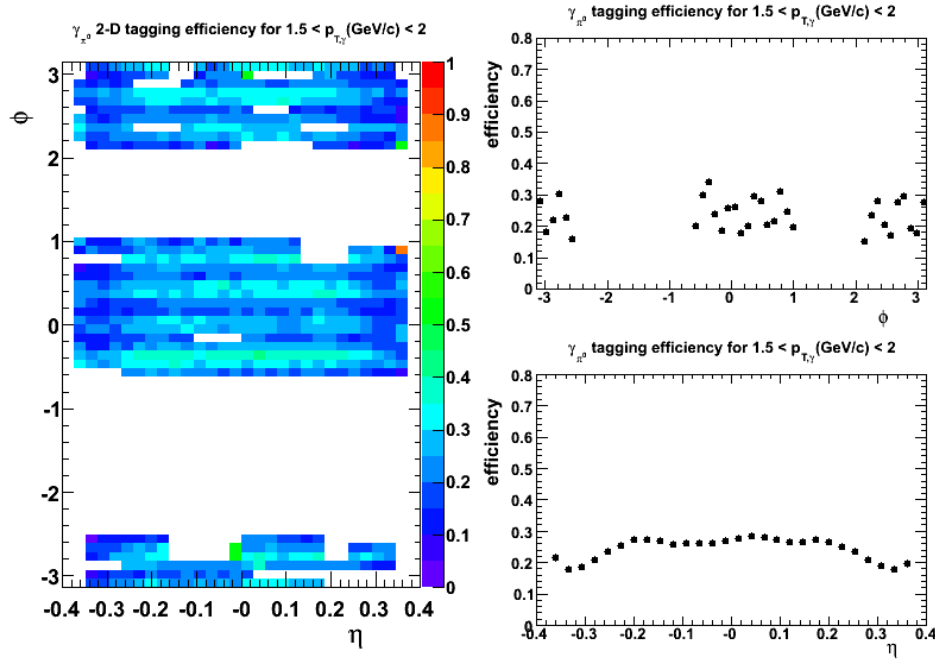


Figure 5.6: 2-D tagging efficiency for γ_{π^0} 's for the full PISA statistics, with the ϕ (top) and η (bottom) projected efficiencies on the right.

For the method used here to obtain hadron-photon pair measurements, where an acceptance and efficiency weight is applied pair-by-pair, the weight is applied to the false-tagged background as well. Eq. (5.2.1) shows that weighting the tagged foreground and background distributions separately is equivalent to applying a global tagging efficiency to determine the decay yields (either π^0 or η). The $\Delta\phi$ dependent correction will be discussed in detail in Section 5.3.5, where a full test of the final

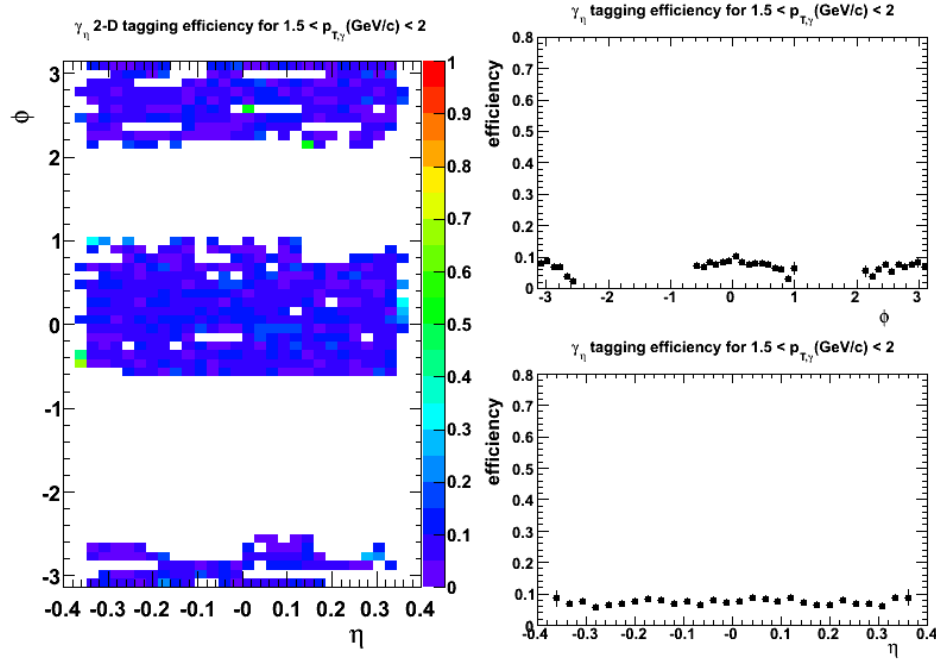


Figure 5.7: 2-D tagging efficiency for γ_η 's for the full PISA statistics, with the ϕ (top) and η (bottom) projected efficiencies on the right.

process is discussed, as this correction depends on false-tagging as well.

$$\begin{aligned}
 Y_{decay} &= \frac{1}{\epsilon_{tag}} Y_{true-tagged} \\
 &= \frac{1}{\epsilon_{tag}} (Y_{tagged} - Y_{false-tagged}) \\
 &= \frac{1}{\epsilon_{tag}} Y_{tagged} - \frac{1}{\epsilon_{tag}} Y_{false-tagged} \\
 &= Y_{tag}^{weighted} - Y_{false-tagged}^{weighted}
 \end{aligned} \tag{5.5}$$

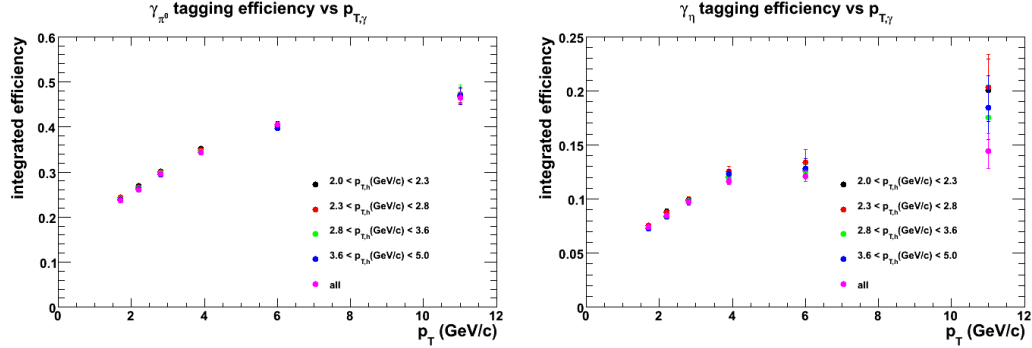


Figure 5.8: Left: Integrated tagging efficiency for γ_{π^0} 's for each hadron trigger bin, and the full PISA statistics (purple). Right: Integrated tagging efficiency for γ_{η} 's for each hadron trigger bin, and the full PISA statistics (purple).

5.2.2 The false-tagged background

Not all pairs of photons in an event will come from the same decay, or indeed any decay at all. However, when combining these pairs there is a finite probability they will still have a pair mass that falls within the π^0 or η mass window. This will lead to some number of falsely tagged photons that are not part of the real decay yield and must be subtracted from the tagged yields measured. Most of the background comes from combinatorics - completely random, uncorrelated photon pairs. This component of the background can be calculated through event mixing, similar to the method described in Chapter 4 for determining the combinatoric background. Figure 5.9 shows the invariant mass distribution for photon pairs. Pairs from the same event, shown in black, show the clear π^0 and η signal. Pairs from different events, shown in red, should reproduce the underlying random pair distribution. Although in the region under the π^0 peak the mixed pairs appear to almost match the same-event background, it is clear that this is not sufficient to account for the

full background or reproduce the background shape. This is especially true near the η peak, where the difference in the shape of the mixed pair distributions leads to a large mismatch.

Invariant mass distribution for γ pairs

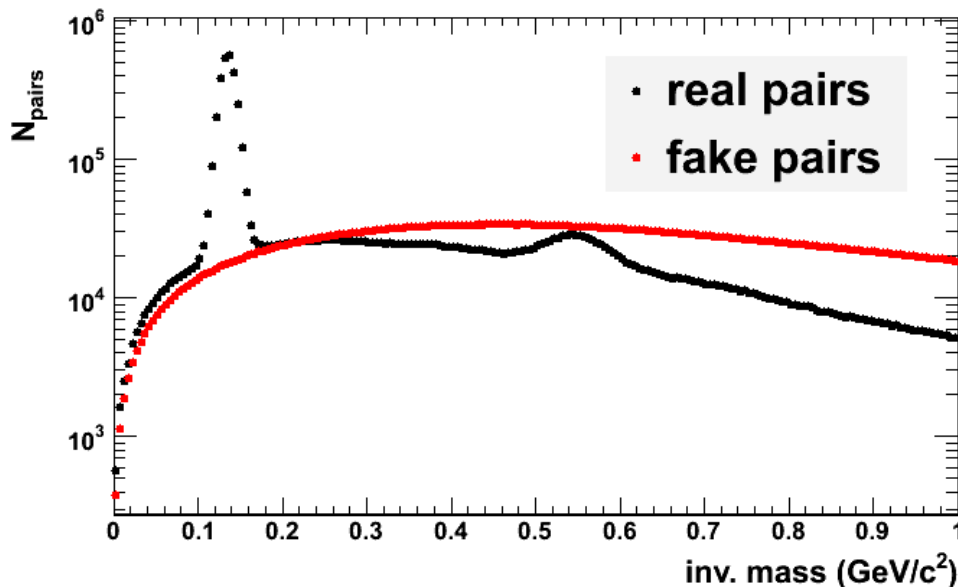


Figure 5.9: Invariant mass distribution for same-event (black) and mixed (red) pairs with the mixed pair distribution scaled by the number of events used for mixing.

There is a component of the background under the π^0 and η mass peaks that is not purely combinatoric, instead resulting from indirect correlations within the event. In the high multiplicity environment of heavy-ion collisions this would not be a concern, as the large uncorrelated background will dominate. However, in $p + p$, especially ERT triggered data where it is likely the event contains jets, the total number of particles in the event is small compared to the strength of the event correlations. These event correlations will have the effect of biasing pairs to lower

invariant masses, as they will be more correlated than truly random photon pairs.

Both the completely combinatoric and correlated backgrounds must be estimated to determine the false-tagging rate correctly. In addition, whatever method is used, for this analysis it is important to preserve the information about how the falsely tagged photons correlate with the trigger hadron. It is therefore necessary to use a method that allows us to tag photons - and estimate the number of false tags - in the same event as the trigger hadron to preserve the $\Delta\phi$ dependence for hadron-photon pairs.

5.2.3 Minimum bias event mixing

As with hadron-photon correlations, the combinatoric background from random pairs can be determined through event mixing. In the case of π^0 and η reconstruction from ERT trigger data, photons from the trigger data set are combined with photons from other events. In principle ERT events could be used for mixing; as long as the photons used to make mixed pairs come from different events, the random background should be reproduced. However, as Figure 5.9 illustrates, the event correlated background will distort the underlying pair background in ways not reproducible by mixing. This effect is exacerbated by the use of ERT events for mixing, where the jet correlations in the mixed event will bias mixed pairs towards larger invariant masses, while real pairs are biased towards lower invariant mass. In addition, the ERT efficiency leads to a non-flat average spatial distribution of photons, which is unrealistic. Minimum bias events will have no such spatial distortions, and while using Minimum bias events will not remove the discrepancy

between real and mixed pairs due to event correlations, it will minimize the correction needed to account for the effect.

To preserve the hadron-photon correlation when determining the falsely tagged photons, event mixing is done using photons from the same ERT event as the trigger hadron and mixing them with photons from MB events. If the photon pair still falls in the mass window for the π^0 , or η , the leading photon (from the trigger event) is counted as a falsely tagged photon. In this way, the false-tagged $h\gamma$ yield can be determined directly and subtracted from the total tagged yield. As noted previously, this mixing method will only provide an estimate of the combinatoric background, and an additional correction is necessary. Assuming the correlated background and combinatoric background will produce similar $h\gamma \Delta\phi$ distributions, one can use the measured false-tagged distributions obtained from mixing when estimating the remaining contribution. This assumption must then be tested, as it may lead to distorted $\Delta\phi$ distributions if incorrect.

When using event-mixing methods, to maximize the statistics we mix a large number of events, and the final false-pair or false-tagging rates must be correctly normalized. For pairs, simply normalizing by the number of mixed events should be sufficient, although from figure 5.9 it is clear that in the case of the η pairs, a scale must be applied to bring the background below the foreground. In the case of hadron-photon pair yields, the rate needed is the per-photon false tagging rate, meaning that photons that are part of multiple tagged pairs have the potential to distort the estimated rate. For π^0 tagging, the probability of a pair of unrelated photons falling within the π^0 mass window is small; however when all the photons from an

event are combined, the correlations within the mixed event can distort this probability. The false-tagging rate can better be determined by mixing ERT photons with N_{mix} photons, each from a different MB event, and normalizing the false-tagged distributions by N_{mix} . For η tagging the issue is complicated by the multiple-tag rate as well as the event correlations. Simply applying a scale correction determined by matching the invariant mass background to the foreground is a rough estimate of how the false-tagged background should be scaled as a result of mixing.

5.2.3.1 Correcting for correlated background

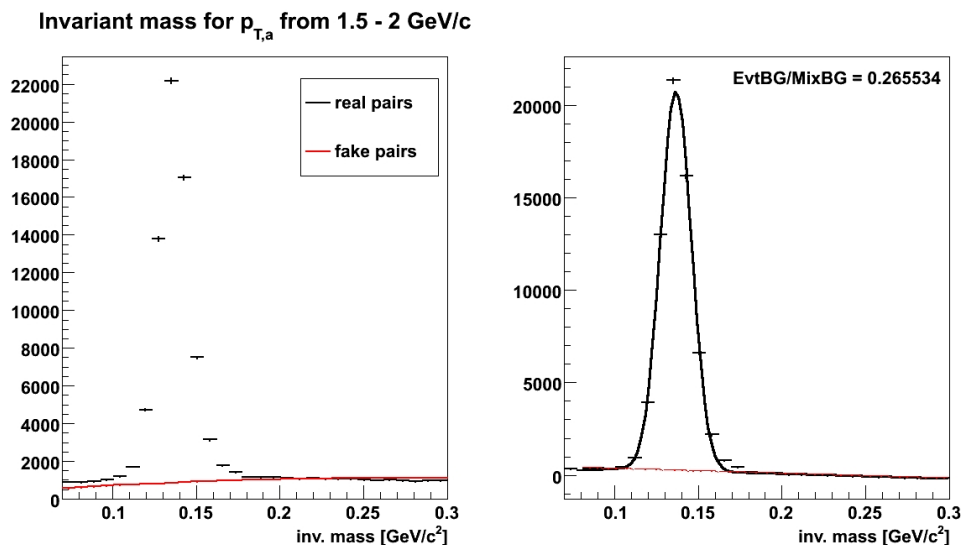


Figure 5.10: Left: Invariant mass distributions for photon pairs from the same event (black) and different events (red). Right: Fit to remaining distribution after subtraction of the mixed yield from the real pair yield, with correlated background fit component shown in red.

The correlated background contribution is determined by first subtracting the mixed background from the invariant mass distributions, after re-scaling in the case of the η . The subtracted invariant mass is fit with a Gaussian plus a 1st order

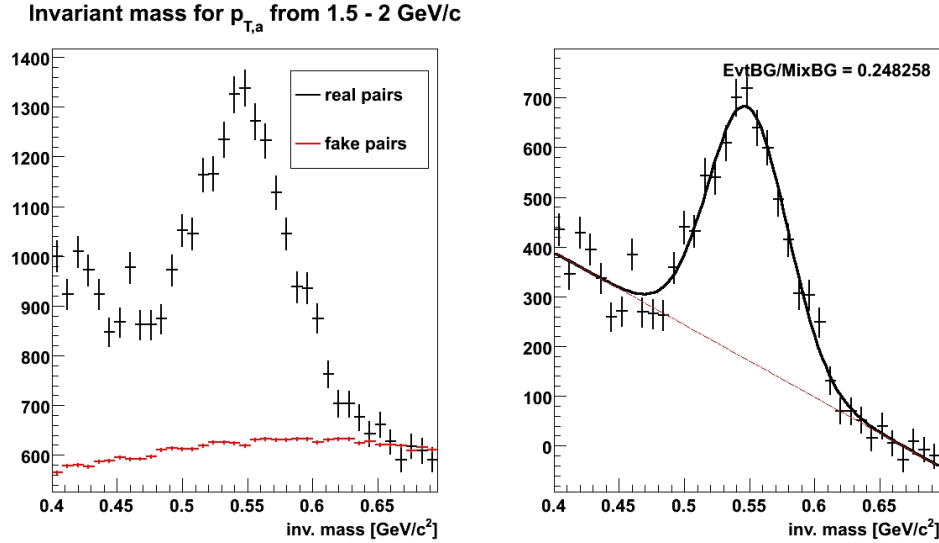


Figure 5.11: Left: Invariant mass distributions for photon pairs from the same event (black) and different events (red). Right: Fit to remaining distribution after subtraction of the mixed yield from the real pair yield, with correlated background fit component shown in red.

polynomial, and this linear term is used to determine the remaining background. To incorporate the residual background contribution into the correlation functions, the background fits are used to determine a correction to the false-tagged hadron-photon distributions. This is done using the mixed mass distribution and the fit function, by integrating within the mass window and determining the scale that must be applied to the combinatoric background to account for the remaining background using the equation

$$\begin{aligned}
 n_{\gamma_{bg}} &= n_{\gamma_{comb\ bg}} + n_{\gamma_{corr\ bg}} \\
 &= \left(1 + \frac{n_{\gamma_{corr\ bg}}}{n_{\gamma_{comb\ bg}}}\right) n_{\gamma_{comb\ bg}}. \tag{5.6}
 \end{aligned}$$

Including this correction and the normalization based on the mixing method,

the resulting tagged yield for the case of per-trigger yields - and similarly for other pair yields - is written as:

$$\frac{1}{N_{trig}^h} \frac{dN^{h-\gamma_{\pi^0-tag}}}{d\Delta\phi} = \frac{1}{N_{trig}^h} \frac{dN^{h-\gamma_{tag-fg}}}{d\Delta\phi} - \left(1 + \frac{n_{\gamma_{corr\,bg}}}{n_{\gamma_{comb\,bg}}}\right) \frac{1}{N_{mix}} \frac{1}{N_{trig}^h} \frac{dN^{h-\gamma_{tag-comb\,bg}}}{d\Delta\phi}. \quad (5.7)$$

for π^0 photons, and:

$$\frac{1}{N_{trig}^h} \frac{dN^{h-\gamma_{\eta-tag}}}{d\Delta\phi} = \frac{1}{N_{trig}^h} \frac{dN^{h-\gamma_{tag-fg}}}{d\Delta\phi} - \left(1 + \frac{n_{\gamma_{corr\,bg}}}{n_{\gamma_{comb\,bg}}}\right) \frac{R_{rescale}}{N_{mix}} \frac{1}{N_{trig}^h} \frac{dN^{h-\gamma_{tag-comb\,bg}}}{d\Delta\phi} \quad (5.8)$$

for η photons. Here $R_{rescale}$ is the scale applied to bring the mixed background below the real pairs for η photons, determined by the invariant mass distributions as a function of photon p_T .

5.2.3.2 Dependence on hadron trigger

The increased jet probability as trigger hadron p_T increases may also have an effect on the correlated background in the invariant mass distributions for photon pairs, which is the result of correlations between particles in the event. Therefore, the fits to the π^0 and η peaks used to determine the scale correction applied to the false-tagged background accounting for the correlated background are done separately for each trigger hadron p_T bin. The resulting correction factors are shown for all trigger p_T bins in figure 5.12. Again, the effect of the hadron trigger is expected to be small when measuring as a function of the leading photon p_T .

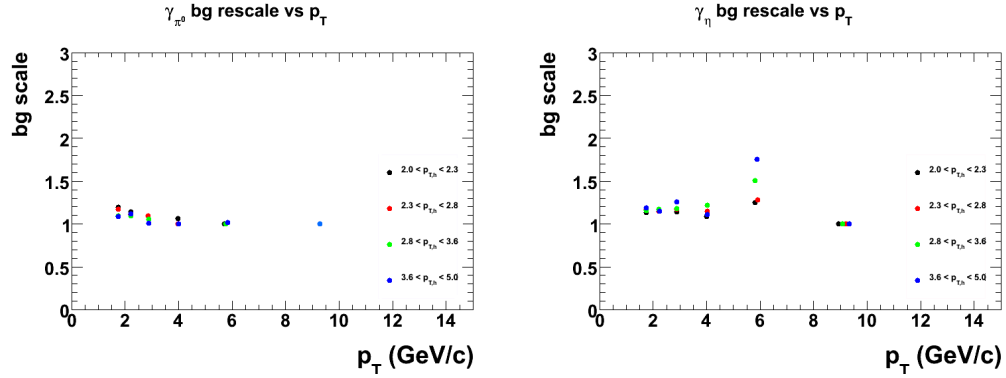


Figure 5.12: False tagged background correction due to correlated background, for the four trigger p_T bins. The correction for the π^0 is shown on the left, and for the η on the right.

5.2.3.3 Testing the method in PYTHIA

To test how well this method works at reproducing the correct tagged photon distributions, a PYTHIA study of the process of estimating the false-tagged background was done. Rather than running the PYTHIA events through a full detector simulation, to mimic the foreground and background tagging results from the data, an energy smearing in the form of a Gaussian with $\frac{\sigma}{E} = \frac{a}{\sqrt{E}} + b$, was applied. The ERT trigger will increase the correlated background, meaning that to check the method it is important to reproduce this trigger condition. This is done by applying an output filter on the simulated data, requiring events to have a photon with $p_T > 1.5$ GeV/c. The data used for mixing comes from events with no such filter, mimicking the MB trigger in the data.

The comparison for π^0 reconstruction is shown in Figure 5.13, plotting the foreground pair distributions in black and the fake background distributions in red. The fit, including the resulting linear fit (red dashed-line), and residual correlated back-

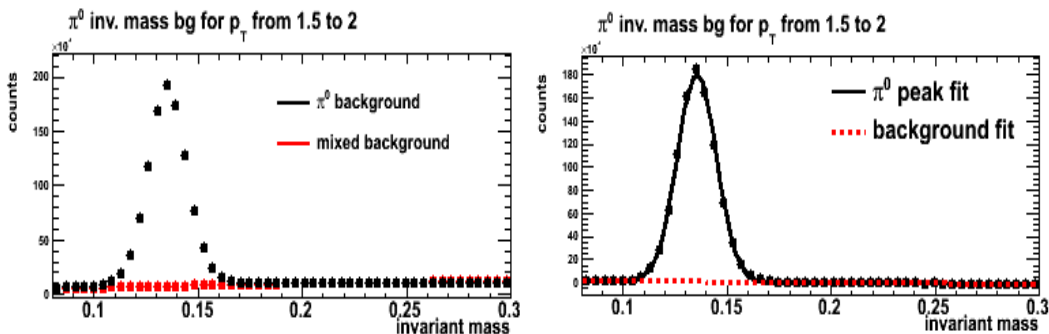


Figure 5.13: Left: The invariant mass distribution in PYTHIA for all photon pairs, around the π^0 mass peak (black) and the background invariant mass distribution for photons in the filtered event mixed with photons from an unfiltered PYTHIA event (red). Right: The mixed background subtracted invariant mass, fit with a Gaussian plus linear function, and the linear background fit result (red dashed line).

ground, are shown on the right. The same comparison for η reconstruction, where the correlated background is much more apparent, is shown in Figure 5.14. These checks confirm that the smeared PYTHIA simulation is reproducing the effect of the correlated background we wish to understand and include in our false-tagged background estimate.

The scale of the correlated background will depend on the p_T of the pair, and therefore on the p_T of the trigger photon being correlated with the trigger hadron. For determining the false tagged correlation - where it is the momentum of the trigger photon that matters - the mass distributions are plotted for momentum ranges of the trigger photon. This ensures that the correction determined from the background fit correctly applies to the corresponding photon p_T ranges used in the hadron-photon yields.

Now the hadron-photon correlations for the foreground and background can

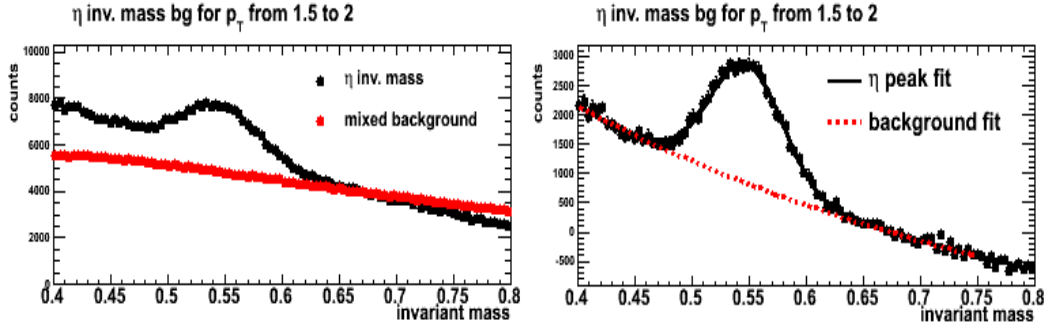


Figure 5.14: Left: The invariant mass distribution in PYTHIA for all photon pairs, around the η mass peak (black) and the background invariant mass distribution for photons in the filtered event mixed with photons from an unfiltered PYTHIA event (red). Right: The mixed background subtracted invariant mass, fit with a Gaussian plus linear function, and the linear background fit result (red dashed line).

be determined. The foreground $h - \gamma_{tagged} \Delta\phi$ distribution comes from tagging all photons within the mass peak for the π^0 or η . The background correlation begins by false-tagging a photon in a trigger event from a mixed pair that falls within the corresponding mass window. To include the remaining background component the weight described earlier is determined by integrating the mixed pair distribution and the background fit function in the relevant mass window to determine $\frac{n_{\gamma_{corr} bg}}{n_{\gamma_{comb} bg}}$, and scaling the background correlation by $(1 + \frac{n_{\gamma_{corr} bg}}{n_{\gamma_{comb} bg}})$. The resulting foreground and background $h - \gamma$ distributions along with the true $h - \gamma_{decay}$ distribution from PYTHIA are shown in Figure 5.15 for both the π^0 (left) and η (right).

The tagging in PYTHIA is done the same way as in the data, using a lower energy cut on the pair photons and applying a mass window around the π^0 and η peaks. This will result in the loss of some real π^0 and η photons, as in the data. For the purposes of this study, the decay photons lost should simply be put back in, in

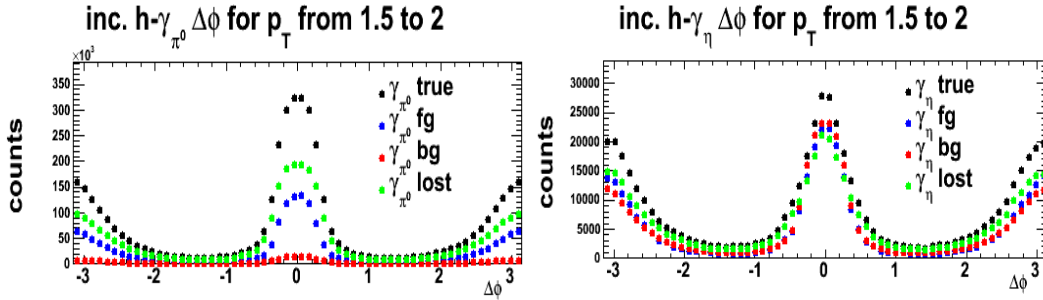


Figure 5.15: $h - \gamma$ $\Delta\phi$ distributions used to test the false-tagging estimate. In black is the same-event(fg) tagged yield (raw counts), in red is the false-tagged background yield, in blue is the true decay yield, and in green is the correction for lost decay photons. The case for π^0 photons is shown on the left, and for η photons on the right.

order to decouple the effect of incorrectly determining the false-tagged background and this tagging efficiency. Therefore, the $h - \gamma$ $\Delta\phi$ distributions of lost π^0 and η photons are determined as well, using the parent information from PYTHIA to find photons that were from decays but didn't get tagged. These "lost" photons are also shown in figure 5.15, and can then be added back in before comparing the final estimate for the tagged distribution with that of true decay photons. Adding these lost photons back in should have no effect on the relative foreground and background distributions, rather it is just a way of correcting for the tagging efficiency in PYTHIA - where we have perfect knowledge of what actually happened - and allowing us to test our understanding of the background.

The final background subtracted $h - \gamma$ $\Delta\phi$ distributions for tagged π^0 and η decays are compared with the true distributions determined from PYTHIA in Figure 5.16. Included in the plot is the systematic difference between the true and subtracted, determined by calculating the percent difference in the integrated yields, as

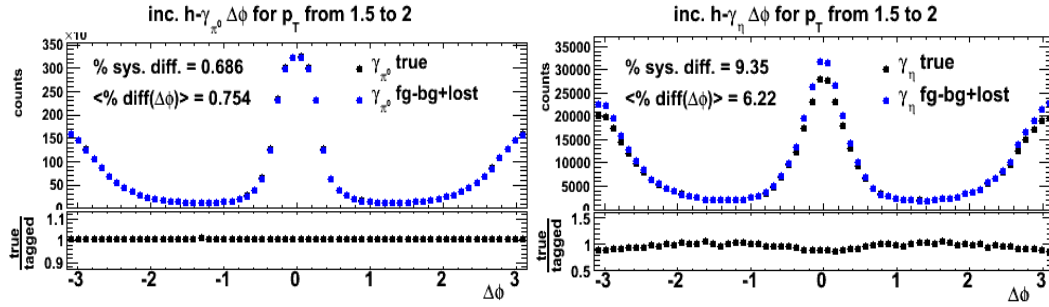


Figure 5.16: In black is the true $h\gamma$ $\Delta\phi$ distribution generated in PYTHIA, and in blue is the (fg-bg+lost) tagged photon distribution. The ratio of the two distributions is shown in the lower plot. The case for π^0 tagging is shown on right and for η tagging on the left.

in Eq. (5.4). These systematic differences appear small, $< 1\%$ for the π^0 and $\sim 10\%$ for the η . However, it is not simply the integrated yields, but more importantly the shapes of the correlated yields, that are of interest. Therefore, it is important to check how well the method matches the $\Delta\phi$ dependence. As a rough measure of how well the method works, the average percent difference as a function of $\Delta\phi$ is also stated - and is generally higher than the integrated difference, indicating that the $\Delta\phi$ dependence is not being reproduced exactly. By looking at the ratio of the true to estimated tagged yields, as a function of $\Delta\phi$, the full $\Delta\phi$ dependent systematic effect can be estimated. These ratios are shown in the bottom panels in Figure 5.16. Because the contribution from η photons is only a small fraction of the total decay photon yield ($\sim 20\%$) this 10% uncertainty translates into only a few percent in the final decay yield, and this method was implemented to obtain the initial fragmentation photon results. Even so, it would be beneficial to understand the source of this uncertainty and either correct for it or apply a more effective method.

The event mixing method is an attempt to estimate the false-tagged background

when measuring the yield of tagged photons from either π^0 or η decays. When measuring reconstructed π^0 's and η 's, this works well to determine the rate of false pairs. However, when simply tagging single photons, the complication of multiple-tagging - which will have a different rate in real events than mixed events - can lead to discrepancies. This is likely the source of the residual uncertainty found when testing event mixing in PYTHIA. The additional complication of correlated background which the mixed event method cannot alone correct helps to motivate considering other ways of estimating the false-tagging rate.

5.3 Tagging probabilities

Each photon in an event has some probability of being tagged as coming from a decay, p_{tag} , which will be a combination of the probability for correctly tagging a π^0 or η photon with the right pair photon and that of falsely tagging with another photon in the event. First, there are several probabilities we need to define:

- p^π, p^η = probability a photon is actually from a π^0 or η decay, respectively
 - p_a = probability other photon (pair photon) from decay was in the acceptance
 - p = probability photon is correctly tagged when other photon is in the acceptance
 - p' = probability photon is tagged with incorrect (wrong pair photon or not from decay)
-

There are several cases that can lead to a photon being tagged. First we will consider a photon that did come from a decay, and the pair photon was also in the acceptance, which has a probability $p^\pi p_a$ (in the case of π^0 photons; the arguments are similar for η photons). It is actually easier to determine the probability of not tagging a photon, so we have: $1 - p$, the probability the photon is not tagged by the pair photon, and $(1 - p')^{n-2}$, the probability photon is not falsely tagged, where n is the total number of photons in the event. For the second type of tagging, the power is $n - 2$ as the two photons from the decay are not included. The total probability of not tagging this photon is then $(1 - p)(1 - p')^{n-2}$, making the probability of tagging the photon $1 - (1 - p)(1 - p')^{n-2}$. The total probability of having a photon of this type and tagging is

$$p^\pi p_a [1 - (1 - p)(1 - p')^{n-2}] . \quad (5.9)$$

The next case is a photon that did come from a decay, but the pair photon was not within the acceptance, which has a probability of $p^\pi(1 - p_a)$. In this case the photon can only be tagged falsely, making the form for the tagging probability somewhat different. Also, now all the other photons in the event will contribute to the probability this photon is falsely tagged. If we again think of the probability of not tagging, this will be $(1 - p')^{n-1}$ in this case, making the probability of tagging $1 - (1 - p')^{n-1}$. From these terms, the total probability of having and tagging a photon under these conditions is

$$p^\pi(1 - p_a) [1 - (1 - p')^{n-1}] . \quad (5.10)$$

The final case is simply if a photon didn't come from a decay at all, which will have a probability of $(1 - p^\pi)$. In this case the probability of tagging will only result from false tagging, with the same total probability as the previous term. The total probability of tagging a photon in this case is

$$(1 - p^\pi) [1 - (1 - p')^{n-1}] . \quad (5.11)$$

Finally, putting these all together, the probability of tagging a photon as from a decay (here using the π^0 as an example) can be written as

$$\begin{aligned} p_{tag}(n) = & p^\pi p_a [1 - (1 - p)(1 - p')^{n-2}] + p^\pi (1 - p_a) [1 - (1 - p')^{n-1}] \\ & + (1 - p^\pi) [1 - (1 - p')^{n-1}] . \end{aligned} \quad (5.12)$$

This is the probability for a photon to be tagged in an event with n photons, where there is an implicit dependence on the probability of having n photons in an event. The tagging probability is only valid for $n > 2$, and the average tagging probability for any event will then involve summing over all n for $n > 2$, weighting by the probability distribution for the number of photons in an event, $P(n)$. After some simplification this leads to the average tagging probability being

$$\begin{aligned} \langle p_{tag} \rangle = & p^\pi p_a p \sum_{n>1} P(n) (1 - p')^{n-2} + p^\pi p_a \left[\sum_{n>1} P(n) (1 - p')^{n-1} - \sum_{n>1} P(n) (1 - p')^{n-2} \right] \\ & + \left[1 - P(1) - \sum_{n>1} P(n) (1 - p')^{n-1} \right] . \end{aligned} \quad (5.13)$$

The yield of true-tagged photons can then be found by scaling the measured tagged photon yield by

$$f_{false} = \frac{\langle p_{true} \rangle}{\langle p_{tag} \rangle} = \frac{\sum_{n>1} P(n) p p^\pi p_a}{\langle p_{tag} \rangle}. \quad (5.14)$$

The next step is to determine each of the probabilities that go into this final formula, as well as the probability distribution for the multiplicity, $P(n)$. The probabilities relying on knowledge of the origin of the photon, such as p^π , p_a , and p , are determined using simulation. The challenge comes in determining p' . Again using simulation, this can be calculated from the number of times a photon is falsely tagged divided by the number of times it is tested, or paired with another photon in the event:

$$p' = \frac{n_{false-tag}}{n_{tests}}.$$

In principle, there should be no uncertainty on this beyond the inherent uncertainty in the simulation; however, when the simulation includes the detector environment, some ambiguity in how n_{test} is determined arises. As a result, although this form can be used as a check of the method, it is preferable to devise a way of estimating - or calculating - the false tagging probability that does not rely on simulation in this way.

The false-tagging probability can be calculated, using the other probabilities described, from the average number of tagged photons per event. The number of tagged photons results from a similar set of conditions as the total tagging proba-

bility and can be written as

$$\begin{aligned} N_{tag} &= p^\pi [p_a(p + p'(n-2)) + (1-p_a)(p'(n-1))] + (1-p^\pi)(p'(n-1)) \\ &= p^\pi p_a p - p^\pi p_a p' + p'(n-1) \end{aligned} \quad (5.15)$$

for an event with n photons.

This can then be solved for p' and averaged over all values of n (for $n \geq 1$), and we have

$$p' = \frac{\langle N_{tag} \rangle - \sum_{n>1} P(n)p^\pi p_a p}{\sum_{n>1} P(n)[(n-1) - p^\pi p_a]} . \quad (5.16)$$

Using this formula, the only inputs needed are now p^π , p_a , and p , which will come from simulation. It is already the case that p_a , and p must be determined to estimate the tagging efficiency, so the work of determining the uncertainty on these will be discussed in the description of how the total method is tested.

5.3.1 Testing the method

Again using PYTHIA data run through the PHENIX detector simulation, PISA, the tagging probabilities that go into the formula, $P(n)$, and $\langle N_{tag} \rangle$, can be calculated. The resulting p_{tag} determined from the formula using these inputs can then be compared with the true p_{tag} from simulation. The p_T dependent tagging probability for photons from π^0 decays is shown in Figure 5.17. The figure shows probabilities determined directly from PISA and using Eq. (5.13), along with the values for p, p_a , and p^π that go into the equation. Also shown is the resulting estimate for p' from

Eq. (5.16). Finally, the percent difference between the true tagging probability from PISA and the estimated tagging probability is shown as a test of the method. The other comparison shown in the figure comes from using a fitting procedure to obtain p_a and p' that will be described in Sections 5.3.2 and 5.3.5. The comparison shows that the estimate for the tagging probability determined using the formulas derived above is able to reproduce the actual tagging probability to within less than 1%. The same set of probabilities and comparisons for η photons is shown in Figure 5.18.

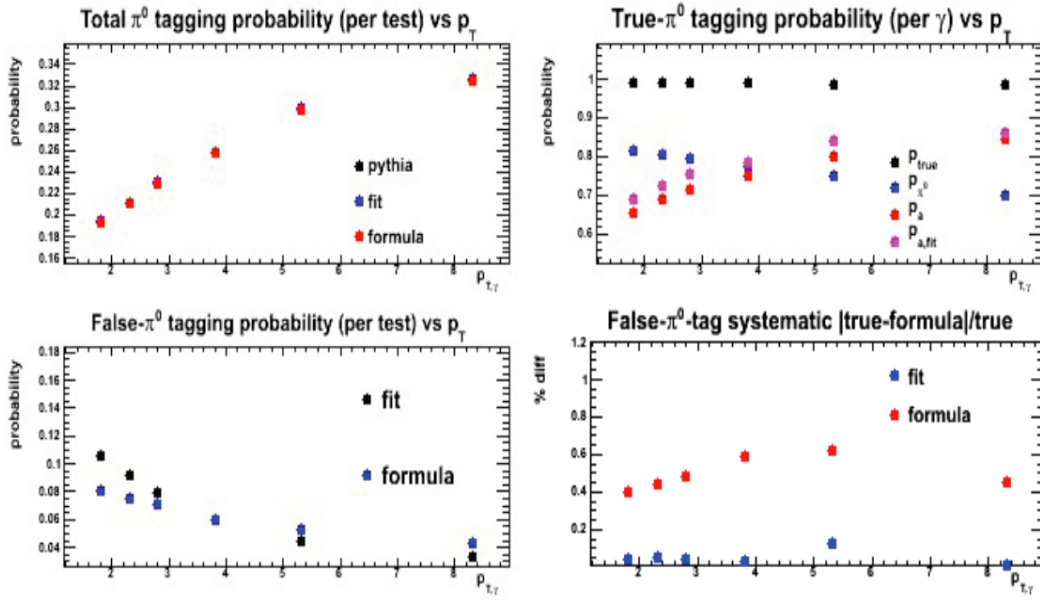


Figure 5.17: Top left: tagging probability for π^0 photons - from PISA (black), using Eq. (5.13) with inputs directly from PISA (red) or obtaining p_a and p' from fits to $p_{\text{tag}}(n)$ (blue). Top right: probabilities from PISA - p , true pair (black); p^π , photon is from a π^0 (blue); p_a , pair photon is accepted (includes all cuts) (red), and p_a determined from fit (magenta). Bottom left: p' from Eq. (5.16) (blue) and from fit (black). Bottom right: % difference between tagging probability from PISA and from the equation with the different inputs. All vs. $p_{T,\gamma}$.

To test how well this method does at reproducing the $\Delta\phi$ dependent distribu-

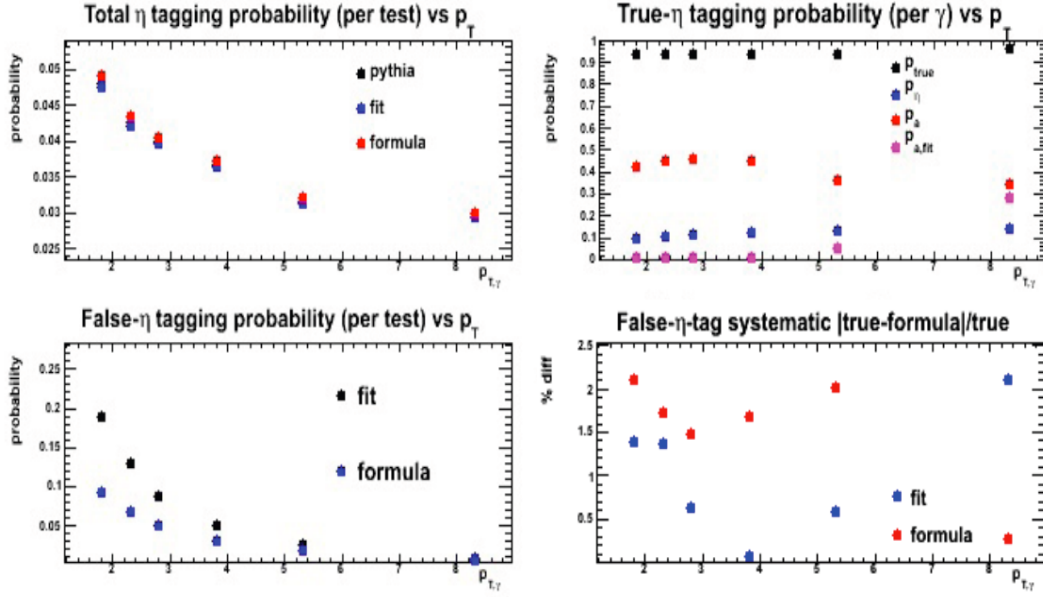


Figure 5.18: Top left: tagging probability for η photons - from PISA (black), using Eq. (5.13) with inputs directly from PISA (red) or obtaining p_a and p' from fits to $p_{tag}(n)$ (blue). Top right: probabilities from PISA - p , true pair (black); p^π , photon is from a η (blue); p_a , pair photon is accepted (includes all cuts) (red), and p_a determined from fit (magenta). Bottom left: p' from Eq. (5.16) (blue) and from fit (black). Bottom right: % difference between tagging probability from PISA and from the equation with the different inputs. All vs. $p_{T,\gamma}$.

tions, we can again compare the true $h\gamma_{\pi^0}$ and $h\gamma_\eta$ distributions to what we estimate through tagging and applying the scale correction. Figure 5.19 shows the true (black) and corrected tagged (blue) $h\gamma_{\pi^0}$ (left) and $h\gamma_\eta$ (right) distributions, as a function of $\Delta\phi$, in the top panel. The ratio of these distributions is shown in the bottom panels. Again, the integrated and $\Delta\phi$ averaged systematic percent differences are quoted to give an estimate of how well the method works. From this, we find that while the discrepancy seen for the π^0 was already small with the mixing method, this method appears to work even better, bringing the difference down to

$\sim 0.1\%$. Similarly, in the case of η tagging, the difference is down from $\sim 6 - 10\%$ to $\sim 2 - 4\%$.

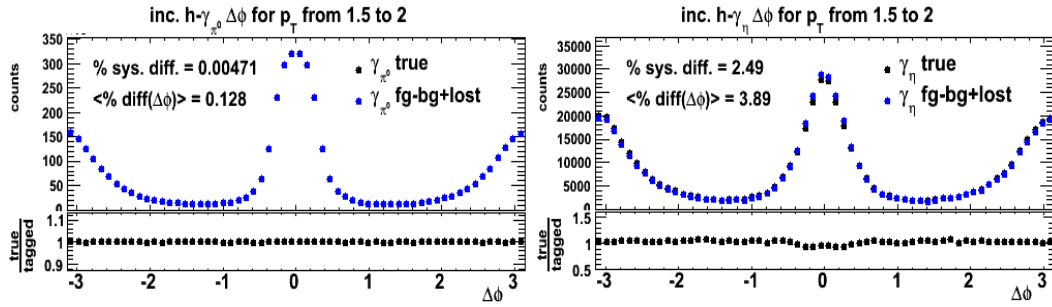


Figure 5.19: In black is the true $h\gamma$ $\Delta\phi$ distribution generated in PYTHIA, and in blue is the $(\frac{p_{true}}{p_{tag}} \cdot \text{fg+lost})$ tagged photon distribution. The ratio of the two distributions is shown in the lower plot. The case for π^0 tagging is shown on right and for η tagging on the left.

5.3.2 Tagging probabilities in the data

The good agreement this method has with the true distributions in simulation is encouraging. The next step is to use inputs from data for $P(n)$ and $\langle N_{tag} \rangle$, combined with the probabilities determined in PISA, to attempt to reproduce the tagging probability seen in the data. Doing so reveals a discrepancy between data and simulation resulting in an overestimation of the pair acceptance that leads to estimates for p_{tag} that differ largely from data. Reducing the dependence on simulation even further, the $p_{tag}(n)$ determined from data was fit using Eq. (5.12) to extract p_a and p' directly from data in each p_T bin, using inputs from p and p^π or p^η from simulation. An example of the fit for both the π^0 and η is shown in Figure 5.20. The resulting values for p_a and p' as a function of photon p_T are shown in Figure 5.21 along with

the values from PISA (blue) for comparison. It is clear that PISA overestimates the pair photon acceptance, which leads to a higher true pair acceptance probability and a higher false-tagging probability.

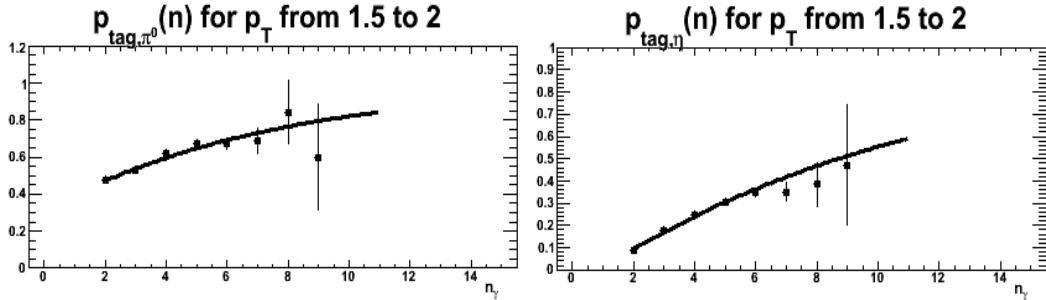


Figure 5.20: The probability of tagging a photon with momentum from 1.5 to 2 GeV/c vs. the number of photons in the event, fit using Eq. (5.12) with input from PISA.

It is useful to note that in Eq. (5.12) and subsequent equations, p_a and p^π do not appear independently, therefore although we use p^π and p^η values determined by PISA, they are constrained by data. When comparing the total average p_{tag} as a function of photon p_T , it is now possible to use inputs from data for everything except the probability for correctly tagging a π^0 or η when the pair is in the acceptance. The estimated $\langle p_{tag} \rangle$, compared to what is measured in the data, is shown in Figure 5.22; the percent difference between them is also shown. The comparison shows extremely good agreement, suggesting negligible systematic effects coming from correcting for false tagging using this method.

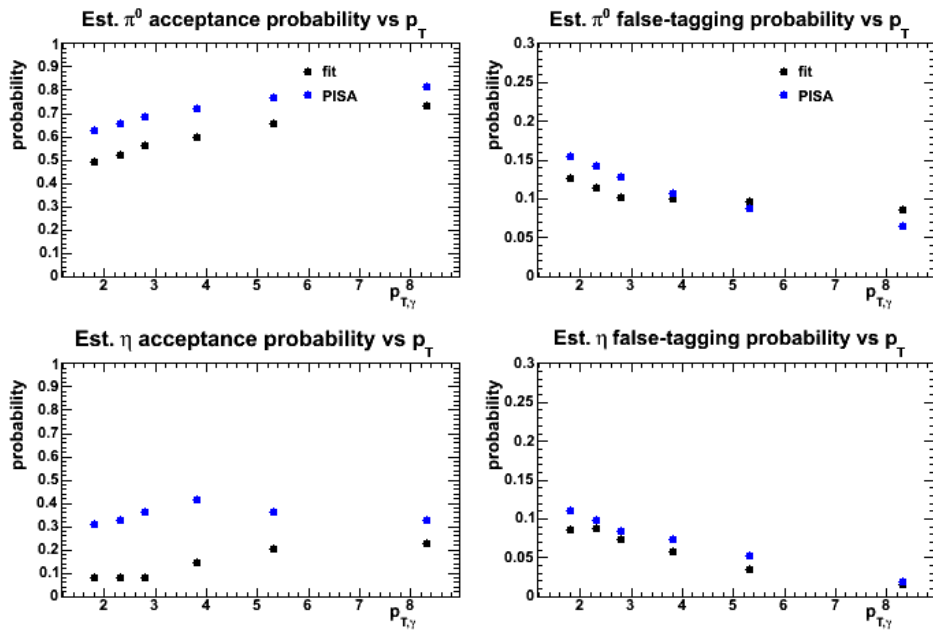


Figure 5.21: The pair acceptance probability vs. $p_{T,\gamma}$ is shown on the left and the false tagging probability vs. $p_{T,\gamma}$ is shown on the right, extracted from fits to data (black) and determined from PISA (blue). The case for π^0 photons is shown on the top, and for η photons on the bottom.

5.3.3 Tagging efficiency revisited

Using fits to the photon multiplicity in the data to overcome discrepancies between data and simulation removes almost all dependence on simulations for determining the final false-tagged background. However, this approach reveals that the tagging efficiency estimated from PISA is also incorrect, as one of the inputs to the efficiency is the pair acceptance, which is now known to be overestimated. This potential problem is resolved using the tagging probability method to determine the tagging efficiency as well as the false-tagging correction, where the efficiency has the form

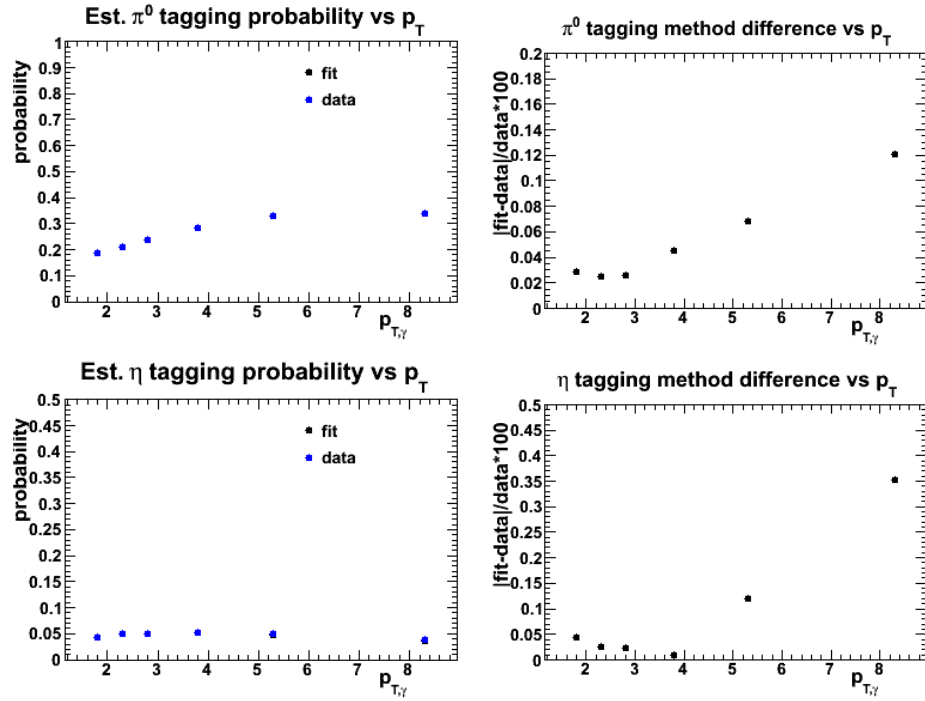


Figure 5.22: The final average tagging probability for π^0 (top) and η (bottom) photons, as a function of photon p_T , comparing data and the value for p_{tag} determined from Eq. (5.13).

$$\begin{aligned} \varepsilon_{tag} &= \frac{pp_a p^\pi}{p^\pi} \\ &= pp_a . \end{aligned} \quad (5.17)$$

More generally, averaging over the photon multiplicity distribution to account for the fact that the tagging probability is only defined when there are two or more photons in an event, we have

$$\epsilon_{tag} = \sum_{n>1} P(n) pp_a . \quad (5.18)$$

We can now obtain both the false-tagging correction factor, f_{false} , and the tagging efficiency, ϵ_{tag} , completely consistently using fits to $p_{tag}(n)$ applied directly to data. The total correction factor applied to the data, in the case of π^0 tagging, is then

$$f_{tag}(p_T) = \frac{f_{false}}{\epsilon_{tag}} = \frac{\sum_{n>1} P(n) pp^\pi p_a}{\langle p_{tag} \rangle} \frac{1}{\sum_{n>1} pp_a} = \frac{p^\pi}{\langle p_{tag} \rangle} , \quad (5.19)$$

and similarly for η photons - here the p_T dependence of the probabilities are not indicated explicitly. Using this method, as long as the fits from the data to $p_{tag}(n)$ are able to reproduce the average p_T dependent tagging probability well, the actual values for p_a and p' need not be exact. The only remaining dependence on PISA is in determining the probability that a photon comes from π^0 or η decay.

5.3.4 Hadron trigger effects

As has been discussed in previous sections, the requirement that the photons we are measuring be associated with trigger hadrons of a certain momentum can affect the total tagging probability. The trigger hadron will change the p_T dependence of the overall tagging efficiency, which can be accounted for by performing fits to $p_{tag}(n)$ for photons only in events with a hadron in each trigger p_T bin. However, the $\Delta\phi$ dependence coming into correlation measurements introduces an additional acceptance effect to the tagging efficiency. This can be understood by considering that there is a higher probability for the pair photon to be detected with photons found

at small $\Delta\phi$ from hadrons that also fall within the PHENIX acceptance. This $\Delta\phi$ dependence can be thought of as a tagging acceptance, includes both true-tagged photons and false-tagged photons, and is determined from PISA, such that the correction to the data is

$$f_{tag}(\Delta\phi) = \frac{p^\pi(\Delta\phi)}{p_{tag}(\Delta\phi)} . \quad (5.20)$$

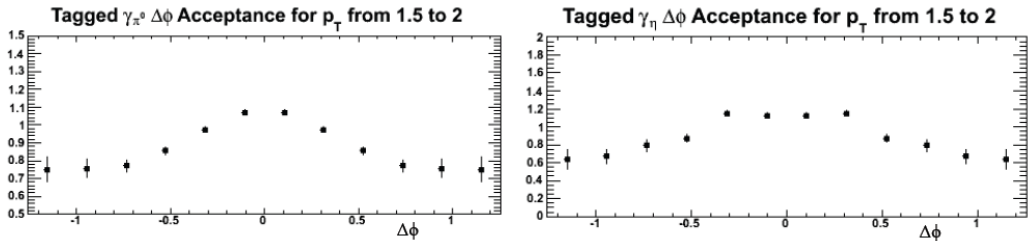


Figure 5.23: Near-side $\Delta\phi$ variation in the tagged photon probability for π^0 photons (left) and η photons (right).

The $\Delta\phi$ dependence has the same form as Eq. (5.19), but it corrects only for the variation in the tagging rate as a function of $\Delta\phi$ and is normalized to one within the angular range chosen for the pairs being analyzed. An example of the variation for both π^0 and η tagging is shown in Figure 5.23 for the lowest trigger and associated p_T bin. Assuming PISA can accurately reproduce the overall acceptance of the PHENIX detector, this should work when applied to data. However, any inconsistencies can be minimized by considering only photons that fall within a fixed angular range of the trigger hadrons when generating the $p_{tag}(n)$ distributions used for fitting. As the pairs considered in the final p_{out} distributions and near-side pair yields are restricted to $|\Delta\phi| < 0.7$ - the restriction placed on the photons used

to obtain the $p_{tag}(n)$ distributions shown in Figure 5.20 - with a hadron trigger p_T between 1.5-2.0 GeV/c.

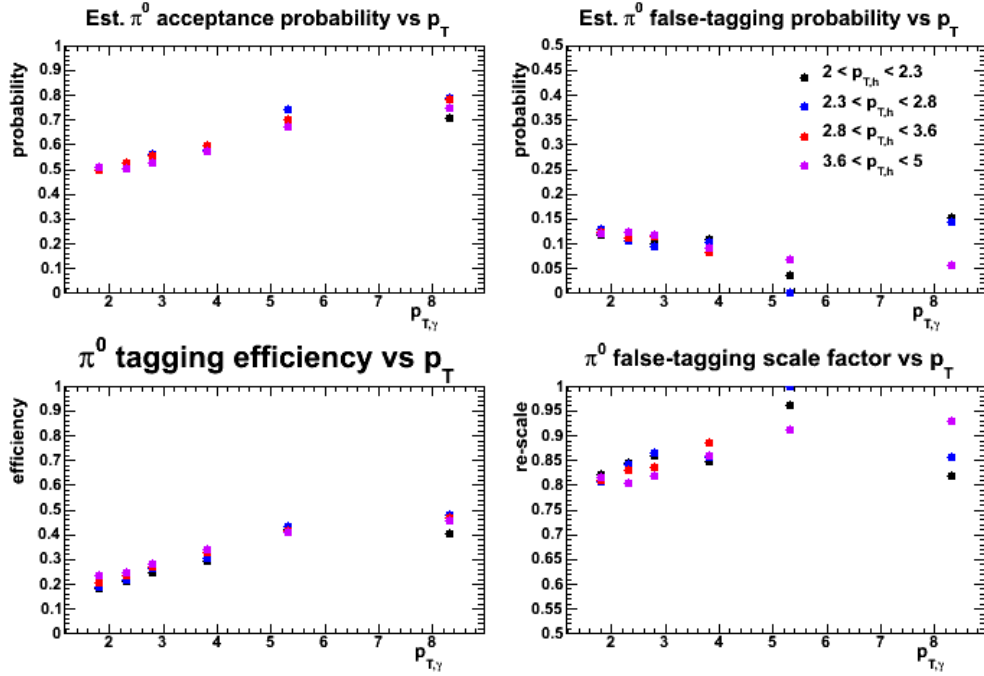


Figure 5.24: Various probabilities that go into tagging π^0 photons. Top left: The pair acceptance probability, p_a , vs. $p_{T,\gamma}$ for the different hadron trigger bins obtained from fits to $p_{tag}(n)$. Top right: The false tagging probability, p' , vs. $p_{T,\gamma}$ for the different hadron trigger bins. Bottom left: the resulting tagging efficiency determined using the p_a shown. Bottom right: the resulting f_{false} correction determined using the p_a and p' shown.

The trigger hadron and associated photon p_T dependent values for p_a and p' are shown in Figures 5.24 and 5.25 for π^0 and η photons respectively, along with the resulting ϵ_{tag} and f_{false} . The final scale factor applied to the tagged π^0 and η yields for each hadron trigger bin is shown in Figure 5.26. The figure also shows the percent difference between the tagging probability determined using p_a and p' from the fits as input to Eq. (5.13) and actual tagging probability in the data. From

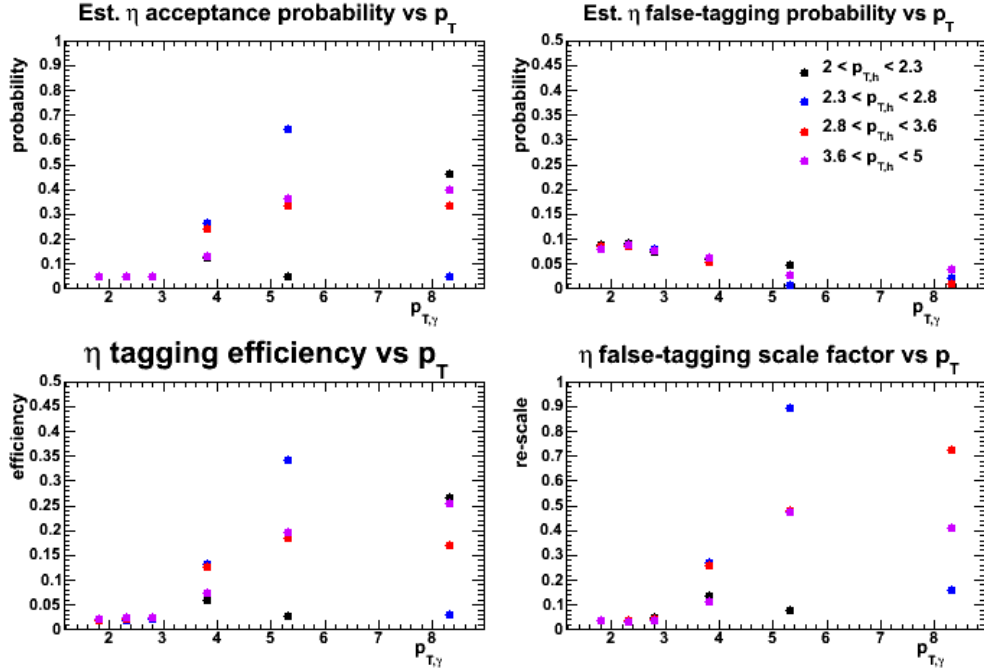


Figure 5.25: Various probabilities that go into tagging η photons. Top left: The pair acceptance probability, p_a , vs. $p_{T,\gamma}$ for the different hadron trigger bins obtained from fits to $p_{tag}(n)$. Top right: The false tagging probability, p' , vs. $p_{T,\gamma}$ for the different hadron trigger bins. Bottom left: the resulting tagging efficiency determined using the p_a shown. Bottom right: the resulting f_{false} correction determined using the p_a and p' shown.

the figures it is clear that although the fits do not always produce smoothly varying values for p_a and p' , the final scale correction applied to the data does appear to follow a basic trend, and the comparison between the tagging probability obtained and what is measured in data is very good for both the π^0 and the η .

5.3.5 Full method in PISA

By obtaining the false-tagging correction and tagging efficiency directly from fits to the tagging probability in data, a careful check that the method was accurately

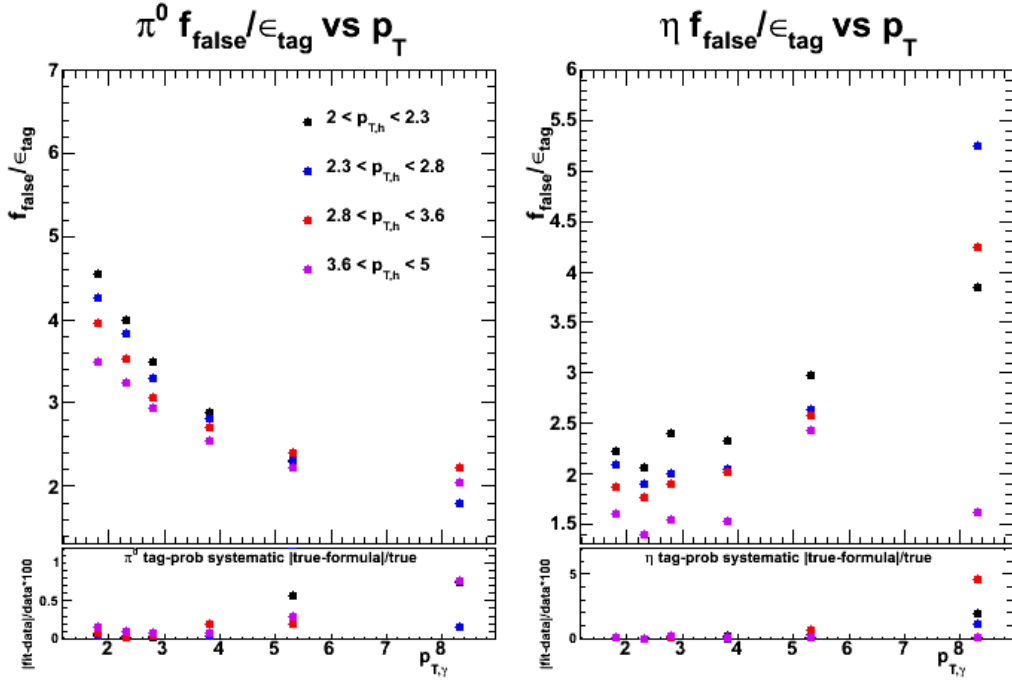


Figure 5.26: The final scale correction for π^0 tagged photons (left) and η tagged photons (right) and the percent difference between the estimated total tagging probability and the tagging probability in the data (bottom panels) as a function of photon p_T for each hadron trigger bin.

reproducing the data can be done, as demonstrated in the previous section. However, as was discovered in initial testing of the tagging method, looking only at the p_T dependence can often hide issues that may arise when more discriminatory measurements, such as the $\Delta\phi$ and p_{out} distributions, are attempted. Although the method no longer relies on direct input from PISA, the full process can be tested using simulations by applying the same fitting procedure to the tagging probabilities in the simulated data.

Figures 5.17 and 5.18 showed the results for p_a and p' from fitting the $p_{\text{tag}}(n)$

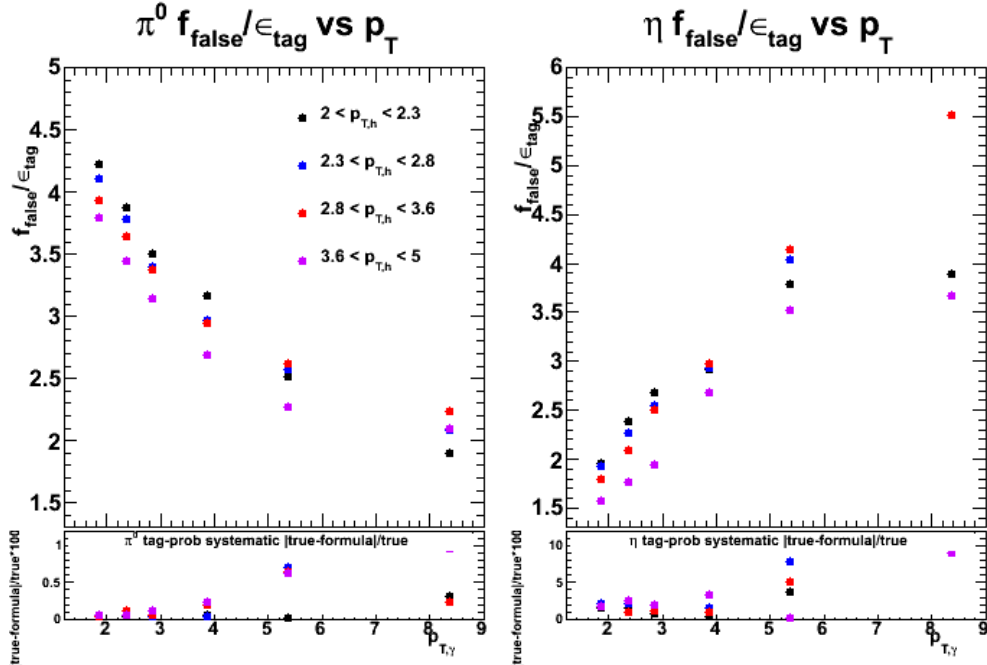


Figure 5.27: The total scale correction for simulated π^0 tagged photons (left) and η tagged photons (right) and the percent difference between the estimated total tagging probability and the tagging probability in the PISA (bottom panels) as a function of photon p_T for each hadron trigger bin.

distributions in PISA. It is clear that they do yield somewhat different results for the false-tagging and acceptance probabilities, and as a result for f_{false} and ϵ_{tag} . However, the estimated tagging probability still agrees with PISA to within one percent, and in fact the fit tends to do slightly better than the previous method of simply determining the various probabilities directly. Figure 5.27 shows the final scale factor applied to the tagged photon distributions that these fits give in PISA for each of the different hadron trigger bins.

Comparing these results to the scale factors obtained in data shown in Figure 5.26, it is clear that PISA does not reproduce the data, emphasizing the need to

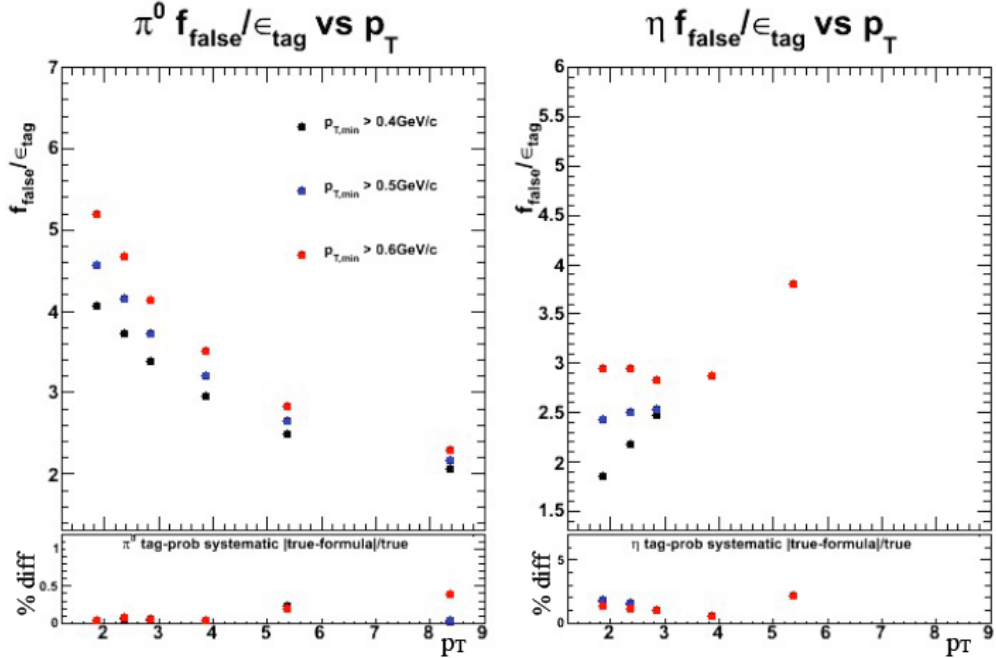


Figure 5.28: The total scale correction for simulated π^0 tagged photons (left) and η tagged photons (right) and the percent difference between the estimated total tagging probability and the tagging probability in the PISA (bottom panels) as a function of photon p_T with different minimum p_T cuts for the pair photon.

minimize any dependence on PISA input. Position-dependent corrections, such as the η vs. ϕ corrections described in Section 5.2.1, should not suffer from such discrepancies, as the differences uncovered by this study are likely due to inconsistencies in the single photon efficiency at low p_T . This claim is supported by the agreement in the general trend seen for π^0 tagging. Similarly, by increasing the minimum p_T for pair photons, as illustrated in Figure 5.28, the correction for η tagging begins to show the same trend seen in the data.

With the p_T dependence of the tagging efficiency and false-tagging rate accounted for using this single scale correction, the remaining corrections are to the

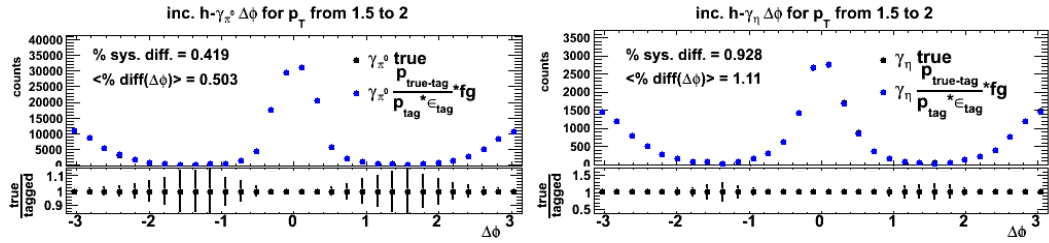


Figure 5.29: True $h - \gamma_{\pi^0}$ (left) and $h - \gamma_{\eta}$ (right) $\Delta\phi$ dependent pair yield (black) and the estimated yield (blue) using the three sets of corrections.

position dependence of the tagging rate, including the fluctuations in the tagging rate in terms of the ϕ and η of the photon, as well as the $h - \gamma$ $\Delta\phi$ dependence. Applying these three sets of corrections for each hadron and photon p_T bin should get back the true π^0 and η $h - \gamma$ pair yields. Figure 5.29 shows the comparison of the full test of the method and the true π^0 (left) and η (right) yields for the lowest hadron/photon p_T bin.

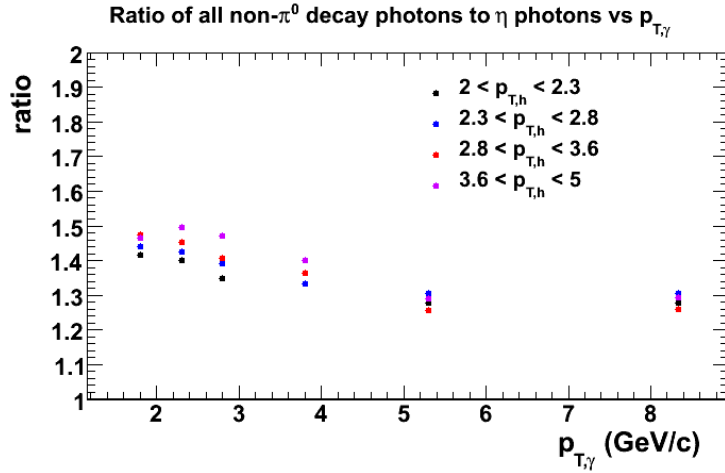


Figure 5.30: Ratio of all non- π^0 decay photons to η decay photons, when paired with trigger hadrons of several p_T ranges on the near-side.

As a result of testing the comparison of the final estimated decay yield combining the estimated π^0 and η photon yields, it was found that a trigger hadron and associated photon p_T dependent scale was needed for estimating heavier mesonic decays using η photons. Figure 5.30 shows the ratio of all non- π^0 photons to η photons as a function of the photon p_T for each of the hadron trigger bins. The ratio is restricted to photons paired within $|\Delta\phi| < 0.7$ of the trigger hadron.

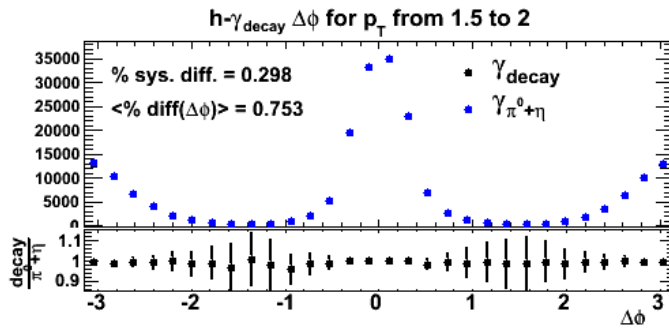


Figure 5.31: True total $h - \gamma_{decay}$ $\Delta\phi$ dependent pair yield (black) and the estimated $\pi^0 + \eta$ yield (blue).

5.3.5.1 Testing p_{out}

The measured p_{out} distributions will have a different sensitivity to the p_T and $\Delta\phi$ dependent nature of corrections to the tagged distributions used to estimate the decay background. For this reason, an important test of the overall method is checking how well tagging reproduces the decay distributions specifically for the decay photon p_{out} . The dependence of p_{out} on the variation in photon p_T within the chosen bins led to a slight modification to the way the tagged distributions were scaled to correct for false tagging and efficiency. Rather than using the average scale correc-

tion within a given p_T bin determined from fits to the tagging probability in that bin, the p_T dependent distribution of the scale corrections were fit as well. The resulting fits to the data are shown in Figure 5.32. Correcting the tagged photon distributions pair-by-pair (hadron-photon pair), determining the tagging scale based on the p_T of the photon by evaluating these fits, includes the full p_T dependent nature of the tagging efficiency and false-tagging rate.

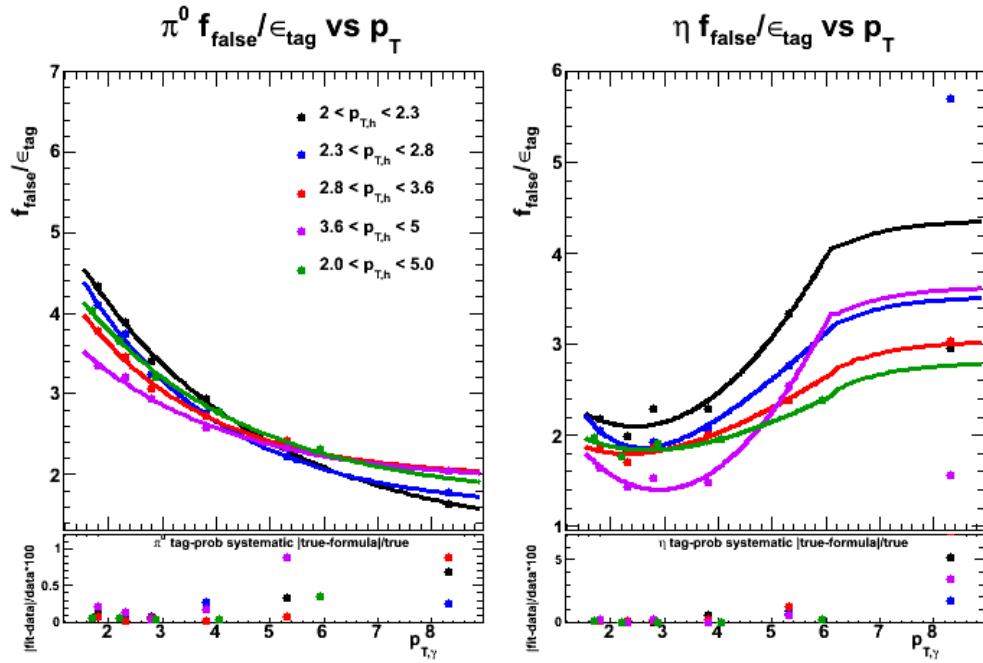


Figure 5.32: The final scale correction for π^0 tagged photons (left) and η tagged photons (right), with fits to get the p_T dependence - and the percent difference between the estimated total tagging probability and the tagging probability in the data (bottom panels) as a function of photon p_T for each hadron trigger bin in data.

The fits do not pass through every point, but give an estimate of the overall p_T dependence of the scale correction. To ensure that the overall value for the correction is accurate, the fits are scaled to match the mean p_T point within each p_T

bin, and then they are used to provide the local slope. Applying the correction to the tagged photon distribution in this way improved the overall systematic difference in the tagged and true decay photon p_{out} distributions by 1 – 2% overall. A test of the resulting decay p_{out} summed over all photon p_T bins, for the lowest hadron trigger bin, is shown in Figure 5.33. The integrated percent difference between the true and estimated distributions is less than 3%, although the average point-to-point difference is slightly higher. The variation shown in this test is included as part of the systematic uncertainty on the final p_{out} distributions, as it represents the limitations of how accurate this method is for estimating the decay background.

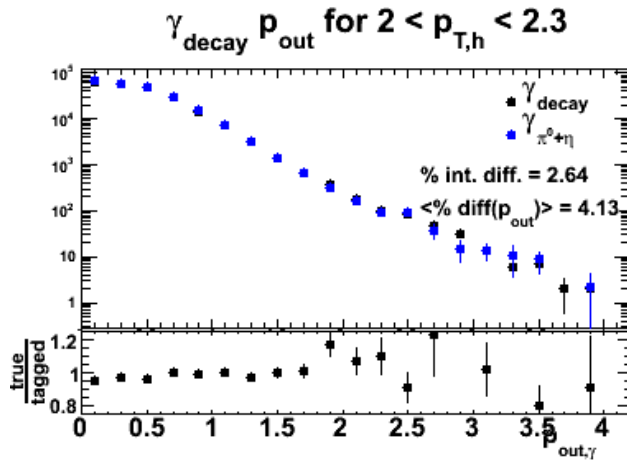


Figure 5.33: Top: the decay photon p_{out} for photons from 1.5 – 15.0 GeV/c, for trigger hadrons from 2.0 – 2.3 GeV/c for true decay photons (black) and the estimate from tagging π^0 and η photons (blue) in PISA. The integrated percent difference between the two distributions is shown, as well as the average point-to-point difference. Bottom: the ratio of the true distributions to the estimated, as a function of p_{out} .

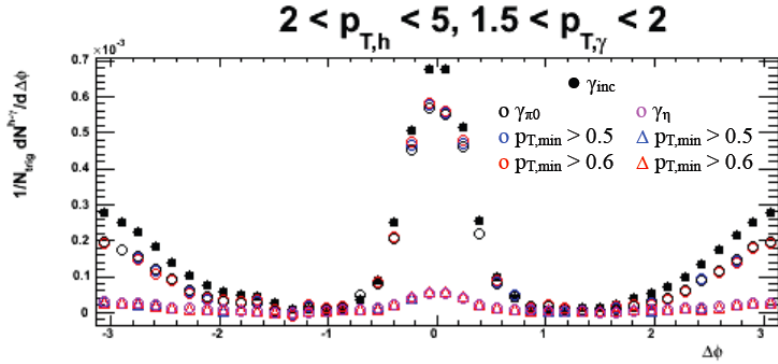


Figure 5.34: Hadron-photon $\Delta\phi$ per trigger yield for hadrons with p_T from $2.0 - 2.3$ GeV/c and photons with p_T from $1.5 - 2.0$ GeV/c. Shows the fully corrected distributions for π^0 photons when tagging included pair photons with p_T above 0.4 GeV/c (black circles), 0.5 GeV/c (blue circles), and 0.6 GeV/c (red circles); and for η photons with the same pair p_T cuts (magenta circles, blue triangles, and red triangles respectively). Also shows inclusive photons (solid black) for comparison.

5.3.6 Systematic Uncertainties

The careful testing of the full method for estimating the decay background gives an estimate for the inherent systematic uncertainty in the result for the decay photon yields, and correspondingly the fragmentation photon yields. From PISA, for the integrated near side yields, a systematic uncertainty of 1% is included. For the estimated p_{out} distributions, the variation from the true distributions seen in PISA is included as a systematic uncertainty as a function of p_{out} , and then propagated to the uncertainty in the p_{out} and j_T rms. Additionally, as the inputs required to estimate the tagged yields depend strongly on the minimum p_T cut placed on pair photons, varying this cut from 400 - 600 MeV/c is used as an estimate of the systematic variation in the resulting π^0 and η photon yields. Figure 5.34 shows the comparison of the tagged $\Delta\phi$ distributions for π^0 and η photons with the different pair photon

p_T cuts; the variation shown is on the order of 1 – 2%.

Chapter 6

Results

6.1 Correlated per-trigger yields

To obtain the hadron-fragmentation photon pair cross-section, as well as jet shape information such as the p_{out} distribution and j_T rms, the first step is to measure the $\Delta\phi$ dependent pair yields, or more commonly the per-trigger yields. As was described in detail in Chapter 5, to obtain the yield of fragmentation photons it is first necessary to estimate the yield of decay photons by tagging π^0 and η photons. Figure 6.1 shows an example of the $\Delta\phi$ dependent per-trigger yields for π^0 (black) and η (blue) decay photons with p_T from 1.5 - 2.0 GeV/c, associated with trigger hadrons with p_T from 2.0 - 2.3 GeV/c. The full set of plots is included in Appendix A. All tagging efficiency and false-tagging corrections are included here, and shaded error bands in the figures presented below and in the Appendix show the associated systematic uncertainties. These distributions are summed using Eq. (5.2), with the hadron and photon p_T dependent $R_{h/\eta}$ determined from PISA (as shown in Figure 5.30), to obtain the full decay photon yield.

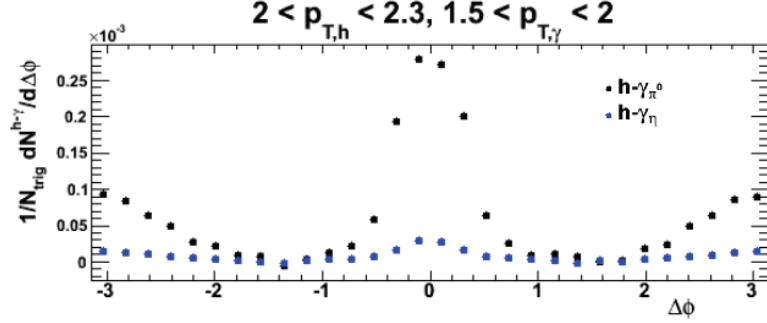


Figure 6.1: Decay photon per-trigger yields, $\frac{1}{N_{trig}} \frac{dN^{h-\gamma}}{d\Delta\phi}$, for trigger hadrons with p_T from $2.0 - 2.3$ GeV/c and associated γ_{π^0} (black) and γ_{η} (blue) photons with p_T from $1.5 - 2.0$ GeV/c.

Figure 6.2 shows the $\Delta\phi$ dependent per-trigger yields for hadron-photon pairs summed over the four hadron p_T bins, from $2.0 - 5.0$ GeV/c, for associated photons in six p_T bins ranging from 1.5 to 15.0 GeV/c. The distributions for the four individual hadron trigger bins are shown in Appendix A. In the figure, the inclusive photon yield is shown in black and the decay photon yield is shown in blue. The fragmentation photon yield, resulting from subtracting the decay yield from the inclusive, is shown in red.

These $\Delta\phi$ dependent distributions can now be used to determine pair properties potentially more directly comparable to quantities calculable in pQCD, such as the pair cross-section and relative yield or the photon p_{out} and $\sqrt{\langle j_T^2 \rangle}$.

6.2 Hadron- γ_{frag} pair cross-section

To obtain the pair cross-section, using Eq. (4.21), the $\Delta\phi$ dependent pair yields are integrated on the near-side, from -0.7 to 0.7 radians. To check the invariance of

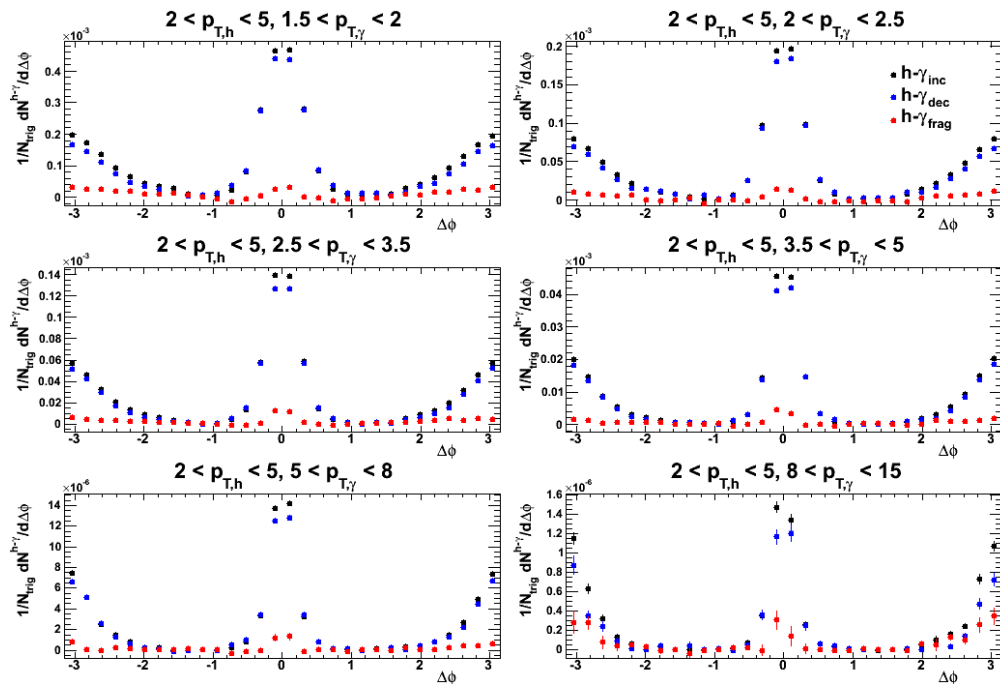


Figure 6.2: $\frac{1}{N_{\text{trig}}} \frac{dN^{h-\gamma}}{d\Delta\phi}$ for trigger hadrons with p_T from 2.0 – 2.3 GeV/c and associated photons in six p_T bins ranging from 1.5-2.0 GeV/c to 8.0 - 15.0 GeV/c. $h - \gamma_{\text{inc}}$ is shown in black, $h - \gamma_{\text{decay}}$ in blue, and $h - \gamma_{\text{frag}}$ in red.

the cross-section, prior to combining data from Run 5 and Run 6, the two runs were compared. Figure 6.3 shows the comparison for inclusive photons associated with hadrons with p_T from 2.0 - 5.0 GeV/c, as a function of photon p_T . The total systematic uncertainty - coming from the uncertainty in the single particle efficiencies, BBC cross-section and efficiency, and the ERT efficiency - is approximately 10%. The comparison shows agreement well within the overall uncertainty, with less than a 5% variation between the two data sets across the full photon p_T range.

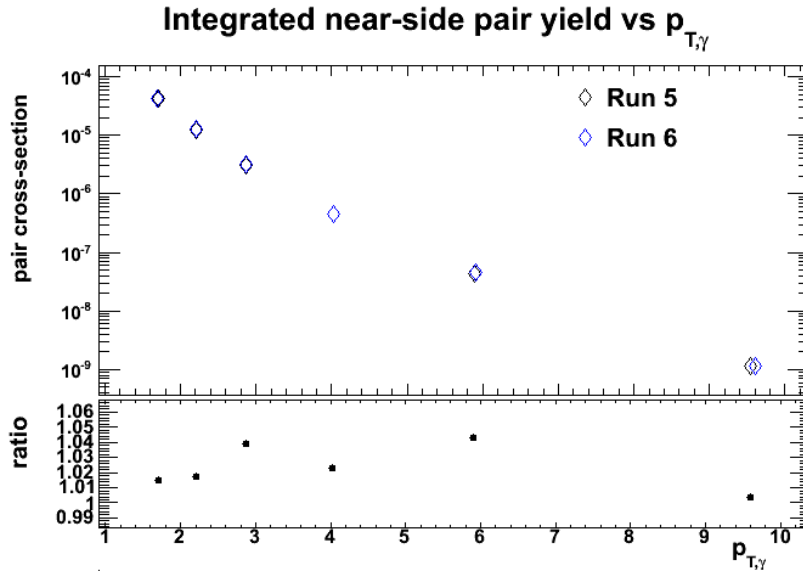


Figure 6.3: Top: Integrated near-side ($-0.7 < \Delta\phi < 0.7$) $h - \gamma_{inc}$ pair cross-section sum over all hadron bins, as a function of photon p_T , for Run 5 (black) and Run 6 (blue). Bottom: ratio of the cross-sections for the two data sets for comparison, with $< 5\%$ variation between the Runs across the full p_T range.

Combining the two runs, we can determine the yield for fragmentation photons using the subtracted $\Delta\phi$ distributions. Figure 6.4 shows the resulting differential cross-section for fragmentation photons in each of the four hadron trigger p_T bins,

as a function of photon p_T . Here the differential is in terms of both the hadron and photon momentum on the left, and integrated over hadron momentum on the right. This pair cross-section is directly related to the pair fragmentation function, $D(h, \gamma)$ [137], which in turn depends on the quark-to-photon fragmentation function. The systematic uncertainties, coming from the limitations in the method for estimating the decay photon background, are indicated by the shaded error bands. The overall scale uncertainty of 10% is not included here.

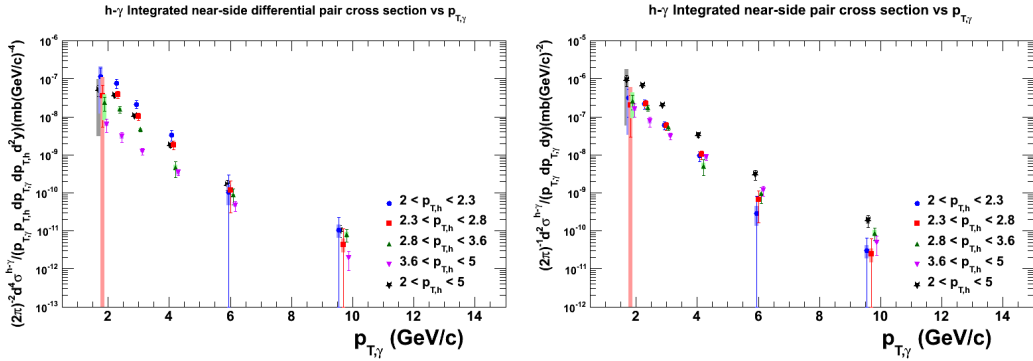


Figure 6.4: Integrated near-side ($-0.7 < \Delta\phi < 0.7$) $h - \gamma_{frag}$ pair cross-section for each trigger hadron p_T bin, as well as for the sum over all hadron bins, as a function of photon p_T . Left: differential in terms of both hadron and photon momentum. Right: integrated over hadron momentum.

6.3 Relative pair yield

The scale uncertainties discussed previously contribute to the total systematic uncertainty for the pair cross-section, weakening the constraining power of the measurement. However, the relative conditional yield for fragmentation photons, com-

pared to inclusive photons, depends only on the uncertainties associated with the estimation of the decay photon contribution. Again, a good check of the accuracy of the estimate for the systematic uncertainty is to compare the results obtained from the two Runs separately, as they will have independent inputs for corrections to the tagged photon yields, leading to different sensitivity to systematic effects. Figure 6.5 shows a comparison of the ratio of fragmentation photon pairs to inclusive for the two Runs, summed over hadron trigger p_T , with the systematic uncertainties determined as described in Section 5.3.6.

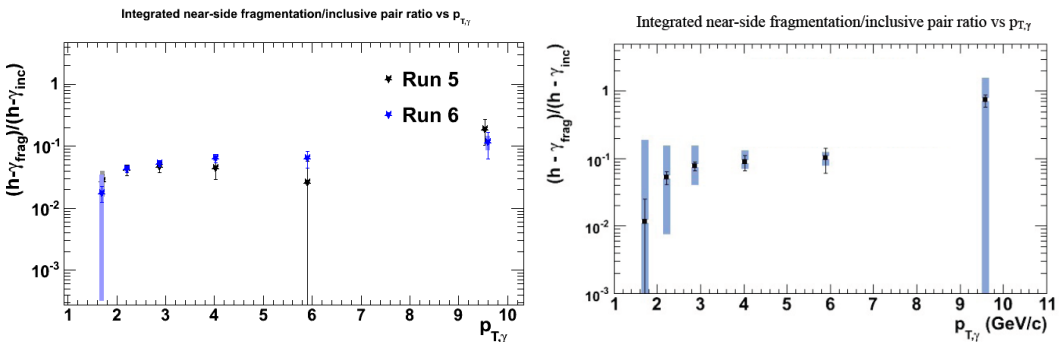


Figure 6.5: Left: ratio of integrated $h - \gamma_{frag}$ to $h - \gamma_{inc}$ yields, integrated from -0.7 to 0.7 in $\Delta\phi$, summed over all hadron trigger p_T bins, as a function of photon p_T for Run 5 (black) and Run 6 (blue) separately. Right: ratio of integrated $h - \gamma_{frag}$ to $h - \gamma_{inc}$, integrated from -0.5 to 0.5 in $\Delta\phi$ from Run 5 with the old method, for hadrons with $2.0 < p_T < 5.0$ GeV/c as a function of photon p_T .

The agreement between the two runs is well within the systematic uncertainties assigned to the method. Also shown in the figure is the ratio determined from Run 5 using the original method for determining the false tagging correction using event mixing. The two methods produce similar results, while the dramatic improvement in systematic uncertainties achieved by using tagging probabilities is clear.

The consistent results across data sets and using two completely different methods demonstrates the robustness of the measurement. For the final result we combine the runs to get the full statistical sample. The ratio of the integrated near-side yield for hadron-photon pairs in each of the hadron trigger p_T ranges, as well as for the combined p_T range, as a function of photon p_T is shown in Figure 6.6.

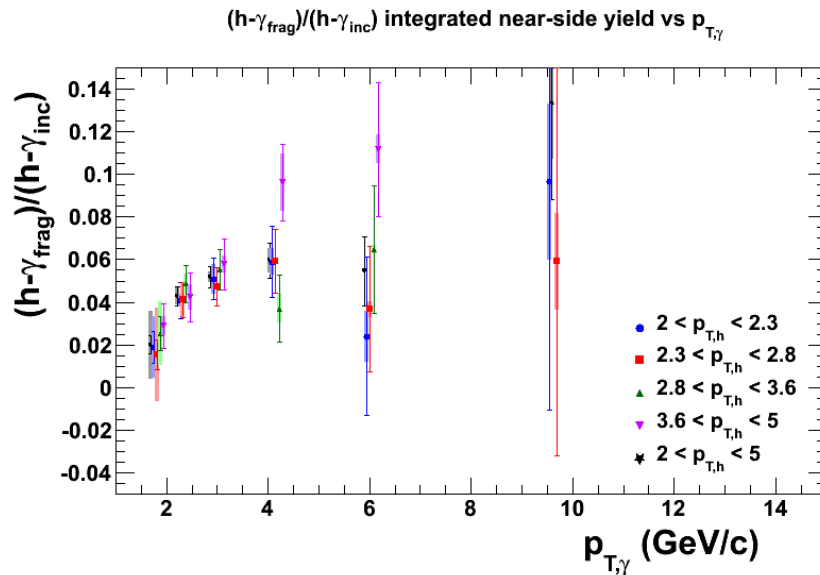


Figure 6.6: Ratio of integrated $h - \gamma_{frag}$ to $h - \gamma_{inc}$ yields, with an integration window from -0.7 to 0.7 in the $\Delta\phi$ for each trigger hadron p_T bin, as well as for the sum over all hadron bins, as a function of photon p_T .

Previous measurements of the direct photon cross-section in $p + p$ at PHENIX have been done with and without an isolation cut. In those cases, the photons were rejected if there was more than 10% of the photon energy deposited in the detector with-in a fixed radius - ~ 0.5 radians - around the photon. The primary motivation of applying the isolation cut was to reduce systematic uncertainties in the cross-

section resulting from residual decay photon contamination, since decay photons are typically not isolated. However, the isolation cut should in principle also remove the contribution to the cross-section from fragmentation photons, leaving only leading order direct photons. Thus, it can be compared to theoretical calculations for the relative yield. Figure 6.7 shows the ratio of isolated photons to inclusive direct photons, with comparisons to various pQCD predictions. There are somewhat large theoretical uncertainties resulting from the complication of including the isolation cut in the calculations [115]. Again, this is a true ratio of cross-sections, as apposed to the ratio of pair yields measured in this analysis; however, a rough comparison is possible.

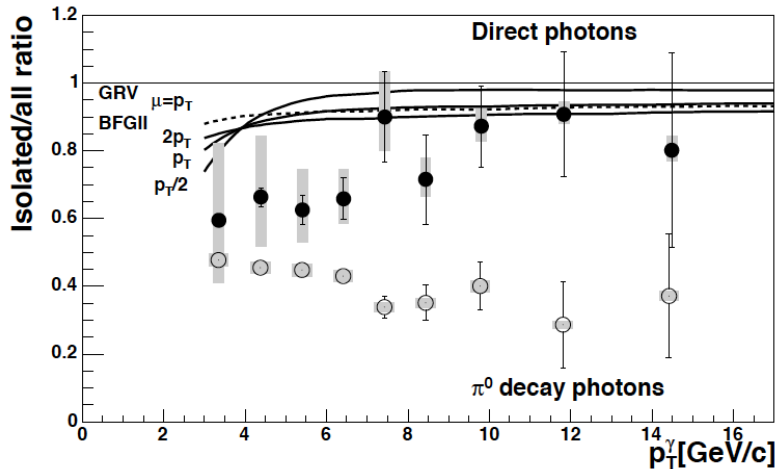


Figure 6.7: Ratio of isolated direct photons to all direct photons as a function of photon p_T (solid points) as well as several theoretical NLO pQCD predictions. Also shown is the same ratio for decay photons (shaded points) which shows the reduction in decay photon background achieved by applying isolation cuts.[115]

To compare with the results obtained here, some manipulation of the data is required, as the ratio shown in Figure 6.7 involves only direct photons, while the

ratio of yields obtained in this analysis is for fragmentation photons to all photons, including decay photons. Using the previously measured ratio of direct photons to inclusive photons as a function of photon p_T , for $p + p$ collisions at the same energy ($\sqrt{s} = 200\text{GeV}$) shown in Figure 6.8, we can convert between the two types of ratios.

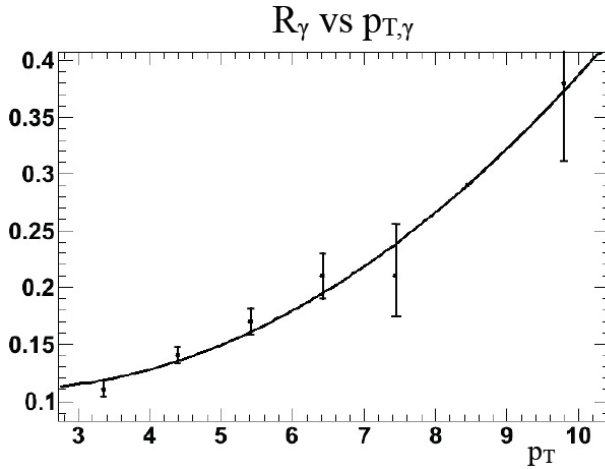


Figure 6.8: Ratio of direct photons to all photons as a function of photon p_T . Plotted from values published in [115], with an approximate polynomial fit to extrapolate between points.

Assuming the cross-section of fragmentation photons can be approximated as $1 - N_{iso}$, the measured ratio of isolated direct photons to all direct photons can be converted to a ratio of fragmentation photons to inclusive photons using

$$\frac{N_{frag}}{N_{inc}} = \frac{1 - N_{iso}}{N_{direct}} R_\gamma \quad (6.1)$$

where

$$R_\gamma = \frac{N_{direct}}{N_{inc}}. \quad (6.2)$$

Figure 6.9 shows the ratio of fragmentation photon-hadron pairs to inclusive photon-hadron pairs summed over hadron p_T compared to the estimate from the previous result using Eq. (6.1). The uncertainties shown on the previous result do not include the uncertainty in R_γ , and are not obtained from a direct subtraction of isolated direct photons from inclusive direct photons, so the statistical errors shown are underestimated. However, the comparison shows good agreement, despite the indirect nature of the relationship between the two measurements.

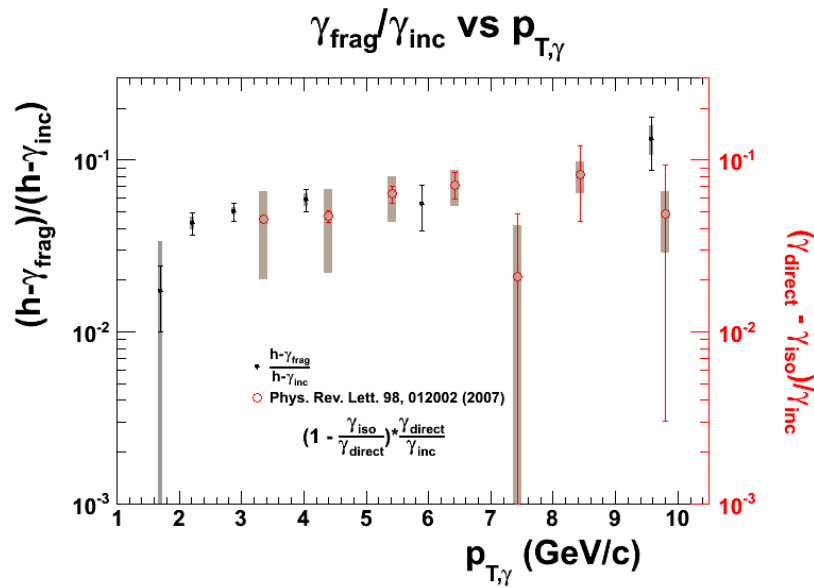


Figure 6.9: Ratio of integrated $h - \gamma_{frag}$ to $h - \gamma_{inc}$ yields, with an integration window from -0.7 to 0.7 in the $\Delta\phi$, summed over all hadron trigger p_T bins, as a function of photon p_T (solid black circles), compared with the estimated fragmentation photon yield using the ratio of isolated direct photons to inclusive direct photons (open red circles) from [115].

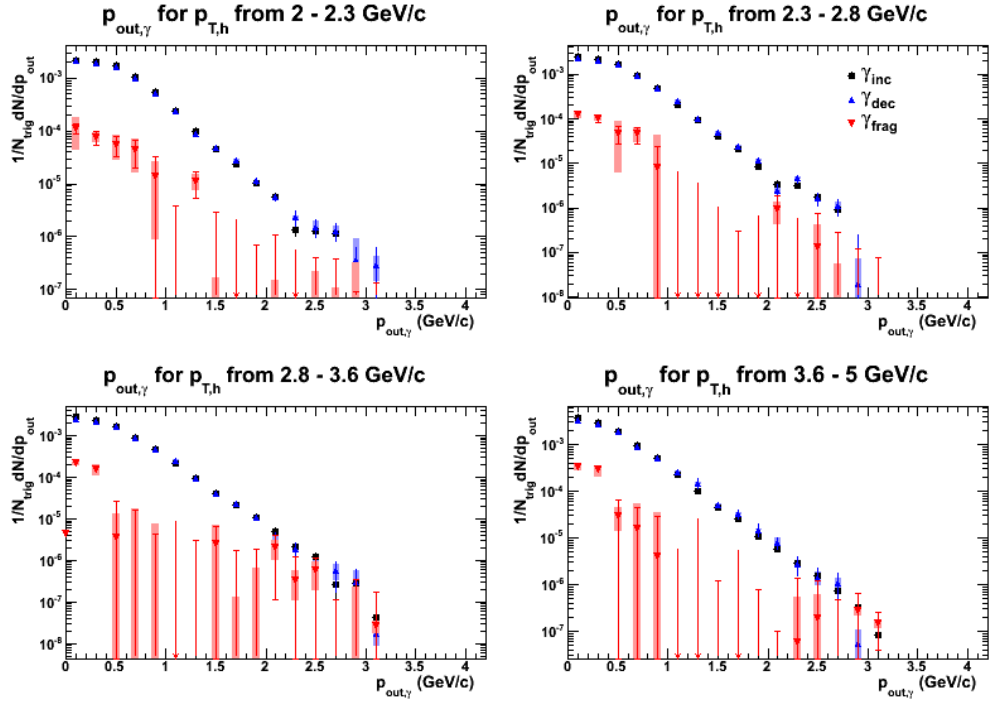


Figure 6.10: p_{out} distribution for photons with p_T from $1.5 - 8.0$ GeV/c, within $|\Delta\phi| < 0.7$ of a trigger hadron, for each of the four trigger p_T bins: $2.0 - 2.3$ GeV/c (top left), $2.3 - 2.8$ GeV/c (top right), $2.8 - 3.6$ GeV/c (bottom left), and $3.6 - 5.0$ GeV/c (bottom right). Inclusive photons are shown in black (circles), decay photons in blue (up triangles), and fragmentation photons in red (down triangles). For fragmentation photons, in the case where the point is more than one σ below zero, the 2σ limit is indicated with an arrow.

6.4 Associated photon p_{out}

Having established that there is a non-zero yield of fragmentation photons correlated with a high p_T hadron, and that both the yield and the $\Delta\phi$ dependent correlation can be resolved, it should be possible to extend the analysis to obtain more differential measurements of how these fragmentation photons are distributed within jets. As discussed previously, this is done using two particle correlations to construct

the near-side p_{out} distribution for photons associated with the trigger hadron.

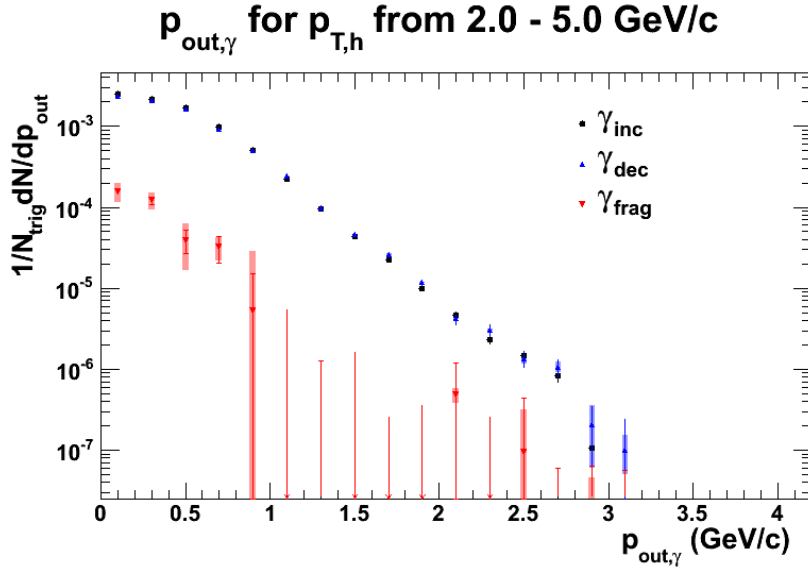


Figure 6.11: p_{out} distribution for photons with p_T from 1.5 – 8.0 GeV/c, within $|\Delta\phi| < 0.7$ of a trigger hadron, over the full hadron p_T range of 2.0 – 5.0 GeV/c. Inclusive photons are shown in black (circles), decay photons in blue (up triangles), and fragmentation photons in red (down triangles). For fragmentation photons, in the case where the point is more than one σ below zero, the 2σ limit is indicated with an arrow.

To obtain the full p_{out} distributions, we sum over photon p_T within each trigger hadron p_T bin. However, to minimize the effects of fluctuations in regions where statistics are poor (large $\Delta\phi$ where there is low acceptance, and high p_T), the p_{out} distributions obtained are restricted to photons with p_T from 1.5 – 8.0 GeV/c, and with $|\Delta\phi| < 0.7$ for the hadron-photon pair. Figure 6.10 shows the resulting p_{out} distributions for inclusive photons (black), decay photons (blue), and fragmentation photons (red), for each trigger hadron momentum range. Summing over hadron p_T bins gives the total p_{out} distribution shown in Figure 6.11.

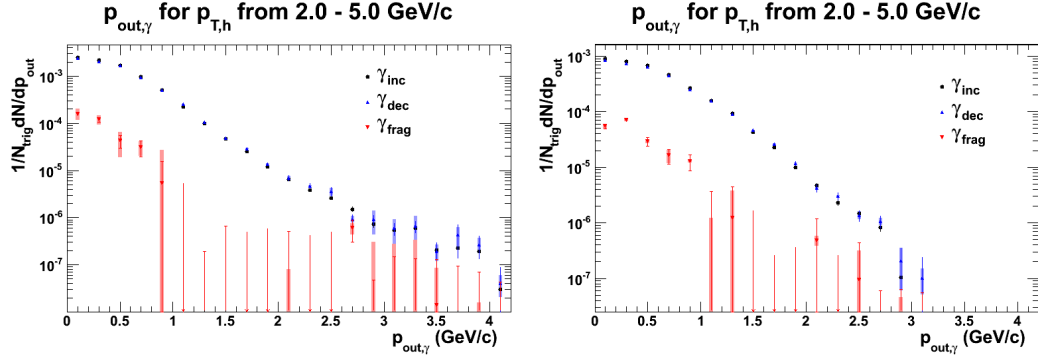


Figure 6.12: Left: p_{out} distribution for photons with p_T from $1.5 - 15.0$ GeV/c. Right: p_{out} distribution for photons with p_T from $2.0 - 8.0$ GeV/c. Both for photons within $|\Delta\phi| < 0.7$ of a trigger hadron, over the full hadron p_T range of $2.0 - 5.0$ GeV/c. Inclusive photons are shown in black (circles), decay photons in blue (up triangles), and fragmentation photons in red (down triangles). For fragmentation photons, in the case where the point is more than one σ below zero, the 2σ limit is indicated with an arrow.

The choice to use photons with p_T from $1.5 - 8.0$ GeV/c was made to limit the effects of the large statistical fluctuations for higher p_T photons. However, it is useful to see how the variation in the p_{out} distributions is effected by the p_T range of the photon. Figure 6.12 shows the summed p_{out} - hadrons with p_T from $2.0 - 5.0$ GeV/c - for the case where the full photon p_T range of $1.5 - 15.0$ GeV/c was included, and where only photons with p_T from $2.0 - 8.0$ GeV/c were included.

6.5 $\sqrt{\langle p_{out}^2 \rangle}$ and $\sqrt{\langle j_T^2 \rangle}$

Although there are regions of p_{out} where the yield for fragmentation photons is consistent with zero, when comparing the general shapes of these distributions for inclusive photons and fragmentation photons we find that they are qualitatively differ-

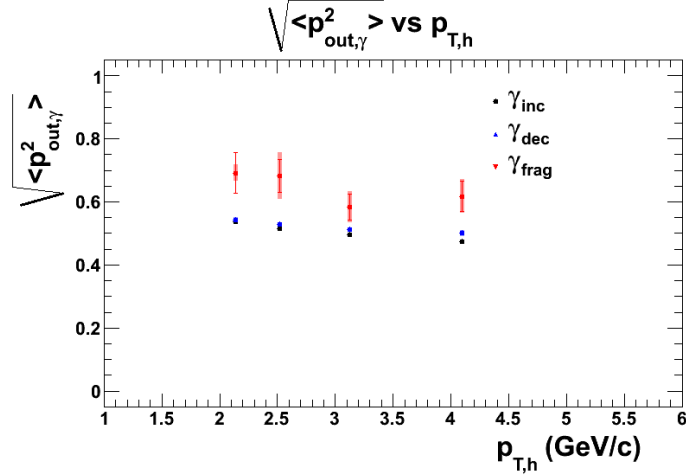


Figure 6.13: $\sqrt{\langle p_{out}^2 \rangle}$ versus trigger hadron p_T , for photons with p_T from $1.5 - 8.0$ GeV/c, within $|\Delta\phi| < 0.7$ of a trigger hadron. The case for inclusive photons is shown in black (circles), decay photons in blue (up triangles), and fragmentation photons in red (down triangles).

ent. To quantify any differences between the distribution of fragmentation photons within the jet and those produced by hadron decays, we measure the root-mean-square (rms) value for p_{out} in each trigger bin. Figure 6.13 shows the comparison of $\sqrt{\langle p_{out}^2 \rangle}$ for inclusive (black), decay (blue), and fragmentation (red) photons. For the full p_{out} distribution combining the four hadron trigger bins, the $\sqrt{\langle p_{out}^2 \rangle}$ is 0.5133 ± 0.00065 (stat) for inclusive photons, 0.5271 ± 0.0012 (stat) ± 0.0018 (sys) for decay photons, and 0.654 ± 0.0278 (stat) ± 0.0240 (sys) for fragmentation photons.

Again, it is useful to study the resulting $\sqrt{\langle p_{out}^2 \rangle}$ based on the choice of momentum range for the associated photon. Figure 6.14 shows the $\sqrt{\langle p_{out}^2 \rangle}$ versus trigger hadron p_T for photons with p_T from $1.5 - 15.0$ GeV/c and for photons with p_T from $2.0 - 8.0$ GeV/c. Here we see that the systematic uncertainties become somewhat

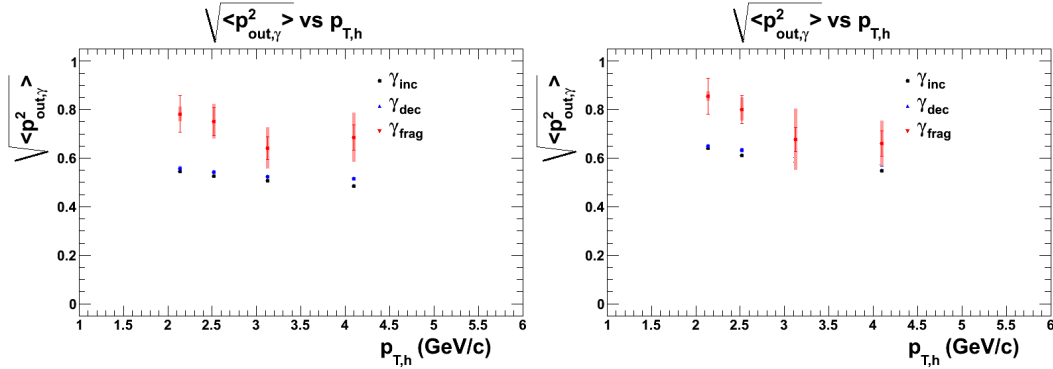


Figure 6.14: $\sqrt{\langle p_{out}^2 \rangle}$ versus trigger hadron p_T , for photons within $|\Delta\phi| < 0.7$ of a trigger hadron, with p_T from 1.5 – 15.0 GeV/c on the left and from 2.0 – 8.0 GeV/c on the right. The case for inclusive photons is shown in black (circles), decay photons in blue (up triangles), and fragmentation photons in red (down triangles).

larger if we include the highest momentum photons or exclude the lowest photon p_T bin, where the large statistics help to reduce sensitivity to systematic variations.

Already, this measure of the p_{out} r.m.s. seems to suggest that fragmentation photons tend to have a broader distribution within the jet compared to photons produced through the decay of hadron fragments. However, p_{out} is not directly related to the distribution of particles relative to the jet axis, as it is related to the $\Delta\phi$ between the photon and the trigger hadron rather than the jet. To get closer to the true distribution of fragmentation photons in jets, then, we use Eq. (4.28) to convert from $\sqrt{\langle p_{out}^2 \rangle}$ to $\sqrt{\langle j_T^2 \rangle}$, removing the effects of the trigger hadron.

The calculation for $\sqrt{\langle j_T^2 \rangle}$ involves inputs from other distributions determined in the data, namely the p_{out} for the hadron with respect to the photon, the ratio of photon to hadron p_T , x_h , and its inverse. Figure 6.15 shows an example of the hadron p_{out} and the x_h for one of the trigger p_T ranges used. The full set of distributions is

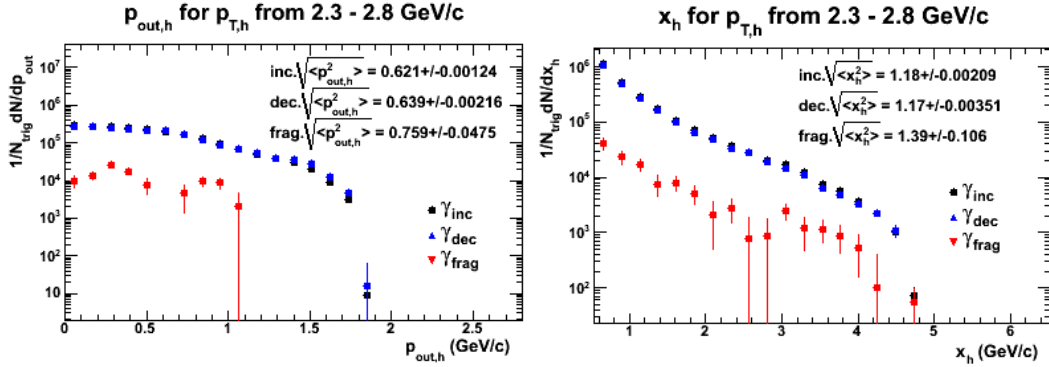


Figure 6.15: Left: p_{out} distribution for hadrons within $|\Delta\phi| < 0.7$ of a photon with p_T from 1.5 – 8.0 GeV/c, for hadrons with p_T from 2.3 – 2.8 GeV/c. Right: $x_h = p_{T,\gamma}/p_{T,h}$ distribution for photons with p_T from 1.5 – 8.0 GeV/c, for hadrons with p_T from 2.3 – 2.8 GeV/c. Inclusive photons are shown in black (circles), decay photons in blue (up triangles), and fragmentation photons in red (down triangles).

shown in Appendix B. Figure 6.16 shows the resulting $\sqrt{\langle j_T^2 \rangle}$ for inclusive (black), decay (blue), and fragmentation (red) photons. Again fragmentation photons are found to have a broader distribution relative to the jet axis.

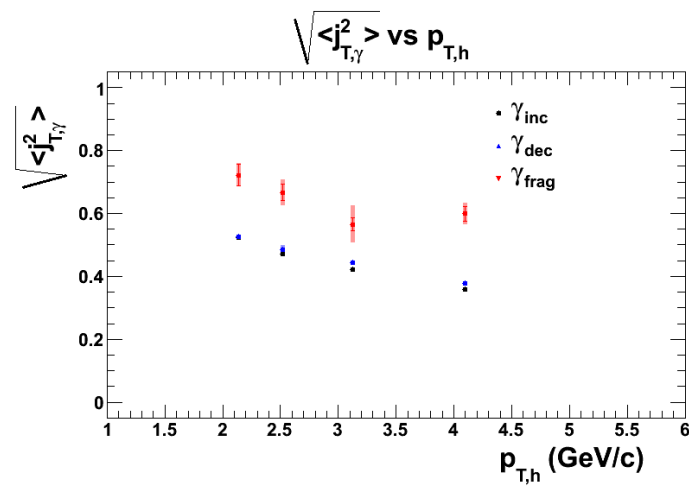


Figure 6.16: $\sqrt{\langle j_{T,\gamma}^2 \rangle}$ versus trigger hadron p_T , for photons with p_T from 1.5 – 8.0 GeV/c, within $|\Delta\phi| < 0.7$ of a trigger hadron. The case for inclusive photons is shown in black (circles), decay photons in blue (up triangles), and fragmentation photons in red (down triangles).

Chapter 7

Conclusions

Using the method of two-particle correlations, the hadron-fragmentation photon pair cross-section has been measured over a range of hadron and photon p_T . The fraction of inclusive hadron-photon pairs produced directly from the parton fragmentation was also determined from the cross-section measurement. A significant yield of fragmentation photons was observed with a relative yield consistent with expectations from previous, less precise and less direct measurements of leading-order direct photons. Additionally, the first measurements of p_{out} , $\sqrt{\langle p_{out}^2 \rangle}$, and $\sqrt{\langle j_T^2 \rangle}$ for fragmentation photons were obtained, and they indicate a slightly broader distribution within the jet relative to photons produced as part of a hadronic decay.

The initial motivation for developing a method for directly measuring fragmentation photons - using correlations to separate them from leading-order direct photons - was to study modification to the production of fragmentation photons in heavy-ion collisions. However, even in $p + p$, where the inclusive direct photon cross-section is well described by pQCD, there are large theoretical uncertainties on the quark-to-photon fragmentation function. Therefore, the analysis presented

here serves two purposes. It establishes the baseline $p + p$ measurement, necessary to quantify possible modifications to the production of fragmentation photons in the heavy ion environment, and it provides important constraints for pQCD calculations of direct photon production.

The ratio of pair yields is not a direct measure of the total relative fragmentation photon cross-section. Nonetheless, the hadron trigger condition and limited angular integration range serve to ensure that the measured photons are in fact produced as part of a jet. Therefore, such restrictions make these pair yields an approximate measure of the yield of jet-associated photons, which should correspond to photons produced beyond leading order in pQCD. For this reason, we can compare this result to predictions for the ratio of the cross-section of fragmentation photons to all direct photons (see Figure 2.23).

As in comparisons with measurements using isolation cuts on single direct photons, some manipulation of the data is necessary; the theoretical prediction is a ratio of direct photons only. Using the fit to R_γ shown in Figure 6.8 as an estimate for the p_T dependence - because the p_T bins used in this analysis do not match those previously used to determine R_γ - the ratio of yields shown in Figure 6.6 can be converted to a ratio of fragmentation to direct photons :

$$\frac{N_{frag}}{N_{dir}} = \frac{1}{R_\gamma} \frac{N_{frag}}{N_{inc}} . \quad (7.1)$$

While this comparison is not direct - meaning some variation between data and theory might be expected - the agreement is relatively good. This comparison gives

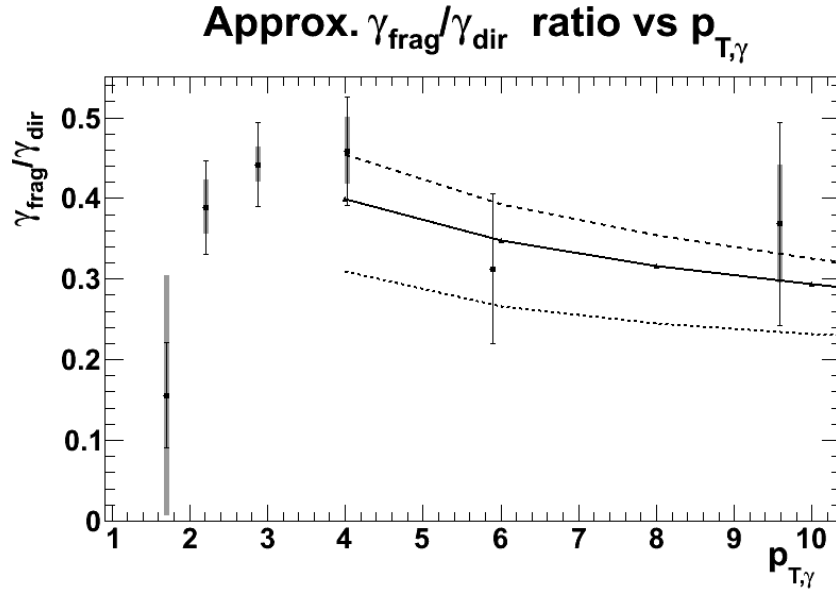


Figure 7.1: Effective ratio of integrated $h - \gamma_{frag}$ to $h - \gamma_{direct}$ yields, integrated within $|\Delta\phi| < 0.7$ and summed over all hadron trigger p_T bins, as a function of photon p_T (solid black points) - errors from R_γ are not shown. A comparison to a prediction based on an NLO pQCD simulation is shown by the solid line, with theoretical uncertainties set by varying the renormalization scale shown by the dashed lines [110].

some idea of the constraining power of the current results. The systematic uncertainties in the region accessible by pQCD are already small, so a simple increase in statistics would serve to further constrain theory.

The use of two-particle correlations allowed for the extension of these basic yield measurements to more discriminatory measures of the distribution of fragmentation photons within the jet, using the associated photon near-side p_{out} distributions. The root-mean-square j_T for photons in jets can be compared to previous measurements of the j_T for hadrons associated with high $p_T \pi^0$ triggers. The j_T for hadrons is expected to be independent of species, so the j_T for π^0 s and η s produc-

ing decay photons should be similar to that of other hadrons. However, the j_T for the decay photons will include the effects of the decay kinematics. Comparing the fragmentation photon $\sqrt{\langle j_T^2 \rangle}$ to that previously measured for hadrons, it appears to be comparable in the overlapping p_T range, but tends to slightly higher values for lower trigger p_T .

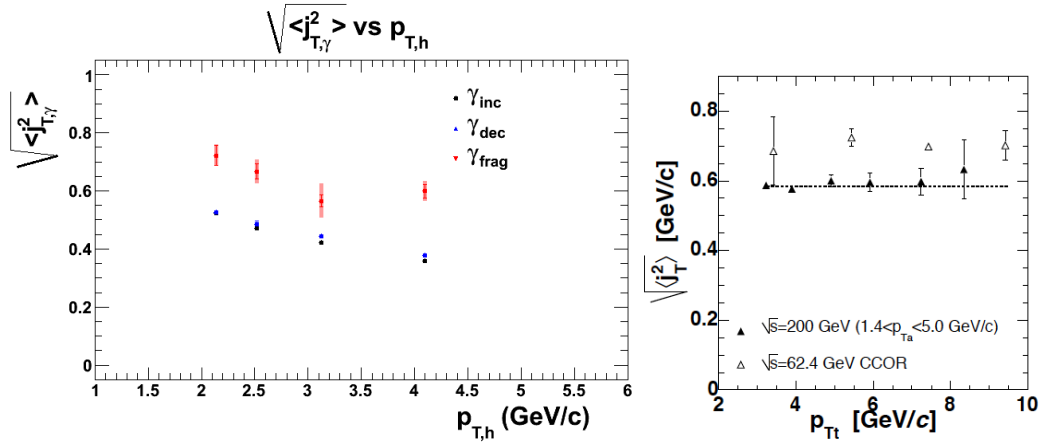


Figure 7.2: Left: $\sqrt{\langle j_T^2 \rangle}$ versus trigger hadron p_T , for photons with p_T from 1.5 – 8.0 GeV/c , within $|\Delta\phi| < 0.7$ of a trigger hadron, for inclusive (black circles), decay (blue up triangles), and fragmentation (red down triangles) photons. Right: $\sqrt{\langle j_T^2 \rangle}$ versus π^0 trigger p_T , for associated hadrons with p_T from 1.4 – 5.0 GeV/c [138].

The j_T distribution of fragmentation photons within jets is a more direct measure of the shower profile for the initial parton. The distribution of radiated photons is not obfuscated by the hadronization process, as it is with gluons. As a result, studies of the p_{out} and j_T for fragmentation photons are useful tests of parton showering models. For example, using PYTHIA simulations to make a qualitative comparison of the inclusive photon p_{out} (black) and fragmentation photon p_{out} (blue), shown in Figure 7.3, we find that standard simulations of parton showers reproduce the more

broad distribution for fragmentation photons indicated by the data. One might expect the hadronization process to lead to a narrowing of the final hadron j_T (or p_{out}) relative to the initial fragmented gluon and quark j_T distributions. This narrowing would not be reflected in the photon p_{out} distributions, which more directly probe the showering of the initial parton, without the need for complex hadronization models. In addition, the observed p_{out} can provide a test of the validity of models for describing the non-perturbative component of the quark-to-photon fragmentation function. The non-perturbative component photon production is typically modeled by the decay of massive vector mesons [139], which conceptually could lead to a depletion of photons at small p_{out} as a result of the vector meson mass. In both cases, comparisons of predictions for the angular distribution of fragmentation photons around the jet axis to what has been measured here is an important test of the model.

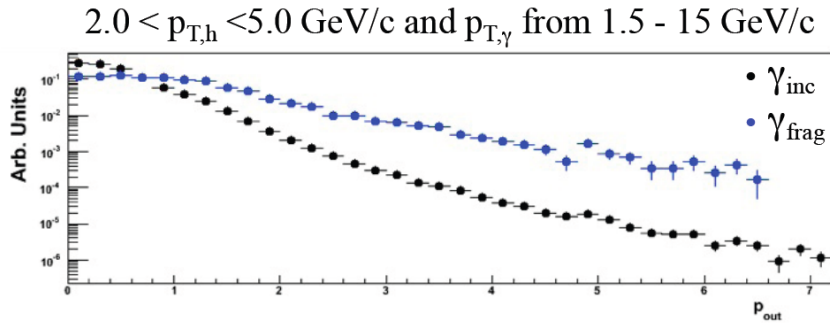


Figure 7.3: p_{out} distribution for inclusive (black) and fragmentation (blue) photons generated using PYTHIA 6.4. [140]

Careful attention to how the background from decay photons is handled has helped keep systematic uncertainties small, even at relatively low photon momen-

tum. This success suggests that future measurements using the same method for slightly higher multiplicity environments, such as $d + Au$, should be possible. In the heavy-ion environment, where the per event multiplicity is much higher, tagging photons from π^0 and η decays becomes much less efficient, and the rate for false-tagging is much higher. As a result, further study of how to optimize the removal of decay photons will be necessary before corresponding measurements of fragmentation photons in $Au + Au$ collisions will be possible. The method used in this analysis may be feasible in the slightly lower multiplicity $Cu + Cu$ environment. However, the large false-tagging background and lower tagging efficiency mean that the current statistics available are unlikely to be sufficient.

Similarly, there has been recent success applying full jet reconstruction, even with the limited acceptance of the PHENIX detector and high multiplicity environment of $Cu + Cu$ collisions [141; 142]. These results suggest that less ambiguous measurements using directly reconstructed jets and associated direct photons to measure the properties of fragmentation photons may be possible in the future. In such measurements, it will be possible to measure the j_T distribution for fragmentation photons within the jet directly and further constrain the parton shower profile, as well as to provide a more direct constraint on the quark-to-photon fragmentation function [143].

Bibliography

- [1] D. J. Gross and F. Wilczek, *Ultraviolet Behavior of Non-Abelian Gauge Theories*, Phys. Rev. Lett. **30** **1343** (1973). [2](#)
- [2] H. D. Politzer, *Reliable Perturbative Results for Strong Interactions*, Phys. Rev. Lett. **30** **1346** (1973). [2](#), [31](#)
- [3] J. C. Collins and M. J. Perry, *Superdense Matter: Neutrons or Asymptotically Free Quarks?*, Phys. Rev. Lett. **34** **1353** (1975). [2](#), [5](#)
- [4] E. V. Shuryak, *Quantum Chromodynamics and the Theory of Superdense Matter*, Phys. Rep. **61** **71** (1980). [3](#)
- [5] K. Wilson, *Confinement of quarks*, Phys. Rev. **D10**, 2445 (1974). [3](#)
- [6] A. Bazavov et al., *Equation of state and QCD transition at finite temperature*, Phys. Rev. **D80**, 014504 (2009) [[0903.4379](#)]. [vi](#), [4](#), [5](#)
- [7] F. Karsch, *Lattice QCD at High Temperature and Density.*, in *Lectures on Quark Matter*, 209–249 (Lecture Notes in Physics, 2002). [5](#), [19](#)
- [8] E. Laermann and O. Philipsen, *Lattice QCD at finite temperature*, Annual Review of Nuclear and Particle Science **53**, 163 (2003) [<http://dx.doi.org/10.1146/annurev.nucl.53.041002.110609>]. [5](#)
- [9] E. Shuryak and I. Zahed, *Towards a theory of binary bound states in the quark gluon plasma*, Phys. Rev. **D70**, 054507 (2004) [[hep-ph/0403127](#)]. [5](#)
- [10] Graphic designed by W. Holtzmann. [vi](#), [5](#)
- [11] J. D. Bjorken, *Highly Relativistic Nucleus-Nucleus Collisions: The Central Rapidity Region*, Phys. Rev. **D27**, 140 (1983). [6](#)

- [12] S. S. Adler et al. (PHENIX), *Systematic Studies of the Centrality and $\sqrt{s_{NN}}$ Dependence of $dE_T/d\eta$ and $dN_{ch}/d\eta$ in Heavy Ion Collisions at Mid-rapidity*, Phys. Rev. C **71** 034908 (2005). [6](#)
- [13] Graphic designed by M. Kaneta. [vi](#), [7](#)
- [14] C. Adler et al., *Elliptic flow from two- and four-particle correlations in Au + Au collisions at $\sqrt{s_{NN}} = 130\text{GeV}$* , Phys. Rev. C **66** 3, 034904 (2002). [vii](#), [8](#)
- [15] K. Adcox et al. (PHENIX), *Flow measurements via two-particle azimuthal correlations in Au + Au collisions at $\sqrt{s_{NN}} = 130\text{ GeV}$* , Phys. Rev. Lett. **89**, 212301 (2002) [[nucl-ex/0204005](#)]. [9](#)
- [16] P. Huovinen et al., *Radial and elliptic flow at RHIC: further predictions*, Phys. Lett. **B503**, 58 (2001) [[hep-ph/0101136](#)]. [9](#)
- [17] T. Hirano and M. Gyulassy, *Perfect Fluidity of the Quark Gluon Plasma Core as Seen through its Dissipative Hadronic Corona*, Nucl. Phys. **A769**, 71 (2006) [[nucl-th/0506049](#)]. [9](#)
- [18] J. D. Bjorken, *Energy Loss of Energetic Partons in Quark - Gluon Plasma: Possible Extinction of High p_T Jets in Hadron - Hadron Collisions* (1982), fERMILAB-PUB-82-059-THY. [10](#), [13](#)
- [19] M. Miller et al., *Glauber modeling in high energy nuclear collisions*, Ann. Rev. Nucl. Part. Sci. **57**, 205 (2007) [[nucl-ex/0701025](#)]. [10](#)
- [20] C. Y. Wong, *Introduction to High-Energy Heavy-Ion Collisions* (World Scientific, 1994). [10](#)
- [21] S. S. Adler et al. (PHENIX), *High p_T charged hadron suppression in Au + Au collisions at $\sqrt{s_{NN}} = 200\text{ GeV}$* , Phys. Rev. **C69**, 034910 (2004) [[nucl-ex/0308006](#)]. [vii](#), [12](#)
- [22] S. S. Adler et al. (PHENIX), *Absence of suppression in particle production at large transverse momentum in $\sqrt{s_{NN}} = 200\text{ GeV}$ d + Au collisions*, Phys. Rev. Lett. **91**, 072303 (2003) [[nucl-ex/0306021](#)]. [12](#)
- [23] X.-N. Wang and M. Gyulassy, *Gluon shadowing and jet quenching in A + A collisions at $\sqrt{s} = 200\text{ GeV}$* , Phys. Rev. Lett. **68**, 1480 (1992) [<http://dx.doi.org/10.1103/PhysRevLett.68.1480>]. [13](#)

- [24] R. Baier, D. Schiff, and B. G. Zakharov, *Energy Loss in Perturbative QCD*, Annual Review of Nuclear and Particle Science **50**, 37 (2000) [<http://dx.doi.org/10.1146/annurev.nucl.50.1.37>]. 13
- [25] M. Gyulassy, P. Levai, and I. Vitev, *Jet tomography of Au + Au reactions including multi-gluon fluctuations*, Phys. Lett. **B538**, 282 (2002) [[nucl-th/0112071](#)].
- [26] P. Arnold, G. Moore, and L. Yaffe, *Transport coefficients in high temperature gauge theories: (I) Leading-log results*, JHEP **11**, 001 (2000) [[hep-ph/0010177](#)].
- [27] C. Salgado and U. Wiedemann, *Calculating quenching weights*, Phys. Rev. **D68**, 014008 (2003) [[hep-ph/0302184](#)].
- [28] A. Majumder, *Resolving the plasma profile via differential single inclusive suppression*, Phys. Rev. **C75**, 021901 (2007) [[nucl-th/0608043](#)]. 13
- [29] K. Adcox et al., *Formation of dense partonic matter in relativistic nucleus-nucleus collisions at RHIC: Experimental evaluation by the PHENIX Collaboration*, Nucl. Phys. **A757**, 184 (2005) [<http://dx.doi.org/10.1016/j.nuclphysa.2005.03.086>]. 14
- [30] A. Adare et al. (PHENIX), *Dihadron azimuthal correlations in Au + Au collisions at $\sqrt{s_{NN}} = 200$ GeV*, Phys. Rev. **C78**, 014901 (2008) [[0801.4545](#)]. vii, 14, 16
- [31] K. Adcox et al. (PHENIX), *Suppression of hadrons with large transverse momentum in central Au + Au collisions at $\sqrt{s_{NN}} = 130$ GeV*, Phys. Rev. Lett. **88**, 022301 (2002) [[nucl-ex/0109003](#)]. 15
- [32] B. Sahlmueller (PHENIX), *Photons at PHENIX*, PoS 035 (2009), hIGH-PTPHYSICS09 [[0904.4764](#)]. vii, 18
- [33] S. S. Adler et al. (PHENIX), *Centrality dependence of direct photon production in $\sqrt{s_{NN}} = 200$ GeV Au + Au collisions*, Phys. Rev. Lett. **94**, 232301 (2005) [[nucl-ex/0503003](#)]. 18
- [34] S. Turbide, R. Rapp, and C. Gale, *Hadronic production of thermal photons*, Phys. Rev. **C69**, 014903 (2004) [<http://dx.doi.org/10.1103/PhysRevC.69.014903>]. 19

- [35] A. Adare et al. (PHENIX), *Enhanced production of direct photons in Au + Au collisions at $\sqrt{s_{NN}} = 200$ GeV and implications for the initial temperature*, Phys. Rev. Lett. **104**, 132301 (2010) [[0804.4168](#)]. [viii](#), [19](#), [20](#)
- [36] S. S. Adler et al. (PHENIX Collaboration), *Measurement of Direct Photon Production in $p + p$ Collisions at $\sqrt{s} = 200$ GeV*, Phys. Rev. Lett. **98**, 012002 (2007) [<http://dx.doi.org/10.1103/PhysRevLett.98.012002>]. [19](#)
- [37] G.-Y. Qin et al., *Radiative and Collisional Energy Loss, and Photon-Tagged Jets at RHIC*, Eur. Phys. J. **C61**, 819 (2009) [[0809.2030](#)]. [viii](#), [21](#)
- [38] S. Turbide et al., *Energy loss of leading hadrons and direct photon production in evolving quark-gluon plasma*, Phys. Rev. **C72**, 014906 (2005) [[hep-ph/0502248](#)]. [20](#)
- [39] R. Fries, B. Muller, and D. Srivastava, *Centrality dependence of direct photons in Au + Au collisions at $\sqrt{s_{NN}} = 200$ GeV*, Phys. Rev. **C72**, 041902 (2005) [[nucl-th/0507018](#)]. [20](#)
- [40] B. G. Zakharov, *Induced photon emission from quark jets in ultrarelativistic heavy-ion collisions*, JETP Lett. **80**, 1 (2004) [[hep-ph/0405101](#)]. [viii](#), [21](#), [22](#), [23](#)
- [41] I. Vitev and B.-W. Zhang, *A systematic study of direct photon production in heavy ion collisions*, Phys. Lett. **B669**, 337 (2008) [[0804.3805](#)]. [viii](#), [22](#)
- [42] G.-Y. Qin et al., *Jet energy loss, photon production, and photon-hadron correlations at RHIC*, Phys. Rev. **C80**, 054909 (2009) [[0906.3280](#)]. [22](#)
- [43] X.-N. Wang, Z. Huang, and I. Sarcevic, *Jet quenching in the opposite direction of a tagged photon in high-energy heavy-ion collisions*, Phys. Rev. Lett. **77**, 231 (1996) [[hep-ph/9605213](#)]. [24](#)
- [44] X.-N. Wang and Z. Huang, *Medium-induced parton energy loss in gamma + jet events of high-energy heavy-ion collisions*, Phys. Rev. **C55**, 3047 (1997) [[hep-ph/9701227](#)]. [24](#)
- [45] A. Adare et al. (PHENIX), *Photon-Hadron Jet Correlations in $p + p$ and Au + Au Collisions at $\sqrt{s_{NN}} = 200$ GeV*, Phys. Rev. **C80**, 024908 (2009) [[0903.3399](#)]. [25](#)

- [46] M. Connors (PHENIX), *Direct Photon-Hadron Correlations Measured with PHENIX*, Nucl. Phys. **A830**, 447c (2009) [[0907.4571](http://dx.doi.org/10.1103/0907.4571)]. [25](#)
- [47] C.-N. Yang and R. L. Mills, *Conservation of isotopic spin and isotopic gauge invariance*, Phys. Rev. **96**, 191 (1954) [<http://dx.doi.org/10.1103/PhysRev.96.191>]. [27](#)
- [48] H. Georgi, *Lie Algebras in Particle Physics* (Reading, Mass. : Perseus Books, Advanced Book Program, 1999). [28](#)
- [49] M. E. Peskin and D. V. Schroeder, *An Introduction to Quantum Field Theory* (Westview Press, 1995). [29](#)
- [50] R. P. Feynman, *Space-time approach to quantum electrodynamics*, Phys. Rev. **76**, 769 (1949) [<http://dx.doi.org/10.1103/PhysRev.76.769>]. [29](#)
- [51] D. J. Gross and F. Wilczek, *Ultraviolet behavior of non-abelian gauge theories*, Phys. Rev. Lett. **30**, 1343 (1973) [<http://dx.doi.org/10.1103/PhysRevLett.30.1343>]. [31](#)
- [52] S. Bethke, *Experimental tests of asymptotic freedom*, Progress in Particle and Nuclear Physics **58**, 351 (2007). [ix](#), [32](#)
- [53] J. Smit, *Introduction to Quantum Fields on a Lattice* (Cambridge University Press, 2002). [33](#)
- [54] K. Schilling and G. Bali, *The Static quark - anti-quark potential: A 'Classical' experiment on the connection machine CM-2*, Int. J. Mod. Phys. **C4**, 1167 (1993). [ix](#), [34](#)
- [55] D. Blaschke et al., *Heavy quark potential and quarkonia dissociation rates*, Eur. Phys. J. **C43**, 81 (2005). [ix](#), [35](#), [36](#)
- [56] J. I. Friedman and H. W. Kendall, *Deep Inelastic Electron Scattering*, Annual Review of Nuclear Science **22**, 203 (1972) [<http://dx.doi.org/10.1146/annurev.ns.22.120172.001223>]. [38](#), [39](#)
- [57] R. Ellis, W. Stirling, and B. Webber, *QCD and collider physics* (Cambridge University Press, 1996). [ix](#), [x](#), [xi](#), [39](#), [57](#), [62](#)

- [58] G. Miller et al., *Inelastic electron-Proton Scattering at Large Momentum Transfers*, Phys. Rev. **D5**, 528 (1972) [<http://dx.doi.org/10.1103/PhysRevD.5.528>]. **39**
- [59] R. P. Feynman, *Very high-energy collisions of hadrons*, Phys. Rev. Lett. **23**, 1415 (1969) [<http://dx.doi.org/10.1103/PhysRevLett.23.1415>]. **40**
- [60] J. D. Bjorken and E. A. Paschos, *Inelastic Electron Proton and gamma Proton Scattering, and the Structure of the Nucleon*, Phys. Rev. **185**, 1975 (1969) [<http://dx.doi.org/10.1103/PhysRev.185.1975>]. **40**
- [61] R. P. Feynman, *Photon Hadron Interactions* (W.A. Benjamin, New York, 1972). **40**
- [62] C. G. Callan, Jr. and D. J. Gross, *High-energy electroproduction and the constitution of the electric current*, Phys. Rev. Lett. **22**, 156 (1969) [<http://dx.doi.org/10.1103/PhysRevLett.22.156>]. **40**
- [63] C. Amsler et al. (Particle Data Group), *Review of particle physics*, Phys. Lett. **B667**, 1 (2008) [<http://dx.doi.org/10.1103/PhysRevD.5.528>]. **ix, x, 42, 43, 46**
- [64] D. S. Collins, J.C. and G. Sterman, *Perturbative Quantum Chromodynamics* (World Scientific, Singapore, 1989), edited by A. H. Mueller. **42**
- [65] V. N. Gribov and L. N. Lipatov, *Deep inelastic e p scattering in perturbation theory*, Sov. J. Nucl. Phys. **15**, 438 (1972). **43, 48**
- [66] L. N. Lipatov, *The parton model and perturbation theory*, Sov. J. Nucl. Phys. **20**, 94 (1975).
- [67] G. Altarelli and G. Parisi, *Asymptotic Freedom in Parton Language*, Nucl. Phys. **B126**, 298 (1977) [[http://dx.doi.org/10.1016/0550-3213\(77\)90384-4](http://dx.doi.org/10.1016/0550-3213(77)90384-4)].
- [68] Y. L. Dokshitzer, *Calculation of the Structure Functions for Deep Inelastic Scattering and e^+e^- Annihilation by Perturbation Theory in Quantum Chromodynamics*, Sov. Phys. JETP **46**, 641 (1977). **44**
- [69] D. Buskalic et al. (ALEPH), *Measurement of alpha-s from scaling violations in fragmentation functions in e^+e^- annihilation*, Phys. Lett. **B357**, 487 (1995) [[http://dx.doi.org/10.1016/0370-2693\(95\)00917-A](http://dx.doi.org/10.1016/0370-2693(95)00917-A)]. **x, 48**

- [70] P. Nason and B. R. Webber, *Scaling violation in e^+e^- fragmentation functions: QCD evolution, hadronization and heavy quark mass effects*, Nucl. Phys. **B421**, 473 (1994) [[http://dx.doi.org/10.1016/0550-3213\(94\)90513-4](http://dx.doi.org/10.1016/0550-3213(94)90513-4)]. 48
- [71] E. A. Kuraev, L. N. Lipatov, and V. S. Fadin, *Multi - Reggeon Processes in the Yang-Mills Theory*, Sov. Phys. JETP **44**, 443 (1976). 49
- [72] E. A. Kuraev, L. N. Lipatov, and V. S. Fadin, *The Pomeranchuk Singularity in Nonabelian Gauge Theories*, Sov. Phys. JETP **45**, 199 (1977).
- [73] I. I. Balitsky and L. N. Lipatov, *The Pomeranchuk Singularity in Quantum Chromodynamics*, Sov. J. Nucl. Phys. **28**, 822 (1978). 49
- [74] R. D. Field and R. P. Feynman, *Quark elastic scattering as a source of high-transverse-momentum mesons*, Phys. Rev. D **15**, 2590 (1977). 50, 52
- [75] F. W. Busser et al., *Observation of π^0 mesons with large transverse momentum in high-energy proton proton collisions*, Phys. Lett. **B46**, 471 (1973) [[http://dx.doi.org/10.1016/0370-2693\(73\)90169-X](http://dx.doi.org/10.1016/0370-2693(73)90169-X)]. 51
- [76] B. Alper et al. (British-Scandinavian), *The Production of Charged Particles with High Transverse Momentum in Proton Proton Collisions at the CERN ISR*, Nucl. Phys. **B87**, 19 (1975) [[http://dx.doi.org/10.1016/0550-3213\(75\)90248-5](http://dx.doi.org/10.1016/0550-3213(75)90248-5)]. 51
- [77] P. Darriulat et al., *Structure of Final States with a High Transverse Momentum π^0 in Proton Proton Collisions*, Nucl. Phys. **B107**, 429 (1976) [[http://dx.doi.org/10.1016/0550-3213\(76\)90146-2](http://dx.doi.org/10.1016/0550-3213(76)90146-2)]. 52
- [78] R. P. Feynman, R. D. Field, and G. C. Fox, *Correlations among particles and jets produced with large transverse momenta*, Nucl. Phys. B **128**, 1 (1977). 52, 60
- [79] J. F. Owens, *Large Momentum Transfer Production of Direct Photons, Jets, and Particles*, Rev. Mod. Phys. **59**, 465 (1987) [<http://dx.doi.org/10.1103/RevModPhys.59.465>]. 53, 72
- [80] R. P. Feynman, R. D. Field, and G. C. Fox, *Quantum-chromodynamic approach for the large-transverse-momentum production of particles and jets*, Phys. Rev. D **18**, 3320 (1978) [<http://dx.doi.org/10.1103/PhysRevD.18.3320>]. 53

- [81] Y. L. Dokshitzer, D. I. D'yakonov, and S. I. Troyan, *Hard semi-inclusive processes in QCD*, Physics Letters B **78**, 290 (1978). [53](#), [64](#)
- [82] J. C. Collins and D. E. Soper, *Back-to-back jets in QCD*, Nucl. Phys. B **193**, 381 (1981). [53](#)
- [83] J. C. Collins and G. S. D. E. Soper, *Transverse momentum distributions in Drell-Yan pair and W and Z boson production*, Nucl. Phys. B **250**, 199 (1985). [53](#)
- [84] M. Cacciari, G. P. Salam, and G. Soyez, *The anti- k_T jet clustering algorithm*, JHEP **04**, 063 (2008) [[0802.1189](#)]. [55](#)
- [85] J. E. Huth et al., *Toward a standardization of jet definitions* (1990), presented at Summer Study on High Energy Physics, Reaearch Directions for the Decade, Snowmass, CO, Jun 25 – Jul 13.
- [86] G. P. Salam and G. Soyez, *A practical Seedless Infrared-Safe Cone jet algorithm*, JHEP **05**, 086 (2007) [[0704.0292](#)].
- [87] S. Catani, Y. L. Dokshitzer, M. H. Seymour, and B. R. Webber, *Longitudinally invariant k_T clustering algorithms for hadron hadron collisions*, Nucl. Phys. **B406**, 187 (1993) [[http://dx.doi.org/10.1016/0550-3213\(93\)90166-M](http://dx.doi.org/10.1016/0550-3213(93)90166-M)].
- [88] S. D. Ellis and D. E. Soper, *Successive combination jet algorithm for hadron collisions*, Phys. Rev. **D48**, 3160 (1993) [[hep-ph/9305266](#)]. [55](#)
- [89] F. Abe et al. (CDF Collaboration), *Inclusive Jet Cross Section in $p\bar{p}$ Collisions at $\sqrt{s} = 1.8$ TeV*, Phys. Rev. Lett. **77**, 438 (1996). [x](#), [56](#)
- [90] E. Farhi, *A QCD Test for Jets*, Phys. Rev. Lett. **39**, 1587 (1977) [<http://dx.doi.org/10.1103/PhysRevLett.39.1587>]. [57](#)
- [91] A. L. S. Angelis et al. (CERN-Columbia-Oxford-Rockefeller), *A measurement of the transverse momenta of partons, and of jet fragmentation as a function of \sqrt{s} in $p+p$ collisions*, Phys. Lett. **B97**, 163 (1980) [[http://dx.doi.org/10.1016/0370-2693\(80\)90572-9](http://dx.doi.org/10.1016/0370-2693(80)90572-9)]. [x](#), [59](#)
- [92] E. M. Levin and M. G. Ryskin, *How Large Is the Average Transverse Momentum of Partons, Is It Larger Than 1 GeV/c?*, Sov. Phys. JETP **42**, 783 (1975). [60](#)

- [93] D. Acosta et al. (CDF), *Study of jet shapes in inclusive jet production in $p\bar{p}$ collisions at $\sqrt{s} = 1.96$ TeV*, Phys. Rev. D **71**, 112002 (2005). [xi](#), [62](#), [65](#), [66](#)
- [94] T. Sjostrand and P. Z. Skands, *Transverse-momentum-ordered showers and interleaved multiple interactions*, Eur. Phys. J. **C39**, 129 (2005) [[hep-ph/0408302](#)]. [64](#)
- [95] G. Marchesini and B. R. Webber, *Monte Carlo Simulation of General Hard Processes with Coherent QCD Radiation*, Nucl. Phys. **B310**, 461 (1988) [[http://dx.doi.org/10.1016/0550-3213\(88\)90089-2](#)]. [64](#)
- [96] A. Krzywicki and B. Petersson, *Breakdown of hadronic scaling or evidence for clustering?*, Phys. Rev. **D6**, 924 (1973) [[http://dx.doi.org/10.1103/PhysRevD.6.924](#)]. [64](#)
- [97] X. Artru and G. Mennessier, *String model and multiproduction*, Nucl. Phys. **B70**, 93 (1974) [[http://dx.doi.org/10.1016/0550-3213\(74\)90360-5](#)].
- [98] B. Andersson, G. Gustafson, and B. Soderberg, *A General Model for Jet Fragmentation*, Z. Phys. **C20**, 317 (1983) [[http://dx.doi.org/10.1007/BF01407824](#)].
- [99] R. D. Field and S. Wolfram, *A QCD Model for e^+e^- Annihilation*, Nucl. Phys. **B213**, 65 (1983) [[http://dx.doi.org/10.1016/0550-3213\(83\)90175-X](#)]. [65](#)
- [100] B. R. Webber, *A QCD Model for Jet Fragmentation Including Soft Gluon Interference*, Nucl. Phys. **B238**, 492 (1984) [[http://dx.doi.org/10.1016/0550-3213\(84\)90333-X](#)]. [64](#), [65](#)
- [101] T. Sjostrand, S. Mrenna, and P. Z. Skands, *PYTHIA 6.4 Physics and Manual*, JHEP **05**, 026 (2006) [[hep-ph/0603175](#)]. [66](#)
- [102] G. Corcella et al., *HERWIG 6.5: an event generator for Hadron Emission Reactions With Interfering Gluons (including supersymmetric processes)*, JHEP **01**, 010 (2001) [[hep-ph/0011363](#)]. [66](#)
- [103] A. L. S. Angelis et al., *Direct photon production at the CERN ISR*, Nucl. Phys. B **327**, 541 (1989). [68](#)

- [104] P. Aurenche et al., *A critical phenomenological study of inclusive photon production in hadronic collisions*, Eur. Phys. J. **C9**, 107 (1999) [[hep-ph/9811382](#)]. [68](#), [69](#)
- [105] H. L. Lai et al. (CTEQ), *Global QCD analysis of parton structure of the nucleon: CTEQ5 parton distributions*, Eur. Phys. J. **C12**, 375 (2000) [[hep-ph/9903282](#)]. [68](#)
- [106] V. M. Abazov et al., *Measurement of the differential cross section for the production of an isolated photon with associated jet in $p\bar{p}$ collisions at $\sqrt{s} = 1.96$ TeV*, Phys. Lett. B **666**, 435 (2008). [xi](#), [69](#), [70](#), [76](#)
- [107] E. Laenen, G. Sterman, and W. Vogelsang, *Higher-Order QCD Corrections in Prompt Photon Production*, Phys. Rev. Lett. **84**, 4296 (2000). [69](#)
- [108] J. Huston et al., *Global QCD study of direct photon production*, Phys. Rev. D **51**, 6139 (1995). [69](#)
- [109] P. Aurenche, M. Fontannaz, J.-P. Guillet, E. Pilon, and M. Werlen, *A New critical study of photon production in hadronic collisions*, Phys. Rev. **D73**, 094007 (2006) [[hep-ph/0602133](#)]. [xi](#), [70](#), [71](#)
- [110] P. Aurenche, J. P. Guillet, M. Werlen, et al., iNCNLO-direct photon and inclusive hadron production code [http://laph.in2p3.fr/PHOX_FAMILY/readme_inc.html]. [xii](#), [xxvii](#), [73](#), [234](#)
- [111] L. Bourhis, M. Fontannaz, and J. P. Guillet, *Quark and gluon fragmentation functions into photons*, Eur. Phys. J. **C2**, 529 (1998) [[hep-ph/9704447](#)]. [xii](#), [73](#), [75](#)
- [112] K. Ackerstaff et al. (OPAL), *Measurement of the quark to photon fragmentation function through the inclusive production of prompt photons in hadronic $Z0$ decays*, Eur. Phys. J. **C2**, 39 (1998) [[hep-ex/9708020](#)]. [xii](#), [74](#)
- [113] Z. Kunszt and Z. Trocsanyi, *QCD corrections to photon production in association with hadrons in e^+e^- annihilation*, Nucl. Phys. **B394**, 139 (1993) [[hep-ph/9207232](#)]. [74](#)
- [114] D. Buskulic et al. (ALEPH), *First measurement of the quark-to-photon fragmentation function*, Z. Phys. C **69**, 365 (1996). [75](#)

- [115] S. S. Adler et al. (PHENIX), *Measurement of direct photon production in $p + p$ collisions at $\sqrt{s} = 200$ -GeV*, Phys. Rev. Lett. **98**, 012002 (2007) [[hep-ex/0609031](https://arxiv.org/abs/hep-ex/0609031)]. [xii](#), [xxiv](#), [xxv](#), [76](#), [77](#), [222](#), [223](#), [224](#)
- [116] M. S. Livingston and J. Blewett, *Particle Accelerators* (McGraw-Hill, New York, 1962). [79](#)
- [117] M. Harrison, T. Ludlam, and S. Ozaki, *RHIC project overview*, Nucl. Inst. Meth. **A499 2-3**, 235 (2003) [[http://dx.doi.org/10.1016/S0168-9002\(02\)01937-X](https://doi.org/10.1016/S0168-9002(02)01937-X)]. [xii](#), [79](#), [83](#)
- [118] K. Adcox et al., *PHENIX detector overview*, Nucl. Inst. Meth. **A499 2-3**, 469 (2003) [[http://dx.doi.org/10.1016/S0168-9002\(02\)01950-2](https://doi.org/10.1016/S0168-9002(02)01950-2)]. [xii](#), [80](#), [84](#)
- [119] K. H. Ackermann et al., *STAR detector overview*, Nucl. Inst. Meth. **A499 2-3**, 624 (2003) [[http://dx.doi.org/10.1016/S0168-9002\(02\)01960-5](https://doi.org/10.1016/S0168-9002(02)01960-5)]. [80](#)
- [120] M. Adamczyk et al., *The BRAHMS experiment at RHIC*, Nucl. Inst. Meth. **A499 2-3**, 437 (2003) [[http://dx.doi.org/doi:10.1016/S0168-9002\(02\)01949-6](https://doi.org/10.1016/S0168-9002(02)01949-6)]. [80](#)
- [121] B. B. Back et al., *The PHOBOS detector at RHIC*, Nucl. Inst. Meth. **A499 2-3**, 603 (2003) [[http://dx.doi.org/10.1016/S0168-9002\(02\)01959-9](https://doi.org/10.1016/S0168-9002(02)01959-9)]. [80](#)
- [122] I. Alekseev et al., *Polarized proton collider at RHIC*, Nucl. Inst. Meth. **A499 2-3**, 392 (2003) [[http://dx.doi.org/10.1016/S0168-9002\(02\)01946-0](https://doi.org/10.1016/S0168-9002(02)01946-0)]. [82](#)
- [123] H. Akikawa et al., *PHENIX Muon Arms*, Nucl. Inst. Meth. **A499 2-3**, 537 (2003) [[http://dx.doi.org/10.1016/S0168-9002\(02\)01955-1](https://doi.org/10.1016/S0168-9002(02)01955-1)]. [83](#)
- [124] K. Adcox et al., *PHENIX central arm tracking detectors*, Nucl. Inst. Meth. **A499 2-3**, 489 (2003) [[http://dx.doi.org/10.1016/S0168-9002\(02\)01952-6](https://doi.org/10.1016/S0168-9002(02)01952-6)]. [xii](#), [85](#), [87](#), [88](#)
- [125] S. H. Aronson et al., *PHENIX magnet system*, Nucl. Inst. Meth. **A499 2-3**, 480 (2003) [[http://dx.doi.org/10.1016/S0168-9002\(02\)01951-4](https://doi.org/10.1016/S0168-9002(02)01951-4)]. [xii](#), [85](#), [86](#)
- [126] L. Aphecetche et al., *PHENIX calorimeter*, Nucl. Inst. Meth. **A499 2-3**, 521 (2003) [[http://dx.doi.org/10.1016/S0168-9002\(02\)01954-X](https://doi.org/10.1016/S0168-9002(02)01954-X)]. [xiii](#), [89](#), [92](#), [106](#)

- [127] M. Allen et al., *PHENIX inner detectors*, Nucl. Inst. Meth. **A499** **2-3**, 549 (2003) [[http://dx.doi.org/10.1016/S0168-9002\(02\)01956-3](http://dx.doi.org/10.1016/S0168-9002(02)01956-3)]. **96**
- [128] C. Adler et al., *The RHIC zero-degree calorimeters*, Nucl. Inst. Meth. **A499** **2-3**, 433 (2003) [<http://dx.doi.org/10.1016/j.nima.2003.08.112>]. **96**
- [129] Y. S. Lai and B. A. Cole, *Full jet reconstruction by Gaussian filtering in Run-5 $p + p$, $Cu + Cu$ and Run-7 $Au + Au$ at PHENIX*. **107**
- [130] Y. S. Lai, private communication. **115**
- [131] M. Connors and A. Sickles, *Efficiency and Occupancy Corrections for Runs 6 and 7*, pHENIX Analysis Note 879. **118**
- [132] A. Sickles, M. P. McCumber, and A. Adare, *Extraction of Correlated Jet Pair Signals in Relativistic Heavy Ion Collisions*, Phys. Rev. **C81**, 014908 (2010) [[0907.4113](http://arxiv.org/abs/0907.4113)]. **139**
- [133] J. N. A. Adare, M. Connors and A. Sickles, *Single-particle and embedding $h \pm$ acceptance and efficiency corrections for central arm analyses in Runs 6 and 7*, pHENIX Analysis Note 808. **151**
- [134] J. Seele, C. Aidala, and F. Ellinghaus, *BBC Efficiency for Neutral Pions and Etas in the Central Arm in Run-06 $p + p$ at $\sqrt{s} = 200$ GeV*, pHENIX Analysis Note 842. **151, 160**
- [135] S. V. der Meer, iSR-PO/68-31,KEK68-64. **159**
- [136] A. Bazilevsky, *Relative measurements of BBC trigger efficiency in pp Runs 2, 3 and 4*, pHENIX Analysis Note 358. **159**
- [137] I. Vendramin, *Two - Hadron Fragmentation Functions: A Study of Their Q^2 Evolutions*, Nuovo Cim. **A66**, 339 (1981). **219**
- [138] S. S. Adler et al. (PHENIX), *Jet properties from dihadron correlations in $p + p$ collisions at $\sqrt{s} = 200$ GeV*, Phys. Rev. **D74**, 072002 (2006) [[hep-ex/0605039](http://arxiv.org/abs/hep-ex/0605039)]. **xxvii, 235**
- [139] L. Bourhis, M. Fontannaz, and J. P. Guillet, *Quark and gluon fragmentation functions into photons*, Eur. Phys. J. **C2**, 529 (1998) [[hep-ph/9704447](http://arxiv.org/abs/hep-ph/9704447)]. **236**

- [140] T. Sjöstrand, S. Mrenna, and P. Skands, *PYTHIA 6.4 Physics and Manual* (2006), fFERMILAB-PUB-06-052-CD-T [[hep-ph/0603175](#)]. [xxvii](#), [236](#)
- [141] Y.-S. Lai (PHENIX), *Direct jet reconstruction in $p + p$ and $Cu + Cu$ at PHENIX* (2009) [[0911.3399](#)]. [237](#)
- [142] Y.-s. Lai (PHENIX), *Measurement of jet fragmentation in $p + p$ collision at $\sqrt{s} = 200$ GeV with the PHENIX detector*, J. Phys. Conf. Ser. **230**, 012010 (2010) [[1005.2801](#)]. [237](#)
- [143] Z. Belghobsi et al., *Photon - Jet Correlations and Constraints on Fragmentation Functions*, Phys. Rev. **D79**, 114024 (2009) [[0903.4834](#)]. [237](#)

Appendix A

h- γ $\Delta\phi$ dependent per-trigger yields

A.1 π^0 and η decay photons

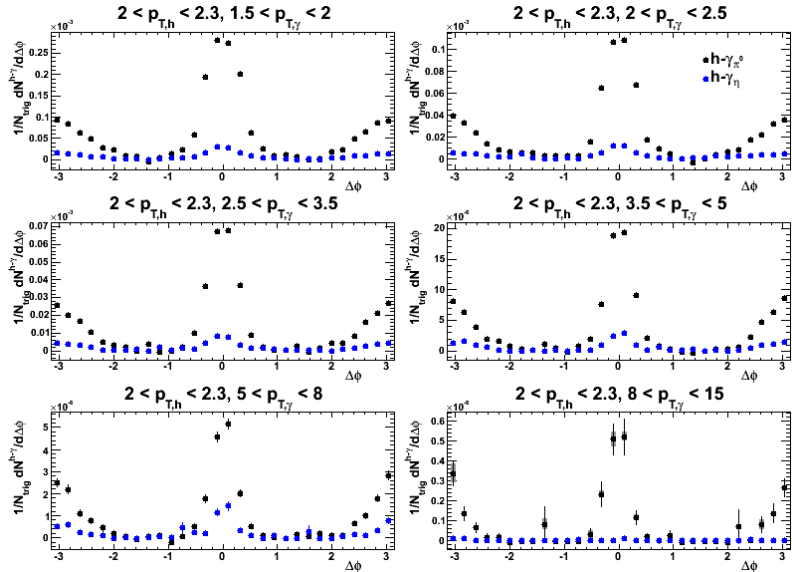


Figure A.1: Decay photon per-trigger yields, $\frac{1}{N_{trig}} \frac{dN^{h-\gamma}}{d\Delta\phi}$, for trigger hadrons with p_T from 2.0 – 2.3 GeV/c and associated photons in six p_T bins ranging from 1.5 – 2.0 GeV/c to 8.0 – 15.0 GeV/c. $h - \gamma_{\pi^0}$ is shown in black, $h - \gamma_{\eta}$ in blue.

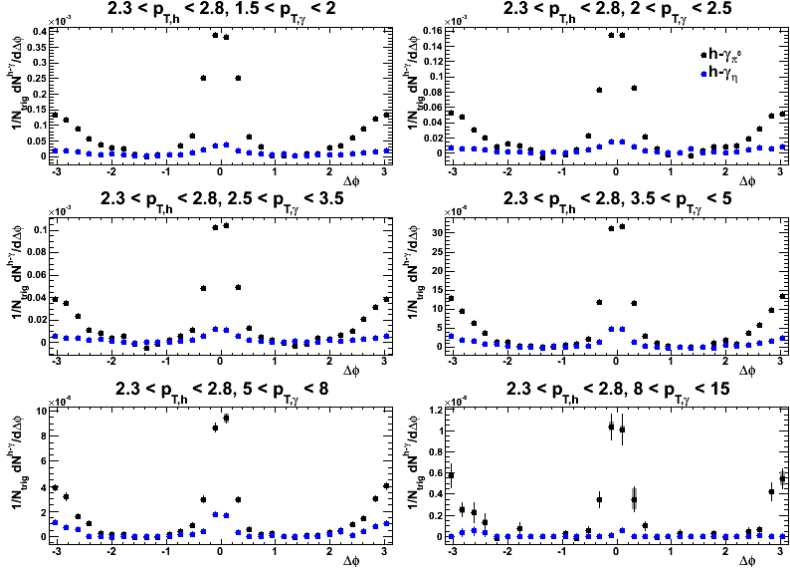


Figure A.2: Decay photon per-trigger yields, $\frac{1}{N_{trig}} \frac{dN^{h-\gamma}}{d\Delta\phi}$, for trigger hadrons with p_T from $2.3 - 2.8$ GeV/c and associated photons in six p_T bins ranging from $1.5-2.0$ GeV/c to $8.0 - 15.0$ GeV/c. $h - \gamma_{\pi^0}$ is shown in black, $h - \gamma_{\eta}$ in blue.

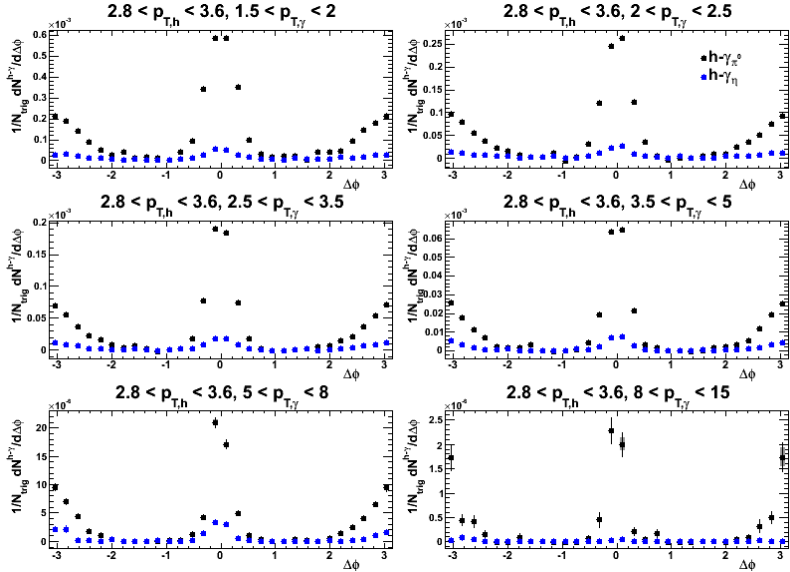


Figure A.3: Decay photon per-trigger yields, $\frac{1}{N_{trig}} \frac{dN^{h-\gamma}}{d\Delta\phi}$, for trigger hadrons with p_T from $2.8 - 3.6$ GeV/c and associated photons in six p_T bins ranging from $1.5-2.0$ GeV/c to $8.0 - 15.0$ GeV/c. $h - \gamma_{\pi^0}$ is shown in black, $h - \gamma_{\eta}$ in blue.

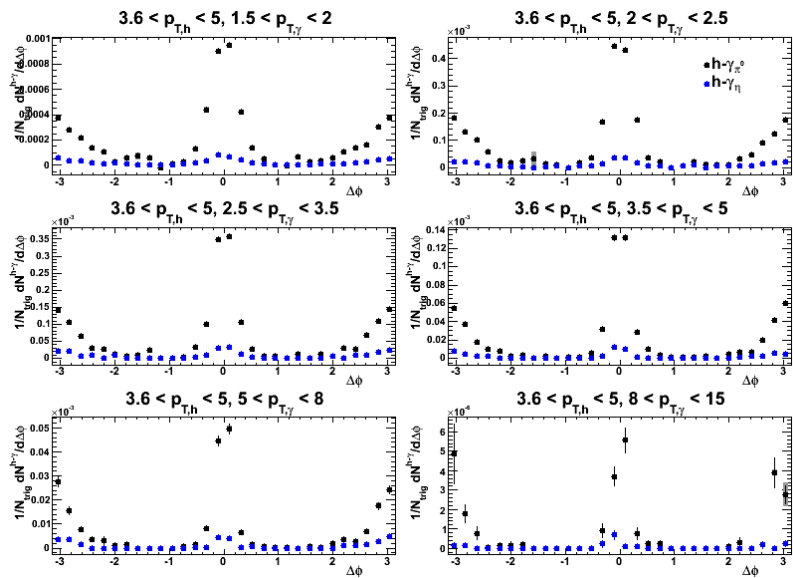


Figure A.4: Decay photon per-trigger yields, $\frac{1}{N_{trig}} \frac{dN^{h-\gamma}}{d\Delta\phi}$, for trigger hadrons with p_T from 3.6 – 5.0 GeV/c and associated photons in six p_T bins ranging from 1.5-2.0 GeV/c to 8.0 - 15.0 GeV/c. $h - \gamma_{\pi^0}$ is shown in black, $h - \gamma_{\eta}$ in blue.

A.2 Inclusive, decay, and fragmentation photons

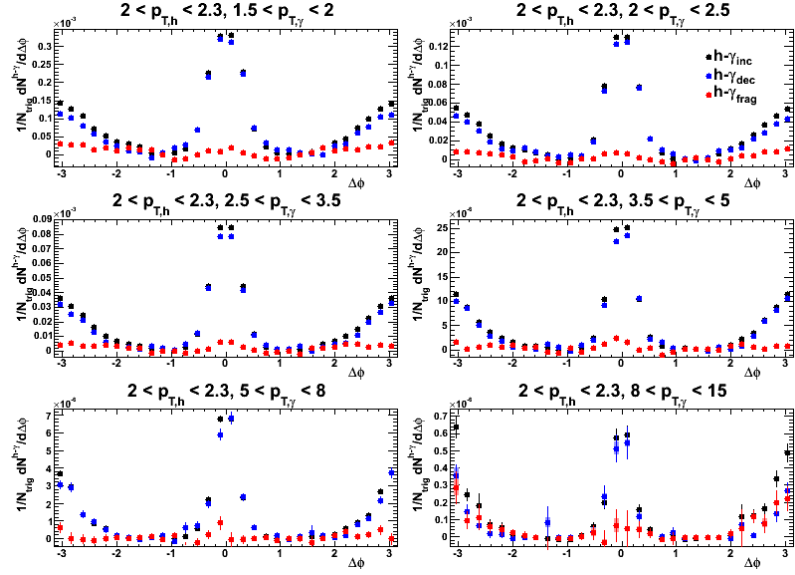


Figure A.5: $\frac{1}{N_{trig}} \frac{dN^{h-\gamma}}{d\Delta\phi}$ for trigger hadrons with p_T from 2.0 – 2.3 GeV/c and associated photons in six p_T bins ranging from 1.5-2.0 GeV/c to 8.0 - 15.0 GeV/c. $h - \gamma_{inc}$ is shown in black, $h - \gamma_{decay}$ in blue, and $h - \gamma_{frag}$ in red.

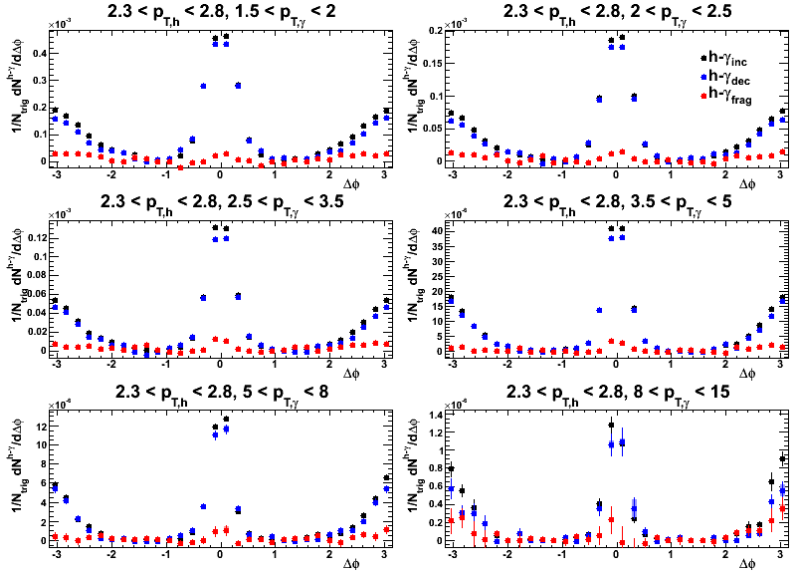


Figure A.6: $\frac{1}{N_{trig}} \frac{dN^{h-\gamma}}{d\Delta\phi}$ for trigger hadrons with p_T from 2.3 – 2.8 GeV/c and associated photons in six p_T bins ranging from 1.5-2.0 GeV/c to 8.0 - 15.0 GeV/c. $h-\gamma_{inc}$ is shown in black, $h-\gamma_{decay}$ in blue, and $h-\gamma_{frag}$ in red.

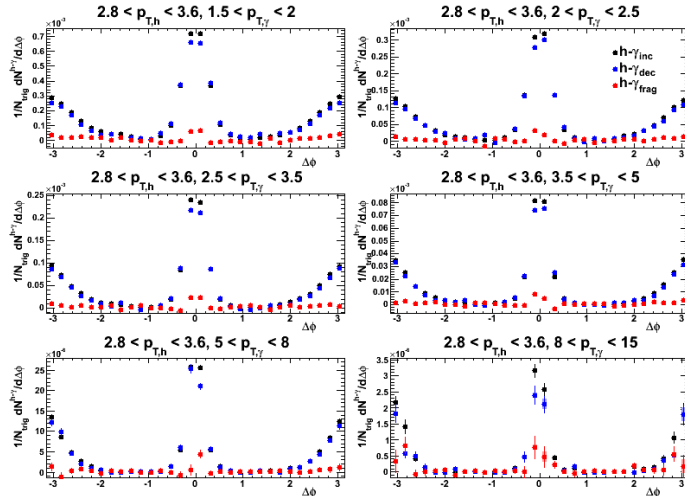


Figure A.7: $\frac{1}{N_{trig}} \frac{dN^{h-\gamma}}{d\Delta\phi}$ for trigger hadrons with p_T from 2.8 – 3.6 GeV/c and associated photons in six p_T bins ranging from 1.5-2.0 GeV/c to 8.0 - 15.0 GeV/c. $h-\gamma_{inc}$ is shown in black, $h-\gamma_{decay}$ in blue, and $h-\gamma_{frag}$ in red.

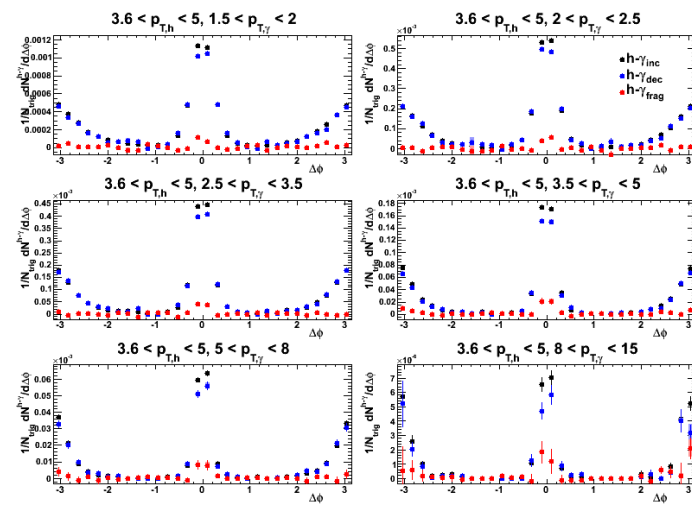


Figure A.8: $\frac{1}{N_{trig}} \frac{dN^{h-\gamma}}{d\Delta\phi}$ for trigger hadrons with p_T from 3.6 – 5.0 GeV/c and associated photons in six p_T bins ranging from 1.5-2.0 GeV/c to 8.0 - 15.0 GeV/c. $h - \gamma_{inc}$ is shown in black, $h - \gamma_{decay}$ in blue, and $h - \gamma_{frag}$ in red.

Appendix B

Distributions to go from p_{out} to j_T

B.1 $p_{out,h}$

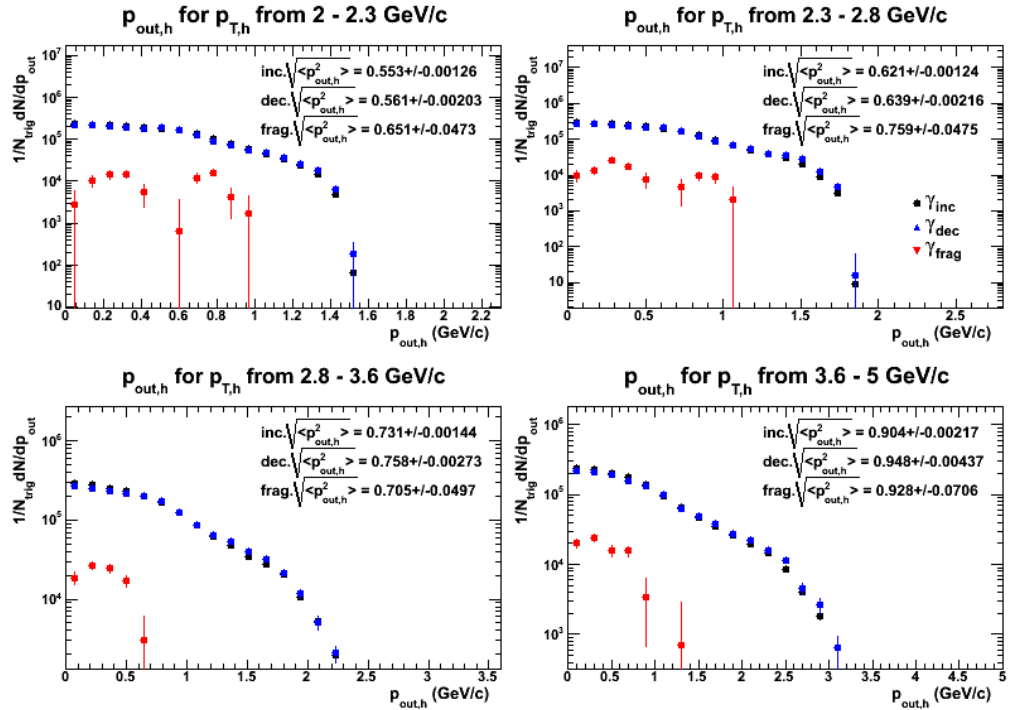


Figure B.1: p_{out} distribution for hadrons within $|\Delta\phi| < 0.7$ of a photon with p_T from 1.5 – 8.0 GeV/c, for each of the four hadron p_T bins: 2.0 – 2.3 GeV/c (top left), 2.3 – 2.8 GeV/c (top right), 2.8 – 3.6 GeV/c (bottom left), and 3.6 – 5.0 GeV/c (bottom right). Inclusive photons are shown in black (circles), decay photons in blue (up triangles), and fragmentation photons in red (down triangles).

B.2 x_h

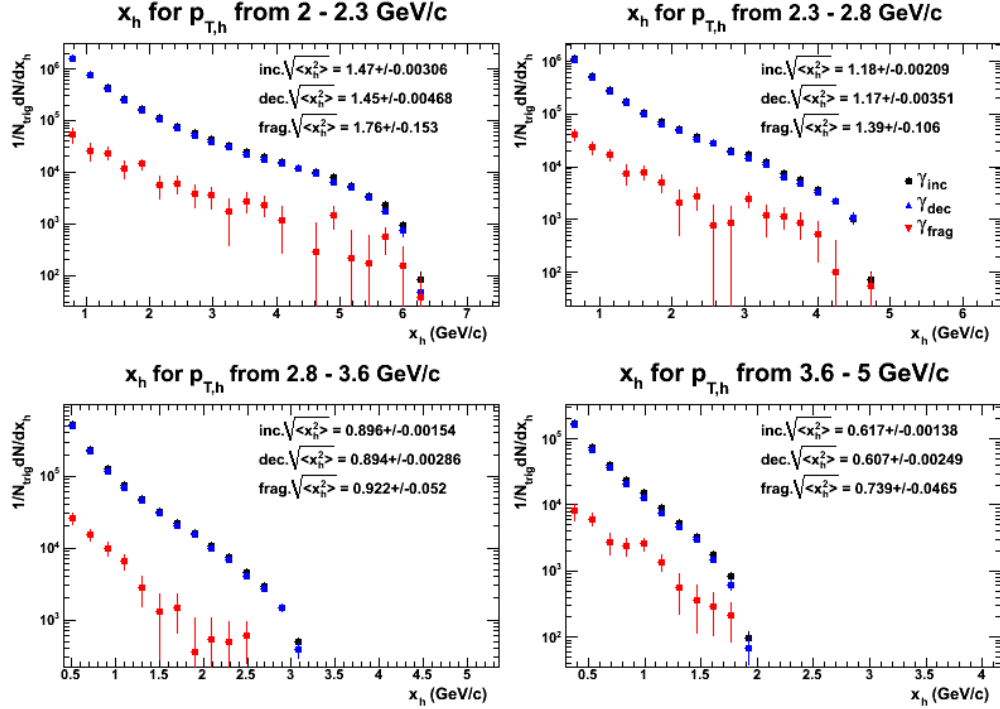


Figure B.2: $x_h = p_{T,\gamma}/p_{T,h}$ distribution for photons with p_T from 1.5 – 8.0 GeV/c, for each of the four hadron p_T bins: 2.0 – 2.3 GeV/c (top left), 2.3 – 2.8 GeV/c (top right), 2.8 – 3.6 GeV/c (bottom left), and 3.6 – 5.0 GeV/c (bottom right), when the pair has $|\Delta\phi| < 0.7$. Inclusive photons are shown in black (circles), decay photons in blue (up triangles), and fragmentation photons in red (down triangles).

B.3 x_h^{-1}

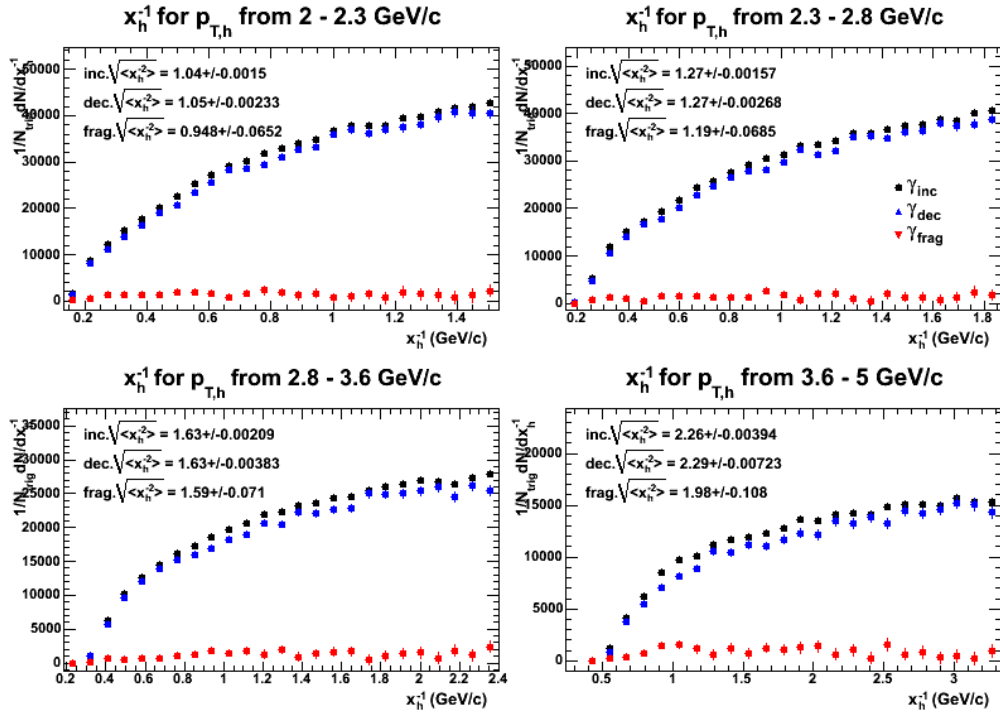


Figure B.3: $x_h^{-1} = p_{T,h}/p_{T,\gamma}$ distribution for photons with p_T from 1.5–8.0 GeV/c, for each of the four hadron p_T bins: 2.0–2.3 GeV/c (top left), 2.3–2.8 GeV/c (top right), 2.8–3.6 GeV/c (bottom left), and 3.6–5.0 GeV/c (bottom right), when the pair has $|\Delta\phi| < 0.7$. Inclusive photons are shown in black (circles), decay photons in blue (up triangles), and fragmentation photons in red (down triangles).

Appendix C

Data Tables

C.1 Pair cross sections and ratios of yields

$p_{T,\gamma}$ (GeV/c)	Inv. cross sec. $\pm\%$ stat. $\pm\%$ sys.	Ratio $\pm\%$ stat. $\pm\%$ sys.
1.5 – 2.0	$2.12 \times 10^{-6} \pm 1.52 \times 10^{-6} \pm 1.95 \times 10^{-6}$	$1.58 \times 10^{-2} \pm 1.13 \times 10^{-2} \pm 1.46 \times 10^{-2}$
2.0 – 2.5	$1.48 \times 10^{-6} \pm 4.07 \times 10^{-7} \pm 1.16 \times 10^{-7}$	$3.95 \times 10^{-2} \pm 1.09 \times 10^{-2} \pm 3.11 \times 10^{-3}$
2.5 – 3.5	$4.14 \times 10^{-7} \pm 9.79 \times 10^{-8} \pm 5.43 \times 10^{-8}$	$4.67 \times 10^{-2} \pm 1.10 \times 10^{-2} \pm 6.13 \times 10^{-3}$
3.5 – 5.0	$6.47 \times 10^{-8} \pm 1.97 \times 10^{-8} \pm 7.15 \times 10^{-9}$	$5.73 \times 10^{-2} \pm 1.74 \times 10^{-2} \pm 6.34 \times 10^{-3}$
5.0 – 8.0	$2.00 \times 10^{-9} \pm 3.71 \times 10^{-9} \pm 1.09 \times 10^{-9}$	$2.04 \times 10^{-2} \pm 3.78 \times 10^{-2} \pm 1.11 \times 10^{-2}$
8.0 – 15.0	$2.06 \times 10^{-10} \pm 2.33 \times 10^{-10} \pm 7.89 \times 10^{-11}$	$9.55 \times 10^{-2} \pm 1.08 \times 10^{-1} \pm 3.65 \times 10^{-2}$

Table C.1: Invariant pair cross section (mb GeV/c $^{-4}$) for fragmentation photons associated with hadrons with p_T from 2.0 – 2.3 GeV/c.

$p_{T,\gamma}$ (GeV/c)	Inv. cross sec. $\pm\%$ stat. $\pm\%$ sys.	Ratio $\pm\%$ stat. $\pm\%$ sys.
1.5 – 2.0	$6.81 \times 10^{-7} \pm 6.04 \times 10^{-7} \pm 1.42 \times 10^{-6}$	$1.11 \times 10^{-2} \pm 9.80 \times 10^{-3} \pm 2.31 \times 10^{-3}$
2.0 – 2.5	$7.56 \times 10^{-7} \pm 1.74 \times 10^{-7} \pm 1.25 \times 10^{-7}$	$4.24 \times 10^{-2} \pm 9.78 \times 10^{-3} \pm 6.99 \times 10^{-3}$
2.5 – 3.5	$2.00 \times 10^{-7} \pm 4.43 \times 10^{-8} \pm 7.68 \times 10^{-10}$	$4.51 \times 10^{-2} \pm 9.97 \times 10^{-3} \pm 1.73 \times 10^{-4}$
3.5 – 5.0	$3.56 \times 10^{-8} \pm 9.47 \times 10^{-9} \pm 4.44 \times 10^{-10}$	$5.84 \times 10^{-2} \pm 1.55 \times 10^{-2} \pm 7.27 \times 10^{-4}$
5.0 – 8.0	$2.30 \times 10^{-9} \pm 1.73 \times 10^{-9} \pm 2.03 \times 10^{-10}$	$3.95 \times 10^{-2} \pm 2.96 \times 10^{-2} \pm 3.49 \times 10^{-3}$
8.0 – 15.0	$8.57 \times 10^{-11} \pm 1.35 \times 10^{-10} \pm 3.37 \times 10^{-11}$	$5.83 \times 10^{-2} \pm 9.17 \times 10^{-2} \pm 2.29 \times 10^{-2}$

Table C.2: Invariant pair cross section (mb GeV/c $^{-4}$) for fragmentation photons associated with hadrons with p_T from 2.2 – 2.8 GeV/c.

$p_{T,\gamma}$ (GeV/c)	Inv. cross sec. $\pm\%$ stat. $\pm\%$ sys.	Ratio $\pm\%$ stat. $\pm\%$ sys.
1.5 – 2.0	$4.56 \times 10^{-7} \pm 1.88 \times 10^{-7} \pm 3.03 \times 10^{-7}$	$2.30 \times 10^{-2} \pm 9.50 \times 10^{-3} \pm 1.53 \times 10^{-2}$
2.0 – 2.5	$3.04 \times 10^{-7} \pm 5.87 \times 10^{-8} \pm 2.86 \times 10^{-8}$	$4.95 \times 10^{-2} \pm 9.56 \times 10^{-3} \pm 4.65 \times 10^{-3}$
2.5 – 3.5	$9.40 \times 10^{-8} \pm 1.63 \times 10^{-8} \pm 3.71 \times 10^{-10}$	$5.67 \times 10^{-2} \pm 9.84 \times 10^{-3} \pm 2.24 \times 10^{-4}$
3.5 – 5.0	$9.01 \times 10^{-9} \pm 4.04 \times 10^{-9} \pm 1.69 \times 10^{-9}$	$3.61 \times 10^{-2} \pm 1.62 \times 10^{-2} \pm 6.760 \times 10^{-3}$
5.0 – 8.0	$1.70 \times 10^{-9} \pm 7.64 \times 10^{-10} \pm 6.80 \times 10^{-11}$	$6.68 \times 10^{-2} \pm 3.01 \times 10^{-2} \pm 2.68 \times 10^{-3}$
8.0 – 15.0	$1.53 \times 10^{-10} \pm 5.55 \times 10^{-11} \pm 2.90 \times 10^{-11}$	$2.15 \times 10^{-1} \pm 7.80 \times 10^{-2} \pm 4.08 \times 10^{-2}$

Table C.3: Invariant pair cross section (mb GeV/c $^{-4}$) for fragmentation photons associated with hadrons with p_T from 2.8 – 3.6 GeV/c.

$p_{T,\gamma}$ (GeV/c)	Inv. cross sec. $\pm\%$ stat. $\pm\%$ sys.	Ratio $\pm\%$ stat. $\pm\%$ sys.
1.5 – 2.0	$1.22 \times 10^{-7} \pm 4.56 \times 10^{-8} \pm 1.51 \times 10^{-8}$	$2.98 \times 10^{-2} \pm 1.12 \times 10^{-2} \pm 3.70 \times 10^{-3}$
2.0 – 2.5	$5.83 \times 10^{-8} \pm 1.65 \times 10^{-8} \pm 8.26 \times 10^{-9}$	$4.21 \times 10^{-2} \pm 1.19 \times 10^{-2} \pm 5.97 \times 10^{-3}$
2.5 – 3.5	$2.38 \times 10^{-8} \pm 4.87 \times 10^{-9} \pm 1.60 \times 10^{-9}$	$5.87 \times 10^{-2} \pm 1.20 \times 10^{-2} \pm 3.94 \times 10^{-3}$
3.5 – 5.0	$6.76 \times 10^{-9} \pm 1.26 \times 10^{-9} \pm 9.05 \times 10^{-10}$	$9.76 \times 10^{-2} \pm 1.82 \times 10^{-2} \pm 1.31 \times 10^{-2}$
5.0 – 8.0	$8.86 \times 10^{-10} \pm 2.51 \times 10^{-10} \pm 5.50 \times 10^{-11}$	$1.11 \times 10^{-1} \pm 3.15 \times 10^{-2} \pm 6.91 \times 10^{-3}$
8.0 – 15.0	$3.69 \times 10^{-11} \pm 1.92 \times 10^{-11} \pm 3.33 \times 10^{-13}$	$1.62 \times 10^{-1} \pm 8.43 \times 10^{-2} \pm 1.46 \times 10^{-3}$

Table C.4: Invariant pair cross section (mb GeV/c $^{-4}$) for fragmentation photons associated with hadrons with p_T from 3.6 – 5.0 GeV/c.

$p_{T,\gamma}$ (GeV/c)	Inv. cross sec. \pm stat. \pm sys.	Ratio \pm stat. \pm sys.
1.5 – 2.0	$9.57 \times 10^{-7} \pm 3.18 \times 10^{-7} \pm 9.17 \times 10^{-7}$	$1.72 \times 10^{-2} \pm 5.69 \times 10^{-3} \pm 1.64 \times 10^{-2}$
2.0 – 2.5	$7.06 \times 10^{-7} \pm 9.04 \times 10^{-8} \pm 6.03 \times 10^{-8}$	$4.29 \times 10^{-2} \pm 5.50 \times 10^{-3} \pm 3.66 \times 10^{-3}$
2.5 – 3.5	$2.10 \times 10^{-7} \pm 2.30 \times 10^{-8} \pm 1.04 \times 10^{-8}$	$5.02 \times 10^{-2} \pm 5.49 \times 10^{-3} \pm 2.48 \times 10^{-3}$
3.5 – 5.0	$3.49 \times 10^{-8} \pm 5.03 \times 10^{-9} \pm 3.18 \times 10^{-9}$	$5.88 \times 10^{-2} \pm 8.49 \times 10^{-3} \pm 5.36 \times 10^{-3}$
5.0 – 8.0	$3.19 \times 10^{-9} \pm 9.45 \times 10^{-10} \pm 1.05 \times 10^{-11}$	$5.51 \times 10^{-2} \pm 1.63 \times 10^{-2} \pm 1.82 \times 10^{-4}$
8.0 – 15.0	$1.97 \times 10^{-10} \pm 6.77 \times 10^{-11} \pm 3.94 \times 10^{-11}$	$1.32 \times 10^{-1} \pm 4.54 \times 10^{-2} \pm 2.65 \times 10^{-2}$

Table C.5: Invariant pair cross section (mb GeV/c $^{-4}$) for fragmentation photons associated with hadrons with p_T from 2.0 – 5.0 GeV/c.

C.2 Associated photon p_{out}

p_{out}	$1/N_{trig} dN/dp_{out,\gamma}$		
	$\gamma_{inc} \pm$ stat.	$\gamma_{dec} \pm$ stat. \pm sys.	$\gamma_{frag} \pm$ stat. \pm sys.
0.1	$2.17 \times 10^{-3} \pm 1.19 \times 10^{-5}$	$2.06 \times 10^{-3} \pm 1.86 \times 10^{-5} \pm 6.84 \times 10^{-5}$	$1.11 \times 10^{-4} \pm 2.21 \times 10^{-5} \pm 6.84 \times 10^{-5}$
0.3	$1.97 \times 10^{-3} \pm 1.20 \times 10^{-5}$	$1.89 \times 10^{-3} \pm 1.93 \times 10^{-5} \pm 1.78 \times 10^{-5}$	$7.58 \times 10^{-5} \pm 2.27 \times 10^{-5} \pm 1.78 \times 10^{-5}$
0.5	$1.66 \times 10^{-3} \pm 1.21 \times 10^{-5}$	$1.61 \times 10^{-3} \pm 1.92 \times 10^{-5} \pm 2.68 \times 10^{-5}$	$5.41 \times 10^{-5} \pm 2.27 \times 10^{-5} \pm 2.68 \times 10^{-5}$
0.7	$1.04 \times 10^{-3} \pm 1.22 \times 10^{-5}$	$1.00 \times 10^{-3} \pm 1.91 \times 10^{-5} \pm 2.63 \times 10^{-5}$	$4.23 \times 10^{-5} \pm 2.27 \times 10^{-5} \pm 2.63 \times 10^{-5}$
0.9	$5.30 \times 10^{-4} \pm 1.08 \times 10^{-5}$	$5.17 \times 10^{-4} \pm 1.61 \times 10^{-5} \pm 1.26 \times 10^{-5}$	$1.31 \times 10^{-5} \pm 1.94 \times 10^{-5} \pm 1.26 \times 10^{-5}$
1.1	$2.31 \times 10^{-4} \pm 5.19 \times 10^{-6}$	$2.38 \times 10^{-4} \pm 9.77 \times 10^{-6} \pm 3.75 \times 10^{-6}$	$-7.53 \times 10^{-6} \pm 1.11 \times 10^{-5} \pm 3.75 \times 10^{-6}$
1.3	$9.78 \times 10^{-5} \pm 2.95 \times 10^{-6}$	$8.68 \times 10^{-5} \pm 5.11 \times 10^{-6} \pm 3.70 \times 10^{-6}$	$1.09 \times 10^{-5} \pm 5.90 \times 10^{-6} \pm 3.70 \times 10^{-6}$
1.5	$4.57 \times 10^{-5} \pm 1.87 \times 10^{-6}$	$4.69 \times 10^{-5} \pm 3.55 \times 10^{-6} \pm 1.24 \times 10^{-6}$	$-1.16 \times 10^{-6} \pm 4.01 \times 10^{-6} \pm 1.24 \times 10^{-6}$
1.7	$2.34 \times 10^{-5} \pm 1.24 \times 10^{-6}$	$2.73 \times 10^{-5} \pm 2.94 \times 10^{-6} \pm 1.34 \times 10^{-6}$	$-3.86 \times 10^{-6} \pm 3.19 \times 10^{-6} \pm 1.34 \times 10^{-6}$
1.9	$1.01 \times 10^{-5} \pm 8.31 \times 10^{-7}$	$1.14 \times 10^{-5} \pm 1.84 \times 10^{-6} \pm 1.50 \times 10^{-7}$	$-1.35 \times 10^{-6} \pm 2.02 \times 10^{-6} \pm 1.50 \times 10^{-7}$
2.1	$5.49 \times 10^{-6} \pm 6.13 \times 10^{-7}$	$5.63 \times 10^{-6} \pm 1.01 \times 10^{-6} \pm 2.68 \times 10^{-7}$	$-1.41 \times 10^{-7} \pm 1.18 \times 10^{-6} \pm 2.68 \times 10^{-7}$
2.3	$1.33 \times 10^{-6} \pm 3.58 \times 10^{-7}$	$2.26 \times 10^{-6} \pm 7.21 \times 10^{-7} \pm 1.97 \times 10^{-7}$	$-9.36 \times 10^{-7} \pm 8.05 \times 10^{-7} \pm 1.97 \times 10^{-7}$
2.5	$1.27 \times 10^{-6} \pm 2.87 \times 10^{-7}$	$1.50 \times 10^{-6} \pm 5.64 \times 10^{-7} \pm 4.52 \times 10^{-7}$	$-2.29 \times 10^{-7} \pm 6.32 \times 10^{-7} \pm 4.52 \times 10^{-7}$
2.7	$1.13 \times 10^{-6} \pm 2.76 \times 10^{-7}$	$1.30 \times 10^{-6} \pm 4.75 \times 10^{-7} \pm 2.81 \times 10^{-7}$	$-1.74 \times 10^{-7} \pm 5.49 \times 10^{-7} \pm 2.81 \times 10^{-7}$
2.9	$1.28 \times 10^{-7} \pm 1.44 \times 10^{-7}$	$3.48 \times 10^{-7} \pm 2.79 \times 10^{-7} \pm 5.49 \times 10^{-7}$	$-2.21 \times 10^{-7} \pm 3.14 \times 10^{-7} \pm 5.49 \times 10^{-7}$
3.1	$5.68 \times 10^{-8} \pm 6.74 \times 10^{-8}$	$2.83 \times 10^{-7} \pm 3.55 \times 10^{-7} \pm 1.41 \times 10^{-7}$	$-2.26 \times 10^{-7} \pm 3.61 \times 10^{-7} \pm 1.41 \times 10^{-7}$

Table C.6: p_{out} (GeV/c) for photons with p_T from 1.5 – 8.0 GeV/c associated with hadrons with p_T from 2.0 – 2.3 GeV/c and $|\Delta\phi| < 0.7$.

p_{out}	$1/N_{trig}dN/dp_{out,\gamma}$		
	$\gamma_{inc} \pm \text{stat.}$	$\gamma_{dec} \pm \text{stat.} \pm \text{sys.}$	$\gamma_{frag} \pm \text{stat.} \pm \text{sys.}$
0.1	$2.38 \times 10^{-3} \pm 1.05 \times 10^{-5}$	$2.26 \times 10^{-3} \pm 1.85 \times 10^{-5} \pm 2.37 \times 10^{-5}$	$1.21 \times 10^{-4} \pm 2.13 \times 10^{-5} \pm 2.37 \times 10^{-5}$
0.3	$2.09 \times 10^{-3} \pm 1.05 \times 10^{-5}$	$1.99 \times 10^{-3} \pm 1.85 \times 10^{-5} \pm 1.50 \times 10^{-5}$	$1.03 \times 10^{-4} \pm 2.12 \times 10^{-5} \pm 1.50 \times 10^{-5}$
0.5	$1.66 \times 10^{-3} \pm 1.04 \times 10^{-5}$	$1.61 \times 10^{-3} \pm 1.81 \times 10^{-5} \pm 4.10 \times 10^{-5}$	$4.68 \times 10^{-5} \pm 2.09 \times 10^{-5} \pm 4.10 \times 10^{-5}$
0.7	$9.37 \times 10^{-4} \pm 9.98 \times 10^{-6}$	$8.90 \times 10^{-4} \pm 1.61 \times 10^{-5} \pm 1.79 \times 10^{-5}$	$4.61 \times 10^{-5} \pm 1.90 \times 10^{-5} \pm 1.79 \times 10^{-5}$
0.9	$4.83 \times 10^{-4} \pm 8.81 \times 10^{-6}$	$4.76 \times 10^{-4} \pm 1.42 \times 10^{-5} \pm 3.58 \times 10^{-5}$	$7.24 \times 10^{-6} \pm 1.67 \times 10^{-5} \pm 3.58 \times 10^{-5}$
1.1	$2.06 \times 10^{-4} \pm 4.51 \times 10^{-6}$	$2.41 \times 10^{-4} \pm 9.64 \times 10^{-6} \pm 1.97 \times 10^{-5}$	$-3.49 \times 10^{-5} \pm 1.06 \times 10^{-5} \pm 1.97 \times 10^{-5}$
1.3	$9.02 \times 10^{-5} \pm 2.65 \times 10^{-6}$	$9.87 \times 10^{-5} \pm 5.82 \times 10^{-6} \pm 2.45 \times 10^{-6}$	$-8.49 \times 10^{-6} \pm 6.39 \times 10^{-6} \pm 2.45 \times 10^{-6}$
1.5	$4.03 \times 10^{-5} \pm 1.69 \times 10^{-6}$	$4.75 \times 10^{-5} \pm 3.91 \times 10^{-6} \pm 3.93 \times 10^{-6}$	$-7.23 \times 10^{-6} \pm 4.26 \times 10^{-6} \pm 3.93 \times 10^{-6}$
1.7	$2.08 \times 10^{-5} \pm 1.16 \times 10^{-6}$	$2.33 \times 10^{-5} \pm 2.54 \times 10^{-6} \pm 1.30 \times 10^{-6}$	$-2.52 \times 10^{-6} \pm 2.79 \times 10^{-6} \pm 1.30 \times 10^{-6}$
1.9	$8.35 \times 10^{-6} \pm 7.53 \times 10^{-7}$	$1.16 \times 10^{-5} \pm 1.87 \times 10^{-6} \pm 5.03 \times 10^{-7}$	$-3.24 \times 10^{-6} \pm 2.01 \times 10^{-6} \pm 5.03 \times 10^{-7}$
2.1	$3.34 \times 10^{-6} \pm 5.37 \times 10^{-7}$	$2.45 \times 10^{-6} \pm 8.56 \times 10^{-7} \pm 4.75 \times 10^{-7}$	$8.88 \times 10^{-7} \pm 1.01 \times 10^{-6} \pm 4.75 \times 10^{-7}$
2.3	$3.21 \times 10^{-6} \pm 4.24 \times 10^{-7}$	$4.64 \times 10^{-6} \pm 9.80 \times 10^{-7} \pm 2.23 \times 10^{-7}$	$-1.43 \times 10^{-6} \pm 1.07 \times 10^{-6} \pm 2.23 \times 10^{-7}$
2.5	$1.73 \times 10^{-6} \pm 3.10 \times 10^{-7}$	$1.60 \times 10^{-6} \pm 5.23 \times 10^{-7} \pm 2.87 \times 10^{-7}$	$1.31 \times 10^{-7} \pm 6.07 \times 10^{-7} \pm 2.87 \times 10^{-7}$
2.7	$8.84 \times 10^{-7} \pm 2.50 \times 10^{-7}$	$1.09 \times 10^{-6} \pm 4.22 \times 10^{-7} \pm 2.59 \times 10^{-7}$	$-2.06 \times 10^{-7} \pm 4.91 \times 10^{-7} \pm 2.59 \times 10^{-7}$

Table C.7: p_{out} (GeV/c) for photons with p_T from 1.5 – 8.0 GeV/c associated with hadrons with p_T from 2.3 – 2.8 GeV/c and $|\Delta\phi| < 0.7$.

p_{out}	$1/N_{trig}dN/dp_{out,\gamma}$		
	$\gamma_{inc} \pm \text{stat.}$	$\gamma_{dec} \pm \text{stat.} \pm \text{sys.}$	$\gamma_{frag} \pm \text{stat.} \pm \text{sys.}$
0.1	$2.78 \times 10^{-3} \pm 1.15 \times 10^{-5}$	$2.57 \times 10^{-3} \pm 2.16 \times 10^{-5} \pm 2.23 \times 10^{-5}$	$2.14 \times 10^{-4} \pm 2.45 \times 10^{-5} \pm 2.23 \times 10^{-5}$
0.3	$2.32 \times 10^{-3} \pm 1.11 \times 10^{-5}$	$2.16 \times 10^{-3} \pm 2.09 \times 10^{-5} \pm 4.97 \times 10^{-5}$	$1.55 \times 10^{-4} \pm 2.36 \times 10^{-5} \pm 4.97 \times 10^{-5}$
0.5	$1.67 \times 10^{-3} \pm 1.03 \times 10^{-5}$	$1.67 \times 10^{-3} \pm 2.16 \times 10^{-5} \pm 9.35 \times 10^{-6}$	$3.41 \times 10^{-6} \pm 2.39 \times 10^{-5} \pm 9.35 \times 10^{-6}$
0.7	$8.77 \times 10^{-4} \pm 9.05 \times 10^{-6}$	$8.81 \times 10^{-4} \pm 1.81 \times 10^{-5} \pm 2.05 \times 10^{-5}$	$-3.64 \times 10^{-6} \pm 2.02 \times 10^{-5} \pm 2.05 \times 10^{-5}$
0.9	$4.63 \times 10^{-4} \pm 8.07 \times 10^{-6}$	$4.77 \times 10^{-4} \pm 1.54 \times 10^{-5} \pm 2.01 \times 10^{-5}$	$-1.33 \times 10^{-5} \pm 1.74 \times 10^{-5} \pm 2.01 \times 10^{-5}$
1.1	$2.09 \times 10^{-4} \pm 4.60 \times 10^{-6}$	$2.49 \times 10^{-4} \pm 1.19 \times 10^{-5} \pm 1.24 \times 10^{-5}$	$-4.01 \times 10^{-5} \pm 1.28 \times 10^{-5} \pm 1.24 \times 10^{-5}$
1.3	$9.05 \times 10^{-5} \pm 2.71 \times 10^{-6}$	$9.40 \times 10^{-5} \pm 5.83 \times 10^{-6} \pm 2.39 \times 10^{-6}$	$-3.50 \times 10^{-6} \pm 6.43 \times 10^{-6} \pm 2.39 \times 10^{-6}$
1.5	$4.14 \times 10^{-5} \pm 1.77 \times 10^{-6}$	$3.89 \times 10^{-5} \pm 3.52 \times 10^{-6} \pm 4.30 \times 10^{-6}$	$2.53 \times 10^{-6} \pm 3.94 \times 10^{-6} \pm 4.30 \times 10^{-6}$
1.7	$2.15 \times 10^{-5} \pm 1.25 \times 10^{-6}$	$2.31 \times 10^{-5} \pm 2.97 \times 10^{-6} \pm 1.63 \times 10^{-6}$	$-1.52 \times 10^{-6} \pm 3.23 \times 10^{-6} \pm 1.63 \times 10^{-6}$
1.9	$1.10 \times 10^{-5} \pm 8.62 \times 10^{-7}$	$1.10 \times 10^{-5} \pm 1.69 \times 10^{-6} \pm 6.75 \times 10^{-7}$	$-4.15 \times 10^{-9} \pm 1.90 \times 10^{-6} \pm 6.75 \times 10^{-7}$
2.1	$4.84 \times 10^{-6} \pm 5.94 \times 10^{-7}$	$2.79 \times 10^{-6} \pm 1.85 \times 10^{-6} \pm 1.09 \times 10^{-6}$	$2.05 \times 10^{-6} \pm 1.94 \times 10^{-6} \pm 1.09 \times 10^{-6}$
2.3	$2.15 \times 10^{-6} \pm 4.05 \times 10^{-7}$	$1.81 \times 10^{-6} \pm 7.62 \times 10^{-7} \pm 2.29 \times 10^{-7}$	$3.37 \times 10^{-7} \pm 8.63 \times 10^{-7} \pm 2.29 \times 10^{-7}$
2.5	$1.25 \times 10^{-6} \pm 3.13 \times 10^{-7}$	$6.95 \times 10^{-7} \pm 4.67 \times 10^{-7} \pm 3.60 \times 10^{-7}$	$5.55 \times 10^{-7} \pm 5.62 \times 10^{-7} \pm 3.60 \times 10^{-7}$
2.7	$2.52 \times 10^{-7} \pm 1.73 \times 10^{-7}$	$5.60 \times 10^{-7} \pm 3.89 \times 10^{-7} \pm 2.40 \times 10^{-7}$	$-3.09 \times 10^{-7} \pm 4.26 \times 10^{-7} \pm 2.40 \times 10^{-7}$
2.9	$2.89 \times 10^{-7} \pm 1.88 \times 10^{-7}$	$3.06 \times 10^{-7} \pm 3.03 \times 10^{-7} \pm 2.46 \times 10^{-7}$	$-1.65 \times 10^{-8} \pm 3.57 \times 10^{-7} \pm 2.46 \times 10^{-7}$
3.1	$4.32 \times 10^{-8} \pm 7.65 \times 10^{-8}$	$1.69 \times 10^{-8} \pm 1.20 \times 10^{-7} \pm 8.44 \times 10^{-9}$	$2.64 \times 10^{-8} \pm 1.43 \times 10^{-7} \pm 8.44 \times 10^{-9}$

Table C.8: p_{out} (GeV/c) for photons with p_T from 1.5 – 8.0 GeV/c associated with hadrons with p_T from 2.8 – 3.6 GeV/c and $|\Delta\phi| < 0.7$.

p_{out}	$1/N_{trig}dN/dp_{out,\gamma}$		
	$\gamma_{inc} \pm \text{stat.}$	$\gamma_{dec} \pm \text{stat.} \pm \text{sys.}$	$\gamma_{frag} \pm \text{stat.} \pm \text{sys.}$
0.1	$3.67 \times 10^{-3} \pm 1.77 \times 10^{-5}$	$3.34 \times 10^{-3} \pm 3.32 \times 10^{-5} \pm 4.99 \times 10^{-5}$	$3.28 \times 10^{-4} \pm 3.76 \times 10^{-5} \pm 4.99 \times 10^{-5}$
0.3	$2.98 \times 10^{-3} \pm 1.67 \times 10^{-5}$	$2.70 \times 10^{-3} \pm 3.20 \times 10^{-5} \pm 7.73 \times 10^{-5}$	$2.83 \times 10^{-4} \pm 3.61 \times 10^{-5} \pm 7.73 \times 10^{-5}$
0.5	$1.86 \times 10^{-3} \pm 1.41 \times 10^{-5}$	$1.84 \times 10^{-3} \pm 3.09 \times 10^{-5} \pm 1.54 \times 10^{-5}$	$2.91 \times 10^{-5} \pm 3.40 \times 10^{-5} \pm 1.54 \times 10^{-5}$
0.7	$9.26 \times 10^{-4} \pm 1.13 \times 10^{-5}$	$9.10 \times 10^{-4} \pm 2.55 \times 10^{-5} \pm 3.75 \times 10^{-5}$	$1.57 \times 10^{-5} \pm 2.79 \times 10^{-5} \pm 3.75 \times 10^{-5}$
0.9	$5.00 \times 10^{-4} \pm 9.81 \times 10^{-6}$	$4.96 \times 10^{-4} \pm 2.23 \times 10^{-5} \pm 3.17 \times 10^{-5}$	$3.54 \times 10^{-6} \pm 2.43 \times 10^{-5} \pm 3.17 \times 10^{-5}$
1.1	$2.26 \times 10^{-4} \pm 6.15 \times 10^{-6}$	$2.59 \times 10^{-4} \pm 1.88 \times 10^{-5} \pm 1.85 \times 10^{-5}$	$-3.25 \times 10^{-5} \pm 1.98 \times 10^{-5} \pm 1.85 \times 10^{-5}$
1.3	$1.03 \times 10^{-4} \pm 3.91 \times 10^{-6}$	$1.49 \times 10^{-4} \pm 3.74 \times 10^{-5} \pm 9.48 \times 10^{-6}$	$-4.53 \times 10^{-5} \pm 3.76 \times 10^{-5} \pm 9.48 \times 10^{-6}$
1.5	$4.51 \times 10^{-5} \pm 2.51 \times 10^{-6}$	$5.15 \times 10^{-5} \pm 7.13 \times 10^{-6} \pm 3.80 \times 10^{-6}$	$-6.38 \times 10^{-6} \pm 7.56 \times 10^{-6} \pm 3.80 \times 10^{-6}$
1.7	$2.55 \times 10^{-5} \pm 1.88 \times 10^{-6}$	$3.31 \times 10^{-5} \pm 6.85 \times 10^{-6} \pm 1.46 \times 10^{-6}$	$-7.60 \times 10^{-6} \pm 7.10 \times 10^{-6} \pm 1.46 \times 10^{-6}$
1.9	$1.10 \times 10^{-5} \pm 1.26 \times 10^{-6}$	$1.49 \times 10^{-5} \pm 4.55 \times 10^{-6} \pm 7.09 \times 10^{-7}$	$-3.95 \times 10^{-6} \pm 4.72 \times 10^{-6} \pm 7.09 \times 10^{-7}$
2.1	$5.56 \times 10^{-6} \pm 9.08 \times 10^{-7}$	$7.84 \times 10^{-6} \pm 2.19 \times 10^{-6} \pm 1.94 \times 10^{-6}$	$-2.28 \times 10^{-6} \pm 2.37 \times 10^{-6} \pm 1.94 \times 10^{-6}$
2.3	$2.85 \times 10^{-6} \pm 5.94 \times 10^{-7}$	$2.80 \times 10^{-6} \pm 1.20 \times 10^{-6} \pm 4.91 \times 10^{-7}$	$5.55 \times 10^{-8} \pm 1.34 \times 10^{-6} \pm 4.91 \times 10^{-7}$
2.5	$1.57 \times 10^{-6} \pm 4.57 \times 10^{-7}$	$1.38 \times 10^{-6} \pm 8.91 \times 10^{-7} \pm 4.33 \times 10^{-7}$	$1.82 \times 10^{-7} \pm 1.00 \times 10^{-6} \pm 4.33 \times 10^{-7}$
2.7	$7.48 \times 10^{-7} \pm 3.15 \times 10^{-7}$	$1.05 \times 10^{-6} \pm 6.96 \times 10^{-7} \pm 3.12 \times 10^{-7}$	$-3.00 \times 10^{-7} \pm 7.64 \times 10^{-7} \pm 3.12 \times 10^{-7}$
2.9	$3.26 \times 10^{-7} \pm 2.79 \times 10^{-7}$	$5.10 \times 10^{-8} \pm 2.53 \times 10^{-7} \pm 5.70 \times 10^{-8}$	$2.75 \times 10^{-7} \pm 3.77 \times 10^{-7} \pm 5.70 \times 10^{-8}$
3.1	$8.09 \times 10^{-8} \pm 1.09 \times 10^{-7}$	$-6.75 \times 10^{-8} \pm 1.06 \times 10^{-8} \pm 3.38 \times 10^{-8}$	$1.48 \times 10^{-7} \pm 1.09 \times 10^{-7} \pm 3.38 \times 10^{-8}$

Table C.9: p_{out} (GeV/c) for photons with p_T from 1.5 – 8.0 GeV/c associated with hadrons with p_T from 3.6 – 5.0 GeV/c and $|\Delta\phi| < 0.7$.

p_{out}	$1/N_{trig}dN/dp_{out,\gamma}$		
	$\gamma_{inc} \pm \text{stat.}$	$\gamma_{dec} \pm \text{stat.} \pm \text{sys.}$	$\gamma_{frag} \pm \text{stat.} \pm \text{sys.}$
0.1	$2.50 \times 10^{-3} \pm 6.30 \times 10^{-6}$	$2.35 \times 10^{-3} \pm 1.07 \times 10^{-5} \pm 4.21 \times 10^{-5}$	$1.55 \times 10^{-4} \pm 1.24 \times 10^{-5} \pm 4.21 \times 10^{-5}$
0.3	$2.17 \times 10^{-3} \pm 6.27 \times 10^{-6}$	$2.05 \times 10^{-3} \pm 1.07 \times 10^{-5} \pm 2.83 \times 10^{-5}$	$1.20 \times 10^{-4} \pm 1.24 \times 10^{-5} \pm 2.83 \times 10^{-5}$
0.5	$1.68 \times 10^{-3} \pm 6.17 \times 10^{-6}$	$1.64 \times 10^{-4} \pm 1.07 \times 10^{-5} \pm 2.27 \times 10^{-5}$	$3.88 \times 10^{-5} \pm 1.23 \times 10^{-5} \pm 2.27 \times 10^{-5}$
0.7	$9.63 \times 10^{-4} \pm 6.00 \times 10^{-6}$	$9.31 \times 10^{-4} \pm 9.89 \times 10^{-6} \pm 9.77 \times 10^{-6}$	$3.16 \times 10^{-5} \pm 1.16 \times 10^{-5} \pm 9.77 \times 10^{-6}$
0.9	$4.98 \times 10^{-4} \pm 5.29 \times 10^{-6}$	$4.93 \times 10^{-4} \pm 8.48 \times 10^{-6} \pm 2.28 \times 10^{-5}$	$4.75 \times 10^{-6} \pm 1.00 \times 10^{-5} \pm 2.28 \times 10^{-5}$
1.1	$2.18 \times 10^{-4} \pm 2.67 \times 10^{-6}$	$2.43 \times 10^{-4} \pm 5.68 \times 10^{-6} \pm 2.25 \times 10^{-6}$	$-2.57 \times 10^{-5} \pm 6.28 \times 10^{-6} \pm 2.25 \times 10^{-6}$
1.3	$9.42 \times 10^{-5} \pm 1.55 \times 10^{-6}$	$9.77 \times 10^{-5} \pm 4.42 \times 10^{-6} \pm 2.61 \times 10^{-7}$	$-3.53 \times 10^{-6} \pm 4.69 \times 10^{-6} \pm 2.61 \times 10^{-7}$
1.5	$4.29 \times 10^{-5} \pm 9.88 \times 10^{-7}$	$4.58 \times 10^{-5} \pm 2.09 \times 10^{-6} \pm 5.20 \times 10^{-7}$	$-2.88 \times 10^{-6} \pm 2.31 \times 10^{-6} \pm 5.20 \times 10^{-7}$
1.7	$2.23 \times 10^{-5} \pm 6.73 \times 10^{-7}$	$2.56 \times 10^{-5} \pm 1.63 \times 10^{-6} \pm 1.32 \times 10^{-6}$	$-3.25 \times 10^{-6} \pm 1.76 \times 10^{-6} \pm 1.32 \times 10^{-6}$
1.9	$9.76 \times 10^{-6} \pm 4.49 \times 10^{-7}$	$1.17 \times 10^{-5} \pm 1.07 \times 10^{-6} \pm 1.90 \times 10^{-7}$	$-1.93 \times 10^{-6} \pm 1.16 \times 10^{-6} \pm 1.90 \times 10^{-7}$
2.1	$4.64 \times 10^{-6} \pm 3.24 \times 10^{-7}$	$4.16 \times 10^{-6} \pm 6.39 \times 10^{-7} \pm 9.78 \times 10^{-8}$	$4.78 \times 10^{-7} \pm 7.16 \times 10^{-7} \pm 9.78 \times 10^{-8}$
2.3	$2.26 \times 10^{-6} \pm 2.18 \times 10^{-7}$	$3.01 \times 10^{-6} \pm 4.63 \times 10^{-7} \pm 1.03 \times 10^{-7}$	$-7.48 \times 10^{-7} \pm 5.12 \times 10^{-7} \pm 1.03 \times 10^{-7}$
2.5	$1.45 \times 10^{-6} \pm 1.67 \times 10^{-7}$	$1.35 \times 10^{-6} \pm 2.99 \times 10^{-7} \pm 2.20 \times 10^{-7}$	$9.21 \times 10^{-8} \pm 3.42 \times 10^{-7} \pm 2.20 \times 10^{-7}$
2.7	$8.29 \times 10^{-7} \pm 1.39 \times 10^{-7}$	$1.05 \times 10^{-6} \pm 2.47 \times 10^{-7} \pm 1.56 \times 10^{-7}$	$-2.24 \times 10^{-7} \pm 2.83 \times 10^{-7} \pm 1.56 \times 10^{-7}$
2.9	$1.01 \times 10^{-7} \pm 7.71 \times 10^{-8}$	$2.02 \times 10^{-7} \pm 1.44 \times 10^{-7} \pm 1.45 \times 10^{-7}$	$-1.01 \times 10^{-7} \pm 1.63 \times 10^{-7} \pm 1.45 \times 10^{-7}$
3.1	$1.04 \times 10^{-8} \pm 3.37 \times 10^{-8}$	$9.95 \times 10^{-8} \pm 1.41 \times 10^{-7} \pm 4.98 \times 10^{-8}$	$-8.91 \times 10^{-8} \pm 1.45 \times 10^{-7} \pm 4.98 \times 10^{-8}$

Table C.10: p_{out} (GeV/c) for photons with p_T from 1.5 – 8.0 GeV/c associated with hadrons with p_T from 2.0 – 5.0 GeV/c and $|\Delta\phi| < 0.7$.

C.3 Associated photon $\sqrt{\langle p_{out}^2 \rangle}$ and $\sqrt{\langle j_T^2 \rangle}$

$p_{T,h}$ (GeV/c)	$\sqrt{\langle p_{out, \gamma_{inc}}^2 \rangle} \pm \text{stat.}$	$\sqrt{\langle j_{T, \gamma_{inc}}^2 \rangle} \pm \text{stat.}$
2.0 – 2.3	0.536 ± 0.00137	0.522 ± 0.001110
2.3 – 2.8	0.514 ± 0.00112	0.471 ± 0.000876
2.8 – 3.6	0.495 ± 0.00103	0.421 ± 0.000788
3.6 – 5.0	0.474 ± 0.00117	0.359 ± 0.000873

Table C.11: Inclusive photon $\sqrt{\langle p_{out}^2 \rangle}$ and $\sqrt{\langle j_T^2 \rangle}$ for each trigger hadron bin. Pairs required to have $|\Delta\phi| < 0.7$ and photons restricted to p_T from 1.5 – 8.0 GeV/c.

$p_{T,h}$ (GeV/c)	$\sqrt{\langle p_{out, \gamma_{dec}}^2 \rangle} \pm \text{stat.} \pm \text{sys.}$	$\sqrt{\langle j_{T, \gamma_{dec}}^2 \rangle} \pm \text{stat.} \pm \text{sys.}$
2.0 – 2.3	$0.542 \pm 0.00229 \pm 0.00653$	$0.527 \pm 0.00188 \pm 0.00577$
2.3 – 2.8	$0.529 \pm 0.00209 \pm 0.00428$	$0.485 \pm 0.00166 \pm 0.01500$
2.8 – 3.6	$0.512 \pm 0.00219 \pm 0.00313$	$0.444 \pm 0.00166 \pm 0.00462$
3.6 – 5.0	$0.500 \pm 0.00313 \pm 0.01070$	$0.378 \pm 0.00237 \pm 0.00384$

Table C.12: Decay photon $\sqrt{\langle p_{out}^2 \rangle}$ and $\sqrt{\langle j_T^2 \rangle}$ for each trigger hadron bin. Pairs required to have $|\Delta\phi| < 0.7$ and photons restricted to p_T from 1.5 – 8.0 GeV/c.

$p_{T,h}$ (GeV/c)	$\sqrt{\langle p_{out, \gamma_{frag}}^2 \rangle} \pm \text{stat.} \pm \text{sys.}$	$\sqrt{\langle j_{T, \gamma_{frag}}^2 \rangle} \pm \text{stat.} \pm \text{sys.}$
2.0 – 2.3	$0.693 \pm 0.0639 \pm 0.0241$	$0.722 \pm 0.0351 \pm 0.0367$
2.3 – 2.8	$0.684 \pm 0.0528 \pm 0.0737$	$0.667 \pm 0.0267 \pm 0.0415$
2.8 – 3.6	$0.585 \pm 0.0413 \pm 0.0498$	$0.565 \pm 0.0208 \pm 0.0592$
3.6 – 5.0	$0.618 \pm 0.0482 \pm 0.0546$	$0.599 \pm 0.0228 \pm 0.0336$

Table C.13: Fragmentation photon $\sqrt{\langle p_{out}^2 \rangle}$ and $\sqrt{\langle j_T^2 \rangle}$ for each trigger hadron bin. Pairs required to have $|\Delta\phi| < 0.7$ and photons restricted to p_T from 1.5 – 8.0 GeV/c.